TU Delft

Delft University of Technology

Sound emission in offshore pile driving by vibratory devices

Gentle driving of piles, the silent way

Molenkamp, T.

DOI
10.4233/uuid:669fde9f-d6cf-41c2-bd2c-20aac24c0417

Publication date
2025

Document Version
Final published version

Citation (APA)
Molenkamp, T. (2025). *Sound emission in offshore pile driving by vibratory devices: Gentle driving of piles, the silent way*. [Dissertation (TU Delft), Delft University of Technology].
https://doi.org/10.4233/uuid:669fde9f-d6cf-41c2-bd2c-20aac24c0417

Important note
To cite this publication, please use the final published version (if applicable).
Please check the document version above.

Copyright
Other than for strictly personal use, it is not permitted to download, forward or distribute the text or part of it, without the consent of the author(s) and/or copyright holder(s), unless the work is under an open content license such as Creative Commons.

Takedown policy
Please contact us and provide details if you believe this document breaches copyrights.
We will remove access to the work immediately and investigate your claim.

This work is downloaded from Delft University of Technology.
For technical reasons the number of authors shown on this cover page is limited to a maximum of 10.

Sound emission in offshore pile driving by vibratory devices

Gentle driving of piles, the silent way

Sound emission in offshore pile driving by vibratory devices

Gentle driving of piles, the silent way

Proefschrift

ter verkrijging van de graad van doctor
aan de Technische Universiteit Delft,
op gezag van de Rector Magnificus Prof.dr.ir. T.H.J.J. van der Hagen,
voorzitter van het College voor Promoties,
in het openbaar te verdedigen op
Woensdag 22 Januari 2025 om 15:00 uur

door

Timo Molenkamp

Master of Science in Civiele Techniek, Technische Universiteit Delft, Nederland
geboren te Enschede, Nederland.

Dit proefschrift is goedgekeurd door de

promotor: Dr.ir. A. Tsouvalas
promotor: Prof.dr. A.V. Metrikine

Samenstelling promotiecommissie bestaat uit:

Rector Magnificus,	voorzitter
Dr. ir. A. Tsouvalas,	Technische Universiteit Delft, promotor
Prof. dr. A.V. Metrikine,	Technische Universiteit Delft, promotor
Onafhankelijke leden:	
Prof.dr. D. Casalino	Technische Universiteit Delft, Nederland
Prof.dr. K.G. Gavin	Technische Universiteit Delft, Nederland
Dr.-Ing. T. Grießler	Leibniz University Hannover, Duitsland
Prof.dr. I. Lopez Arteaga	Technische Universiteit Eindhoven, Nederland
Prof. dr. S. Sorokin	Aalborg Universiteit, Denemarken

This work is part of the GDP project (GROW joint research programme), which is (partly) financed by the *Topsector Energiesubsidie van het Ministerie van Economische Zaken* under grant number TEHE117100.





Keywords: underwater sound, vibratory pile driving, Gentle Driving of Piles

Printed by: Gildeprint B.V. - Enschede

Front & Back: Stijn van der Grinten

Copyright © 2025 by Timo Molenkamp

ISBN 978-94-6496-319-9

An electronic version of this dissertation is available at
https://repository.tudelft.nl/.

Success comes through rapidly fixing our mistakes rather than getting things right the first time.

Tim Harford

Contents

Acronyms xi

Summary xiii

Samenvatting xv

Preface xvii

1 Introduction 1
- 1.1 Offshore pile driving and environmental impact . . . 1
- 1.2 Sound mitigation . . . 4
- 1.3 Sound prediction models . . . 6
- 1.4 Knowledge gaps . . . 8
- 1.5 Objective . . . 9
- 1.6 Outline . . . 10

2 Overview of the mathematical considerations in the development of a three-dimensional pile fluid-soil interaction model 11
- 2.1 Model description . . . 12
- 2.2 Governing equations . . . 13
- 2.3 Modal solution for a thin cylindrical shell . . . 16
  - 2.3.1 Verification of the pile modes . . . 19
- 2.4 Fluid-soil boundary element description . . . 19
  - 2.4.1 Fluid ring source . . . 22
  - 2.4.2 Soil ring source . . . 22
  - 2.4.3 Green's functions of the fluid-soil domain . . . 25
  - 2.4.4 Boundary element matrix . . . 28
- 2.5 Coupling procedure of pile and fluid-soil substructures . . . 29

3 Sound generated in offshore monopile installation by impact pile driving and the effect of asymmetries 31
- 3.1 Introduction . . . 32
- 3.2 Model description . . . 32
- 3.3 The non-symmetric noise field . . . 35
  - 3.3.1 Small-diameter pile . . . 35
  - 3.3.2 Large diameter pile . . . 38

3.3.3 Inclined pile . . . 43
3.4 Conslusions . . . 47

4 The influence of contact relaxation on underwater noise emission and seabed vibrations due to offshore vibratory pile installation 49
4.1 Introduction . . . 50
4.2 Noise and seabed vibrations . . . 51
4.2.1 Model description . . . 51
4.2.2 Governing equations . . . 52
4.2.3 Solution method . . . 54
4.3 Fluid-soil Green's functions . . . 56
4.3.1 Fluid source . . . 57
4.3.2 Soil source . . . 58
4.4 Model verification . . . 59
4.5 Effect of pile-soil interface conditions . . . 61
4.5.1 Pile vibrations . . . 62
4.5.2 Underwater noise field and seabed vibrations . . . 63
4.5.3 Reduced soil shear stiffness . . . 67
4.6 Conclusions . . . 69

5 Underwater noise from vibratory pile driving with non-linear frictional pile-soil interaction 71
5.1 Introduction . . . 72
5.2 Methodology . . . 74
5.2.1 Geometrical characteristics and fundamental equations . . . 74
5.2.2 Driveability analysis . . . 76
5.2.3 Noise prediction analysis . . . 78
5.2.4 Integrating driveability effects in noise prediction analysis . . . 79
5.3 Underwater noise field of a small-size monopile . . . 79
5.3.1 Single harmonic force . . . 80
5.3.2 Periodic force . . . 82
5.3.3 Comparison with limit cases . . . 84
5.3.4 Sensitivity to the driving frequency . . . 86
5.4 Underwater noise field of a large-diameter monopile . . . 88
5.4.1 Comparison with limit cases . . . 88
5.4.2 Effect of driving depth . . . 90
5.4.3 Sensitivity to driving frequency . . . 92
5.5 Conclusions . . . 92

6 Sound generated during gentle driving of piles **95**
6.1 Introduction . . . 96
6.2 Experimental campaign . . . 97
6.2.1 Observations during pile installation . . . 98
6.3 Underwater sound predictions . . . 100
6.3.1 Case study . . . 101
6.3.2 Perfect contact between pile and soil . . . 102
6.3.3 No friction between pile and soil . . . 103
6.4 Discussion . . . 106

7 Conclusions **109**

Bibliography **113**

A Dynamic response of two interacting extensible bars in frictional contact **123**
A.1 Introduction . . . 124
A.2 Mathematical Formulation . . . 125
A.2.1 Governing equations . . . 125
A.2.2 Solution method . . . 126
A.2.3 Linear equivalent model . . . 128
A.3 Results . . . 130
A.4 Convergence . . . 133
A.5 Conclusions on two extensible bars in frictional contact . . . 133
References . . . 135

B Analytical expressions for the inverse Hankel Transforms **137**

Curriculum Vitæ **141**

List of Publications **143**

Acronyms

ATP Auxiliary Test Pile.

BBC Big Bubble Curtain.

BEM Boundary Element Method.

CPT Cone Penetration Test.

DA Driveability Analysis.

DBBC Double Big Bubble Curtain.

DL Driving Logging.

FEM Finite Element Method.

FFT Fast Fourier Transform.

GDP Gentle Driving of Piles.

HBM Harmonic Balance Method.

IH Impact Hammer.

MTP Main Test Pile.

NF No Friction.

PC Perfect Contact.

PML Perfectly Matched Layer.

PTS Permanent Threshold Shift.

RP Reaction Pile.

SAFE Semi-Analytical Finite Element.

SBBC Single Big Bubble Curtain.

SEL Sound Exposure Level.

SEL_{ss} single-strike Sound Exposure Level.

SPL Sound Pressure Level.

TLM Thin-Layer Method.

TTS Temporary Threshold Shift.

VH Vibratory Hammer.

Summary

Offshore wind energy has gained recognition in Europe as a pivotal solution for transitioning to renewable energy sources. Due to limited land space, the European seas offer immense potential for offshore wind energy. The EU Offshore Renewable Energy Strategy advocates for an accelerated expansion of offshore wind, aiming to achieve 60 GW of capacity by 2030 and an ambitious target of 300 GW by 2050. This growth necessitates substantial investments and has been further underscored by the need to replace Russian fossil fuel imports, prompting additional targets for offshore wind capacity.

A major environmental concern in offshore wind farm construction is the substantial underwater sound generated during the installation of wind turbine foundations. Most North Sea wind turbines are founded on monopile structures, which involve driving a single hollow cylindrical steel pile into the seabed using impact hammers. This process emits powerful underwater pressure waves that impact marine animals dependent on underwater sound for navigation, communication, and predator-prey relationships. Studies have shown that elevated underwater noise adversely affects marine animals' physical health and behaviour, with severity dependent on sound pressure levels, frequency bands, and water particle motion. Constructing these wind farms, especially installing monopile foundations, is one of the loudest human-induced underwater sound sources and generates substantial underwater noise that adversely affects marine life. This results in the need for effective noise mitigation strategies, such as quieter driving tools, to protect marine ecosystems while supporting the expansion of renewable energy infrastructure

This research aims to comprehensively understand and model the sound generation mechanisms during the likely less disturbing installation with vibratory tools, emphasizing the newly developed Gentle Driving of Piles (GDP) technology. Additionally, it extends existing knowledge on impact piling by examining how asymmetric impact forces and pile inclination influence underwater noise and seabed vibrations.

Vibratory pile driving differs from impact piling because the driving procedure is continuous, whereas impact pile driving uses pulses. Therefore, a sound prediction model tailored to vibratory piling has been developed to describe the sound source. Using cylindrical symmetry, the model describes the pile with modes and uses an indirect Boundary Element Method (BEM) formulation to describe the interior and exterior soil and fluid domains. For the sound prediction model developed, the distinct difference compared to traditional sound prediction models for impact pile driving lies in the model description of the pile-soil interaction. First, the effect of linearly relaxing the interface condition between the pile and soil is explored, allowing vertical motion of the pile relative to the soil. This new

model is verified against Finite Element Method (FEM) computations, leading to a parametric study that demonstrates the inadequacy of traditional models for impact pile driving when applied to vibratory pile driving due to the different sound generation mechanisms involved.

Advancing the research further, the complexity of describing the pile-soil interface increases, approaching the physical reality closer to predicting underwater noise during vibratory pile driving. This incorporates a non-linear driveability model to derive realistic interface friction forces, emphasizing the integration of driveability analysis into noise prediction models. The results reveal significant differences from traditional linear models, highlighting the sensitivity of the noise field to system dynamics due to the potential risk of resonance behaviour and, therefore, the sensitivity to excitation spectra during pile driving.

Exploring alternative techniques, the study examines the GDP method as a promising solution for reducing sound levels during vibratory pile driving. Through an experimental campaign, GDP is shown to be more efficient in driveability than traditional vibratory installation. A subsequent analysis is based on hypothetical scenarios to compare sound fields of GDP and traditional vibratory installation, underscoring the potential of GDP in mitigating noise emissions despite the risks posed by resonance at higher harmonics.

In conclusion, the research summarises key insights and contributions to understanding underwater noise generation mechanisms and proposing effective noise mitigation strategies. The key finding, which might be an open door, is that models developed for sound predictions during impact pile driving are not suitable for sound predictions during installation with a vibratory tool because of the complex dynamic continuous interaction of pile, fluid, and soil. One of the important steps in future research is acquiring and validating against measurement data, an important step to enhance sound prediction models and to stimulate sustainable monopile installation with vibratory techniques.

Samenvatting

Windenergie op zee wordt in Europa gezien als cruciale oplossing voor de transitie naar hernieuwbare energiebronnen. Vanwege beperkte ruimte op land bieden de Europese zeeën enorme mogelijkheden voor het opwekken van windenergie. De EU-strategie voor hernieuwbare energie pleit voor een versnelde uitbreiding van wind op zee, met als doel om een capaciteit te behalen van 60 GW tegen 2030 en de ambitieuze doelstelling van 300 GW tegen 2050. De groei van wind op zee vereist aanzienlijke investeringen, maar de noodzaak is tegenwoordig onderstreept door de Russische fossiele brandstofimporten die vervangen moet worden. Dit heeft geleid tot aanvullende Europese doelstellingen voor de windenergie op zee.

Een belangrijk probleem bij de bouw van windparken op zee is het aanzienlijke onderwatergeluid dat wordt geproduceerd tijdens de installatie van windturbine fundaties. De meeste windturbines in de Noordzee staan op zogenoemde monopile fundaties, waarbij een enkele holle cilindrische stalen paal met behulp van een slaghamer in de zeebodem wordt geheid. Dit proces leidt tot krachtige geluidsdrukgolven onder water die invloed hebben op zeezoogdieren die afhankelijk zijn van onderwatergeluid voor navigatie, communicatie en voedselvoorziening. Studies hebben aangetoond dat verhoogd onderwatergeluid een negatieve invloed heeft op de fysieke gezondheid en het gedrag van zeezoogdieren, waarbij de ernst afhangt van geluidsdrukniveaus, frequentiebanden en trilling van waterdeeltjes. Het bouwen van deze windparken, vooral het installeren van monopile fundaties, is een van de luidste door de mens veroorzaakte geluidsbronnen onder water en genereert aanzienlijk onderwatergeluid dat schadelijk is voor het zeeleven. Dit resulteert in de noodzaak van effectieve geluidbeperkende maatregelen, zoals stillere installatiemethoden, om de ecosystemen in de zee te beschermen en tegelijkertijd de uitbreiding van hernieuwbare energie-infrastructuur te ondersteunen.

Dit onderzoek heeft als doel het in detail begrijpen en modelleren van de geluidsgeneratiemechanismen tijdens de waarschijnlijk minder storende paal installatie methoden die gebruikt maken van trillen in plaats van heien. Er is speciale aandacht voor de nieuw ontwikkelde Gentle Driving of Piles (GDP) technologie, die belooft nog stiller te zijn. Bovendien wordt de bestaande kennis over heigeluid uitgebreid door te onderzoeken hoe asymmetrische hei krachten en paal rotatie invloed hebben op onderwatergeluid en trillingen van de zeebodem.

Paal installatie door middel van trillen verschilt van traditioneel heien omdat de installatie continu is, terwijl heien van pulsen gebruik maakt. Daarom is er een geluidsvoorspellingsmodel van de geluidsbron op maat ontwikkeld voor installatie door middel van

trillen. Gebruik makend van de cilindrische symmetrie, beschrijft het model de paal met modes en wordt de indirecte Boundary Element Method (BEM) gebruikt om het water en de grond rondom en in de paal te modelleren. Het duidelijke verschil van ontwikkelde geluidsvoorspellingsmodel vergeleken met traditionele modellen voor heien ligt in de beschrijving van de interactie tussen paal en grond. Eerst wordt de monolithische beschrijving van de paal-grond interactie linear afgezwakt, waardoor verticale beweging van de paal ten opzichte van de grond mogelijk is. Dit nieuwe model is geverifieerd aan de hand van Finite Element Method (FEM) berekeningen. Vervolgens toont een parametrische studie aan dat traditionele modellen voor heien niet geschikt zijn voor geluidsvoorstellingen gedurende intrillen vanwege de verschillende geluidsgeneratiemechanismen.

Vervolgens wordt de complexiteit van de beschrijving van de paal-grond interactie verhoogd om de realiteit beter te benaderen en het onderwatergeluid tijdens intrillen beter te voorspellen. Dit word bewerktstelligd door een niet-lineair model dat de installatie van de paal voorspeld te gebruiken om de frictie krachten tussen paal en grond af te leiden en deze te integreren in het geluidsvoorstellingsmodel. De resultaten laten significante verschillen zien met traditionele lineaire modellen, waarbij de gevoeligheid van het geluidsveld voor de dynamische eigenschappen van het systeem wordt benadrukt vanwege het potentiële risico op resonantiegedrag.

Bij het verkennen van alternatieve technieken wordt de GDP methode onderzocht, als een veelbelovende oplossing voor het verminderen van geluidsniveaus tijdens het intrillen van palen. Door middel van een experimentele campagne wordt aangetoond dat GDP efficiënter is in paal installatie dan een traditionele intril installatietool. Gebaseerd op een hypothetisch scenario gebaseerd op de experimentele campagne, worden vervolgens de geluidsvelden van GDP en traditioneel intrillen vergeleken, waarbij het potentieel van GDP voor het verminderen van geluidsemissies wordt benadrukt ondanks een groter risico op resonantie.

Het onderzoek geeft inzicht in de belangrijkste mechanismen van onderwatergeluidsgeneratie en effectieve geluidbeperkende oplossingen. De belangrijkste bevinding, misschien een open deur, is dat modellen ontwikkeld voor geluidsvoorspellingen tijdens heien niet geschikt zijn voor geluidsvoorspellingen tijdens installatie door middel van trillen vanwege de complexe dynamische interactie tussen paal, water en grond. Een van de belangrijke stappen in toekomstig onderzoek is het verkrijgen van en valideren aan de hand van meetgegevens, een belangrijke stap om geluidsvoorspellingsmodellen te verbeteren en daarmee monopile installatie door middel van trillen te stimuleren.

Preface

Holy moly, hoe vet is dit!

Freek Vonk

Finalising a PhD trajectory after years of hard work is both a personal and professional journey. While it is a task that ultimately requires individual effort, I am grateful for the huge support I received along the way. I would like to take a moment to reflect on this incredible period of my life.

As a young child, I have been fascinated by solving puzzles and working with technology. My parents told me that jigsaw puzzles were so popular that I started doing them upside down or mixing pieces from multiple boxes. Later on, I enjoyed playing with Lego and Knex and following technical workshops for kids, which naturally led me to choose a technical profile in high school. After receiving excellent marks for the technical courses (and barely passing the languages), I decided to pursue a Bachelor's in Architecture, Urbanism, and Building Sciences in Eindhoven, seeking to combine creativity with technology. However, I soon realised my strengths lay more in technology than design, leading me to a Master's in Structural Engineering at the Faculty of Civil Engineering. Here, I discovered structural dynamics—a field that intrigued me with its counterintuitive principles, such as how adding stiffness can weaken a structure or how mass can improve strength under dynamic loads. This ultimately led to successfully completing a Master's thesis on earthquake engineering.

After my Master's, Apostolos invited me to apply for a PhD position in underwater acoustics. He assured me that seismic and acoustic waves are mathematically similar, and I was enthused by the opportunity to delve deeply into a specialised topic. The journey, however, came with its challenges—particularly during the COVID-19 pandemic, which brought isolation and unforeseen personal hurdles. Despite these difficulties, this thesis is a testament to the hard work and support I have received over the years.

I would like to thank Apostolos and Andrei for their technical guidance throughout the process. Your supervision has been invaluable, from solving mathematical puzzles to qualitative discussions about model assumptions, results and their physical implications.

My Delft University of Technology colleagues also played a significant role in making this journey memorable. You brought joy to my work, from coffee breaks and lunch conversations to social activities and insightful discussions. I am particularly grateful to Athanasios and Evangelos, my office mates and GDP companions for about five years, for enduring my

oddities and engaging in countless discussions. Special thanks also go to Peter for maintaining the Dutch spirit in our chats, Andrei for never missing out on an in-depth non-work discussion, Francesca for her infectious passion (especially for Italian food), Cody for our fun chats, never having enough cup holders in a car, Marco for always trying to get everyone involved, Yaxi for inspiring underwater acoustics debates and co-founding Delft Cymatics, Rens for our nerdy coding humour, Laura for early our morning coffee chats and Tim for your unmistankingly funny German humour and memes. Thank you to you and everyone who made office life enjoyable.

For the most important part, I will switch to Dutch, our shared mother language, to address those closest to me:

Lieve Sofia, jij bent van onschatbare waarde geweest om deze PhD af te ronden. Je steun door de jaren heen, je vertrouwen in mij, en je pogingen om mijn werk te begrijpen betekenen heel veel voor mij. Jij hebt mij geholpen met een meer open en tolerante blik naar de wereld te kijken. Bedankt voor de vele kopjes koffie en lekkernijen die je tijdens het thuiswerken bracht, en voor je zorg voor de kinderen, waardoor ik de tijd en rust had om deze PhD af te maken. Lieve Sverre en Maya, ondanks de slapeloze nachten gaven jullie mij de energie om door te zetten, efficient te werken om zo snel mogelijk weer thuis bij jullie te zijn. Ik had nooit gedacht dat ik tijdens mijn PhD ook zo'n prachtig gezin zou starten, dat binnenkort compleet zal zijn met de komst van de laatste twee.

Lieve ouders, bedankt voor jullie onvoorwaardelijke vertrouwen in mij. Jullie vertrouwen is een stille kracht die mij het vertrouwen gaf om mijn eigen keuzes te maken. Het zou vast niet makkelijk zijn geweest je 17 jaar oude zoon uit huis te zien vertrekken maar ik ben dankbaar dat ik die kans heb mogen krijgen om mijn eigen pad te bewandelen. Manon, ik weet dat het niet altijd makkelijk was om een nerdie broer te hebben, maar ik ben blij dat we de afgelopen jaren naar elkaar toe zijn gegroeid en voor de zorgen die jij thuis met Pim wegneemt. Lieve schoonfamilie, ook jullie steun, interesse, en liefde waardeer ik enorm,van design tot inhoudelijke gesprekken en van oppassen tot spuien over werk, ook bij jullie kon ik mijn ei kwijt. Dank jullie wel.

Tenslotte wil ik al mijn vrienden bedanken, uit Eindhoven, Delft en Haaksbergen. Velen van jullie hebben pogingen gewaagd om te begrijpen wat mijn onderzoek inhoudt, met wisselend succes. De afleiding van alle gezellige momenten die we de afgelopen jaren hebben gehad, maakt het zoveel gemakkelijker om een traject te volbrengen waar eenzaamheid altijd op de loer ligt, zeker tijdens Corona. Ik heb enorm genoten van de biertjes, festivals, spelletjes en tegenwoordig zelfs uitstapjes met kinderen. Uiteindelijk zijn het de sociale activiteiten waarvoor je het doet in het leven. Ook ben ik blij dat het niet altijd lachen, gieren, brullen hoeft te zijn, maar dat de gesprekken de laatste jaren meer diepgang hebben gekregen, zodat ik zelfs, laat ik mij hier beperken tot, werkgerelateerde problemen kon bespreken. Ik ben trots dat ik jullie mijn vrienden mag noemen.

Returning to English, this PhD has been a challenge on both personal and technical levels. Looking back, I am proud to have taken it on, but looking forward excites me even

more. I am glad to be part of Delft Cymatics, where we aim to bridge the gap between academic knowledge and commercial application. I do this with great joy and, therefore, a big shout-out to the Delft Cymatics team. Combining technology and business ignites my enthusiasm once again. The Freek Vonk quote at the start captures this feeling perfectly. His shows, which I now watch with my son, remind me how important it is to communicate science with enthusiasm and accessibility. His passion for sharing his work inspires me, and I hope to channel a fraction of that energy into my career.

Hoe vet is dit—finishing a PhD and embracing a bright future!

Timo Molenkamp
Delft, January 2025

1

Introduction

Wind energy has garnered recognition in Europe as a pivotal solution for transitioning to renewable energy sources. Due to the limited land space, the European seas present immense potential for offshore wind energy. The EU Offshore Renewable Energy Strategy advocates for an accelerated expansion of offshore wind, intending to achieve 60 GW of capacity by 2030 and an ambitious target of 300 GW by 2050 (European Commission, 2020). To contextualise, the cumulative energy generated by offshore wind in Europe in 2020, including the UK, was approximately 25 GW. Figure 1.1 illustrates the anticipated growth in operational capacity and installed sites necessary to meet these targets. This growth necessitates substantial investments, estimated at 24.2 billion euros in 2020 alone (Ramirez et al., 2021). The 2022 Ukraine crisis has further underscored the need for offshore wind to replace Russian fossil fuel imports, prompting the European committee to aim for an additional 30 GW of offshore wind by 2030. Besides the targets mentioned above, the EU Offshore Renewable Energy Strategy emphasises achieving these goals in "happy coexistence" with maritime ecosystems, necessitating minimal environmental impact (Ramirez et al., 2021).

1.1. Offshore pile driving and environmental impact

One major environmental concern in offshore wind farm construction is the substantial underwater sound generated, particularly during the installation of wind turbine foundations. Most North Sea windmills are founded on a monopile structure, a single hollow cylindrical steel pile driven into the seabed using impact hammers. This process emits powerful underwater pressure waves, impacting marine animals that strongly depend on underwater sound for navigation, communication, and predator-prey relationships.

In 2006, the first comprehensive study on the environmental impact of offshore construction and pile driving highlighted significant sound levels extending over long distances

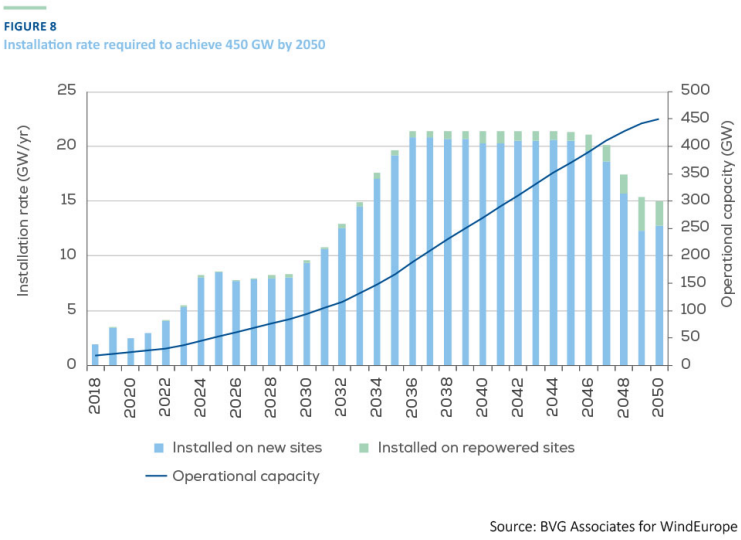


Figure 1.1: Planned offshore wind by 2030 and annual installation in GW (Ramirez et al., 2021)

(Madsen et al., 2006). Elevated underwater noise adversely affects marine animals' physical health and behaviour, with severity dependent on sound pressure levels, frequency bands, and water particle motion. For instance, marine mammals are sensitive to sound pressure, while fishes and invertebrates utilise pressure and particle motion for hearing (Popper and Hawkins, 2018). Exposure to high sound levels, particularly near pile driving sites, can lead to fatal consequences for marine mammals. Mitigation measures can minimise the impact zone size, e.g. a 6 dB reduction of sound levels results in a 4 to 8 times reduction in the exposed water volume (Madsen et al., 2006).

Studies categorise marine mammals based on hearing sensitivities, introducing frequency-dependent weighting functions and noise impact thresholds for changes in auditory sensitivity (Temporary Threshold Shift (TTS) and Permanent Threshold Shift (PTS)) (Southall et al., 2007). These thresholds, based on Sound Exposure Level (SEL), a measure of accumulated sound energy over time, and peak Sound Pressure Level (SPL), a measure of absolute maximum exposure, have been refined through subsequent research (Dekeling et al., 2014; Finneran and Jenkins, 2012; Finneran, 2015; Tougaard et al., 2015). An updated overview, presented by Southall et al. (2019), includes thresholds for impulsive and non-impulsive sound sources (e.g., impact and vibratory piling). The thresholds for various marine species groups are summarised in Table 1.1. Non-impulsive sound is assessed solely based on the threshold for accumulated sound exposure, as this threshold is reached earlier in all cases than the peak sound threshold.

Marine mammal hearing group	TTS onset: SEL non-impulsive	PTS onset: SEL non-impulsive	TTS onset: SEL impulsive	TTS onset: peak SPL impulsive	PTS onset: SEL impulsive	PTS onset: peak SPL impulsive
LF	179	199	168	213	183	219
HF	178	198	170	224	185	230
VHF	153	173	140	196	155	202
SI	186	206	175	220	190	226
PCW	181	201	170	212	185	218
OCW	199	219	188	226	203	232

Table 1.1: TTS- and PTS-onset thresholds for marine mammals exposed to impulsive noise: SEL (weighted) and SPL (unweighted) thresholds in dB re 1 μPa^2s for low-frequency cetaceans (LF), high-frequency cetaceans (HF), Very high-frequency cetaceans (VHF), Sirenians (SI), Phocid carnivores in water (PCW), and other marine carnivores in water (OCW) (Southall et al., 2019).

Other studies have quantified the behavioural changes of marine mammals exposed to construction-related noise, particularly pile driving. Southall et al. (2019) indicates that severe injuries and death are at risk within the first few hundred meters near a pile driving site, with behavioural changes extending over possibly more than 100 km from the source. The extent of impact varies by species; hence, exposure thresholds are developed based on their specific hearing range and auditory weight function (Southall et al., 2019). For instance, Benhemma-Le Gall et al. (2021) demonstrates that porpoise occurrence declined by 8-17% in a 576 km^2 square area during impact pile driving. The probability of detecting porpoises increased with distance to the vessel and the construction activity but decreased with higher background noise. Behavioural impact on porpoises has been observed up to 12 km from pile-driving sites and 4 km from construction vessels. Another study by Fernandez-Betelu et al. (2021) reveals that bottlenose dolphins are less noise-sensitive than porpoises or some other whales. Nonetheless, behavioural changes, such as vocalisation alterations, occur at greater distances over 100 km from the sound source, potentially affecting many animals. However, bottlenose dolphins did not significantly change their location at distances >20 km from pile driving sites. Both studies underscore the critical importance of noise emission assessments and advocate for stringent regulations on offshore activities.

In developing regulations, providing non-specialists with insights into the harmfulness of underwater noise to sea mammals and fish is crucial (Dahl et al., 2007). Dahl et al. (2007) outlined typical underwater sound levels and spectra for common aquatic noise sources, facilitating a comprehensive comparison between air and underwater sound. Notably, underwater transmission loss is significantly lower than in the air due to significantly longer wavelengths, underscoring the critical need to comprehend that underwater construction noise spreads more expansively than in the air. This observation aligns with empirical findings that animal behaviour is affected over distances exceeding 100 km from a pile driving site.

At national and international levels, regulations address disturbance and physical harm to marine life. Standardised sound metrics, outlined in underwater acoustic terminology

(ISO, 2017a) and acoustic measurement guidelines during pile driving (ISO, 2017b), provide a common foundation for formulating national guidelines.

However, national guidelines exhibit significant variation. Notable examples include the Netherlands and Germany, where thresholds are predicated on single-strike Sound Exposure Level (SEL_{ss}). The Netherlands has established a threshold of 160 dB re 1 μPa^2s, supplemented by additional measures to mitigate harbour porpoise disturbance (Heinis et al., 2022). In Germany, thresholds are derived from $SEL_{ss,5\%}$, wherein 95% of the SEL_{ss} should remain below 160 dB re 1 μPa^2s, coupled with a peak SPL not exceeding 190 dB re 1 μPa^2s (BSH, 2013). Additionally, "the installation of the wind farm foundation must be conducted according to state-of-the-art methods aiming at minimum noise emissions, with installation to be materially completed within 18 months. Next to that, the project proponent must implement a noise mitigation concept tailored to the chosen foundation type" and during installation, "Monitoring shall pertain to construction-related noise from vessels and pile driving, with measuring to take place at 750 and 1,500 meters from the pile driving" (Burghardt-Kaufmann, 2019, April 26).

Conversely, Belgium's guidelines exclusively consider the zero-to-peak SPL, capping it at 185 dB re 1 μPa^2s (Belgische Staat, 2018). In the United Kingdom, each constituent country has developed its guidelines, with a primary emphasis on recommending the use of acoustic deterrent devices before commencing pile driving activities (Marine Scotland et al., 2014). The United States of America employs diverse legislations anchored in species-specific thresholds (Southall et al., 2019). Despite these legislations and guidelines, the absence of international consistency complicates the design of required sound mitigation measures. Additionally, thresholds for vibratory piling are glaringly omitted in all instances.

From the author's perspective, there is a compelling case for standardising guidelines at a fundamental European level. Existing European legislation predominantly fixates on one or two thresholds, which oversimplifies the intricate dynamics of marine life impact. Adhering to the proposed weighted sound thresholds by Southall (2021) and Southall et al. (2019), tailored for distinct species, would yield a more nuanced understanding of the effects on marine life. Furthermore, considering particle motion in regulatory frameworks (Popper and Hawkins, 2018) and incorporating sound emissions by novel driving techniques, such as vibratory pile driving methods, are imperative steps towards comprehensive legislation.

1.2. Sound mitigation

A comprehensive European regulation for assessing underwater noise emission during pile driving remains elusive. Instead, individual countries adhere to distinct guidelines and regulations. When sound levels surpass permissible thresholds, operations may be halted until remedial measures are implemented and assessments forecast reduced sound levels. This procedural interruption incurs significant costs, creating a substantial financial incentive for the industry to invest in underwater sound prediction and reduction, aside

from its fundamental importance for aquatic life. Noise mitigation strategies offer a viable solution to alleviate sound distortion.

Two primary approaches exist for mitigating sound generated by offshore pile driving. First, sound can be mitigated by obstructing the sound path and employing techniques such as air bubble curtains, resonator-based sound dampers, or double-walled steel mitigation screens. Second, innovative pile driving techniques can reduce the sound source itself, including standard vibratory pile driving, BlueHammer, controlled soil liquefaction, and Gentle Driving of Piles (GDP) (Grow, 2021).

The most prevalent mitigation methods for underwater pile driving involve the application of Big Bubble Curtain (BBC) positioned at specific distances from the pile (Würsig et al., 2000). Sound reductions are contingent on operational factors such as employment radii and airflow, with a Single Big Bubble Curtain (SBBC) achieving SEL_{ss} reduction between 7 and 15 dB, and a Double Big Bubble Curtain (DBBC) reducing SEL_{ss} between 8 and 18 dB (Bellmann et al., 2023). Notably, air compression requirements increase with water depth to maintain similar bubble curtain performance (Peng et al., 2023). Alternatively, resonator-based dampers like HSD (Peng et al., 2018) or AdBm (Elzinga et al., 2019) can be positioned near the pile, demonstrating SEL_{ss} reductions of 10 to 12 dB (Bellmann et al., 2023), though there is evidence that low-frequency sound can be amplified rather than attenuated. Another promising option involves piling the monopile within a double-walled steel sleeve, where the air layer between the steel walls theoretically obstructs nearly all sound transmission into the water, achieving SEL_{ss} reductions of 13 to 17 dB with the IHC NMS for piles up to 8 m in diameter (Bellmann et al., 2023)[*].

All sound path-blocking mitigation measures share a common challenge: mitigating low-frequency noise is more challenging than mitigating high-frequency noise. Piles of increasing dimensions emit more low-frequent noise; thus, noise becomes harder to mitigate with increasing dimensions. Figure 1.2 provides an overview of spectral insertion losses at various frequency bands[†].

In addition to mitigating sound paths, alternative pile driving methods show promise in reducing sound levels. Large vibratory devices can drive monopile foundations into the soil, applying a quasi-periodic force on top of the pile excited by rotating eccentric masses (Jonker, 1987; Warrington, 1989). Extended methods to traditional vibratory pile driving are currently under development.

GDP emerges as a particularly promising technique for silent pile driving. GDP combines torsional vibrations with axial vibrations, reducing vertical friction adequately (Tsetas et al., 2023a). The energy required to drive the pile vertically decreases, resulting in a lower amplitude of the vertical vibratory hammer than in traditional vibratory pile driving. Moreover,

[*] Data presented by Bellmann et al. (2023) consists of large spreads due to environmental and geometrical variants. Due to the case-specific behaviour, the achieved performances of the systems cannot straightforwardly be extrapolated to new cases.

[†] The figure shows a statistical overview of obtained SEL_{ss} reductions under different environmental conditions and foundation sizes for different mitigation measures; thus noise reductions cannot straightforwardly be compared

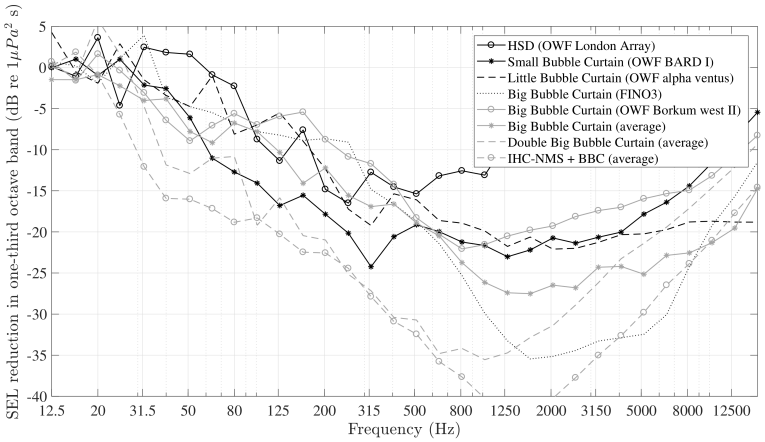


Figure 1.2: Insertion loss of noise mitigation measures per frequency band (Tsouvalas, 2020)

pure torsional motion does not generate any pressure waves underwater, as water is practically inviscid. Consequently, this thesis will focus on sound prediction for this promising technique and general vibratory pile driving.

1.3. Sound prediction models

Accurate underwater sound prediction models play a crucial role in the design phase of underwater sound systems, ensuring regulatory compliance and aiding decision-making on mitigation strategies. Traditional models have primarily focused on predicting underwater noise from impact pile driving. Reinhall and Dahl (2011) pioneered detailed numerical modelling for this purpose, introducing a Finite Element Method (FEM) model incorporating the parabolic equation for wave propagation. This FEM approach, comprising near-field and propagation models, has since been widely adopted and refined by subsequent studies (Göttsche et al., 2015; Lippert and Lippert, 2012; Lippert and von Estorff, 2014a; Lippert et al., 2013; Nijhof et al., 2014; Wilkes et al., 2016; Zampolli et al., 2013). For example, Fricke and Rolfes (2015) introduced a module to estimate force from an impact hammer, whereas Lippert and von Estorff (2014b) conducted a Monte Carlo analysis to assess parameter uncertainties.

Furthermore, finite-difference models have been proposed as an alternative to FEM (MacGillivray, 2013). Various propagation algorithms, including normal modes (Wilkes et al., 2016), wave number integration (Lippert and Lippert, 2012; Lippert and von Estorff, 2014a; Lippert et al., 2013), energy flux-based methods (Zampolli et al., 2013), and parabolic equations (Göttsche et al., 2015; Reinhall and Dahl, 2011; Schecklman et al., 2015), have been utilized. Some other models couple the structural domain described by FEM with Boundary Element Method (BEM) for exterior domains (Masoumi et al., 2007). Semi-analytical

approaches have also been explored, simplifying calculations by replacing sediment with distributed springs (Deng et al., 2016; Hall, 2015; Tsouvalas and Metrikine, 2013).

These early sound prediction models often represented sediment as an acoustic fluid due to computational efficiency (Wood, 2016). However, modelling soil as an elastic medium introduces a secondary sound path, describing sound transmission via the soil into the water, such as through Scholte interface waves along the seabed-water interface. Second-generation models incorporate elastic seabed properties, accounting for significant energy absorption during pile driving and predicting additional waves, like Scholte interface waves (Fricke and Rolfes, 2015; Tsouvalas and Metrikine, 2014a; Tsouvalas and Metrikine, 2014b). These models can also simulate waves in soil layers or waves travelling along interfaces between soil layers. As an advancement, Peng et al. (2021b) developed an improved sound propagation model, integrating an elastic layered half-space to describe the seabed.

Alternatively, empirical models based on available data offer a practical means of predicting sound levels. Transmission loss formulas relate source and receiver distances (Lippert et al., 2015, 2018; Von Pein et al., 2022; von Pein et al., 2022). However, considering sound mitigation proves more difficult while introducing additional uncertainties due to the increased number of parameters (Von Pein et al., 2022).

The COMPILE benchmark case was established to assess sound prediction models, widely accepted within the field for evaluating various solution techniques in offshore pile driving scenarios (Lippert et al., 2016). Although predictions from these models align well in the near field, discrepancies arise with increasing distance from the noise source. Notably, the COMPILE case has limitations, particularly in representing sediment as an acoustic fluid.

A comprehensive literature review by Tsouvalas (2020) identifies five prominent challenges in state-of-the-art sound prediction. These challenges encompass the development of sound prediction models for vibratory pile driving, noise mitigation modelling, enhancement of computational efficiency for uncertainty analysis, incorporation of the three-dimensional domain, and collaboration with marine biologists for a unified environmental impact assessment.

Recent endeavours have made strides in addressing some of these challenges. Tsouvalas and Metrikine (2016b) conducted a theoretical comparison of the wave field emitted by impact-driven and vibratory-driven piles, highlighting that the highest sound levels manifest just above the seabed. In a separate study, Dahl et al. (2015) presented experimental results on underwater sound from vibratory pile driving and subsequently propagated the measured field using an acoustic propagation model. Notably, there is a gap in the detailed and accurate modelling of sound generated by the vibratory driving of monopiles.

Within the realm of models featuring a simplified elastic seabed, Deng et al. (2016) and Tsouvalas and Metrikine (2013) briefly addressed inclined forces; however, further verification of the impact of potential unexpected non-symmetries in the sound field during the installation of monopiles is largely missing.

Significant strides have been made in recent contributions by Peng et al. (2021a, 2023), representing substantial advancements in modelling air-bubble curtains as a sound mitigation system. These contributions delve into both pneumatic and hydrodynamic behaviours, contributing significantly to understanding the effectiveness of air-bubble curtains in mitigating underwater noise.

In summary, accurate underwater noise prediction models are essential in the design phase, and several contributions have been made to improve sound predictions. However, several challenges remain to be addressed.

1.4. Knowledge gaps

The surging demand for offshore wind energy necessitates the installation of increasingly large monopile foundations. To address the challenge of noise pollution, particularly in sensitive marine environments, methods enabling silent driving, such as vibratory pile driving or GDP, become imperative. However, existing models designed to accurately predict noise generated by impact pile driving may not directly apply to vibratory pile driving, given the distinct shift in sound generation mechanisms.

Impact pile driving is characterised by the propagation of the Mach cone resulting from the radial expansion of the pile, leading to supersonic pressure wave radiation. In contrast, during vibratory pile driving, the pile is anticipated to radiate sound in a quasi-steady state continuously. Consequently, pile-soil interaction is a critical factor influencing pile vibrations, with friction playing a pivotal role. The presence or absence of friction between the pile and soil is crucial for precisely predicting pile vibrations, acting as the sound source that directly radiates sound into the water. Additionally, the Scholte interface waves, generated through the excitation of the soil, contribute to sound emission into the water, particularly noteworthy at low excitation frequencies inherent in vibratory pile driving. Notably, friction is highly non-linear, introducing complexity in the energy distribution, potentially shifting energy from the dominant driving frequency to higher harmonics. The effect of this non-linear behaviour on underwater sound fields remains unknown.

In light of these observations, the current state-of-the-art models cannot accurately predict underwater sound generated by vibratory pile driving techniques. Improving models that describe sound generation mechanisms by altering the pile-soil interface conditions becomes essential in predicting the sound generated by vibratory piling. This is particularly relevant with the emergence of novel techniques like GDP, introducing further complexity to the wave generation dynamics.

Beyond vibratory pile driving, the impact of unintended non-symmetries around the circumference arising from imperfections in excitation, such as eccentricities or inclined loads, may play a pivotal role in noise generation. Measurements have indicated the presence of non-symmetries in the sound field during impact pile driving, e.g. the R&D project BORA exhibited a variation in measurements of a few decibels at the same distance across different spatial directions (Bellmann et al., 2023). However, it is unknown where these non-

symmetries originate from, but unintended non-symmetries in the excitation or geometry possibly explain these asymmetric sound fields.

1.5. Objective

This research is motivated by the knowledge gaps mentioned above and endeavours to address a primary objective: **to provide insight into the physics of the sound generation mechanism during vibratory pile driving, specifically emphasising GDP**. Therefore, a comprehensive computationally efficient model is developed to help also reveal the essential physics of sound generation and propagation in light of the new non-impact driving technologies.

Integrating the frictional force in a sound prediction model suitable for vibratory pile driving presents a challenge. The strongly non-linear equations governing friction present computational demands that must be carefully managed, especially when dealing with multiple frequencies in a three-dimensional elastic medium.

Therefore, the main focus is on existing models' assumed perfect contact between the pile and soil. The reality of vibratory pile driving reveals that the pile slides through the soil, rendering the assumed interface condition invalid. This prompts an exploration into the significance of this modelling decision and its potential implications for accurately predicting the noise field. The pile-soil interface description is improved by relaxing the perfect contact in a simplified linear manner and by replacement with a complex non-linear description of the friction forces obtained by employing a non-linear driveability model.

The novel GDP method has a crucial phase in the research, with expectations that GDP may yield quieter outcomes than traditional vibratory techniques. Leveraging on-shore pile driving data obtained during the thesis, an initial noise prediction is conducted to compare GDP with standard vibratory pile driving, adding empirical depth to the theoretical expectations.

A side objective is to investigate the influence of unintended asymmetries in excitation sources on the generated noise field. While underwater noise prediction models typically assume perfect cylindrical symmetry, real-world scenarios introduce non-symmetric elements, such as inclined or eccentrically placed impact hammers. Assessing the potential significance of these asymmetries in induced sound levels, particularly the non-symmetric pile modes, enriches this research.

In summary, the presented research primarily aims to provide nuanced insights into the intricacies of predicting underwater sound sources, specifically in the context of vibratory pile-driving techniques. The primary objectives are to enhance our understanding of the noise generation mechanism, identify potential risks associated with noise production, and propose practical solutions for mitigating noise at its source. To the best of the author's knowledge, this work is the first complete piece of investigation into underwater sound generation and propagation when vibratory devices install piles.

1.6. Outline

This thesis navigates the complexities of underwater noise in offshore vibratory pile driving, starting with delving into the mathematical foundations in Chapter 2. This chapter summarises the mathematical formulations used from the literature to develop the presented model in the sequential chapters. The sound generation mechanisms in impact pile driving are explained using an underwater sound prediction model in Chapter 3. Additionally, a numerical study describes asymmetric sound emission due to unintended asymmetries during impact pile driving. Chapters 4 and 5 explore the impact of relaxation of the pile-soil interface condition. In Chapter 4, the interface condition is relaxed linearly by introducing complex valued springs in the frequency domain between pile and soil. Chapter 5 introduces a non-linear frictional interaction model for predicting the wave field in the case of vibratory pile driving, including frictional forces obtained by non-linear driveability analysis. Chapter 6 compares expected sound emissions using GDP and traditional vibratory piling. The sound predictions follow an onshore experimental campaign described in the chapter. Finally, Chapter 7 summarises key insights and outlines future research directions.

2

Overview of the mathematical considerations in the development of a three-dimensional pile fluid-soil interaction model

This chapter provides a comprehensive overview of the methodology and model developed within this thesis. The model consists of two interconnected substructures: the pile and fluid-soil domains, linked by interface conditions designed to accommodate shear motion between the pile and soil. The representation of the pile substructure involves cylindrical shell modes, which are validated against existing literature and subjected to a hammer-induced force applied at the top. The fluid-soil domain employs a frequency domain Boundary Element Method (BEM) constructed from Green's functions and Green's tensors for fluid and soil ring sources. The coupling between the substructures is facilitated through orthogonal pile mode relations. Furthermore, the chapter delves into numerical considerations, highlights assumptions intrinsic to the methods, and lays the groundwork for subsequent chapters where the model undergoes further verification and application. Consequently, this chapter refrains from presenting novel findings.

2.1. Model description

This study investigates noise emissions while installing a monopile foundation for offshore wind turbines. Monopile foundations are considered viable for water depths up to 60 meters (Kallehave et al., 2015). The installation involves shipping a hollow cylindrical pile offshore and lifting it by a crane to the designated location for monopile installation. Under its weight, the pile penetrates the soil and needs to be driven further into the sediment using available techniques. While the pile dimensions may vary along its length, we assume they are constant for this study. This assumption has been proven to be adequate for sound and vibration predictions in almost all cases of practical interest since the variation of the pile properties along the pile length, i.e. thickness and/or diameter, are smooth, and wavelengths of excited waves in the pile are long in comparison with those variations. Moreover, the natural frequencies and modal shapes of the pile with the exact geometry compared to those of the simplified pile in which the average values of the pile dimensions are used are the same in the frequency range of interest in most cases. Due to the limited water depth, fluid properties are considered constant over depth. Soil properties are obtained from site-specific Cone Penetration Test (CPT). It is important to note that the soil is likely to be layered with depth-dependent characteristics. In this work, we assume the soil to be a homogeneous elastic material. However, the methodology presented here can be extended trivially to include multi-layered elastic solids. We refrain from presenting such an extension here since it can be found in the scientific literature and adds no further complication to the method of solution adopted.

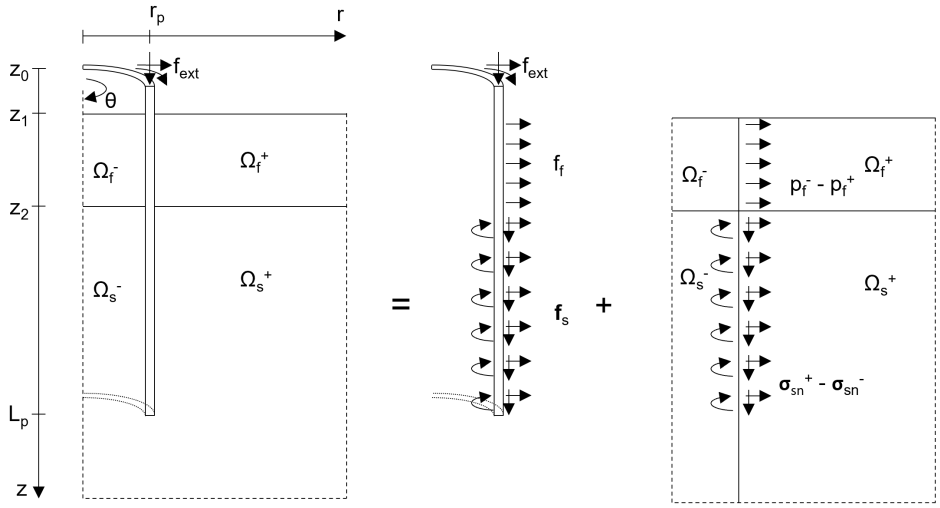


Figure 2.1: Schematic representation of the model and substructuring approach, illustrating the pile and interior/exterior (-/+) fluid-soil domains in the cylindrical coordinate system.

Figure 2.1 depicts the offshore configuration of a monopile installation with a hollow cylinder driven into the soil. The monopile occupies the domain $z_2 - L_\mathrm{p} < z < z_2$, with pile length L_p, thickness h_p, and diameter $2r_\mathrm{p}$. The geometry is cylindrically symmetric, using the cylindrical coordinate system (r, θ, z).

The solution method employed hereafter involves substructuring the problem, seeking solutions separately for the pile and fluid-soil domains, as shown in Fig. 2.1. Both domains are coupled through a set of interface conditions. Traditionally, in linear acoustic models, the pile and soil domains are connected monolithically, i.e. with perfect contact. However, our model allows for variation in these interface conditions, offering the flexibility to choose more physically representative conditions, including a frictional interface.

The pile-soil interface conditions addressed in this section are crucial to the model, allowing for varying frictional interactions throughout the study. A preliminary exploration (see Appendix A) investigates frictional contact between two flexible bars to gain insights into modelling frictional interaction between loose bodies. Recognizing the computational complexity and the required computational time for obtaining trustworthy results in three-dimensional noise predictions, an alternative linear and computationally efficient model for underwater noise prediction is favoured, combined with output from pile driveability analysis to derive accurately the frictional forces at the pile-soil interface.

2.2. Governing equations

The solution for the two substructures is obtained sequentially. Here, we present the governing equations for both substructures and the interface conditions that couple them. Subscripts p, f, and s denote the pile, fluid, and soil domains, while subscripts r, θ, and z indicate the radial, circumferential, and vertical directions.

The pile is idealized as a thin shell, characterized by its modulus of elasticity, Poisson's ratio, wall thickness and density denoted as E_p, ν_p, h_p and ρ_p, respectively. The equation of motion for the pile is expressed as:

$$\boldsymbol{L}_\mathrm{p}\boldsymbol{u}_\mathrm{p}(\theta,z,t) + \rho_\mathrm{p} h_\mathrm{p} \ddot{\boldsymbol{u}}_\mathrm{p}(\theta,z,t) = \boldsymbol{f}_\mathrm{p}(\theta,z,t) + \boldsymbol{f}_\mathrm{ext}(\theta,t)\delta(z - z_\mathrm{top}) \tag{2.1}$$

where $\boldsymbol{L}_\mathrm{p}$ represents stiffness components corresponding to Flügge's thin shell theory (Leissa, 1973). The vector of pile displacements in cylindrical coordinates is denoted by $\boldsymbol{u}_\mathrm{p}(\theta,z,t)$, $\boldsymbol{f}_\mathrm{ext}(\theta,z,t)$ provides the external load vector on top of the pile, and $\boldsymbol{f}_\mathrm{p}(\theta,z,t)$ contains distributed fluid and soil interaction forces. The double dots overhead denote the second derivative with respect to time: $\partial^2/\partial t^2$.

Seawater and soil are modelled as continua, occupying the domains $z_0 < z < z_1$ and $z > z_1$, respectively. The former is described as an acoustic fluid, while the latter is modelled as an elastic medium. The fluid wave speed and density are given by c_f and ρ_f, respectively. The soil is characterized by the Lamé constants λ_s and μ_s, and density ρ_s. The equations of

motion for the two domains are given by:

$$\nabla^2\phi_\mathrm{f}(r,\theta,z,t)-\frac{1}{c_\mathrm{f}^2}\ddot{\phi}_\mathrm{f}(r,\theta,z,t)=s_\mathrm{f}(\theta,z,t)\delta(r-r_\mathrm{p}) \tag{2.2}$$

$$(\lambda_\mathrm{s}+\mu_\mathrm{s})\nabla(\nabla\cdot\boldsymbol{u}_\mathrm{s}(r,\theta,z,t))+\mu_\mathrm{s}\nabla^2\boldsymbol{u}_\mathrm{s}(r,\theta,z,t)+\boldsymbol{f}_\mathrm{s}(\theta,z,t)\delta(r-r_\mathrm{p})=\rho_\mathrm{s}\ddot{\boldsymbol{u}}_\mathrm{s}(r,\theta,z,t) \tag{2.3}$$

The motion of the acoustic fluid is described by the displacement potential $\phi_\mathrm{f}(r,\theta,z,t)$, related to the displacement field via $\boldsymbol{u}_\mathrm{f}(r,z,t)=\nabla\phi_\mathrm{f}(r,z,t)$, and the fluid pressure $p_\mathrm{f}(r,z,t)=-\rho_\mathrm{f}\ddot{\phi}_\mathrm{f}(r,z,t)$ (Jensen et al., 2011). The scalar quantity $s_\mathrm{f}(\theta,z,t)$ defines an omnidirectional volume injection ring source at the radius of the pile's middle surface. The soil equation of motion contains the displacement vector $\boldsymbol{u}_\mathrm{s}(r,z,t)$ and body loads $\boldsymbol{f}_\mathrm{s}(z,t)$ applied at $r=r_\mathrm{p}$. Please note that the soil and fluid reaction forces are actually applied at the outer and inner pile surfaces. However, their difference is considered here when applied to the middle surface of the shell in accordance with the thin shell theory. The small error introduced by the difference between the actual position of application of these forces and the middle surface of the shell is minor and may introduce a correction term in the involved boundary and interface conditions of the pile, which is of higher order, i.e. similar in order to the terms related to shear deformation in accordance with the Mindlin-Reissner theory (Kaplunov et al., 1998). Since no terms of this order are expected to play a role in the dynamics of the problem considered here due to the relatively low acoustic frequencies considered for practical purposes, there is no need to refine either the equation of motion of the shell or the boundary conditions to include this effect.

The fluid and soil are coupled through a standard set of interface conditions along the horizontal coordinate, valid at $r<r_\mathrm{p}$ and $r>r_\mathrm{p}$:

$$p_\mathrm{f}(r,\theta,z_1,t)=0 \tag{2.4}$$

$$p_\mathrm{f}(r,\theta,z_2,t)+\sigma_{\mathrm{s,zz}}(r,\theta,z_2,t)=0 \tag{2.5}$$

$$u_{\mathrm{f,z}}(r,\theta,z_2,t)-u_{\mathrm{s,z}}(r,\theta,z_2,t)=0 \tag{2.6}$$

$$\sigma_{\mathrm{s,zr}}(r,\theta,z_2,t)=\sigma_{\mathrm{s,z\theta}}(r,\theta,z_2,t)=0 \tag{2.7}$$

Additionally, the Sommerfeld radiation condition is invoked at an infinite distance from the pile.

The coupling of the fluid and soil with the pile at $r=r_\mathrm{p}$ deviates from standard linear underwater noise prediction models while allowing relative motion between the pile and soil. The traditional set of interface conditions prescribing Perfect Contact (PC) between the pile and soil reads:

$$u_{\mathrm{p,r}}(\theta,z,t)=u_{\mathrm{f,r}}(r_\mathrm{p},\theta,z,t) \qquad z_1<z<z_2 \tag{2.8}$$

$$f_{\mathrm{p,r}}(\theta,z,t)=-p_\mathrm{f}(r_\mathrm{p}^+,\theta,z,t)+p_\mathrm{f}(r_\mathrm{p}^-,z,t) \qquad z_1<z<z_2 \tag{2.9}$$

$$u_{\mathrm{p,r}}(\theta,z,t)=u_{\mathrm{s,r}}(r_\mathrm{p},\theta,z,t) \qquad z_2<z<L_\mathrm{p} \tag{2.10}$$

$$f_{\mathrm{p,r}}(\theta,z,t) = \sigma_{\mathrm{s,rr}}(r_{\mathrm{p}}^{+},\theta,z,t) - \sigma_{\mathrm{s,rr}}(r_{\mathrm{p}}^{-},\theta,z,t) \qquad z_2 < z < L_{\mathrm{p}} \qquad (2.11)$$

$$u_{\mathrm{p},\theta}(\theta,z,t) = u_{\mathrm{s},\theta}(r_{\mathrm{p}},\theta,z,t) \qquad z_2 < z < L_{\mathrm{p}} \qquad (2.12)$$

$$f_{\mathrm{p},\theta}(\theta,z,t) = \sigma_{\mathrm{s,r}\theta}(r_{\mathrm{p}}^{+},z,t) - \sigma_{\mathrm{s,r}\theta}(r_{\mathrm{p}}^{-},z,t) \qquad z_2 < z < L_{\mathrm{p}} \qquad (2.13)$$

$$u_{\mathrm{p,z}}(\theta,z,t) = u_{\mathrm{s,z}}(r_{\mathrm{p}},\theta,z,t) \qquad z_2 < z < L_{\mathrm{p}} \qquad (2.14)$$

$$f_{\mathrm{p,z}}(\theta,z,t) = \sigma_{\mathrm{s,rz}}(r_{\mathrm{p}}^{+},z,t) - \sigma_{\mathrm{s,rz}}(r_{\mathrm{p}}^{-},z,t) \qquad z_2 < z < L_{\mathrm{p}} \qquad (2.15)$$

The interior and exterior domains are indicated with superscripts '-' and '+', respectively. Equations (2.8) and (2.9) describe the pile-fluid interaction perpendicular to the pile surface. Equations (2.10) and (2.11) prescribe continuity of stresses and displacements between pile and soil perpendicular to the pile surface. These four interface conditions remain the same for model variations considered in this work. Equations (2.13) and (2.15) prescribe equilibrium of forces in the circumferential and vertical direction, which also holds in all models considered hereafter. Equations (2.12) and (2.14), which imply that there is no separation between the pile and the soil in the respective directions, hold only in the case of the classical models used in vibroacoustics. In this work, these conditions are altered to account for variations in the pile and soil interaction forces.

The most thorough linear alternative for relative motion between pile and soil is having no frictional forces between pile and soil, i.e. in the case of No Friction (NF), all shear reaction forces are equal to zero. Interface conditions Eqs. (2.12) to (2.15) at $z_2 < z < L_{\mathrm{p}}$ then are replaced by:

$$f_{\mathrm{p},\theta}(\theta,z,t) = 0 \qquad (2.16)$$

$$\sigma_{\mathrm{s,r}\theta}(r_{\mathrm{p}}^{+},z,t) = \sigma_{\mathrm{s,r}\theta}(r_{\mathrm{p}}^{-},z,t) = 0 \qquad (2.17)$$

$$f_{\mathrm{p,z}}(\theta,z,t) = 0 \qquad (2.18)$$

$$\sigma_{\mathrm{s,rz}}(r_{\mathrm{p}}^{+},z,t) = \sigma_{\mathrm{s,rz}}(r_{\mathrm{p}}^{-},z,t) = 0 \qquad (2.19)$$

Alternatively, the perfect contact can be relaxed by introducing distributed spring-dashpot elements between the pile and soil along the circumferential and vertical directions. Adjusting stiffness and damping coefficients allows relative motion between pile and soil. The interface conditions accordingly replace Eqs. (2.12) and (2.14) of the PC interface conditions by conditions including distributed interface springs (k_{F}) and dashpots (c_{F}) at $z_2 < z < L_{\mathrm{p}}$:

$$f_{\mathrm{p},\theta}(\theta,z,t) = \left(k_{\mathrm{F},\theta} + c_{\mathrm{F},\theta}\frac{\partial}{\partial t}\right)\left(2u_{\mathrm{p},\theta}(\theta,z,t) - u_{\mathrm{s},\theta}(r_{\mathrm{p}}^{+},\theta,z,t) - u_{\mathrm{s},\theta}(r_{\mathrm{p}}^{-},\theta,z,t)\right) \qquad (2.20)$$

$$f_{\mathrm{p,z}}(\theta,z,t) = \left(k_{\mathrm{F,z}} + c_{\mathrm{F,z}}\frac{\partial}{\partial t}\right)\left(2u_{\mathrm{p,z}}(\theta,z,t) - u_{\mathrm{s,z}}(r_{\mathrm{p}}^{+},\theta,z,t) - u_{\mathrm{s,z}}(r_{\mathrm{p}}^{-},\theta,z,t)\right) \qquad (2.21)$$

Finally, the actual friction forces can be obtained directly from a non-linear pile driveability model. In this case, the interface conditions given by Eqs. (2.12) and (2.14) at $z_1 < z < z_2$

of the PC interface conditions are replaced with conditions introducing the actual frictional forces:

$$f_{\mathrm{p},\theta}(\theta, z, t) = F_{\mathrm{Fr},\theta}(\theta, z, t) \tag{2.22}$$

$$f_{\mathrm{p},z}(\theta, z, t) = F_{\mathrm{Fr},z}(\theta, z, t) \tag{2.23}$$

The pile and fluid-soil substructures are solved in the frequency domain since both problems are linear. The non-linear frictional forces obtained from driveability analysis appear quasi-periodic, slowly changing with driving depth. Thus, the system behaves nearly periodically around a certain driving depth, and the sound modelling can be performed linearly. Therefore, a frequency domain solution is sought to obtain the acoustic emissions at each reference depth. The following Fourier transform pair is used throughout the work:

$$f(t) = \frac{1}{2\pi}\int_{-\infty}^{\infty} \tilde{f}(\omega) e^{\mathrm{i}\omega t}\,\mathrm{d}\omega, \qquad \tilde{f}(\omega) = \int_{-\infty}^{\infty} f(t) e^{-\mathrm{i}\omega t}\,\mathrm{d}t \tag{2.24}$$

The tilde signifies a complex-valued quantity in the frequency domain. The equations above can straightforwardly be transformed to the frequency domain.

Material damping in the fluid and soil is introduced through wave attenuation in complex-valued material properties in the frequency domain. The attenuation of waves is described by $\alpha = \frac{20\pi}{\beta}\log_{10}\mathrm{e}$ in dB per wavelength. In the fluid, the bulk modulus ($K_\mathrm{f} = c_\mathrm{f}^2\rho_\mathrm{f}$) becomes complex-valued:

$$\tilde{K}_\mathrm{f} = K_\mathrm{f}(1 + \mathrm{i}\beta_\mathrm{f}) \tag{2.25}$$

In the soil, damping is accounted for through the complex-valued Lamé parameters:

$$\tilde{\lambda}_\mathrm{f} + 2\tilde{\mu} = (\lambda_\mathrm{f} + 2\mu)(1 + \mathrm{i}\beta_\mathrm{p}) \tag{2.26}$$

$$\tilde{\mu} = \mu(1 + \mathrm{i}\beta_\mathrm{s}) \tag{2.27}$$

Here, β_p and β_s denote the relative attenuation of compressional and shear waves, respectively (Jensen et al., 2011).

2.3. Modal solution for a thin cylindrical shell

The equation of motion for the pile, as established based on Flügge's thin shell theory, is given by Eq. (2.1). To efficiently handle this, a frequency domain analysis employing a modal decomposition approach is adopted, particularly suitable for solving the problem of an in-vacuo cylindrical shell of finite length (Tsouvalas and Metrikine, 2014a; Zhou et al., 2012).

Given the geometrical azimuthal symmetry of a cylinder, the displacement fields are expressed using a Fourier series in the azimuthal degree of freedom, with circumferential mode number n. The solution of the shell can generally be assumed in the form (Leissa,

1973):

$$\tilde{u}_{\mathrm{p,z}}(z,\theta) = \tilde{U}_{\mathrm{p,z},n}(z)\cos(n\theta) \tag{2.28}$$

$$\tilde{u}_{\mathrm{p},\theta}(z,\theta) = -\tilde{U}_{\mathrm{p},\theta,n}(z)\sin(n\theta) \tag{2.29}$$

$$\tilde{u}_{\mathrm{p,r}}(z,\theta) = \tilde{U}_{\mathrm{p,r},n}(z)\cos(n\theta) \tag{2.30}$$

where the vertical component of the displacement field is expressed as a function of the wave number $k_{\mathrm{z},n}$:

$$\tilde{U}_{\mathrm{p,z},n}(z) = A_n e^{k_{\mathrm{z},n}\frac{z}{r_\mathrm{p}}}, \quad U_{\mathrm{p},\theta,n}(z) = B_n e^{k_{\mathrm{z},n}\frac{z}{r_\mathrm{p}}}, \quad \tilde{U}_{\mathrm{p,r},n}(z) = C_n e^{k_{\mathrm{z},n}\frac{z}{r_\mathrm{p}}} \tag{2.31}$$

The introduction of a minus sign in Eq. (2.29), contrary to the standard convention, is made to accommodate the downward-pointing z-axis, aligning with soil elastodynamics conventions. Substituting the above equations into the homogeneous form of Eq. (2.1) in the frequency domain, where no forces are present on the right-hand side, is expressed as follows:

$$\begin{bmatrix} L_{11}(k_{\mathrm{z},n}) - \rho_\mathrm{p} h_\mathrm{p}\omega^2 & L_{12}(k_{\mathrm{z},n}) & L_{13}(k_{\mathrm{z},n}) \\ L_{21}(k_{\mathrm{z},n}) & L_{22}(k_{\mathrm{z},n}) - \rho_\mathrm{p} h_\mathrm{p}\omega^2 & L_{23}(k_{\mathrm{z},n}) \\ L_{31}(k_{\mathrm{z},n}) & L_{32}(k_{\mathrm{z},n}) & L_{33}(k_{\mathrm{z},n}) - \rho_\mathrm{p} h_\mathrm{p}\omega^2 \end{bmatrix}_n \begin{bmatrix} A_n \\ B_n \\ C_n \end{bmatrix} = \mathbf{0} \tag{2.32}$$

A polynomial equation, expressed as a function of $k_{\mathrm{z},n}$, is derived by setting the determinant of the matrix in Eq. (2.32) equal to zero (Zhou et al., 2012):

$$g_{8,n}k_{\mathrm{z},n}^8 + g_{6,n}k_{\mathrm{z},n}^6 + g_{4,n}k_{\mathrm{z},n}^4 + g_{2,n}k_{\mathrm{z},n}^2 + g_{0,n} = 0 \tag{2.33}$$

The solution yields eight complex-valued roots. By substituting these roots back into the equation of motion, Eq. (2.1), the amplitudes of A_n, B_n, and C_n can be expressed in terms of each other for each solution of $k_{\mathrm{z},n}$, i.e., $A_{nj} = \alpha_{nj}C_{nj}$ and $B_{nj} = \beta_{nj}C_{nj}$. The displacement components of the shell then read:

$$\tilde{U}_{\mathrm{p,z},n}(z) = \sum_{j=1}^{8} \alpha_{nj}C_{n,j}e^{k_{\mathrm{z},nj}\frac{z}{r_\mathrm{p}}} \tag{2.34}$$

$$\tilde{U}_{\mathrm{p},\theta,n}(z) = \sum_{j=1}^{8} \beta_{nj}C_{nj}e^{k_{\mathrm{z},nj}\frac{z}{r_\mathrm{p}}} \tag{2.35}$$

$$\tilde{U}_{\mathrm{p,r},n}(z) = \sum_{j=1}^{8} C_{nj}e^{k_{\mathrm{z},nj}\frac{z}{r_\mathrm{p}}} \tag{2.36}$$

The coefficients C_{nj} are determined through the boundary conditions of the finite cylinder. Three types of boundary conditions are considered, denoted as free (F), clamped (C), and

shear diaphragm (SD) boundary conditions, corresponding to the following equations:

$$\mathrm{F}\rightarrow \left.\begin{matrix} N_z(z) \\ T_z(z) \\ S_z(z) \\ M_z(z) \end{matrix}\right\}_{z=z_\mathrm{b}} = 0, \quad \mathrm{C}\rightarrow \left.\begin{matrix} U_{\mathrm{p,z}}(z) \\ U_{\mathrm{p\theta}}(z) \\ U_{\mathrm{p,r}}(z) \\ \frac{\partial}{\partial z}U_{\mathrm{p,r}}(z) \end{matrix}\right\}_{z=z_\mathrm{b}} = 0, \quad \mathrm{SD}\rightarrow \left.\begin{matrix} N_z(z) \\ U_{\mathrm{p\theta}}(z) \\ U_{\mathrm{p,r}}(z) \\ M_z(z) \end{matrix}\right\}_{z=z_\mathrm{b}} = 0 \tag{2.37}$$

where z_b represents the boundary position on the shell. It is crucial to acknowledge that, in reality, none of these boundary conditions align perfectly with the actual forces and displacements experienced at the boundaries. The presented model embraces free-free boundary conditions, a choice made intentionally. In this setup, the force on top of the pile is applied through a delta function near the pile surface while both ends are free to move. The pile modes, therefore, will approach the stresses applied at the top of the pile but will not be able to satisfy the boundary condition exactly. This assumption is proven efficient in most cases where the pile tip is above the sea surface. However, if one likes to find the response with the shell being entirely submerged in water, this assumption may yield inaccurate acoustic emissions. At the tip of the pile, the expected response is anticipated to be smaller than the sleeve stresses and, therefore, will cause no errors.

Solving the boundary value problem results in the derivation of eigenfrequencies ω_k and corresponding eigenmodes $\boldsymbol{U}_{\mathrm{p},k}(z)$. Notably, these modes manifest as an infinite series with increasing frequency:

$$\tilde{\boldsymbol{U}}_{\mathrm{p},n}(z) = \sum_{k=1}^{\infty} \tilde{\eta}_{nk}\tilde{\boldsymbol{U}}_{\mathrm{p},nk}(z) \tag{2.38}$$

where $\boldsymbol{U}_{\mathrm{p},k}(z)$ represents the mode shapes in the three degrees of freedom, and η_{nk} is the modal amplitude, later derived from the forced equation of motion upon coupling with the fluid-soil domain. Substituting the modal representation of the displacement field into the frequency domain equation of motion yields:

$$\sum_{k=1}^{\infty} \tilde{\eta}_{nk}\rho_\mathrm{p}h_\mathrm{p}(\omega_k^2-\omega^2)\tilde{\boldsymbol{U}}_{\mathrm{p},nk}(z) = \tilde{\boldsymbol{f}}_{\mathrm{p},n}(z) + \tilde{\boldsymbol{f}}_{\mathrm{ext},n}\delta(z) \tag{2.39}$$

The modal amplitude η_{nk} is computed by pre-multiplying Eq. (2.39) with another mode l, integrating over the pile's length, and summing over all modes l (Tsouvalas and Metrikine, 2014a):

$$\sum_{l=1}^{\infty}\sum_{k=1}^{\infty}\int_0^{L_\mathrm{p}} \tilde{\eta}_{nk}\rho_\mathrm{p}h_\mathrm{p}(\omega_k^2-\omega^2)\tilde{\boldsymbol{U}}_{\mathrm{p},nl}^T(z)\tilde{\boldsymbol{U}}_{\mathrm{p},nk}(z)\mathrm{d}z = \sum_{l=1}^{\infty}\int_0^{L_\mathrm{p}} \tilde{\boldsymbol{U}}_{\mathrm{p},nl}^T(z)\tilde{\boldsymbol{f}}_{\mathrm{p},n}(z) + \tilde{\boldsymbol{U}}_{\mathrm{p},nl}^T(z)\tilde{\boldsymbol{f}}_{\mathrm{ext},n}\delta(z)\mathrm{d}z \tag{2.40}$$

Making use of the orthogonality relation of the pile modes:

$$\rho_{\mathrm{p}} h_{\mathrm{p}} \int_0^L \tilde{\boldsymbol{U}}_{\mathrm{p},nl}^T(z) \tilde{\boldsymbol{U}}_{\mathrm{p},nk}(z) \mathrm{d}z = \Gamma_{nk} \delta_{lk} \tag{2.41}$$

where δ_{lk} is the Kronecker delta function, and Γ_{nk} is an integration constant, the modes are normalized in the computational scheme to increase numerical stability, such that $\Gamma_{nk} = 1$. Substituting the pile orthogonality, Eq. (2.41), into the equation of motion, Eq. (2.40), the modal amplitude, η_{nk}, of each mode k is found as:

$$\tilde{\eta}_{nk} = \frac{1}{\rho_{\mathrm{p}} h_{\mathrm{p}} (\omega_k^2 - \omega^2) \Gamma_{nk}} \left(\sum_{l=1}^{\infty} \int_0^{L_{\mathrm{p}}} \tilde{\boldsymbol{U}}_{\mathrm{p},nl}^T(z) \tilde{\boldsymbol{f}}_{\mathrm{p},n}(z) \mathrm{d}z + \tilde{\boldsymbol{U}}_{\mathrm{p},nl}^T(0) \tilde{\boldsymbol{f}}_{\mathrm{ext},n} \right) \tag{2.42}$$

Hence, the modal amplitude is found after the substitution of the correct distributed forces $\tilde{\boldsymbol{f}}_{\mathrm{p},n}(z)$ and the external load atop the pile $\tilde{\boldsymbol{f}}_{\mathrm{ext},n}$.

2.3.1. Verification of the pile modes

The proposed modal solution is compared with existing literature to verify the modal solution. To this end, the frequency is normalized with the ring frequency of the pile as follows:

$$\Omega_k = \frac{\omega_k R_{\mathrm{p}}}{c_{\mathrm{p},L}} \tag{2.43}$$

where the longitudinal wave speed is defined as $c_{\mathrm{p},L} = \sqrt{E_{\mathrm{p}} / \rho_{\mathrm{p}} (1 - \nu_{\mathrm{p}}^2)}$.

Table 2.1 presents a comparison of the first ten eigenfrequencies for $n = 0$ with shear diaphragm boundary conditions (SD-SD), alongside the works by Leissa (1969) and the low order theory utilized in Tsouvalas and Metrikine (2014a). The eigenfrequencies found are in good agreement, with identical values observed up to the first three digits.

Furthermore, a comparison is conducted with Zhou et al. (2012) and Finite Element Method (FEM) simulations (ANSYS) (Zhou et al., 2012) for circumferential modes larger than 0 and clamped boundary conditions, as presented in Table 2.2. The agreement among the modal frequencies is remarkably good.

Table 2.3 demonstrates excellent agreement for the first longitudinal mode for the first five circumferential modes between the present model, Zhou et al. (2012), and Loy et al. (1997), for both shear diaphragms and clamped boundary conditions. The results from Loy et al. (1997), derived through a model based on the generalized differential quadrature method, are identical to the present study up to six digits.

2.4. Fluid-soil boundary element description

The methodology uses the Fourier series around the azimuth to analyze the responses to ring sources within the frequency-wave number domain and per cylindrical mode. The chosen

Table 2.1: The first ten eigenfrequencies, excluding the ones corresponding to rigid body motions, for $n = 0$ of a thin cylindrical shell with shear diaphragms boundary conditions (SD-SD) for normalized frequency Ω_k and parameters: $E_\mathrm{p} = 2.1 \times 10^{-11}\mathrm{N/m}^2$, $h_\mathrm{p}/R_\mathrm{p} = 0.04$, $L_\mathrm{p}/R_\mathrm{p} = 20$, $\rho_\mathrm{p} = 7850\mathrm{kg/m}^3$ and $\nu_\mathrm{p} = 0.28$.

k	Present	Tsouvalas (2015)	Leissa (1969)
1	0.150648	0.150647	0.150647
2	0.300319	0.300318	0.300319
3	0.447543	0.447544	0.447548
4	0.589367	0.589373	0.589386
5	0.718856	0.718874	0.718904
6	0.821203	0.821237	0.821296
7	0.882854	0.882898	0.882983
8	0.913266	0.913317	0.913417
9	0.928701	0.928762	0.928875
10	0.937487	0.937562	0.937689

Table 2.2: First eigenfrequencies for $n > 0$ of a thin cylindrical shell with clamped boundary conditions (C-C) for normalized frequency Ω_k and parameters: $E_\mathrm{p} = 2.1 \times 10^{-11}\mathrm{N/m}^2$, $h_\mathrm{p}/R_\mathrm{p} = 0.1$, $L_\mathrm{p}/R_\mathrm{p} = 20$, $\rho_\mathrm{p} = 7850\mathrm{kg/m}^3$ and $\nu_\mathrm{p} = 0.30$.

k,n	Present	FEM (ANSYS)	Zhou et al. (2012)
1,2	0.013897	0.013891	0.013898
1,3	0.022666	0.022653	0.022666
2,3	0.026757	0.026743	0.026762
2,2	0.031450	0.031449	0.031464
1,1	0.032778	0.032750	0.032781
3,3	0.036442	0.036452	0.036465
1,4	0.042207	0.042088	0.041998
2,4	0.043193	0.043071	0.043194
3,4	0.045866	0.045752	0.045875

approach utilizes the indirect BEM, as detailed in (Kirkup, 2019). The method involves an indirect boundary integral formulation, where a field ϕ at point $\boldsymbol{p}$ is related to a source σ at point $\boldsymbol{q}$ through the following expressions:

$$\phi(\boldsymbol{p}) = \int_\Gamma G(\boldsymbol{p},\boldsymbol{q})\sigma(\boldsymbol{q})\mathrm{d}\Gamma_q \tag{2.44}$$

$$\frac{\partial}{\partial n_p}\phi(\boldsymbol{p}) = \int_\Gamma \frac{\partial}{\partial n_p} G(\boldsymbol{p},\boldsymbol{q})\sigma(\boldsymbol{q})\mathrm{d}\Gamma_q + c_p\sigma(\boldsymbol{p}) \tag{2.45}$$

Here, n_p signifies the normal vector, and $c_p = \frac{1}{2}$ when point $\boldsymbol{p}$ lies on Γ_q, otherwise $c_p = 0$. The fluid and soil equations of motion are expressed in terms of scalar potentials for simplicity, a common practice in the field. While the fluid equation of motion, Eq. (2.2), is already in potential form, a decomposition of the soil equation of motion, Eq. (2.3), leads to

Table 2.3: The first eigenfrequency $n > 0$ of a thin cylindrical shell with clamped and shear diaphragm boundary conditions (C-C), (SD-SD) for normalized frequency Ω_k and parameters: $E_\mathrm{p} = 2.1 \times 10^{-11}\,\mathrm{N/m^2}$, $h_\mathrm{p}/R_\mathrm{p} = 0.1$, $L_\mathrm{p}/R_\mathrm{p} = 20$, $\rho_\mathrm{p} = 7850\mathrm{kg/m^3}$ and $\nu_\mathrm{p} = 0.30$.

	C-C			SD-SD		
n	Present	Loy et al. (1997)	Zhou et al. (2012)	Present	Loy et al. (1997)	Zhou et al. (2012)
1	0.032778	0.032885	0.032781	0.016101	0.016101	0.016101
2	0.013897	0.013932	0.013898	0.009382	0.009382	0.009381
3	0.022666	0.022672	0.022666	0.022105	0.022105	0.022105
4	0.042207	0.042208	0.041998	0.042095	0.042095	0.041967
5	0.068046	0.068046	0.067936	0.068008	0.068008	0.067936

three potential wave equations. The displacement field $\boldsymbol{u}_\mathrm{s}(r,\theta,z)$ is decomposed as:

$$\boldsymbol{u}_\mathrm{s}(r,\theta,z) = \nabla\phi_\mathrm{s}(r,\theta,z) + \nabla\times\nabla\times\psi_\mathrm{s}(r,\theta,z)\hat{\mathrm{e}}_\mathrm{z} + \nabla\times\chi_\mathrm{s}(r,\theta,z)\hat{\mathrm{e}}_\mathrm{z} \tag{2.46}$$

The potentials are then transformed to the radial wavenumber domain using the Hankel transform pair:

$$\tilde{\phi}_n(r,z) = \int_0^\infty \hat{\Phi}_b(k,z)\mathrm{J}_n(kr)k\mathrm{d}k \quad \longleftrightarrow \quad \hat{\Phi}_n(k,z) = \int_0^\infty \tilde{\phi}_b(r,z)\mathrm{J}_n(kr)r\mathrm{d}r \tag{2.47}$$

Here, the hat denotes complex-valued quantities in the frequency-wavenumber domain. The subscript n is dropped here, as all potentials, displacements, and stresses depend on the same n. To satisfy the homogeneous equations of motion for both fluid and soil, a general homogeneous solution for the potential is presented:

$$\hat{\Phi}_\mathrm{f}(k,z) = A_1 e^{-\alpha_\mathrm{f} z} + A_2 e^{\alpha_\mathrm{f} z} \tag{2.48}$$

$$\hat{\Phi}_\mathrm{s}(k,z) = A_3 e^{-\alpha_\mathrm{s} z} + A_4 e^{\alpha_\mathrm{s} z} \tag{2.49}$$

$$\hat{\Psi}_\mathrm{s}(k,z) = A_5 e^{-\beta_\mathrm{s} z} + A_6 e^{\beta_\mathrm{s} z} \tag{2.50}$$

$$\hat{X}_\mathrm{s}(k,z) = A_7 e^{-\beta_\mathrm{s} z} + A_8 e^{\beta_\mathrm{s} z} \tag{2.51}$$

In these equations, α_f, α_s, and β_s are related to the radial wave number k as follows:

$$\alpha_\mathrm{f} = \sqrt{k^2 - \frac{\omega^2}{c_\mathrm{f}^2}}, \quad \alpha_\mathrm{s} = \sqrt{k^2 - \frac{\omega^2}{c_\mathrm{p}^2}}, \quad \beta_\mathrm{s} = \sqrt{k^2 - \frac{\omega^2}{c_\mathrm{s}^2}} \tag{2.52}$$

Here, c_f represents the fluid wave speed, while c_p and c_s denote the compressional and shear wave speeds in the soil, respectively.

The indirect BEM is applied to describe the boundary stiffness at the piles' radius and ascertain the field's response. This technique involves integrating Green's functions over the boundary. The full-space response of a ring source in both fluid and soil is initially derived

to determine the Green's functions that fulfil the boundary value problem. Subsequently, the full-space particular solution is incorporated into the boundary value problem, yielding the overall response.

2.4.1. Fluid ring source

In the fluid domain, a body source corresponds to a volume injection, and thus, $s_{\mathrm{f}}(r,\theta,z)$ has units of $\mathrm{m}^3/\mathrm{m}^3$. The fluid potential $\tilde{\phi}_{\mathrm{f}}(r,\theta,z)$ describes the fluid fields. To determine the potential response to a ring load, denoted as $\boldsymbol{s}_{\mathrm{f}}(r,\theta,z)=\hat{\boldsymbol{s}}_{\mathrm{f}}(\theta)\delta(r-r_{\mathrm{p}})\delta(z-z_{\mathrm{f0}})$, a Fourier series in the azimuthal direction is initially applied to the potential field $\tilde{\phi}_{\mathrm{f}}(r,\theta,z)$. Subsequently, the problem is transformed to the frequency-wavenumber domain through the equation:

$$\tilde{\phi}_{\mathrm{f}}(r,\theta,z)=\sum_{n=0}^{\infty}\cos(n\theta)\int_0^{\infty}\mathrm{J}_n(kr)\hat{\Phi}_{\mathrm{f}}(k,z)k\mathrm{d}k \tag{2.53}$$

By substituting Eq. (2.53) into the equation of motion, Eq. (2.2), and transforming the right-hand side as well, we obtain:

$$\hat{S}_{\mathrm{f}}(k)\delta(z-z_{\mathrm{f0}})=\hat{s}_{\mathrm{f}}\mathrm{J}_n(kr_{\mathrm{p}})r_{\mathrm{p}}\delta(z-z_{\mathrm{f0}}) \tag{2.54}$$

Substituting the above two into the equation of motion Eq. (2.2) and eliminating the Bessel functions, one obtains:

$$\frac{\partial^2}{\partial z^2}\hat{\Phi}_{\mathrm{f}}(k,z)-\alpha_{\mathrm{f}}^2\hat{\Phi}_{\mathrm{f}}(k,z)=-\hat{S}_{\mathrm{f}}(k)\delta(z-z_{\mathrm{f0}}) \tag{2.55}$$

where subscript n is omitted and will be omitted hereafter for simplicity. The fundamental solution for $\hat{\Phi}_{\mathrm{f}}(k,z)$ is the full-space Green's function reads:

$$\hat{\Phi}_{\mathrm{f}}^{\mathrm{P}}(k,z)=-\frac{\hat{S}_{\mathrm{f}}(k)}{2\alpha_{\mathrm{f}}}\begin{cases}e^{\alpha_{\mathrm{f}}(z-z_{\mathrm{f0}})} & z<z_{\mathrm{f0}}\\ e^{-\alpha_{\mathrm{f}}(z-z_{\mathrm{f0}})} & z>z_{\mathrm{f0}}\end{cases} \tag{2.56}$$

2.4.2. Soil ring source

For a ring source of radius r_{p} located at $z=z_{\mathrm{s0}}$, the corresponding body forces are represented as $\tilde{\boldsymbol{f}}_{\mathrm{s}}(r,\theta,z)=\bar{\boldsymbol{f}}_{\mathrm{s}}(\theta)\delta(r-r_{\mathrm{p}})\delta(z-z_{\mathrm{s0}})$, where δ denotes the Dirac function. The soil displacements in the frequency-wavenumber domain are as follows:

$$\tilde{\boldsymbol{u}}_s(r,\theta,z)=\sum_{n=0}^{\infty}\tilde{\boldsymbol{T}}_n(\theta)\int_0^{\infty}\boldsymbol{C}_n(k,r)\hat{\boldsymbol{U}}_s(k,z)k\mathrm{d}k \tag{2.57}$$

$$\hat{\boldsymbol{U}}_s(k,z)=a_n\int_0^{2\pi}\tilde{\boldsymbol{T}}_n(\theta)\int_0^{\infty}\boldsymbol{C}_n(k,r)\tilde{\boldsymbol{u}}_s(r,\theta,z)r\mathrm{d}r\mathrm{d}\theta \tag{2.58}$$

where $\hat{\boldsymbol{U}}_\mathrm{s} = [\hat{U}_{\mathrm{s},1}, \hat{U}_{\mathrm{s},2}, \hat{U}_{\mathrm{s},3}]^T$, and a_n normalizes the contribution per circumferential mode as follows:

$$a_n = \begin{cases} \frac{1}{2\pi} & n = 0 \\ \frac{1}{\pi} & n > 0 \end{cases} \tag{2.59}$$

The matrices $\boldsymbol{C}_n(k,z)$ and $\tilde{\boldsymbol{T}}_n(\theta)$ contain the Bessel functions of the Hankel transform and the components of the Fourier series, respectively:

$$\boldsymbol{C}_n(k,z) = \begin{bmatrix} \frac{1}{k}\frac{\partial}{\partial r}\mathrm{J}_n(kr) & \frac{n}{kr}\mathrm{J}_n(kr) & 0 \\ \frac{n}{kr}\mathrm{J}_n(kr) & \frac{1}{k}\frac{\partial}{\partial r}\mathrm{J}_n(kr) & 0 \\ 0 & 0 & \mathrm{J}_n(kr) \end{bmatrix} \tag{2.60}$$

$$\tilde{\boldsymbol{T}}_n(\theta) = \mathrm{diag}\left[\cos(n\theta), -\sin(n\theta), \cos(n\theta)\right] \tag{2.61}$$

The actual Hankel transforms corresponding to Eqs. (2.57) and (2.58) can be derived by diagonalizing the $\boldsymbol{C}_s$ matrix, resulting in a standard definition of the Hankel transform (Kausel, 1974):

$$\begin{bmatrix} \tilde{u}_{\mathrm{s},1} + \tilde{u}_{\mathrm{s},2} \\ \tilde{u}_{\mathrm{s},2} - \tilde{u}_{\mathrm{s},1} \\ \tilde{u}_{\mathrm{s},3} \end{bmatrix} = \int_0^\infty \begin{bmatrix} \mathrm{J}_{n-1} & 0 & 0 \\ 0 & \mathrm{J}_{n+1} & 0 \\ 0 & 0 & \mathrm{J}_n \end{bmatrix} \begin{bmatrix} \hat{U}_{\mathrm{s},1} + \hat{U}_{\mathrm{s},2} \\ \hat{U}_{\mathrm{s},2} - \hat{U}_{\mathrm{s},1} \\ \hat{U}_{\mathrm{s},3} \end{bmatrix} k\mathrm{d}k \tag{2.62}$$

$$\begin{bmatrix} \hat{U}_{\mathrm{s},1} + \hat{U}_{\mathrm{s},2} \\ \hat{U}_{\mathrm{s},2} - \hat{U}_{\mathrm{s},1} \\ \hat{U}_{\mathrm{s},3} \end{bmatrix} = \int_0^\infty \begin{bmatrix} \mathrm{J}_{n-1} & 0 & 0 \\ 0 & \mathrm{J}_{n+1} & 0 \\ 0 & 0 & \mathrm{J}_n \end{bmatrix} \begin{bmatrix} \tilde{u}_{\mathrm{s},1} + \tilde{u}_{\mathrm{s},2} \\ \tilde{u}_{\mathrm{s},2} - \tilde{u}_{\mathrm{s},1} \\ \tilde{u}_{\mathrm{s},3} \end{bmatrix} r\mathrm{d}r \tag{2.63}$$

The displacements $\hat{\boldsymbol{U}}_\mathrm{s}(k,z)$ are expressed in terms of potentials using the potential decomposition:

$$\begin{bmatrix} \hat{U}_{\mathrm{s},1}(k,z) \\ \hat{U}_{\mathrm{s},2}(k,z) \\ \hat{U}_{\mathrm{s},3}(k,z) \end{bmatrix} = \begin{bmatrix} k\left(\hat{\Phi}_\mathrm{s}(k,z) + \frac{\partial}{\partial z}\hat{\Psi}_\mathrm{s}(k,z)\right) \\ -k\hat{X}_\mathrm{s}(k,z) \\ \frac{\partial}{\partial z}\hat{\Phi}_\mathrm{s}(k,z) + k^2\hat{\Psi}_\mathrm{s}(k,z) \end{bmatrix} \tag{2.64}$$

The transforms for the displacements Eqs. (2.57) and (2.58) also apply to the stresses normal to the horizontal plane, $\tilde{\boldsymbol{\sigma}}_\mathrm{s} \cdot \mathrm{n}_\mathrm{z}$, and the body forces $\tilde{\boldsymbol{f}}_\mathrm{s}$:

$$\begin{bmatrix} \tilde{\sigma}_{\mathrm{s},zr}(r,\theta,z) \\ \tilde{\sigma}_{\mathrm{s},z\theta}(r,\theta,z) \\ \tilde{\sigma}_{\mathrm{s},zz}(r,\theta,z) \end{bmatrix} \quad \leftrightarrow \quad \begin{bmatrix} \hat{S}_{\mathrm{s},1}(k,z) \\ \hat{S}_{\mathrm{s},2}(k,z) \\ \hat{S}_{\mathrm{s},3}(k,z) \end{bmatrix}, \qquad \begin{bmatrix} \tilde{f}_{\mathrm{s},r}(r,\theta,z) \\ \tilde{f}_{\mathrm{s},\theta}(r,\theta,z) \\ \tilde{f}_{\mathrm{s},z}(r,\theta,z) \end{bmatrix} \quad \leftrightarrow \quad \begin{bmatrix} \hat{F}_{\mathrm{s},1}(k,z) \\ \hat{F}_{\mathrm{s},2}(k,z) \\ \hat{F}_{\mathrm{s},3}(k,z) \end{bmatrix} \tag{2.65}$$

By performing some algebra and employing well-known constitutive relations in elasticity, we can express the transformed stresses in terms of the transformed displacements:

$$\begin{bmatrix} \hat{S}_{s,1}(k,z) \\ \hat{S}_{s,2}(k,z) \\ \hat{S}_{s,3}(k,z) \end{bmatrix} = \begin{bmatrix} \mu_s \left(\frac{\partial}{\partial z} \hat{U}_{s,1}(k,z) + k\hat{U}_{s,3}(k,z) \right) \\ \mu_s \frac{\partial}{\partial z} \hat{U}_{s,2}(k,z) \\ (\lambda_s + 2\mu_s) \frac{\partial}{\partial z} \hat{U}_{s,3}(k,z) - \lambda_s k \hat{U}_{s,1}(k,z) \end{bmatrix} \tag{2.66}$$

The transformation of the soil equation of motion Eq. (2.3) by Eq. (2.57) separates the P-SV and SH waves and introduces the Dirac delta in the force component at $z = z_{s0}$. The resulting equations of motion in the wave number domain are as follows:

$$\mu_s \left(\beta_s^2 - \frac{\partial^2}{\partial z^2} \right) \hat{U}_{s,1}(k,z) + (\lambda_s + \mu_s) \left[k^2 \hat{U}_{s,1}(k,z) - k\hat{U}_{s,3}(k,z) \right] = \hat{F}_{s,1}(k)\delta(z - z_{s0}) \tag{2.67}$$

$$\mu_s \left(\beta_s^2 - \frac{\partial^2}{\partial z^2} \right) \hat{U}_{s,2}(k,z) = \hat{F}_{s,2}(k)\delta(z - z_{s0}) \tag{2.68}$$

$$(\lambda_s + 2\mu_s) \left(\alpha_s^2 - \frac{\partial^2}{\partial z^2} \right) \hat{U}_{s,3}(k,z) - (\lambda_s + \mu_s) \left[k^2 \hat{U}_{s,3}(k,z) - k\hat{U}_{s,1}(k,z) \right] = \hat{F}_{s,3}(k)\delta(z - z_{s0}) \tag{2.69}$$

For ring sources at $r = r_p$ and $n = 0$ or $n = 1$, the values for $\hat{\boldsymbol{F}}(k)$ are obtained through the Hankel transform, as described in Eq. (2.58):

$$\hat{\boldsymbol{F}}_{s,n=0}(k) = \begin{bmatrix} -J_1(kr_p) r_p \hat{f}_{s,r} \\ -J_1(kr_p) r_p \hat{f}_{s,\theta} \\ J_0(kr_p) r_p \hat{f}_{s,z} \end{bmatrix} \tag{2.70}$$

$$\hat{\boldsymbol{F}}_{s,n=1}(k) = \begin{bmatrix} J_0(kr_p) r_p - \frac{J_1(kr_p)}{k} & \frac{J_1(kr_p)}{k} & 0 \\ \frac{J_1(kr_p)}{k} & J_0(kr_p) r_p - \frac{J_1(kr_p)}{k} & 0 \\ 0 & 0 & J_1(kr_p) r_p \end{bmatrix} \begin{bmatrix} \hat{f}_{s,r} \\ \hat{f}_{s,\theta} \\ \hat{f}_{s,z} \end{bmatrix} \tag{2.71}$$

It is clear from Eqs. (2.64), (2.66) and (2.68) that the SH waves are decoupled from the P-SV waves, resulting in a decoupled solution. Although the response to $\hat{F}_{s,2}(k)$ is well-known as the fundamental solution of Eq. (2.68), it is approached in a similar way to the P-SV problem.

The body forces are transformed into an interface problem to find the full space Green's function of a ring source, where the domain is split horizontally into two half-spaces with only waves propagating outwards from the interface. The two half-spaces for $z < z_{s0}$ and $z > z_{s0}$ are denoted as $^-$ and $^+$, respectively. In the half-space $z < z_{s0}$ and $z > z_{s0}$, the coefficients A_4, A_6, and A_8 or A_3, A_5, and A_7 are set to 0 based on the Sommerfeld radiation

condition. At the interface $z = z_{s0}$, the following interface conditions need to be satisfied:

$$\hat{\boldsymbol{S}}_s^-(k, z_{s0}^-) = \hat{\boldsymbol{S}}_s^+(k, z_{s0}^+) + \hat{\boldsymbol{F}}_s(k), \qquad \hat{\boldsymbol{U}}_s^-(k, z_{s0}^-) = \hat{\boldsymbol{U}}_s^+(k, z_{s0}^+) \tag{2.72}$$

Solving the set of equations in Eq. (2.72) yields the particular solution to the potentials. By substituting Eqs. (2.49) to (2.51), (2.64) and (2.66), we find the particular solutions of the potentials:

$$\hat{\Phi}_s^P(k, z) = \frac{k\hat{F}_{s,1}(k)}{2\rho_s\omega^2\alpha_s}\begin{cases} e^{\alpha_s(z-z_{s0})} \\ e^{-\alpha_s(z-z_{s0})} \end{cases} + \frac{\hat{F}_{s,3}(k)}{2\rho_s\omega^2}\begin{cases} -e^{\alpha_s(z-z_{s0})} & z < z_{s0} \\ e^{-\alpha_s(z-z_{s0})} & z > z_{s0} \end{cases} \tag{2.73}$$

$$\hat{\Psi}_s^P(k, z) = \frac{\hat{F}_{s,1}(k)}{2\rho_s\omega^2 k}\begin{cases} -e^{\beta_s(z-z_{s0})} \\ e^{-\beta_s(z-z_{s0})} \end{cases} + \frac{\hat{F}_{s,3}(k)}{2\rho_s\omega^2\beta_s}\begin{cases} e^{\beta_s(z-z_{s0})} & z < z_{s0} \\ e^{-\beta_s(z-z_{s0})} & z > z_{s0} \end{cases} \tag{2.74}$$

$$\hat{X}_s^P(k, z) = -\frac{\hat{F}_{s,2}(k)}{2\mu_s k\beta_s}\begin{cases} e^{\beta_s(z-z_{s0})} & z < z_{s0} \\ e^{-\beta_s(z-z_{s0})} & z > z_{s0} \end{cases} \tag{2.75}$$

2.4.3. Green's functions of the fluid-soil domain

The equations above describe the potential responses to ring sources in fluid and soil media. The mathematical framework and derivations provided here are extensive, involving various mathematical tools such as Hankel transforms, Fourier series, and complex variables. The equations provide a foundation for understanding the behaviour of waves in these media due to ring sources. They are essential for solving the boundary value problem of a fluid layer over a half-space.

The derivation of Green's functions of a fluid layer overlying a soil half-space entails the substitution of specific potential solutions into the boundary value problem. This substitution takes place in the wavenumber domain, thus transforming the original boundary value problem, as given by Eqs. (2.4) to (2.7), into the following transformed forms:

$$\rho_f\omega^2\hat{\Phi}_f(k, z_1) = 0 \tag{2.76}$$

$$\frac{d}{dz}\hat{\Phi}_f(k, z_2) - \hat{U}_{s,3}(k, z_2) = 0 \tag{2.77}$$

$$\rho_f\omega^2\hat{\Phi}_f(k, z_2) + \hat{S}_{s,3}(k, z_2) = 0 \tag{2.78}$$

$$\hat{S}_{s,1}(k, z_2) = \hat{S}_{s,2}(k, z_2) = 0 \tag{2.79}$$

The boundary value problem is reformulated in terms of potentials by introducing Eqs. (2.64) and (2.66) while considering the Sommerfeld radiation condition in the vertical direction and incorporating the particular solutions derived in Sections 2.4.1 and 2.4.2. To ensure convergence, the vertical coordinate in the potential's exponent is normalized to the

layer interfaces. This leads to the following expressions for the potentials:

$$\hat{\Phi}_{\mathrm{f}}(k,z) = A_1 e^{-\alpha_{\mathrm{f}}(z-z_1)} + A_2 e^{\alpha_{\mathrm{f}}(z-z_2)} + \hat{\Phi}_{\mathrm{f}}^{\mathrm{P}}(k,z) \tag{2.80}$$

$$\hat{\Phi}_{\mathrm{s}}(k,z) = A_3 e^{-\alpha_{\mathrm{s}}(z-z_2)} + \hat{\Phi}_{\mathrm{s}}^{\mathrm{P}}(k,z) \tag{2.81}$$

$$\hat{\Psi}_{\mathrm{s}}(k,z) = A_5 e^{-\beta_{\mathrm{s}}(z-z_2)} + \hat{\Psi}_{\mathrm{s}}^{\mathrm{P}}(k,z) \tag{2.82}$$

$$\hat{X}_{\mathrm{s}}(k,z) = A_7 e^{-\beta_{\mathrm{s}}(z-z_2)} + \hat{X}_{\mathrm{s}}^{\mathrm{P}}(k,z) \tag{2.83}$$

Note, the boundary value problem of a single ring source at $z = z_{\mathrm{f0}}$ or $z = z_{\mathrm{s0}}$ contains only the particular solution related to the domain in which the source is located, i.e. either the fluid or solid. For completion, both are introduced in the boundary value problem hereafter. The coefficients A_i are determined by substituting these potentials into the boundary value problem, yielding a set of equations:

$$\begin{bmatrix} 1 & e^{-\alpha_{\mathrm{f}}h_{\mathrm{f}}} & 0 & 0 & 0 \\ \alpha_{\mathrm{f}} e^{-\alpha_{\mathrm{f}}h_{\mathrm{f}}} & \alpha_{\mathrm{f}} & 0 & k^2 & 0 \\ \rho_{\mathrm{f}}\omega^2 e^{-\alpha_{\mathrm{f}}h_{\mathrm{f}}} & \rho_{\mathrm{f}}\omega^2 & \mu_{\mathrm{s}}(k^2+\beta_{\mathrm{s}}^2) & -(\lambda_{\mathrm{s}}+2\mu_{\mathrm{s}})k^2\beta_{\mathrm{s}} & 0 \\ 0 & 0 & -\mu_{\mathrm{s}}k\alpha_{\mathrm{s}} & \mu_{\mathrm{s}}k(\beta_{\mathrm{s}}^2+k^2) & 0 \\ 0 & 0 & 0 & 0 & \beta_{\mathrm{s}}k\mu_{\mathrm{s}} \end{bmatrix} \begin{bmatrix} A_1 \\ A_2 \\ A_3 \\ A_5 \\ A_7 \end{bmatrix} = \begin{bmatrix} -\hat{\Phi}_{\mathrm{f}}^{\mathrm{P}}(k,z_1) \\ \frac{\partial}{\partial z}\hat{\Phi}_{\mathrm{f}}^{\mathrm{P}}(k,z=z_2) - \hat{U}_{\mathrm{s},3}^{\mathrm{P}}(k,z_2) \\ -\hat{S}_{\mathrm{s},3}^{\mathrm{P}}(k,z_2) - \rho_{\mathrm{f}}\omega^2\hat{\Phi}_{\mathrm{f}}^{\mathrm{P}}(k,z_2) \\ -\hat{S}_{\mathrm{s},1}^{\mathrm{P}}(k,z_2) \\ -\hat{S}_{\mathrm{s},2}^{\mathrm{P}}(k,z_2) \end{bmatrix} \tag{2.84}$$

In this equation, h_{f} represents the height of the fluid layer. The particular solutions on the right-hand side are obtained by substituting Eqs. (2.81) to (2.83) into Eqs. (2.64) and (2.66). Equation (2.84) again illustrates the decoupling of the P-SV and SH problems.

Solving for the unknown coefficients A_i in Eq. (2.84) yields expressions for the frequency-wavenumber domain Green's functions associated with potentials arising from either a fluid ring source at z_{f0} or a soil ring source at z_{s0}. The soil sources $\hat{F}_{\mathrm{s},1}$, $\hat{F}_{\mathrm{s},2}$, and $\hat{F}_{\mathrm{s},3}$ can be expressed in terms of $\tilde{f}_{\mathrm{s},r}$, $\tilde{f}_{\mathrm{s},\theta}$, and $\tilde{f}_{\mathrm{s},z}$ using Eq. (2.70) or Eq. (2.71).

The obtained potentials are incorporated into the pressure, displacements, and stress expressions. The subsequent step involves applying the inverse Hankel transform to derive the frequency domain space Green's functions and Green's tensors. This transformation is carried out using direct wavenumber integration in accordance with the methodology outlined by Jensen et al. (2011). An adaptive integration scheme ensures precise integration around the singularities near the real axis. The truncation limit and step size choice depend on the distance between the source and receiver. Specifically, receivers close to the source require a high truncation limit for the integral, while those farther away can be accurately addressed with a smaller integration step.

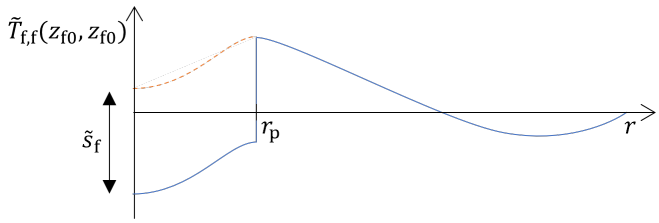


Figure 2.2: Example of a fluid Green's tensor function at the location of the source to indicate the discontinuity.

Green's tensors at the source require special attention in the inverse Hankel transform, particularly when the source and receiver coincide, hence the introduction of $\pm 1/2$. Achieving numerical convergence of the inverse transform becomes challenging when the receiver location is at the vertical location of the source and near the source in the radial direction, requiring high wave numbers (k) to approach the sharp transition. One approach is to apply analytical modifications to the integrand, solving parts of the inverse Hankel transforms analytically, as discussed in Appendix B. However, these modifications shift the convergence problem to other terms of the integrand that cannot be analytically inverted.

A direct and effective solution employed in the numeric scheme involves artificially removing the discontinuity by adding a Heaviside function in the wave-number domain, as illustrated by the orange dashed line in Fig. 2.2. In the spatial domain, the Heaviside function can then be subtracted again. The Heaviside function in the wavenumber domain, denoted by $\tilde{s}_{\mathrm{f}}$ as indicated in Fig. 2.2, one obtains:

$$\int_0^\infty \tilde{s}_{\mathrm{f}} H(r_{\mathrm{p}} - r) \mathrm{J}_n(kr) r \mathrm{d}r = -\frac{\tilde{s}_{\mathrm{f}} r_p}{2k} \left(\pi \mathrm{J}_n(kr_p) \tan\left(\frac{\pi(n+1)}{2}\right) \boldsymbol{J}_{n+1}(kr_p) n \right.$$
$$\left. - \pi \mathrm{J}_n(kr_p) \mathrm{E}_{n+1}(kr_p) n - 2\mathrm{J}_{n+1}(kr_p) \mathrm{s}_{1,n}(kr_p) \right) \quad (2.85)$$

Here, $\boldsymbol{J}_{n+1}(kr_p)$ represents the Anger function, $\mathrm{E}_{n+1}(kr_p)$ corresponds to the Weber function, and $\mathrm{s}_{1,n}(kr_p)$ is the Lommel s function.

Subsequently, after the inverse Hankel transform, the Green's functions and Green's tensors are integrated into the boundary integral transforms, forming a comprehensive solution. The formulations for the boundary integrals involving Green's functions (G) and Green's tensors (T) are presented below:

$$\tilde{p}_{\mathrm{f}}(z) = \int_{z_0}^{z_1} \tilde{G}_{\mathrm{f,f}}(z, z_{\mathrm{f0}}) \tilde{s}_{\mathrm{f}}(z_{\mathrm{f0}}) \mathrm{d}z_{\mathrm{f0}} + \sum_{\alpha=r,\theta,z} \int_{z_1}^{\infty} \tilde{G}_{\mathrm{f,s}\alpha}(z, z_{\mathrm{s0}}) \tilde{f}_{\mathrm{s},\alpha}(z_{\mathrm{f0}}) \mathrm{d}z_{\mathrm{s0}} \quad (2.86)$$

$$\tilde{u}_{\mathrm{f,r}}(z) = \int_{z_0}^{z_1} \tilde{T}_{\mathrm{f,f}}(z, z_{\mathrm{f0}}) \tilde{s}_{\mathrm{f}}(z_{\mathrm{f0}}) \mathrm{d}z_{\mathrm{f0}} \pm \frac{1}{2} \tilde{s}_{\mathrm{f}}(z)$$
$$+ \sum_{\alpha=r,\theta,z} \int_{z_1}^{\infty} \tilde{T}_{\mathrm{f,s}\alpha}(z, z_{\mathrm{s0}}) \tilde{f}_{\mathrm{s},\alpha}(z_{\mathrm{f0}}) \mathrm{d}z_{\mathrm{s0}} \quad (2.87)$$

$$\begin{aligned}\tilde{u}_{\mathrm{s},\alpha}(z) = &\int_{z_0}^{z_1} \tilde{G}_{\mathrm{s}\alpha,\mathrm{f}}(z, z_{\mathrm{f}0})\tilde{s}_{\mathrm{f}}(z_{\mathrm{f}0})\mathrm{d}z_{\mathrm{f}0} \\ &+ \sum_{\beta=r,\theta,z}\int_{z_1}^{\infty} \tilde{G}_{\mathrm{s}\alpha,\mathrm{s}\beta}(z, z_{\mathrm{s}0})\tilde{f}_{\mathrm{s},\alpha}(z_{\mathrm{f}0})\mathrm{d}z_{\mathrm{s}0}\end{aligned} \tag{2.88}$$

$$\begin{aligned}\tilde{\sigma}_{\mathrm{s},\mathrm{r}\alpha}(z) = &\int_{z_0}^{z_1} \tilde{T}_{\mathrm{s}\alpha,\mathrm{f}}(z, z_{\mathrm{f}0})\hat{s}_{\mathrm{f}}(z_{\mathrm{f}0})\mathrm{d}z_{\mathrm{f}0} \\ &+ \sum_{\beta=r,\theta,z}\int_{z_1}^{\infty} \tilde{T}_{\mathrm{s}\alpha,\mathrm{s}\beta}(z, z_{\mathrm{s}0})\tilde{f}_{\mathrm{s},\alpha}(z_{\mathrm{f}0})\mathrm{d}z_{\mathrm{s}0} \pm \frac{1}{2}\tilde{f}_{\mathrm{s},\alpha}(z)\end{aligned} \tag{2.89}$$

where the ± terms arise from the normal direction within the boundary element formulation, referring to the exterior or interior boundary domain, respectively.

2.4.4. Boundary element matrix

The numerical integration of Eqs. (2.86) to (2.89) leads to a matrix that establishes a relationship between fluid and soil displacements, pressure and stresses with the ring sources. This procedure is conducted for exterior and interior boundary elements, distinguished by the superscripts ±. The resulting matrix equation is given by:

$$\begin{bmatrix} \tilde{\boldsymbol{u}}^{\pm}_{\mathrm{fr}} \\ \tilde{\boldsymbol{u}}_{\mathrm{sr}} \\ \tilde{\boldsymbol{u}}_{\mathrm{s}\theta} \\ \tilde{\boldsymbol{u}}_{\mathrm{sz}} \\ \boldsymbol{p}_{\mathrm{f}} \\ \tilde{\boldsymbol{\sigma}}^{\pm}_{\mathrm{srr}} \\ \tilde{\boldsymbol{\sigma}}^{\pm}_{\mathrm{sr}\theta} \\ \tilde{\boldsymbol{\sigma}}^{\pm}_{\mathrm{srz}} \end{bmatrix} = \begin{bmatrix} \tilde{\boldsymbol{T}}_{\mathrm{f,f}} \pm \frac{1}{2}\boldsymbol{I} & \tilde{\boldsymbol{T}}_{\mathrm{f,sr}} & \tilde{\boldsymbol{T}}_{\mathrm{f,s}\theta} & \tilde{\boldsymbol{T}}_{\mathrm{f,sz}} \\ \tilde{\boldsymbol{G}}_{\mathrm{sr,f}} & \tilde{\boldsymbol{G}}_{\mathrm{sr,sr}} & \tilde{\boldsymbol{G}}_{\mathrm{sr,s}\theta} & \tilde{\boldsymbol{G}}_{\mathrm{sr,sz}} \\ \tilde{\boldsymbol{G}}_{\mathrm{s}\theta,\mathrm{f}} & \tilde{\boldsymbol{G}}_{\mathrm{s}\theta,\mathrm{sr}} & \tilde{\boldsymbol{G}}_{\mathrm{s}\theta,\mathrm{s}\theta} & \tilde{\boldsymbol{G}}_{\mathrm{s}\theta,\mathrm{sz}} \\ \tilde{\boldsymbol{G}}_{\mathrm{sz,f}} & \tilde{\boldsymbol{G}}_{\mathrm{sz,sr}} & \tilde{\boldsymbol{G}}_{\mathrm{sz,s}\theta} & \tilde{\boldsymbol{G}}_{\mathrm{sz,sz}} \\ \tilde{\boldsymbol{G}}_{\mathrm{f,f}} & \tilde{\boldsymbol{G}}_{\mathrm{f,sr}} & \tilde{\boldsymbol{G}}_{\mathrm{f,s}\theta} & \tilde{\boldsymbol{G}}_{\mathrm{f,sz}} \\ \tilde{\boldsymbol{T}}_{\mathrm{sr,f}} & \tilde{\boldsymbol{T}}_{\mathrm{sr,sr}} \pm \frac{1}{2}\boldsymbol{I} & \tilde{\boldsymbol{T}}_{\mathrm{sr,s}\theta} & \tilde{\boldsymbol{T}}_{\mathrm{sr,sz}} \\ \tilde{\boldsymbol{T}}_{\mathrm{sr,f}} & \tilde{\boldsymbol{T}}_{\mathrm{s}\theta,\mathrm{sr}} & \tilde{\boldsymbol{T}}_{\mathrm{s}\theta,\mathrm{s}\theta} \pm \frac{1}{2}\boldsymbol{I} & \tilde{\boldsymbol{T}}_{\mathrm{s}\theta,\mathrm{sz}} \\ \tilde{\boldsymbol{T}}_{\mathrm{sz,f}} & \tilde{\boldsymbol{T}}_{\mathrm{sz,sr}} & \tilde{\boldsymbol{T}}_{\mathrm{s}\theta,\mathrm{sz}} & \tilde{\boldsymbol{T}}_{\mathrm{sz,sz}} \pm \frac{1}{2}\boldsymbol{I} \end{bmatrix} \begin{bmatrix} \tilde{\boldsymbol{s}}_{\mathrm{f}} \\ \tilde{\boldsymbol{f}}_{\mathrm{sr}} \\ \tilde{\boldsymbol{f}}_{\mathrm{s}\theta} \\ \tilde{\boldsymbol{f}}_{\mathrm{sz}} \end{bmatrix} \tag{2.90}$$

The terms in the matrix follow from numerical integration over the source and discretization of the lefthand side, as illustrated below:

$$\tilde{u}_{\mathrm{f,r}}(z) = \int_{z_0}^{z_1} \tilde{T}_{\mathrm{f,f}}(z, z_{\mathrm{f}0})\tilde{s}_{\mathrm{f}}(z_{\mathrm{f}0})\mathrm{d}z_{\mathrm{f}0} \pm \frac{1}{2}\tilde{s}_{\mathrm{f}}(z) \rightarrow \tilde{\boldsymbol{u}}^{\pm}_{\mathrm{fr}} = \left[\tilde{\boldsymbol{T}}_{\mathrm{f,f}} \pm \frac{1}{2}\boldsymbol{I}\right]\tilde{\boldsymbol{s}}_{\mathrm{f}} \tag{2.91}$$

$$\tilde{u}_{\mathrm{s},z}(z) = \int_{z_0}^{z_1} \tilde{G}_{\mathrm{sz,f}}(z, z_{\mathrm{f}0})\tilde{s}_{\mathrm{f}}(z_{\mathrm{f}0})\mathrm{d}z_{\mathrm{f}0} \rightarrow \tilde{\boldsymbol{u}}_{\mathrm{sz}} = \tilde{\boldsymbol{G}}_{\mathrm{sz,f}}\tilde{\boldsymbol{s}}_{\mathrm{f}} \tag{2.92}$$

These equations encapsulate the relationship between various displacements, pressures, stresses, and source terms. Upon further analysis, the boundary stiffness matrix is

constructed from Eq. (2.90), leading to a concise expression:

$$\begin{bmatrix} -\tilde{\boldsymbol{p}}_{\mathrm{f}} \\ \tilde{\boldsymbol{\sigma}}^{\pm}_{\mathrm{srr}} \\ \tilde{\boldsymbol{\sigma}}^{\pm}_{\mathrm{sr}\theta} \\ \tilde{\boldsymbol{\sigma}}^{\pm}_{\mathrm{srz}} \end{bmatrix} = \tilde{\boldsymbol{K}}^{\pm}_{\mathrm{fs}} \begin{bmatrix} \tilde{\boldsymbol{u}}^{\pm}_{\mathrm{fr}} \\ \tilde{\boldsymbol{u}}_{\mathrm{sr}} \\ \tilde{\boldsymbol{u}}_{\mathrm{s}\theta} \\ \tilde{\boldsymbol{u}}_{\mathrm{sz}} \end{bmatrix} \tag{2.93}$$

Notably, the matrix $\tilde{\boldsymbol{K}}_{\mathrm{fs}}$ should be constructed with care as the columns in submatrices $\tilde{\boldsymbol{G}}_{\mathrm{f,s}}$, $\tilde{\boldsymbol{T}}_{\mathrm{f,s}}$, $\tilde{\boldsymbol{G}}_{\mathrm{s,f}}$, and $\tilde{\boldsymbol{T}}_{\mathrm{s,f}}$ have nearly linear dependent columns and therefore are almost singular and hard to inverse without losing precision. Therefore, it is better to invert the matrix in Eq. (2.44) by parts starting by collecting the degrees of freedom of the soil and splitting the matrix into two square matrices:

$$\begin{bmatrix} \tilde{\boldsymbol{u}}_{\mathrm{fr}} \\ \tilde{\boldsymbol{u}}_{\mathrm{s}} \end{bmatrix} = \begin{bmatrix} \tilde{\boldsymbol{T}}^{\pm}_{\mathrm{f,f}} & \tilde{\boldsymbol{T}}_{\mathrm{f,s}} \\ \tilde{\boldsymbol{G}}_{\mathrm{s,f}} & \tilde{\boldsymbol{G}}_{\mathrm{s,s}} \end{bmatrix} \begin{bmatrix} \tilde{\boldsymbol{s}}_{\mathrm{f}} \\ \tilde{\boldsymbol{f}}_{\mathrm{s}} \end{bmatrix}, \qquad \begin{bmatrix} -\boldsymbol{p}_{\mathrm{f}} \\ \tilde{\boldsymbol{\sigma}}_{\mathrm{sr}} \end{bmatrix} = \begin{bmatrix} -\tilde{\boldsymbol{G}}_{\mathrm{f,f}} & -\tilde{\boldsymbol{G}}_{\mathrm{f,s}} \\ \tilde{\boldsymbol{T}}_{\mathrm{s,f}} & \tilde{\boldsymbol{T}}_{\mathrm{s,s}} \end{bmatrix} \begin{bmatrix} \tilde{\boldsymbol{s}}_{\mathrm{f}} \\ \tilde{\boldsymbol{f}}_{\mathrm{s}} \end{bmatrix} \tag{2.94}$$

Then, the inverse of the first matrix is taken in steps, while the off-diagonal matrices contain linear dependent columns:

$$\begin{bmatrix} \tilde{\boldsymbol{T}}_{\mathrm{f,f}} & \tilde{\boldsymbol{T}}_{\mathrm{f,s}} \\ \tilde{\boldsymbol{G}}_{\mathrm{s,f}} & \tilde{\boldsymbol{G}}_{\mathrm{s,s}} \end{bmatrix}^{-1} = \begin{bmatrix} \tilde{\boldsymbol{T}}^{-1}_{\mathrm{f,f}} + \tilde{\boldsymbol{T}}^{-1}_{\mathrm{f,f}} \tilde{\boldsymbol{T}}_{\mathrm{f,s}} \tilde{\boldsymbol{H}}^{-1}_{\mathrm{f,s}} \tilde{\boldsymbol{G}}_{\mathrm{s,f}} \tilde{\boldsymbol{T}}^{-1}_{\mathrm{f,f}} & -\tilde{\boldsymbol{T}}^{-1}_{\mathrm{f,f}} \tilde{T}_{\mathrm{f,s}} \tilde{\boldsymbol{H}}^{-1}_{\mathrm{f,s}} \\ -\tilde{\boldsymbol{H}}^{-1}_{\mathrm{f,s}} \tilde{\boldsymbol{G}}_{\mathrm{s,f}} \tilde{\boldsymbol{T}}^{-1}_{\mathrm{f,f}} & \tilde{\boldsymbol{H}}^{-1}_{\mathrm{f,s}} \end{bmatrix} \tag{2.95}$$

with:

$$\tilde{\boldsymbol{H}}_{\mathrm{f,s}} = (\tilde{\boldsymbol{G}}_{\mathrm{s,s}} - \tilde{\boldsymbol{G}}_{\mathrm{s,f}} \tilde{\boldsymbol{T}}^{-1}_{\mathrm{f,f}} \tilde{\boldsymbol{T}}_{\mathrm{f,s}}) \tag{2.96}$$

and

$$\begin{bmatrix} -\boldsymbol{p}_{\mathrm{f}} \\ \tilde{\boldsymbol{\sigma}}_{\mathrm{sr}} \end{bmatrix} = \begin{bmatrix} -\tilde{\boldsymbol{G}}_{\mathrm{f,f}} & -\tilde{\boldsymbol{G}}_{\mathrm{f,s}} \\ \tilde{\boldsymbol{T}}_{\mathrm{s,f}} & \tilde{\boldsymbol{T}}_{\mathrm{s,s}} \end{bmatrix} \cdot \begin{bmatrix} \tilde{\boldsymbol{T}}^{-1}_{\mathrm{f,f}} + \tilde{\boldsymbol{T}}^{-1}_{\mathrm{f,f}} \tilde{\boldsymbol{T}}_{\mathrm{f,s}} \tilde{\boldsymbol{H}}^{-1}_{\mathrm{f,s}} \tilde{\boldsymbol{G}}_{\mathrm{s,f}} \tilde{\boldsymbol{T}}^{-1}_{\mathrm{f,f}} & -\tilde{\boldsymbol{T}}^{-1}_{\mathrm{f,f}} \tilde{\boldsymbol{T}}_{\mathrm{f,s}} \tilde{\boldsymbol{H}}^{-1}_{\mathrm{f,s}} \\ -\tilde{\boldsymbol{H}}^{-1}_{\mathrm{f,s}} \tilde{\boldsymbol{G}}_{\mathrm{s,f}} \tilde{\boldsymbol{T}}^{-1}_{\mathrm{f,f}} & \tilde{\boldsymbol{H}}^{-1}_{\mathrm{f,s}} \end{bmatrix} \begin{bmatrix} \tilde{\boldsymbol{u}}_{\mathrm{fr}} \\ \tilde{\boldsymbol{u}}_{\mathrm{s}} \end{bmatrix} \tag{2.97}$$

The outlined procedure in this section is repeated for receivers within the propagated field, i.e., those not situated on the surface of the pile. This iterative process yields a propagation matrix, complementing the previously acquired boundary stiffness matrix. It is important to note that the propagation matrix is not inherently square, as the number of receivers can be freely chosen and is independent of the discretization of the pile-fluid-soil interface. Once the boundary pressure, displacements, and stress are determined, the propagation matrix enables the computation of waves at any designated receiver location within the fluid or soil.

2.5. Coupling procedure of pile and fluid-soil substructures

In summary, the model addresses the problem in several sequential steps. Initially, the pile modes are determined using a root-finding algorithm decomposition, as detailed in

Section 2.3. Subsequently, the fluid-soil boundary element matrix and propagating matrix are derived based on the ring sources in the fluid and soil, as elucidated in Section 2.4.

Following this, the derived boundary element matrix is substituted into the chosen set of interface conditions, described by Eqs. (2.8) to (2.23), resulting in functions that define the distributed pressure acting on the pile ($\tilde{\boldsymbol{f}}_{\mathrm{p},n}(z)$), as expressed in Eq. (2.40):

$$\sum_{l=1}^{\infty}\sum_{k=1}^{\infty}\int_0^{L_\mathrm{p}} \tilde{\eta}_{nk}\rho_\mathrm{p}h_\mathrm{p}(\omega_k^2-\omega^2)\tilde{\boldsymbol{U}}_{\mathrm{p},nl}^T(z)\tilde{\boldsymbol{U}}_{\mathrm{p},nk}(z)\mathrm{d}z = \sum_{l=1}^{\infty}\int_0^{L_\mathrm{p}} \tilde{\boldsymbol{U}}_{\mathrm{p},nl}^T(z)\tilde{\boldsymbol{f}}_{\mathrm{p},n}(z) + \tilde{\boldsymbol{U}}_{\mathrm{p},nl}^T(z)\tilde{\boldsymbol{f}}_{\mathrm{ext},n}\delta(z)\mathrm{d}z \tag{2.98}$$

For the PC case, substituting the reaction forces into the interface condition is straightforward since pile and exterior displacements are equal:

$$\tilde{\boldsymbol{f}}_{\mathrm{p},n}(z) = \begin{bmatrix} -\tilde{p}_\mathrm{f}^+(z)+\tilde{p}_\mathrm{f}^-(z) & 0 & 0 \\ \tilde{\sigma}_\mathrm{srr}^+(z)-\tilde{\sigma}_\mathrm{srr}^+(z) & \tilde{\sigma}_\mathrm{sr\theta}^+(z)-\tilde{\sigma}_\mathrm{sr\theta}^-(z) & \tilde{\sigma}_\mathrm{srz}^+(z)-\tilde{\sigma}_\mathrm{srz}^-(z) \end{bmatrix}^T \begin{matrix} z<z_1 \\ z>z_1 \end{matrix} \tag{2.99}$$

where the degrees of freedom are found at the interface in a discretized manner by:

$$\begin{bmatrix} -\tilde{\boldsymbol{p}}_\mathrm{f}^+ + \tilde{\boldsymbol{p}}_\mathrm{f}^- \\ \tilde{\boldsymbol{\sigma}}_\mathrm{srr}^+ - \tilde{\boldsymbol{\sigma}}_\mathrm{srr}^+ \\ \tilde{\boldsymbol{\sigma}}_\mathrm{sr\theta}^+ - \tilde{\boldsymbol{\sigma}}_\mathrm{sr\theta}^- \\ \tilde{\boldsymbol{\sigma}}_\mathrm{srz}^+ - \tilde{\boldsymbol{\sigma}}_\mathrm{srz}^- \end{bmatrix} = \left[\tilde{\boldsymbol{K}}_\mathrm{fs}^+ - \tilde{\boldsymbol{K}}_\mathrm{fs}^-\right] \begin{bmatrix} \tilde{\boldsymbol{u}}_\mathrm{pr} \\ \tilde{\boldsymbol{u}}_\mathrm{pr} \\ \tilde{\boldsymbol{u}}_\mathrm{p\theta} \\ \tilde{\boldsymbol{u}}_\mathrm{pz} \end{bmatrix} \tag{2.100}$$

The other interface conditions are treated similarly by applying straightforward linear algebra.

Solving the system yields the pile, fluid, and soil displacements at the interface based on the coupled solution. Finally, the fluid and soil fields are propagated to any desired receiver location using the propagation matrix, relying on pressure, displacements, and stresses at the pile surface. This comprehensive approach ensures a thorough understanding and representation of the structural and acoustic responses in the system.

3

Sound generated in offshore monopile installation by impact pile driving and the effect of asymmetries

This chapter introduces acoustic predictions for impact piling. The major sound generation mechanisms are physically explained. As an extension of the existing knowledge, the influence of asymmetric impact forces and pile-inclination on the generated underwater noise and seabed vibrations are examined based on cases of small- and large-diameter foundation piles. The study focuses on scenarios involving inclined and eccentric forces and tilted piles. The analysis reveals that non-symmetrical conditions significantly impact the sound pressure levels around the ring frequency of the pile due to various noise generation mechanisms. However, it is observed that the vertical component of the impact force predominantly contributes to the generation of underwater noise, primarily due to its considerably higher amplitude than the horizontal component.

This chapter has been published in Ocean Engineering, Volume 299, 10 March 2024, Molenkamp et al. (2024c).

3.1. Introduction

Monopiles are intended to be installed perfectly vertically. However, imperfections are inherent in installing foundations in offshore circumstances. Inclined forces have been touched upon in (Deng et al., 2016; Tsouvalas and Metrikine, 2013) via simplified acoustic models representing soil with springs. However, quantifying the effect on noise emission has not been systematically studied. Wilkes and Gavrilov (2017) modelled and studied the sound radiated from impact-driven raked piles, where the raked piles are installed under an angle of 14.5° and have significantly smaller dimensions than monopile foundations. The soil is modelled herein as an acoustic fluid, disregarding pile-soil interaction.

This chapter focuses on the effect of unintended non-symmetric sound fields generated during the impact piling of monopile foundations for wind farms. Specifically, the cases with an inclined force, an eccentric force and a tilted pile are studied. Since measurements sometimes show substantial azimuthal variation of the acoustic field, the impact of non-symmetries in the force and geometry on noise levels should be investigated.

This chapter quantifies and explains the effect of non-symmetric force excitations on underwater acoustics noise fields, focusing on inclined forces, eccentric forces, and an inclined pile. The effects are studied using frequency domain analysis based on the case of a small- and large-diameter monopile. The chapter provides physical explanations of the results and offers advice for engineering applications.

A COMSOL Multiphysics® Finite Element Method (FEM) model is built to model the pile and its vicinity, predicting sound pressure levels, sound exposure levels, and peak pressures in the frequency domain. The model description is provided in section 2, containing governing equations and modelling assumptions. Section 3 examines two case studies on installing a small and large-diameter monopile. The small pile is modelled to compare conclusions with (Deng et al., 2016) and can represent a pin pile. The large-diameter monopile described by Peng et al. (2021b) is modelled to verify the conclusions in relation to the water particle motion. Lastly, the conclusions are given in section 4.

3.2. Model description

A model is created in COMSOL Multiphysics® (2022) to evaluate the non-symmetric excitation forces. COMSOL Multiphysics® is a finite element package often used for near-field noise generation, i.e. the first tens of meters. In the Compile benchmark case Lippert et al., 2016, four out of seven participants used COMSOL Multiphysics® as a noise generation model, and it has been validated against measurements by Reinhall and Dahl (2011) and Zampolli et al. (2013). The disadvantage of a finite element package is the computational expenses; therefore, separate models are used for far-field propagation, i.e., hundreds of meters to kilometres, and the software is unsuitable for uncertainty analysis. The near-field results can be propagated with different methods, such as the wave number integration, normal modes or parabolic equation method, to predict the acoustic far-field. To reduce

computational costs, mode extension around the circumferential azimuth is used, reducing the discretization from 3D to 2D for the cases of inclined and eccentric forces. The tilted pile is modelled in 3D with significant computational costs.

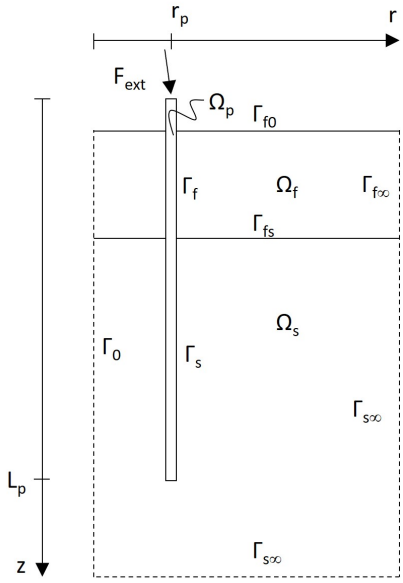


Figure 3.1: Model geometry

The model geometry presented in Fig. 3.1 shows the model domains and boundaries. Ω_f indicates the fluid domain, modelled with acoustic elements and is described by:

$$\nabla \cdot \left(\nabla p_{\mathrm{f}}(r,\theta,z) - \boldsymbol{q}_{\mathrm{f}}(r,\theta,z)\right) + \frac{\omega^2}{c_{\mathrm{f}}} p_{\mathrm{f}}(r,\theta,z) = -\rho_{\mathrm{f}} Q_{\mathrm{f}}(r,\theta,z) \tag{3.1}$$

with pressure field $p_{\mathrm{f}}(r,\theta,z)$, $Q_{\mathrm{f}}(r,\theta,z)$ being a monopole domain source and $\boldsymbol{q}_{\mathrm{f}}(r,\theta,z)$ contains dipole domain sources. The parameters ρ_{f}, c_{f} and ω are the fluid density, fluid wave speed and angular frequency, respectively. The pile and soil domains, Ω_p and Ω_s are modelled with solid elements described by:

$$\nabla \cdot \boldsymbol{\sigma}_{\mathrm{s}}(r,\theta,z) + \boldsymbol{F}_{\mathrm{s}}(r,\theta,z) = -\rho_{\mathrm{s}} \omega^2 \boldsymbol{u}_{\mathrm{s}}(r,\theta,z) \tag{3.2}$$

with stress vector $\boldsymbol{\sigma}_{\mathrm{s}}(r,\theta,z)$, displacement vector $\boldsymbol{u}_{\mathrm{s}}(r,\theta,z)$ and force vector $\boldsymbol{F}_{\mathrm{s}}(r,\theta,z)$ containing the external hammer forces (F_{ext}) at the top of the pile; ρ_{s} is the solid density.

The 2D axisymmetric model has a symmetry axis at $r = 0$, i.e. boundary Γ_0. Boundaries $\Gamma_{\mathrm{f}\infty}$ and $\Gamma_{\mathrm{s}\infty}$ are prescribed by Sommerfeld's radiation condition and modelled in COMSOL Multiphysics® as Cylindrical Wave Radiation and Low-reflecting boundaries, respectively. The sea surface, $\Gamma_{\mathrm{f}0}$, is modelled as a pressure release boundary, i.e. $p_{\mathrm{f}} = 0$. The interfaces

between pile and fluid, and soil and fluid, Γ_{fs} and Γ_f are modelled with Acoustic-Structure Boundary conditions, prescribing continuity of normal displacements and pressure and allowing no shear stresses. The pile-soil interface needs no specific description since both are modelled with the same type of elements with different material properties. Pile and soil are connected monolithically, i.e. no pile slip or separation is allowed relative to the soil. The model is truncated five m below the bottom of the pile and at $r = 75$ and $r = 150$ m for the small and large piles, respectively. A frequency-dependent adaptive mesh size is used that guarantees five elements per wavelength.

The 3D model is similar to the 2D axisymmetric model, but the entire 3D domain is modelled, and the axis of symmetry is removed. The pile is rotated around the y-axis halfway through its length. A symmetry plane boundary is introduced at $y = 0$. The domain is truncated at $r = 50$ m to reduce computation costs as computational costs grow exponentially with an extended domain in r. The domain truncations are considered sufficient (compared to 6.5 m in Wilkes and Gavrilov, 2017) to describe the noise generation mechanism, whereas propagation can be obtained by other than FEM methods.

This chapter considers two types of non-symmetric forces: An inclined force and an eccentric force. The relation between the vertical and horizontal comments of the force, $F_z(t)$ and $F_x(t)$, are found via:

$$F_x(t) = \tan(\alpha) F_z(t), \qquad \rightarrow \qquad F_{\text{ext}} = \sqrt{F_x^2 + F_z^2} \tag{3.3}$$

with α being the time-independent angle of inclination. During installation, the maximally allowable tilt at the seabed level is 0.25 degree (Veritas, 2004), and due to modern motion-compensated pile grippers, the monopile installation happens almost vertically. This chapter assumes an angle of 3 degrees, which is assumed to be a practical upper limit. Therefore, the $F_x(t)$ is approximately 5% of $F_z(t)$.

The eccentric force induces a moment around the y-axis next to the vertical force. The moment $M_y(t)$ is found via:

$$M_y(t) = \beta r_p F_z(t) \tag{3.4}$$

with a relative eccentricity $\beta = \epsilon / r_p$ and ϵ being the absolute eccentricity. This chapter assumes that the eccentricity is proportional to 5% of the pile's radius, again assuming to be an extreme case. These forces translate to distributed loads on top of the pile per azimuthal mode number via:

$$q_{z0}(t) = \frac{1}{2\pi r_p} F_z(t) \tag{3.5}$$

$$q_{r1}(t) = \frac{1}{2\pi r_p} F_x(t) \cos(\theta) \tag{3.6}$$

$$q_{\theta 1}(t) = -\frac{1}{2\pi r_p} F_x(t) \sin(\theta) \tag{3.7}$$

$$q_{z1}(t) = \frac{1}{\pi r_{\mathrm{p}}^2} M_y(t) \cos(\theta) \tag{3.8}$$

The effect of each force component is examined in the case studies hereafter.

The case with the tilted pile assumes a tilt of 3 degrees; this limit case is reviewed to find pressure level differences and seabed vibrations on both sides of the pile. The force is assumed to be parallel to the pile.

3.3. The non-symmetric noise field

The non-symmetric noise field is examined for the case of a small- and large-diameter monopile taken from Deng et al. (2016) and Peng et al. (2021b), respectively. In both cases, the effect of non-symmetry of noise is examined; the conclusions are compared for the small monopile with those of Deng et al. (2016). The physical explanation of the noise generation is accomplished based on the large monopile case. A frequency domain analysis is performed, and the time domain response is retrieved using an inverse Fast Fourier Transform (FFT). To quantify the noise emission, the sound exposure levels, L_{E}, sound pressure levels, L_{p} and the peak sound pressure level, L_{peak} are calculated by the definition of ISO (2017a):

$$L_{\mathrm{E}} = 10 \log_{10} \left(2 \int_0^{\infty} \frac{|p_{\mathrm{f}}(f)|^2}{p_0^2} \mathrm{d}f \right) \tag{3.9}$$

$$L_{\mathrm{P}} = 20 \log_{10} \left(\frac{p_{\mathrm{rms}}(f)}{p_0} \right) \tag{3.10}$$

$$L_{\mathrm{peak}} = 20 \log_{10} \left(\frac{p_{\mathrm{peak}}}{p_0} \right) \tag{3.11}$$

in which real mean square pressure $p_{\mathrm{rms}}(f) = \frac{1}{\sqrt{2}} |p_{\mathrm{f}}(f)|$ and peak pressure $p_{\mathrm{peak}} = \max(|p_{\mathrm{f}}(t)|)$. The reference pressure $p_0 = 1\mu\mathrm{Pa}$ for underwater acoustic calculations. The force transfer functions are defined by:

$$T_{p_{\mathrm{f}}, F_\alpha} = \frac{p_{\mathrm{f}}}{F_\alpha} \tag{3.12}$$

with F_α being F_z, F_x or M_y.

3.3.1. Small-diameter pile

Deng et al. (2016) show the case of a 2 m diameter monopile of 28 m length partially driven in the soil. Piles of these dimensions are relatively small in the current offshore wind industry but are used for jacket foundations. The corresponding ring frequency is $f_{\mathrm{ring}} \approx 857$ Hz. The water is shallow, resulting in a cut-off frequency of the first propagating mode of about 47 Hz. Further material and geometry properties are summarized in Table 3.1.

Table 3.1: Small diameter pile geometry and material properties (Deng et al., 2016)

Parameter		unit
Pile Youngs modulus [E_p]	210	GPa
Pile Poison's ratio [ν_p]	0.28	-
Pile Density [ρ_p]	7800	kgm^{-3}
Structural damping [ν_p]	0.002	-
Pile length [L_p]	28	m
Pile radius [r_p]	1	m
Pile thickness [h_p]	0.02	m
Pile soil penetration	10	m
Fluid wave speed [c_f]	1500	ms^{-1}
Fluid density [ρ_f]	1000	kgm^{-3}
Water depth	8	m
Soil Youngs modulus [E_s]	50	MPa
Soil Poison's ratio [ν_s]	0.40	-
Soil Density [ρ_p]	1600	kgm^{-3}

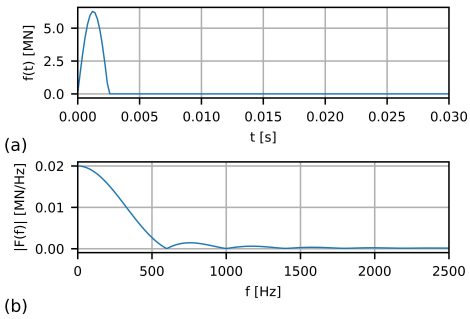


Figure 3.2: (a) Time and (b) frequency domain representation of the force on the small-diameter pile (Deng et al., 2016).

The external load on top of the pile is described by:

$$F_{ext}(t) = F_0 \sin\left(\frac{\pi t}{\tau}\right) \qquad 0 < t < \tau \tag{3.13}$$

with $F_0 = 1\ MNm^{-1}$ and $\tau = 2.5$ ms. Figure 3.2a shows the time signature of the applied force while Fig. 3.2b shows the amplitude spectrum of the force. Frequencies up to 2500 Hz with a stepsize of 1 Hz are included in the frequency response analysis.

The absolute value of the frequency response transfer functions in Fig. 3.3 shows the pressure levels at $z = 4$ m and $r = 25$. The transfer functions are plotted on a decibel scale after substitution in Eq. (3.10). The transfer function shows almost no sound propagation

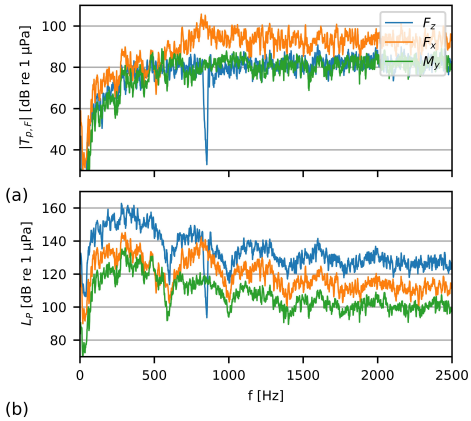


Figure 3.3: (a) Absolute value of the transfer functions and (b) sound pressure levels for a vertical load, horizontal load and moment on top of the pile at $z = 4$ m and $r = 25$ m.

below ≈ 37.5 Hz, the cut-off frequency of the fluid and around ≈ 857 Hz, the ring frequency of the pile.

The ring frequency of the pile indicates the frequency at which the wavelength is equal to the circumference of the pile. The modal density around this frequency is high (Leissa, 1973). The vertical group velocity of waves close to the ring frequency is almost zero. Thus, almost no energy propagates downwards the pile from the hammer impact location. This is further discussed in Section 3.3.2.

The sound waves generated by a horizontal force or a moment do not propagate below the fluid's cut-off frequency but propagate at the pile's ring frequency, while the ring frequency corresponds solely to the axisymmetric shell. The absolute value of the transfer functions of a horizontal load is significantly higher than those of a vertical load. Nonetheless, the sound pressure levels, shown in Fig. 3.3b, are significantly lower compared to the vertical load since the amplitude of the non-symmetric force components is significantly lower than the vertical component of the force, with the ring-frequency as the only exception.

Deng et al. (2016) concludes that the non-uniformity of the load is strongest around the ring frequency for an inclined load. The results presented here agree with that, and the same conclusion holds for a force moment on top of the pile.

Figure 3.4 compares the peak pressure and sound exposure levels of the inclined and eccentric loads with the vertical load. Despite different approaches, the sound exposure levels and peak pressure levels compare well to Deng et al. (2016) for the symmetric force, i.e. $L_{\text{Peak}} = 198$dB and $L_{\text{E}} = 177$dB at $r = 20$m. The levels are taken at the worst azimuth; thus, either $\theta = 0$ or $\theta = \pi$, dependent on the phase of the forces. As expected from the sound pressure levels, the sound exposure and peak pressure levels are all very close. Especially, the sound exposure levels seem uninfluenced, while the peak pressure levels are all within 1 dB.

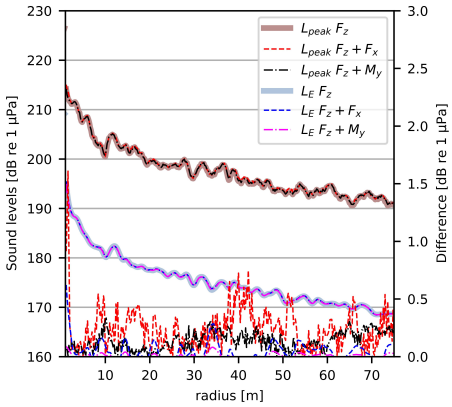


Figure 3.4: Peak pressure and sound exposure levels at 4 meters depth to radius caused by the vertical, inclined, and eccentric load on the left axis and the dB difference compared to only the vertical load on the right axis.

Deng et al. (2016) state that underwater noise measurements at one location around the circumference are insufficient when the impact force has a significant non-symmetric component. This work supports this statement if one is interested in detailed frequency content around the ring frequency. The differences around the circumference are insignificant if one is interested in more general sound levels, such as the peak pressure and sound exposure levels. Other uncertainties, such as bathymetry variation or seabed composition with strong azimuthal dependence, likely influence sound variations around the azimuthal direction more.

3.3.2. Large diameter pile

The effects of non-symmetric forces for a large-diameter monopile are studied based on the case of a windmill installed in the German North Sea presented by Peng et al. (2021b). First, the case of the pile driven as described is examined; after that, the pile penetration depth and the impact duration are changed. The pile is eight m in diameter and 76.9 m in length. The soil consists of a thin upper layer founded on the bottom sediment. The material and geometry parameters are given in Table 3.2. The ring frequency of the pile is 216 Hz, and the fluid cut-off frequency is approximately 9 Hz.

The force on top of the pile corresponds to a hammer blow of approximately 1750 kJ and is described by:

$$F_{\text{ext}}(t) = F_A \sin\left(F_B(t - t_0)\right) \exp^{-F_c(t-t_0)} \qquad t_0 < t < t_1 \tag{3.14}$$

The force parameters are: $F_A = 503$, $F_B = 149$, $F_c = 150$, $t_0 = 0.001$ s and $t_1 = 0.05$ s, i.e. the force plotted in Fig. 3.5 with the accompanying Fourier amplitude spectrum. For the analysis, frequencies up to 750 Hz are included with a step of 1 Hz. Figure 3.5 shows that the described

Table 3.2: Large diameter pile geometry and material properties (Peng et al., 2021b)

Parameter		unit
Pile Youngs modulus [E_p]	210	GPa
Pile Poison's ratio [ν_p]	0.30	-
Pile Density [ρ_p]	7850	$\mathrm{kg m^{-3}}$
Structural damping [ν_p]	0.001	-
Pile length [L_p]	76.9	m
Pile radius [r_p]	4	m
Pile thickness [h_p]	0.09	m
Pile soil penetration	40.1	m
Fluid wave speed [c_f]	1500	$\mathrm{m s^{-1}}$
Fluid density [ρ_f]	1000	$\mathrm{kg m^{-3}}$
Water depth	39.9	m
Soil layer compressional wave speed [$c_{\mathrm{s},p}$]	1560	$\mathrm{m s^{-1}}$
Soil layer shear wave speed [$c_{\mathrm{s},s}$]	94	$\mathrm{m s^{-1}}$
Soil layer Density [ρ_p]	1670	$\mathrm{kg m^{-3}}$
Soil layer thickness	1.5	m
Soil bottom compressional wave speed [$c_{\mathrm{s},p}$]	1979	$\mathrm{m s^{-1}}$
Soil bottom shear wave speed [$c_{\mathrm{s},s}$]	349	$\mathrm{m s^{-1}}$
Soil bottom Density [ρ_p]	1950	$\mathrm{kg m^{-3}}$

force contains less high-frequency content than the force applied on the small-diameter monopile, which justifies the upper limit frequency truncation.

Figure 3.6 shows the absolute value of the transfer functions and the sound pressure levels corresponding to the case. Similar to the small-diameter monopile, negligible sound is propagated around the ring frequency of the pile due to an axisymmetric vertical load. On the other hand, the absolute value of the transfer function of the horizontal load peaks around these frequencies. This is because the modal density at the first azimuthal mode is high and contains many modes governed by shear motion. Examining the sound pressure levels in Fig. 3.6b, the noise generated by the horizontal or moment component of the force is significantly smaller at all frequencies except around the ring frequency. This phenomenon is the same at both small- and large-diameter monopiles.

The ring frequency explains the drop in the noise levels at axisymmetric vertical excitation, while the waves excited around the ring frequency have a vertical group velocity approaching zero. Therefore, energy can not propagate through the pile and remains close to the hammer impact location. This can be observed by comparing the radial pile vibrations at multiple locations along the pile length around these frequencies.

Figure 3.7a shows that the radial displacements peak around the ring frequency at the top of the pile due to a high modal density and little energy propagating downwards. Therefore, this peak is not observed anymore halfway through the fluid column in Fig. 3.7b.

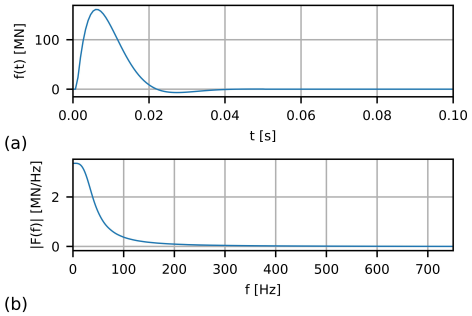


Figure 3.5: (a) Time and (b) frequency domain representation of the force on the large-diameter pile (Peng et al., 2021b).

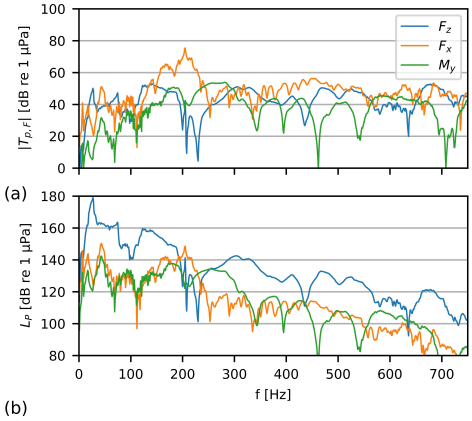


Figure 3.6: (a) Absolute value of the transfer functions and (b) sound pressure levels for a vertical load, horizontal load and moment on top of the pile at $z = 20$ m and $r = 100$ m.

The horizontal load and moment do not excite horizontal motion around the ring frequency since this mode does not exist in non-symmetric configurations. The largest radial vibrations are observed at low frequencies, where the first bending modes are located (the first between 1.4 and 8.3 Hz assuming fixed-free and free-free boundary conditions, respectively). However, the first bending modes do not cause significant sound levels, as seen in Fig. 3.6, while the fluid pressure is proportional to acceleration that scales quadratically with frequency.

Figure 3.8 shows the time response at $\theta = 0$ for each component of the force individually. It should be stressed that the scales of the horizontal and moment components are 20 times smaller than the colour scale of the vertical component. The vertical force induces a Mach-cone that reflects up and down, as indicated with the arrows at 0.02 s and 0.04 s. The noise generation mechanism and the angle of the Mach-cone, $\phi = \sin^{-1}\left(c_\mathrm{f}/c_\mathrm{p,p}\right) \approx 17°$, are in agreement with theory (Reinhall and Dahl, 2011), with $c_\mathrm{p,p}$ corresponding to the

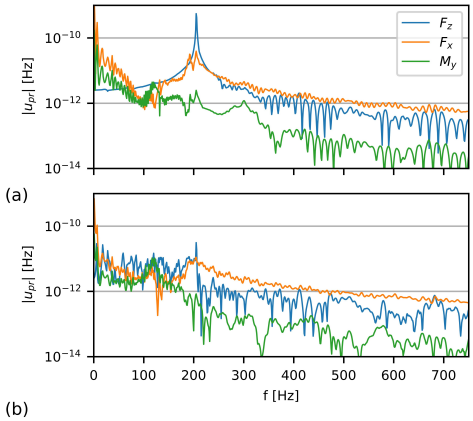


Figure 3.7: Absolute value of the transfer functions of the absolute value of the radial pile displacement (a) 0.5 m below the top of the pile and (b) in the centre of the fluid column ($z = 20$).

compressional wave speed of the pile. Furthermore, at $t = 0.08$ s, Scholte interface waves are visible in the wave field.

The noise generation mechanism due to a horizontal load or moment differs from the case of a vertical load. At $t = 0.02$ s, two Mach-cones are identifiable, as the arrows indicate.

The second Mach-cone is activated by the slower travelling shear wave with a shorter length. The shorter wavelength is clearly observable at 0.03 s, where the positive and negative pressure levels along the pile alter more quickly than the field generated by a vertical load. It also shows that sound is radiated along a longer timespan.

The Mach-cone generated by the shear wave has an angle of $\phi = \sin^{-1}\left(\frac{c_f}{c_{p,s}}\right) \approx 27°$, in which $c_{p,s}$ refers to the shear-wave velocity of the pile. The transmission loss model presented by Lippert et al. (2018) shows a relation between the propagation angle of the wave and transmission losses. The Mach waves with an angle of 27° are expected to propagate less efficiently due to a larger number of reflections with the seabed and a smaller reflection coefficient due to a greater angle between water and soil. Therefore, at more considerable distances, the contribution of the non-symmetrical components of the noise field will be less prominent than in the near field. Depending on the water depth and the reflection coefficient of the seabed, the added transmission loss is more or less significant.

Scholte interface waves at the seabed are less prominent because the horizontally dominated pile vibrations excite Love waves. The latter does not radiate noise into the fluid domain because they have no vertical component in the displacement field and contain only horizontally polarized shear waves (SH waves).

In practice, the peak pressure and sound exposure levels are usually reported and checked against noise thresholds imposed by regulators. Figure 3.9 shows that the non-symmetric components do not influence noise levels at the critical azimuth ($\theta = 0$ or $\theta = \pi$). This aligns with the observations of the sound pressure levels; the horizontal load and moment only

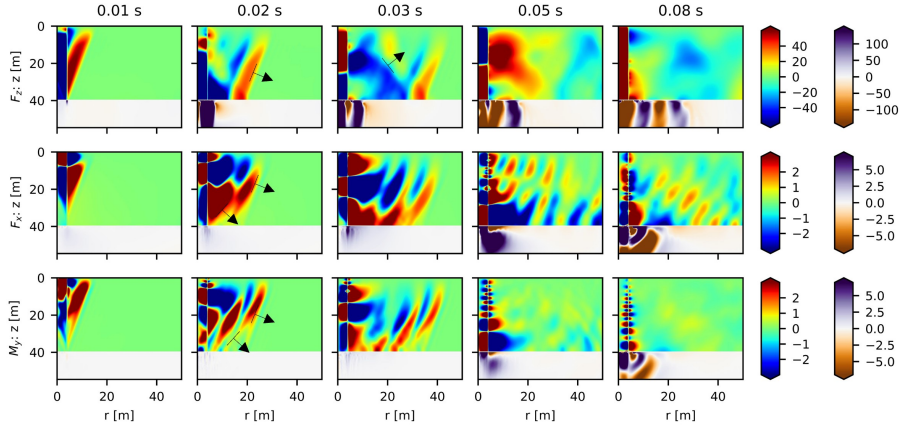


Figure 3.8: 2D-time response at $\theta = 0$ of fluid pressure [kPa] and vertical soil velocity [mm s^{-1}] due to a vertical, horizontal and moment load on top of the pile at five subsequent time moments.

contribute around the ring frequency, and there is little energy at these frequencies. Besides that, it should be remembered that waves at a particular frequency rarely fully sum up because of a phase difference. Furthermore, it can be concluded that an inclined load causes higher noise levels than an eccentric load, though both are insignificant in this case. These conclusions can alter if the force has more energy around the ring frequency or when the system properties change. Both cases are examined hereafter.

Variation of the pile penetration depth

In impact pile driving, the hammer energy to drive the pile usually increases with the pile penetration depth in cases with relatively homogeneous soil. Therefore, the deeper pile penetration depths are often critical in noise predictions. However, this statement might deviate for inclined and eccentric loads. Figure 3.10 shows the sound pressure levels around three pile penetration depths, assuming the same force. It is observed that the three lines in the same colour in all cases are comparable and mostly overlap. Therefore, the effect of inclination and eccentricity of the force is expected to be similarly small throughout the driving process.

Shorter impact duration

The hammer impact presented by Peng et al. (2021b) has relatively little energy at the ring frequency. A case with more energy around the ring frequency can alter previous observations. Therefore, the pulse duration is four times shortened. At the same time, the amplitude is proportionally enlarged to keep the same energy in the hammer blow but with higher frequency content in the amplitude spectrum.

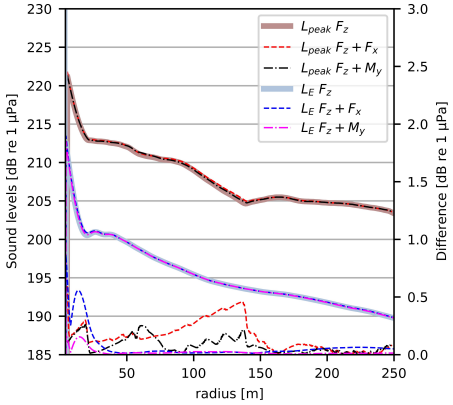


Figure 3.9: Peak pressure and sound exposure levels at $z = 35$ m to radius caused by the vertical, inclined, and eccentric load on the left axis and the difference to only the vertical load on the right axis.

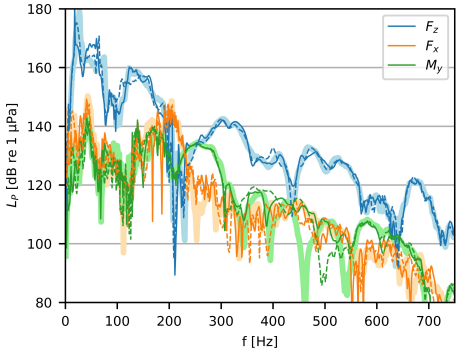


Figure 3.10: Sound pressure levels per force component at $z = 20$ m and $r = 100$ m around three pile penetration depths: 19.9 m - solid, 29.9 m - dashed, and 39.9 m - light and thick.

Figure 3.11 shows the resulting sound exposure and peak pressure levels. Both levels have increased due to the shorter duration of the pulse. The effect of inclination or eccentricity is slightly higher, but still in all cases below 1 dB within the first 250 m. Thus, due to an impact force with more energy around the ring frequency, the effect of inclination and eccentricity of the force is larger but still limited.

3.3.3. Inclined pile

This section describes the sound generation of a slightly inclined pile, with a hammer force in parallel with the pile. The case refers to unintended tilting of the pile during the installation of monopile foundations. This particular scenario may occur at the initial stages of a pile-driving process. The effect of pile inclination is examined by considering an extreme case

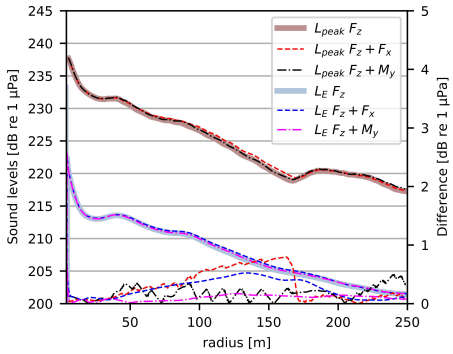


Figure 3.11: Peak pressure and sound exposure level at $z = 35$ m for a vertical, inclined, and eccentric load and on the left axis the differences compared to the vertical load on the right axis.

where a large-diameter monopile is inclined at an angle of three degrees at $z_2 = 50$ m. A 3D Comsol Multiphysics model is used for the study, where symmetry around $y = 0$ is applied to reduce the model size. However, the computational considerations lead to the truncation of the domain at $r = 50$ m and the frequencies at $f = 400$ Hz.

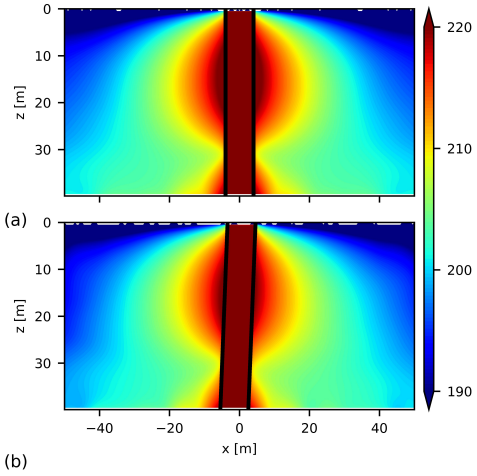


Figure 3.12: Sound exposure levels of the vertical pile (a) compared with the incline pile (b).

Figure 3.12 presents the comparison of SEL for a vertical pile (a) and an inclined pile (b). Upon initial observation, the inclination appears to have a negligible impact on SEL. Both cases exhibit similar spatial distributions and amplitudes. However, slight variations between positive and negative x-coordinates are observed in Fig. 3.12b, particularly above the seabed.

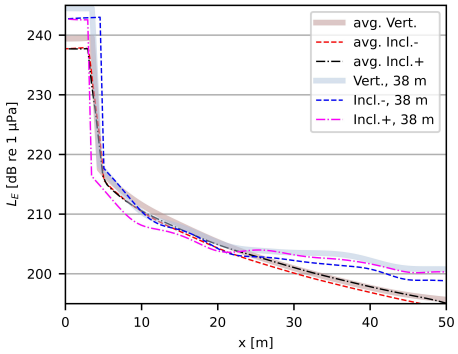


Figure 3.13: Sound exposure levels to the distance at $z = 38$ m and averaged over the fluid column for the vertical and inclined piles. The + and - refer to the positive and negative x-coordinate, respectively.

Examination of Fig. 3.13 confirms the slight variation in SEL between positive and negative x-coordinates. The variation is the largest close to the pile, just above the seabed, as visually observed in Fig. 3.12. The variation on both sides is in the first 10 m up to 5 dB. However, at a slightly larger distance (> 20 m), SELs converge with a maximum variation of 2 dB. The differences on both sides are largest due to the presence of the seabed. The average SEL over the water depth shows significantly less variation on both sides. SEL stay within 2 dB.

In both cases, the SEL values are higher at positive x-coordinates, i.e., the side where the top of the pile leans. This can be explained by additional reflections caused by the smaller angle between the pile and soil compared to the negative x-coordinate. Though a very conservative case is modelled, noise levels at the positive and negative sides deviate mainly in the vicinity of the pile but up to only two decibels.

In Fig. 3.14, the frequency distribution of the generated noise is analyzed through transfer functions and SPLs. The absolute value of the transfer functions, which describe the system behaviour, exhibit similar trends in inclined and vertical pile cases. The absolute value of the transfer functions for the inclined pile at positive and negative x-coordinates fluctuates around the function belonging to the vertical pile. When multiplied by the force function, the SPL presented in Fig. 3.14b peaks at 18 Hz, which dominates the SEL above. The substantial decrease in noise at the ring frequency indicates that the pile mainly vibrates at its cylindrically symmetric modes excited by the aligned hammer force despite the non-symmetric geometric coupling with fluid and soil.

Figure 3.15 shows a snapshot of the emitted noise field after 0.03 s. The primary noise generation mechanism in the inclined pile is similar to the vertical pile, the Mach wave radiation. Next, the surface wave is generated along the seabed. The vertical soil vibrations are excited along the inclined surface of the pile. Nonetheless, seabed vibrations do not deviate significantly on both sides of the pile.

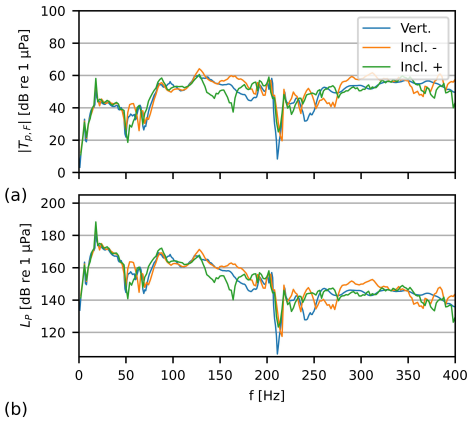


Figure 3.14: Absolute value of the transfer functions and sound pressure levels at $x = +/-40$ m and $z = 20$ m for the vertical and inclined pile.

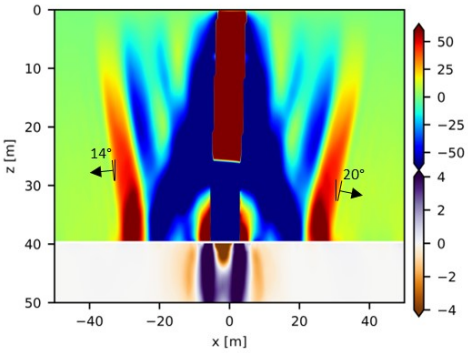


Figure 3.15: Snapshot of the fluid pressure [kPa] and vertical soil velocity [mm s^{-1}] at $y = 0$ m and $t = 0.03$ s.

The primary noise generation mechanism can explain the minor changes in observed frequency domain pressure fields since there is a significant difference on both sides of the pile, namely, the angle of the Mach cones with the seabed. Due to the inclination of the pile of three degrees, the Mach cones have a rotated angle of three degrees compared to the vertical pile. The Mach wave with an angle of 14 and 20 ° will have fewer and more reflections at some horizontal distance, respectively, with the seabed compared to the Mach wave from the vertical pile. This will affect the transmission losses over large distances. The significance of the effect on the transmission loss depends on the reflection coefficient of the sediment and the water depth (Lippert et al., 2018).

The presented results do not provide conclusive evidence that inclination plays an insignificant role in noise prediction, given that slight variations of one decibel can be significant in underwater noise predictions. Slightly higher noise levels are observed on the side where

the top of the pile leans; however, it remains inconclusive if these observations hold at more considerable distances. Regardless, it can be indicated that even with a more considerable inclination at the beginning of piling, the tip of the pile does not significantly alter the results obtained for a vertical pile, considering the allowable inclination at the end of the driving process is 0.25 degrees.

3.4. Conslusions

This study investigates the impact of non-symmetric impact forces and pile inclination on underwater noise for small- and large-diameter monopiles cases. Specifically, the study examines the case of an inclined and eccentric force and a tilted pile. First, the response to the non-symmetric forces is studied. The absolute value of the transfer functions of the horizontal force and moment are comparable to or larger than those of the vertical force. However, the vertical component generates most underwater noise due to a much higher force amplitude. The inclined force produces slightly higher noise levels than the eccentric force. Still, the increased sound levels seem insignificant, even at the least favourable azimuth, since more likely factors to occur are introducing small variations of the sound exposure levels, such as a strike-to-strike variation. Nevertheless, in some cases, half a decibel can be decisive in crossing allowable thresholds.

Non-symmetries strongly affect only the sound pressure levels around the ring frequency of the pile. The drop in sound pressure levels around the ring frequency for a purely vertical load disappears when a non-symmetric component is present. Furthermore, seabed vibrations are barely induced by inclined and excentric forces, while these forces excite Love waves instead of Rayleigh waves. Based on the presented cases, inclined or eccentric forces should be examined when:

- there is a strong interest in the frequency distribution of the noise levels; for example, to examine noise levels for species sensitive to the noise around the ring frequency of the pile,
- The excitation force contains significant energy around the ring frequency, for example, when a vibratory hammer is used with energy in the ring frequency through its driving frequency or superharmonic.

Nevertheless, the inclination or eccentricity of an impact hammer on top of the pile is unlikely to significantly affect noise levels in most cases since the conclusions could be generalized for all pile sizes, pile penetration depths, and impact duration studied in this work.

An inclined pile radiates a comparable noise field as the vertical pile, generated mainly by Mach wave radiation and Scholte interface waves. Due to the inclination of the pile in its surroundings, slightly higher noise levels are observed at the side of the pile with a smaller angle with the seabed. In the far field, the rotation of the Mach cone may affect the

measured noise levels. Nonetheless, sound level variations in the near field were relatively small, especially considering the large inclination assumed in the analysis.

4

The influence of contact relaxation on underwater noise emission and seabed vibrations due to offshore vibratory pile installation

State-of-the-art models cannot predict sound emissions and seabed vibrations from vibratory pile driving. This is because the interaction between the sediment and the driven pile is not adequately described in these models intended for impact piling. In principle, linear vibroacoustic models assume perfect contact between pile and soil, i.e., no pile slip. In this chapter, the pile-soil interface condition is relaxed, and a slip condition is implemented that allows vertical motion of the pile relative to the soil. First, the developed model is presented under the assumption of cylindrical symmetry, employing contact spring elements between the pile and the soil, allowing the former to move relative to the latter in the vertical direction. The developed model is then verified against finite element software computations. Second, a parametric study is conducted to investigate the effect of the interface conditions on the emitted wave field. The results show that the sound generation mechanism depends strongly on the interface conditions. Third, this chapter concludes that models developed to predict sound emission from impact pile driving are not suitable for vibratory pile driving since the pile-soil interaction becomes essential in the latter case due to the inherently different mechanism of generation of the vibroacoustic sources in the fluid and soil media.

This chapter has been published in Frontiers in Marine Sciences, Sec. Ocean Observation, Volume 10 - 2023, 27 March 2023, Molenkamp et al. (2023b).

4.1. Introduction

Few attempts have been made to model vibratory pile driving. Tsouvalas and Metrikine, 2016b compare the wave fields emitted by an impact-driven and a vibratory-driven pile. They observe that the highest noise levels are just above the seabed; this phenomenon is more substantial in vibratory pile driving due to the presence of the Scholte waves. The Scholte waves are even more dominant under low-frequency excitation, consistent with the primary driving frequency in vibratory pile driving (10~40 Hz). Furthermore, Tsouvalas and Metrikine note that the system almost reaches a steady state during vibratory pile driving. Consequently, pile-soil interaction is critical to accurately describe the dynamic behaviour in this steady state.

Dahl et al., 2015 discuss results from an experimental campaign on underwater noise from vibratory pile driving and propagate the measured field with an acoustic propagation model. Though the pile vibrations, as a noise source, are not directly measured, the acoustic measurements clearly show the presence of the primary driving frequency and several super-harmonics. In a review paper, Tsouvalas (2020) addresses the development of noise prediction models for vibratory pile driving as one of the five open challenges in state-of-the-art noise prediction. Other challenges include noise mitigation modelling, improvement of computational efficiency for uncertainty analysis, incorporation of the three-dimensional domain, and knowledge integration with marine biologists for a unified environmental impact assessment.

The concept of (non-linear) pile-soil interaction is not novel. Various related fields note the importance of pile-soil interaction during dynamic loading, for example, post-installation modelling of wind and wave loads (Markou and Kaynia, 2018), piles in earthquake analysis (Nogami and Konagai, 1987; Novak, 1991), pile bearing capacity under vertical vibration (Nogami and Konagai, 1987) and onshore vibratory pile driving (Holeyman, 2002). Cui et al. (2022) introduce a Winkler spring connection between the pile and surrounding soil to study the effect of incomplete pile-soil bonding on the vibrations of a floating pile. All cases justify further research in pile-soil interaction for vibratory pile driving. The above-mentioned cases mainly focus on pile vibrations, though the emitted wave field is of interest in noise predictions.

State-of-the-art models in impact pile driving are not directly suitable for vibratory installation because sufficiently accurate modelling of the pile-soil slip is essential for predicting underwater noise in the latter case. In vibratory pile driving, the system reaches a quasi-steady state where pile-soil interaction plays an essential role in describing the state. On the contrary, a wave travelling through the pile governs the motion in impact pile driving and the associated primary noise emission, while pile-soil interaction mainly affects the amplitude of the wave reflections and a short-lived transient slip. Thus, relative motion between pile and soil and the resulting soil dynamics should be modelled to improve the accuracy of noise predictions. In addition, improved accuracy should not cost significant

computational power since computational efficiency is a substantial challenge in noise prediction models (Tsouvalas, 2020).

This chapter introduces a model allowing relative motion between pile and soil in acoustic predictions of vibratory pile driving. It relaxes the perfect contact, i.e., monolithic, interface conditions between pile and soil, that is standard in acoustic pile driving models, by introducing a contact stiffness element comparable as done by Cui et al. (2022). Friction is essential in vibratory pile installation but is strongly non-linear by definition. Regardless, the contact stiffness element allows for relative motion between the pile and the soil, which is assumed to be sufficient for acoustic predictions. The model separates pile and fluid-soil substructures; a summation of the in-vacuo eigenmodes describes the pile vibration. The fluid-soil reaction to the pile is modelled via an indirect boundary element method. This model allows for relative motion between pile and soil, which is the first novel contribution of this chapter. The model is then validated based on the COMPILE benchmark case (Lippert et al., 2016) with the finite element software 'COMSOL Multiphysics®' (COMSOL Multiphysics®, 2022). A realistic case study is conducted to analyse the noise and seabed vibrations based on the variation in contact element stiffness. The stiffness varies between two extreme cases: the case of perfect contact and the case of no frictional force, i.e., perfect slip, between pile and soil. Last, the effect of the interface condition on the noise generation mechanism is highlighted. The analysis confirms that models that do not account for pile slip are not directly applicable to the vibratory installation. To the author's knowledge, this influence is discussed for the first time in scientific literature.

This chapter introduces a new model with the governing equations and mathematical considerations discussed in Section 2. The Green's functions of ring sources in the fluid and soil domain are vital for the developed model and are derived in Section 3. The model is verified for a limit case in Section 4. Section 5 investigates the effect of pile-soil slip on noise generation mechanisms, noise pollution, and seabed vibrations. Finally, conclusions are drawn in Section 6.

4.2. Noise and seabed vibrations

4.2.1. Model description

The problem at hand is a pile driven offshore. A thin shell theory describes the motion of the pile. The shell occupies the domain $0 < z < L_\mathrm{p}$, having constant thickness h_p and diameter $2r_\mathrm{p}$. The constants E_p, ν_p, and ρ_p correspond to the modulus of elasticity, Poisson's ratio, and pile density, respectively. The seawater is described as an acoustic fluid, and the soil is modelled as an elastic continuum. The fluid occupies the domain $z_1 < z < z_2$ and depends on constants c_f and ρ_f, the fluid wave speed and density, respectively. The soil half-space at $z_2 < z$ is defined by Lamé constants λ_s and μ_s and density ρ_s. The model geometry and sub-structuring approach are visualised in Fig. 4.1. The problem is modelled in a cylindrical coordinate system, assuming symmetry over the azimuth (r, z). The pile and fluid-soil

domains are first considered individually, i.e., a substructuring approach, and subsequently coupled via kinematic and dynamic interface conditions at the pile surface, i.e., $r = r_p$.

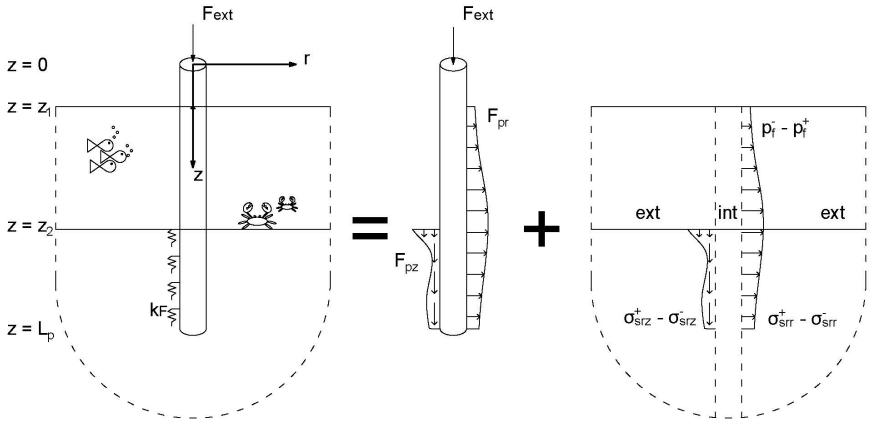


Figure 4.1: The sub-structuring approach of the model: **(A)** the model geometry, **(B)** the in-vacuo pile substructure with an external load on top and distributed loads representing the fluid and soil response, and **(C)** the internal and external fluid-soil substructures with the pile load acting on the boundaries at $r = r_p$.

The interface conditions between the pile and soil are crucial in the modelling approach. The present model allows for relative motion between pile and soil via a contact stiffness element that varies in stiffness between the ultimate cases of Perfect Contact (PC), and No Friction (NF), i.e. frictionless sliding. The author believes that introducing the contact stiffness element improves noise prediction without computationally expensive non-linear time-domain calculations because it allows for limited relative motion between pile and soil, which is considered necessary for noise emission modelling. This study considers a frequency- and depth-independent contact spring element, though the element can theoretically contain both spring and damper and can be depth- and frequency-dependent. The idea behind this approach is that the pile is considered around a particular equilibrium state, i.e., the penetration depth is fixed. The contact spring element can be calibrated further based on a driveability model, i.e., (Tsetas et al., 2023c) or experimental data.

4.2.2. Governing equations

The analysis in this study is performed in the frequency domain, making use of the following Fourier transform pair:

$$f(t) = \frac{1}{2\pi}\int_{-\infty}^{\infty} \tilde{f}(\omega) e^{\mathrm{i}\omega t}\,\mathrm{d}\omega, \qquad \tilde{f}(\omega) = \int_{-\infty}^{\infty} f(t) e^{-\mathrm{i}\omega t}\,\mathrm{d}t \tag{4.1}$$

The pile, fluid, and soil domains are referred to by subscript p, f, and s, respectively. Subscripts r and z refer to the radial and the vertical direction, respectively. The equations of

motion of the pile read:

$$\boldsymbol{L}_\mathrm{p}\tilde{\boldsymbol{u}}_\mathrm{p}(z) - \rho_\mathrm{p} h_\mathrm{p}\omega^2\tilde{\boldsymbol{u}}_\mathrm{p}(z) = \tilde{\boldsymbol{f}}_\mathrm{p}(z) + \tilde{f}_\mathrm{ext}\delta(z)\hat{\mathrm{e}}_\mathrm{z} \tag{4.2}$$

where $\boldsymbol{L}_\mathrm{p}$ represents the stiffness components of Flügge's thin shell theory (Leissa, 1973) and depends on the shell material and geometrical properties. $\tilde{\boldsymbol{u}}_\mathrm{p}(z) = [\tilde{u}_\mathrm{p,r}(z), \tilde{u}_\mathrm{p,z}(z)]^T$ contains the displacements of the pile. The excitation force is modelled as a load on top of the pile via $\tilde{f}_\mathrm{ext}\delta(z)\hat{\mathrm{e}}_\mathrm{z}$, while the fluid and soil reactions are lumped in $\tilde{\boldsymbol{f}}_\mathrm{p}(z) = [\tilde{f}_\mathrm{p,r}(z), \tilde{f}_\mathrm{p,z}(z)]^T$. The interaction with fluid and soil can be written as a convolution over the length of the pile of the effective dynamic stiffness of the fluid-soil domain and the pile displacements: $\tilde{\boldsymbol{f}}_\mathrm{p}(z) = -\left(\tilde{\boldsymbol{K}}^\mathrm{F}_\mathrm{fs} * \tilde{\boldsymbol{u}}_\mathrm{p}\right)(z)$. $\tilde{\boldsymbol{K}}^\mathrm{F}_\mathrm{fs}(z)$ is the analytical description of the effective dynamic stiffness, including the contact spring element, coupling the radial and the vertical direction. This convolution is later evaluated numerically and substituted by the boundary element matrix. The fluid and soil media are modelled as acoustic and linearly elastic continua. The equations of motion read:

$$\left(\nabla^2 + \frac{\omega^2}{c_\mathrm{f}^2}\right)\tilde{\phi}_\mathrm{f}(r,z) = -\tilde{s}_\mathrm{f}(z)\delta(r - r_\mathrm{p}) \tag{4.3}$$

$$(\lambda_\mathrm{s} + 2\mu_\mathrm{s})\nabla\nabla\cdot\tilde{\boldsymbol{u}}_\mathrm{s}(r,z) - \mu_\mathrm{s}\nabla\times\nabla\times\tilde{\boldsymbol{u}}_\mathrm{s}(r,z) + \rho_\mathrm{s}\omega^2\tilde{\boldsymbol{u}}_\mathrm{s}(r,z) = -\tilde{\boldsymbol{f}}_\mathrm{s}(z)\delta(r - r_\mathrm{p}) \tag{4.4}$$

The fluid equation of motion is written as a function of the displacement potential $\phi_\mathrm{f}(r,z)$, with $\tilde{\boldsymbol{u}}_\mathrm{f}(r,z) = \nabla\tilde{\phi}_\mathrm{f}(r,z)$ and fluid pressure $\tilde{p}_\mathrm{f}(r,z) = \rho_\mathrm{f}\omega^2\phi_\mathrm{f}(r,z)$, including $\tilde{s}_\mathrm{f}(z)$ as volume injection source at the location of the pile (Jensen et al., 2011). The soil equation of motion contains displacements vector $\tilde{\boldsymbol{u}}_\mathrm{s}(r,z) = [\tilde{u}_\mathrm{s,r}(r,z), \tilde{u}_\mathrm{s,z}(r,z)]^T$ and body forces vector $\tilde{\boldsymbol{f}}_\mathrm{s}(z) = [\tilde{f}_\mathrm{s,r}(z), \tilde{f}_\mathrm{s,z}(z)]^T$ at the radius of the pile. The boundary value problem for the fluid-soil substructure is composed of a single fluid layer overlaying a soil half-space. The accompanying interface conditions read:

$$\tilde{p}_\mathrm{f}(r,z_1) = 0 \tag{4.5}$$

$$\tilde{p}_\mathrm{f}(r,z_2) + \tilde{\sigma}_\mathrm{s,zz}(r,z_2) = 0 \tag{4.6}$$

$$\tilde{u}_\mathrm{f,z}(r,z_2) - \tilde{u}_\mathrm{s,z}(r,z_2) = 0 \tag{4.7}$$

$$\tilde{\sigma}_\mathrm{s,zr}(r,z_2) = 0 \tag{4.8}$$

Next to the interface conditions, the Sommerfeld radiation condition is applied at the infinite boundaries. Last, the two substructures are coupled via the interface conditions on the pile's interior and exterior surfaces. The interior surface is indicated with superscript '-' and the exterior with '+'. The interface conditions read:

$$\tilde{u}_\mathrm{p,r}(z) = \tilde{u}_\mathrm{f,r}(r_\mathrm{p},z) \qquad z_1 < z < z_2 \tag{4.9}$$

$$\tilde{F}_\mathrm{p,r}(z) = -\tilde{p}_\mathrm{f}(r_\mathrm{p}^+,z) + \tilde{p}_\mathrm{f}(r_\mathrm{p}^-,z) \qquad z_1 < z < z_2 \tag{4.10}$$

$$\tilde{u}_{\mathrm{p,r}}(z) = \tilde{u}_{\mathrm{s,r}}(r_{\mathrm{p}}, z) \qquad z_2 < z < L_{\mathrm{p}} \tag{4.11}$$

$$\tilde{F}_{\mathrm{p,r}}(z) = \tilde{\sigma}_{\mathrm{s,rr}}(r_{\mathrm{p}}^{+}, z) - \tilde{\sigma}_{\mathrm{s,rr}}(r_{\mathrm{p}}^{-}, z) \qquad z_2 < z < L_{\mathrm{p}} \tag{4.12}$$

$$\tilde{F}_{\mathrm{p,z}}(z) = \tilde{k}_{\mathrm{F}}\left(2\tilde{u}_{\mathrm{p,z}}(z) - \tilde{u}_{\mathrm{s,z}}(r_{\mathrm{p}}^{+}, z) - \tilde{u}_{\mathrm{s,z}}(r_{\mathrm{p}}^{-}, z)\right) \qquad z_2 < z < L_{\mathrm{p}} \tag{4.13}$$

$$\tilde{\sigma}_{\mathrm{s,rz}}(r_{\mathrm{p}}^{+}, z) - \tilde{\sigma}_{\mathrm{s,rz}}(r_{\mathrm{p}}^{-}, z) = \tilde{k}_{\mathrm{F}}\left(2\tilde{u}_{\mathrm{p,z}}(z) - \tilde{u}_{\mathrm{s,z}}(r_{\mathrm{p}}^{+}, z) - \tilde{u}_{\mathrm{s,z}}(r_{\mathrm{p}}^{-}, z)\right) \qquad z_2 < z < L_{\mathrm{p}} \tag{4.14}$$

in which $\tilde{k}_{\mathrm{F}}$ is the introduced contact stiffness element that allows for relative motion between pile and soil in the vertical direction. The limit cases of PC and NF are approached by the limits of $\tilde{k}_{\mathrm{F}} \to \infty$ and $\tilde{k}_{\mathrm{F}} \to 0$, respectively. In all cases, the continuity of displacements in the radial direction and equilibrium of stresses are satisfied.

4

4.2.3. Solution method

A solution for the pile and fluid-soil substructure is found independently and coupled via the interface conditions. A summation of in-vacuo modes describes the pile substructure, and an indirect boundary element approach defines the fluid-soil domain. Green's functions for a layered medium are obtained in the wavenumber domain (Section 4.3) and retrieved in space by the wavenumber integration technique (Jensen et al., 2011). A boundary element matrix for the interior and exterior fluid-soil domains is first obtained and subsequently substituted into the interface conditions: Eqs. (4.9) to (4.14). From the interface conditions, an effective boundary element matrix is derived based on the pile displacements, which is then substituted back into the equation of motion of the pile. Last, the orthogonality relation of the structural modes is applied to find the complex-valued modal coefficients.

First, the equation of motion of the pile is rewritten:

$$\boldsymbol{L}_{\mathrm{p}}\tilde{\boldsymbol{u}}_{\mathrm{p}}(z) - \rho_{\mathrm{p}} h_{\mathrm{p}} \omega^2 \tilde{\boldsymbol{u}}_{\mathrm{p}}(z) + \left(\tilde{\boldsymbol{K}}_{\mathrm{fs}}^{\mathrm{F}} * \tilde{\boldsymbol{u}}_{\mathrm{p}}\right)(z) = \tilde{f}_{\mathrm{ext}}\delta(z)\hat{\mathbf{e}}_{\mathrm{z}} \tag{4.15}$$

Then, the displacement field of the pile is decomposed into a summation of structural modes, i.e.:

$$\tilde{\boldsymbol{u}}_{\mathrm{p}}(z) = \sum_{k=1}^{\infty} \tilde{\eta}_k \boldsymbol{U}_{\mathrm{p},k}(z) \tag{4.16}$$

The mode shapes $\boldsymbol{U}_{\mathrm{p},k}(z)$ are found by solving the eigenvalue problem of the in-vacuo pile with free-end boundary conditions. The modal amplitudes $\tilde{\eta}_k$ are obtained after pre-multiplying Eq. (4.15) with another mode l once expressed in the modal domain, and subsequently, integrating over the length of the pile:

$$\tilde{\eta}_k = \sum_{l}\left[(\omega_k^2 - \omega^2)N_k\delta_{lk} + \int_{z_1}^{L_{\mathrm{p}}} \boldsymbol{U}_{\mathrm{p},l}^{T}(z)\left(\tilde{\boldsymbol{K}}_{\mathrm{fs}}^{\mathrm{F}} * \boldsymbol{U}_{\mathrm{p},k}\right)(z)\mathrm{d}z\right]^{-1} U_{pz,l}(0)\, f_{\mathrm{ext}} \tag{4.17}$$

in which δ_{lk} is the Kronecker delta function, and N_k is expressed as:

$$N_k = \rho_\mathrm{p} h_\mathrm{p} \int_0^{L_\mathrm{p}} \boldsymbol{U}_{\mathrm{p},k}^T(z) \boldsymbol{U}_{\mathrm{p},k}(z) \mathrm{d}z \tag{4.18}$$

The boundary element matrix of the fluid-soil substructure is derived based on the indirect boundary element method. The indirect boundary integral for a field ϕ at $\boldsymbol{p}$ and a source σ at $\boldsymbol{q}$ reads (Kirkup, 2019):

$$\phi(\boldsymbol{p}) = \int_\Gamma G(\boldsymbol{p}, \boldsymbol{q}) \sigma(\boldsymbol{q}) \mathrm{d}\Gamma_q \tag{4.19}$$

$$\frac{\partial}{\partial n_p} \phi(\boldsymbol{p}) = \int_\Gamma \frac{\partial}{\partial n_p} G(\boldsymbol{p}, \boldsymbol{q}) \sigma(\boldsymbol{q}) \mathrm{d}\Gamma_q + c_p \sigma(\boldsymbol{p}) \tag{4.20}$$

with n_p being the normal vector and the constant $c_p = \frac{1}{2}$ when $\boldsymbol{p}$ is on Γ_q and $c_p = 0$ otherwise. The boundary element matrix is found after substituting Eq. (4.20) in Eq. (4.19) and eliminating the sources $\sigma(\boldsymbol{q})$. The boundary element matrices for the interior and exterior domains are found based on the same Green's function, though the normal vector n_p changes direction. Since the problem is cylindrically symmetric with sources at the pile radius $r = r_\mathrm{p}$, Green's functions are derived for ring sources in both domains. The displacements and stress fields in fluid and soil are expressed in terms of Green's functions. The displacements, pressure, and stresses are expressed as integrals over all sources on the pile surface.

$$\tilde{u}_{\mathrm{f,f}}^{\pm}(z) = \int_{z_1}^{z_2} \tilde{T}_{\mathrm{f,f}}(z, z_s) \tilde{s}_\mathrm{f}(z_s) \mathrm{d}z_s \pm \frac{\tilde{s}_\mathrm{f}(z)}{2} + \int_{z_2}^{\infty} \tilde{T}_{\mathrm{f,sr}}(z, z_s) \tilde{f}_{\mathrm{s,r}}(z_s) + \tilde{T}_{\mathrm{f,sz}}(z, z_s) \tilde{f}_{\mathrm{s,z}}(z_s) \mathrm{d}z_s \tag{4.21}$$

$$p_{\mathrm{f,f}}(z) = \int_{z_1}^{z_2} \tilde{G}_{\mathrm{f,f}}(z, z_s) \tilde{s}_\mathrm{f}(z_s) \mathrm{d}z_s + \int_{z_2}^{\infty} \tilde{G}_{\mathrm{f,sr}}(z, z_s) \tilde{f}_{\mathrm{s,r}}(z_s) + \tilde{G}_{\mathrm{f,sz}}(z, z_s) \tilde{f}_{\mathrm{s,z}}(z_s) \mathrm{d}z_s \tag{4.22}$$

$$\tilde{u}_{\mathrm{s}\alpha,\mathrm{f}}(z) = \int_{z_1}^{z_2} \tilde{G}_{\mathrm{s}\alpha,\mathrm{f}}(z, z_s) \tilde{s}_\mathrm{f}(z_s) \mathrm{d}z_s + \int_{z_2}^{\infty} \tilde{G}_{\mathrm{s}\alpha,\mathrm{sr}}(z, z_s) \tilde{f}_{\mathrm{s,r}}(z_s) + \tilde{G}_{\mathrm{s}\alpha,\mathrm{sz}}(z, z_s) \tilde{f}_{\mathrm{s,z}}(z_s) \mathrm{d}z_s \tag{4.23}$$

$$\begin{aligned} \tilde{\sigma}_{\mathrm{sr}\alpha,\mathrm{f}}^{\pm}(z) = &\int_{z_1}^{z_2} \tilde{T}_{\mathrm{s}\alpha,\mathrm{f}}(z, z_s) \tilde{s}_\mathrm{f}(z_s) \mathrm{d}z_s \\ &+ \int_{z_2}^{\infty} \tilde{T}_{\mathrm{s}\alpha,\mathrm{sr}}(z, z_s) \tilde{f}_{\mathrm{s,r}}(z_s) + \tilde{T}_{\mathrm{s}\alpha,\mathrm{sz}}(z, z_s) \tilde{f}_{\mathrm{s,z}}(z_s) \mathrm{d}z_s \pm \frac{\tilde{f}_{\mathrm{s},\alpha}(z)}{2} \end{aligned} \tag{4.24}$$

in which $\alpha = \mathrm{r}, \mathrm{z}$, corresponds to the radial and vertical direction. The frequency domain Green's functions and Green's tensors are given by $\tilde{G}_{..,\mathrm{f}}(z, z_s)$ and $\tilde{T}_{..,\mathrm{f}}(z, z_s)$, respectively. The superscript and operator $\pm$ in Eqs. (4.21) and (4.24) corresponds to the exterior (+) and interior (−) domain and originates from the direction of the normal vector n_p in Eq. (4.20). Numerical integration of Eqs. (4.21) to (4.24) results in a discrete matrix relating displace-

ments, pressure, and stresses to the ring sources, both in the exterior and the interior domain, indicated with ± respectively. Because Green's functions are singular at the source, it is chosen to have a source of constant amplitude over the height of an element to circumvent the singularity; i.e., the integrals are evaluated by the midpoint rule. Additionally, the integration scheme positively affects the convergence rate of the inverse Hankel transforms addressed later. The Green's functions and Green's tensor functions are derived in Section 4.3.

$$\begin{bmatrix} \bar{\boldsymbol{u}}^{\pm}_{\mathrm{fr}} \\ \bar{\boldsymbol{u}}_{\mathrm{sr}} \\ \bar{\boldsymbol{u}}_{\mathrm{sz}} \\ \bar{\boldsymbol{p}}_{\mathrm{f}} \\ \bar{\boldsymbol{\sigma}}^{\pm}_{\mathrm{srr}} \\ \bar{\boldsymbol{\sigma}}^{\pm}_{\mathrm{srz}} \end{bmatrix} = \begin{bmatrix} \bar{\boldsymbol{T}}_{\mathrm{f,f}} \pm \frac{1}{2}\boldsymbol{I} & \bar{\boldsymbol{T}}_{\mathrm{f,sr}} & \bar{\boldsymbol{T}}_{\mathrm{f,sz}} \\ \bar{\boldsymbol{G}}_{\mathrm{sr,f}} & \bar{\boldsymbol{G}}_{\mathrm{sr,sr}} & \bar{\boldsymbol{G}}_{\mathrm{sr,sz}} \\ \bar{\boldsymbol{G}}_{\mathrm{sz,f}} & \bar{\boldsymbol{G}}_{\mathrm{sz,sr}} & \bar{\boldsymbol{G}}_{\mathrm{sz,sz}} \\ \bar{\boldsymbol{G}}_{\mathrm{f,f}} & \bar{\boldsymbol{G}}_{\mathrm{f,sr}} & \bar{\boldsymbol{G}}_{\mathrm{f,sz}} \\ \bar{\boldsymbol{T}}_{\mathrm{sr,f}} & \bar{\boldsymbol{T}}_{\mathrm{sr,sr}} \pm \frac{1}{2}\boldsymbol{I} & \bar{\boldsymbol{T}}_{\mathrm{sr,sz}} \\ \bar{\boldsymbol{T}}_{\mathrm{sz,f}} & \bar{\boldsymbol{T}}_{\mathrm{sz,sr}} & \bar{\boldsymbol{T}}_{\mathrm{sz,sz}} \pm \frac{1}{2}\boldsymbol{I} \end{bmatrix} \begin{bmatrix} \bar{\boldsymbol{s}}_{\mathrm{f}} \\ \bar{\boldsymbol{f}}_{\mathrm{sr}} \\ \bar{\boldsymbol{f}}_{\mathrm{sz}} \end{bmatrix} \tag{4.25}$$

with $\boldsymbol{I}$ being the identity matrix, the overhead bar indicating that the variables are discretised. After some standard linear algebra, stresses and displacements are related via the dynamic stiffness matrix of the fluid-soil domain:

$$\begin{bmatrix} -\bar{\boldsymbol{p}}_{\mathrm{f}} \\ \bar{\boldsymbol{\sigma}}_{\mathrm{srr}} \\ \bar{\boldsymbol{\sigma}}_{\mathrm{srz}} \end{bmatrix} = \bar{\boldsymbol{K}}_{\mathrm{fs}} \begin{bmatrix} \bar{\boldsymbol{u}}_{\mathrm{fr}} \\ \bar{\boldsymbol{u}}_{\mathrm{sr}} \\ \bar{\boldsymbol{u}}_{\mathrm{sz}} \end{bmatrix} \tag{4.26}$$

The effective fluid-soil stiffness matrix in Eq. (4.17) is a function of the pile displacements and, therefore, includes the description of the pile-soil interface condition. Thus, the convolution integral $\left(\tilde{\boldsymbol{K}}^{\mathrm{F}}_{\mathrm{fs}} * \tilde{\boldsymbol{u}}_{\mathrm{p}}\right)(z)$ is numerically evaluated by substituting Eq. (4.26) into Eqs. (4.9) to (4.14). In the PC case, the effective stiffness fluid-soil matrix is equal to the matrix found in Eq. (4.26), i.e., $\left(\tilde{\boldsymbol{K}}^{\mathrm{F}}_{\mathrm{fs}} * \tilde{\boldsymbol{u}}_{\mathrm{p}}\right)(z) \rightarrow \bar{\boldsymbol{K}}_{\mathrm{fs}}\bar{\boldsymbol{u}}_{\mathrm{p}}$

4.3. Fluid-soil Green's functions

The Green's functions for a layered medium are derived in two steps. First, Green's functions for the infinite space are derived from a ring source in both fluid and soil media. Second, the infinite space Green's functions are substituted in the boundary value problem. Since the problem is cylindrically symmetric with sources at $r = r_{\mathrm{p}}$, Green's functions are derived for ring sources in both domains. First, the soil displacements are decomposed into potentials: $\tilde{\boldsymbol{u}}_{\mathrm{s}}(r,z) = \nabla\tilde{\phi}_{\mathrm{s}}(r,z) + \nabla\times\nabla\times\tilde{\psi}_{\mathrm{s}}(r,z)\hat{\mathrm{e}}_{\mathrm{z}}$. Hereafter, the problem is transformed to the frequency-wavenumber domain by making use of the following Hankel transform pair:

$$\tilde{\phi}(r,z) = \int_0^\infty \hat{\Phi}(k,z)\mathrm{J}_0(kr)\,k\,\mathrm{d}k \quad \longleftrightarrow \quad \hat{\Phi}(k,z) = \int_0^\infty \tilde{\phi}(r,z)\mathrm{J}_0(kr)\,r\,\mathrm{d}r \tag{4.27}$$

The fluid-soil domain is split into an interior and an exterior domain at the position of the pile, $r = r_\mathrm{p}$. The applied indirect boundary method includes Green's functions of ring sources at the pile's location and derives the displacement and stress field at the boundary as a function of the sources. The potential solution is sought in the form of a homogeneous solution and a particular solution:

$$\hat{\Phi}_\mathrm{f}(k,z) = A_1 e^{-\alpha_\mathrm{f} z} + B_1 e^{\alpha_\mathrm{f} z} + \hat{\Phi}_\mathrm{f}^\mathrm{P}(k,z) \tag{4.28}$$

$$\hat{\Phi}_\mathrm{s}(k,z) = A_2 e^{-\alpha_\mathrm{s} z} + \hat{\Phi}_\mathrm{s}^\mathrm{P}(k,z) \tag{4.29}$$

$$\hat{\Psi}_\mathrm{s}(k,z) = A_3 e^{-\beta_\mathrm{s} z} + \hat{\Psi}_\mathrm{s}^\mathrm{P}(k,z) \tag{4.30}$$

The particular solutions in Eqs. (4.28) to (4.30) are derived from the infinite space Green's functions introduced in Sections 4.3.1 and 4.3.2. The homogeneous part is based on the boundary value problem, given by Eqs. (4.5) to (4.8). The problem is transformed to the wavenumber domain by applying Eq. (4.27):

$$\rho_\mathrm{f}\omega^2 \hat{\Phi}_\mathrm{f}(k,z_1) = 0 \tag{4.31}$$

$$\rho_\mathrm{f}\omega^2 \hat{\Phi}_\mathrm{f}(k,z_2) + \hat{S}_{\mathrm{s},3}(k,z_2) = 0 \tag{4.32}$$

$$\frac{\mathrm{d}}{\mathrm{d}z}\hat{\Phi}_\mathrm{f}(k,z_2) - \hat{U}_{\mathrm{s},3}(k,z_2) = 0 \tag{4.33}$$

$$\hat{S}_{\mathrm{s},1}(k,z_2) = 0 \tag{4.34}$$

which can be expressed in potentials via:

$$\hat{U}_{\mathrm{s},1}(k,z) = \left(\hat{\Phi}_\mathrm{s}(k,z) + \frac{\mathrm{d}}{\mathrm{d}z}\hat{\Psi}_\mathrm{s}(k,z)\right) k \tag{4.35}$$

$$\hat{U}_{\mathrm{s},3}(k,z) = \frac{\mathrm{d}}{\mathrm{d}z}\hat{\Phi}_\mathrm{s}(k,z) + \hat{\Psi}_\mathrm{s}(k,z) k^2 \tag{4.36}$$

$$\hat{S}_{\mathrm{s},1}(k,z) = \mu_\mathrm{s}\left(\frac{\mathrm{d}}{\mathrm{d}z}\hat{U}_{\mathrm{s},1}(k,z) + k\hat{U}_{\mathrm{s},3}(k,z)\right) \tag{4.37}$$

$$\hat{S}_{\mathrm{s},3}(k,z) = -k\lambda_\mathrm{s}\hat{U}_{\mathrm{s},1}(k,z) + \left(\lambda_\mathrm{s} + 2\mu_\mathrm{s}\right)\frac{\mathrm{d}}{\mathrm{d}z}\hat{U}_{\mathrm{s},3}(k,z) \tag{4.38}$$

The Green's functions and Green's tensors in Eqs. (4.21) to (4.24) are found by substituting the potential in the displacements and stresses and by applying the inverse Hankel transform.

4.3.1. Fluid source

The ring source in the fluid is introduced in the form of a ring volume injection $\tilde{s}_\mathrm{f}(z_s)$, of which the wavenumber counterpart is designated as $\hat{S}_\mathrm{f}(z_s)$. Equation (4.3) is transformed

to the wavenumber domain by applying Eq. (4.27) to give:

$$\left(\frac{\mathrm{d}^2}{\mathrm{d}z^2} - \alpha_\mathrm{f}^2\right)\hat{\Phi}_\mathrm{f}(k,z) = \hat{S}_\mathrm{f}(z_s)\mathrm{J}_0(kr_\mathrm{p})r_\mathrm{p}\delta(z-z_s) \tag{4.39}$$

with $\alpha_\mathrm{f} = \sqrt{k^2 - \frac{\omega^2}{c_\mathrm{f}^2}}$ and z_s the source position. The infinite space Greens function for a ring load in the wavenumber domain is given by Peng et al., 2021b:

$$\hat{\Phi}_\mathrm{f}^\mathrm{P}(k,z) = -\frac{\hat{S}_\mathrm{f}(z_s)}{2\alpha_\mathrm{f}}\mathrm{J}_0(kr_\mathrm{p})r_\mathrm{p}\begin{cases} e^{\alpha_\mathrm{f}(z-z_s)} & z < z_s \\ e^{-\alpha_\mathrm{f}(z-z_s)} & z > z_s \end{cases} \tag{4.40}$$

The Green's functions for a layered medium are obtained after substituting the free field particular solution given by Eq. (4.40) into Eq. (4.28) and the boundary value problem: Eqs. (4.31) to (4.34), and applying the inverse Hankel transform.

4.3.2. Soil source

Similarly to the fluid source, a distributed ring load at $r = r_\mathrm{p}$ excites the infinite space. The force is directed either in the radial or the vertical direction. Equation (4.4) is first transformed to the wavenumber domain, resulting in the following coupled equations:

$$\left(\mu_\mathrm{s}\frac{\mathrm{d}^2}{\mathrm{d}z^2} - \left(\lambda_\mathrm{s}+2\mu_\mathrm{s}\right)\alpha_\mathrm{s}^2\right)\hat{U}_{\mathrm{s},1}(k,z) + k(\lambda_\mathrm{s}+\mu_\mathrm{s})\frac{\mathrm{d}}{\mathrm{d}z}\hat{U}_{\mathrm{s},3}(k,z) = \hat{F}_{\mathrm{s,r}}(z_s)\mathrm{J}_1(kr_\mathrm{p})r_\mathrm{p}\delta(z-z_s) \tag{4.41}$$

$$\left(\left(\lambda_\mathrm{s}+2\mu_\mathrm{s}\right)\frac{\mathrm{d}^2}{\mathrm{d}z^2} - \mu_\mathrm{s}\beta_\mathrm{s}^2\right)\hat{U}_{\mathrm{s},3}(k,z) - k(\lambda_\mathrm{s}+\mu_\mathrm{s})\frac{\mathrm{d}}{\mathrm{d}z}\hat{U}_{\mathrm{s},1}(k,z) = -\hat{F}_{\mathrm{s,z}}(z_s)\mathrm{J}_0(kr_\mathrm{p})r_\mathrm{p}\delta(z-z_s) \tag{4.42}$$

with $\alpha_\mathrm{s} = \sqrt{k^2 - \frac{\omega^2}{c_\mathrm{L}^2}}$, $\beta_\mathrm{s} = \sqrt{k^2 - \frac{\omega^2}{c_\mathrm{L}^2}}$, $c_\mathrm{L} = \sqrt{\frac{\lambda_\mathrm{s}+2\mu_\mathrm{s}}{\rho_\mathrm{s}}}$, and $c_\mathrm{T} = \sqrt{\frac{\mu_\mathrm{s}}{\rho_\mathrm{s}}}$. The potentials for a ring load in the radial direction in an infinite elastic space read:

$$\hat{\Phi}_{\mathrm{s}\hat{F}_\mathrm{sr}}^\mathrm{P}(k,z) = \frac{\hat{F}_{\mathrm{s,r}}(z_s)k}{2\mu_\mathrm{s}\alpha_\mathrm{s}k_\mathrm{s}^2}\mathrm{J}_1(kr_\mathrm{p})r_\mathrm{p}\begin{cases} e^{\alpha_\mathrm{s}(z-z_s)} & z < z_s \\ e^{-\alpha_\mathrm{s}(z-z_s)} & z > z_s \end{cases} \tag{4.43}$$

$$\hat{\Psi}_{\mathrm{s}\hat{F}_\mathrm{sr}}^\mathrm{P}(k,z) = \frac{\hat{F}_{\mathrm{s,r}}(z_s)}{2\mu_\mathrm{s}kk_\mathrm{s}^2}\mathrm{J}_1(kr_\mathrm{p})r_\mathrm{p}\begin{cases} -e^{\beta_\mathrm{s}(z-z_s)} & z < z_s \\ e^{-\beta_\mathrm{s}(z-z_s)} & z > z_s \end{cases} \tag{4.44}$$

Similarly, the potentials for a vertical load read:

$$\hat{\Phi}_{\mathrm{s}\hat{F}_\mathrm{sz}}^\mathrm{P}(k,z) = \frac{\hat{F}_{\mathrm{s,z}}(z_s)}{2\mu_\mathrm{s}k_\mathrm{s}^2}\mathrm{J}_0(kr_\mathrm{p})r_\mathrm{p}\begin{cases} e^{\alpha_\mathrm{s}(z-z_s)} & z < z_s \\ -e^{-\alpha_\mathrm{s}(z-z_s)} & z > z_s \end{cases} \tag{4.45}$$

$$\hat{\Psi}_{\mathrm{s}\hat{F}_\mathrm{sz}}^\mathrm{P}(k,z) = -\frac{\hat{F}_{\mathrm{s,z}}(z_s)}{2\mu_\mathrm{s}\beta_\mathrm{s}k_\mathrm{s}^2}\mathrm{J}_0(kr_\mathrm{p})r_\mathrm{p}\begin{cases} e^{\beta_\mathrm{s}(z-z_s)} & z < z_s \\ e^{-\beta_\mathrm{s}(z-z_s)} & z > z_s \end{cases} \tag{4.46}$$

Again, the displacement and stress field at boundary $r = r_p$ are found in terms of Green's functions and Green's tensor functions by substitution of the particular solutions in the boundary value problem.

4.4. Model verification

The model developed in this chapter is verified against a finite element model in 'COMSOL Multiphysics®' (COMSOL Multiphysics®, 2022), with input data from the COMPILE benchmark case (Lippert et al., 2016), together with the near-field responses in the companion paper (Lippert et al., 2016). In the COMPILE case, the soil domain is represented by an acoustic fluid. Therefore, soil parameters are adapted from Peng et al., 2021b to validate the elastic soil case, and all properties are summarised in Table 4.1. The verification is performed under perfect contact conditions in which no sliding is allowed between the pile and the soil.

Table 4.1: Model properties for model verification Section 4.4. Parameters adapted from Lippert et al. (2016) and Peng et al. (2021b)

Parameter		unit	Parameter		unit
Sea surface depth [z_1]	0	m	Structural damping	0.001	-
Seabed depth [z_2]	10	m	Fluid wave speed [c_f]	1500	$\mathrm{m\,s^{-1}}$
Final penetration depth	25	m	Fluid density [ρ_f]	1025	$\mathrm{kg\,m^{-3}}$
Pile length [L_p]	25	m	Compression wave speed soil [c_L]	1800	$\mathrm{m\,s^{-1}}$
Pile thickness [t_p]	0.05	m	Shear wave speed soil [c_T]	170	$\mathrm{m\,s^{-1}}$
Pile radius [r_p]	1	m	Soil density [ρ_s]	2000	$\mathrm{kg\,m^{-3}}$
Pile Poisons ratio [ν_p]	0.30	-	Compressional wave attenuation [α_L]	0.469	dB/λ
Pile Young's modulus [E_p]	210	GPa	Shear wave attenuation [α_T]	1.69	dB/λ
Pile density [ρ_p]	7850	$\mathrm{kg\,m^{-3}}$			

For the validation of the near field model, a harmonic load on top of the pile is considered at frequencies up to 500 Hz. Boundary elements of 0.05 m are used; the mesh is sufficiently small compared to the shortest wavelength of 0.34 m. The upper limit in the inverse Hankel transform is fixed at $k = 500\ \mathrm{m^{-1}}$, which is sufficiently large because it guarantees that all integrands are smaller than 0.2% of the maximum amplitude. The truncation might seem unnecessarily high compared to the Scholte wavenumber at $f = 500$ Hz, i.e., $k_{\mathrm{Scholte}} \approx 20.5\ \mathrm{m^{-1}}$, however, it is deemed necessary when source and receiver are positioned at close distance. Pile, fluid, and soil transfer functions are validated for a load amplitude of 1 MN on top of the pile throughout the frequency range. Figure 4.2 shows the pile displacements at three frequencies distributed within the frequency domain of interest for vibratory pile driving ($\sim 15 \rightarrow 500$ Hz). The pile displacements predicted by COMSOL and the present model are in excellent agreement.

The sound pressure level (L_p) in the fluid is calculated by (ISO, 2017a):

$$L_p = 20 \log_{10} \left(\frac{p_{\mathrm{rms}}}{p_{\mathrm{ref}}} \right) \tag{4.47}$$

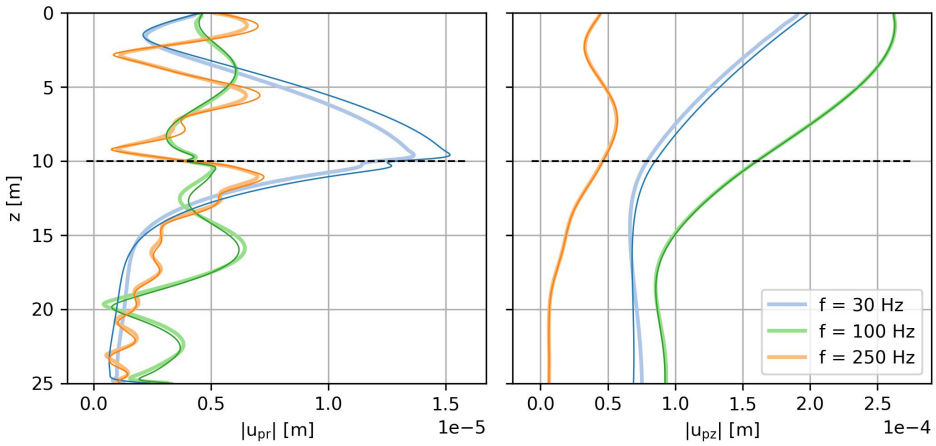


Figure 4.2: Comparison of the amplitudes of the pile vibrations between COMSOL (dark colours) and the present model (light colours) for a harmonic load of 1MN on top of the pile at 30, 100 and 250 Hz

in which the real mean square in the frequency domain is found by $p_{\mathrm{rms}}^2 = \frac{1}{2}|\tilde{p}^2|$ and the reference pressure in underwater acoustics is $p_{\mathrm{ref}} = 1$ µPa. The sound pressure levels in the

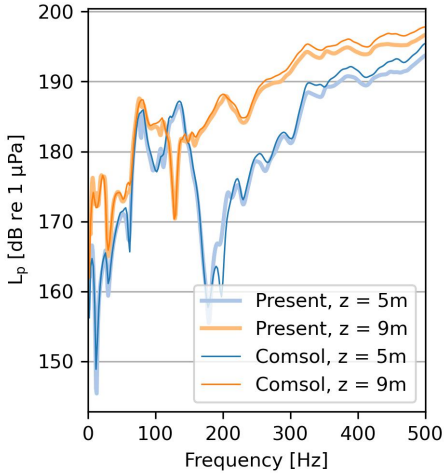


Figure 4.3: Comparison of the sound pressure levels in the water at a radius of 10 m between COMSOL (dark colours) and the present model (light colours) for a harmonic load of 1 MN

near field are in excellent agreement between COMSOL and the present model, both in the centre of the fluid layer ($z = 5$ m) and at one meter above the seabed surface ($z = 9$ m) as shown in Fig. 4.3.

4.5. Effect of pile-soil interface conditions

A realistic case study is considered hereafter to examine the effect of varying pile-soil interface conditions based on the geometry and material parameters described in Dahl et al., 2015 and measurements of a representative vibratory force by Tsetas et al., 2023a. The data can be used together since both campaigns used piles with an equal diameter of 0.762 m and comparable driving depths into the soil. Table 4.2 includes all parameters used in the case study.

Table 4.2: Model properties used to examine the effect of pile-soil interface conditions based on parameters in Section 4.5. Parameters adapted from Dahl et al., 2015

Parameter		unit	Parameter		unit
Sea surface depth [z_1]	1.4	m	Structural damping	0.001	-
Seabed depth [z_2]	8.9	m	Fluid wave speed [c_f]	1475	ms^{-1}
Penetration depth	16	m	Fluid density [ρ_f]	1000	kgm^{-3}
Pile length [L_p]	17.4	m	Compression wave speed soil [c_L]	1850	ms^{-1}
Pile thickness [t_p]	2.54	cm	Shear wave speed soil [c_T]	400	ms^{-1}
Pile radius [r_p]	0.381	m	Soil density [ρ_s]	1900	kgm^{-3}
Pile Poisons ratio [ν_p]	0.28	-	Compressional wave attenuation [α_L]	0.03	dB/λ
Pile Young's modulus [E_p]	210	GPa	Shear wave attenuation [α_T]	0.20	dB/λ
Pile density [ρ_p]	7850	kgm^{-3}			

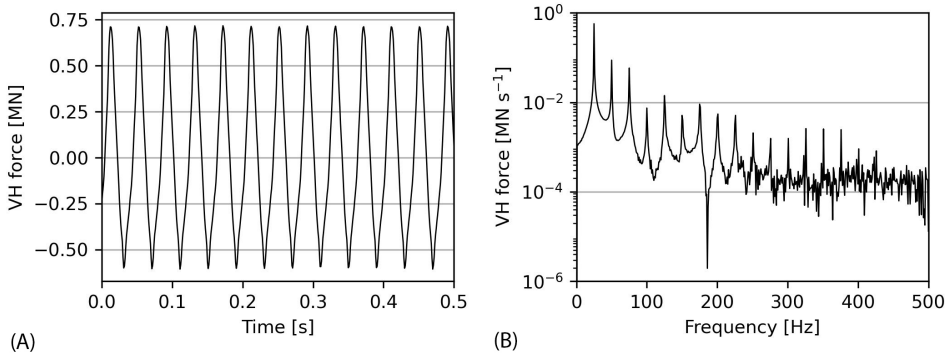


Figure 4.4: Estimated vibratory force exerted by the installation tool at the pile head as a function. Figure **(A)** shows the time signature, and Figure **(B)** shows the amplitude spectrum of the force (Tsetas et al., 2023a).

The applied force at the top of the pile is derived from actual strain measurements as shown in Fig. 4.4. The force is periodic and consists of a primary driving frequency of 25 Hz and strong super-harmonics every 25 Hz. Superharmonics play a major role in noise emission because sound radiation is more efficient at these frequencies than the main driving frequency. This is confirmed by Dahl et al. (2015, fig. 3), where the measured sound pressure levels at the super-harmonics are of higher amplitude than the sound pressure level at the main driving frequency.

The Scholte wave often plays a significant role in underwater noise at relatively low frequencies. The intensity of this wave is often overestimated if the pile and soil are assumed to be in perfect contact. Hereafter, relative motion is allowed between the pile and soil via a linear spring element introduced at the pile-soil interface. Four cases are evaluated: a case with PC between pile and soil, a case of NF forces, and two cases with relaxed pile-soil contact via the interface element. The interface element relaxes the static ($f = 0$ Hz) vertical soil stiffness to 75% and 5% of its original stiffness. The cases are abbreviated to k_F 75% and k_F 5%, and correspond to values of $\tilde{k}_F = 5 \times 10^6$ N m^{-1} and $\tilde{k}_F = 5 \times 10^8$ N m^{-1}, respectively.

4.5.1. Pile vibrations

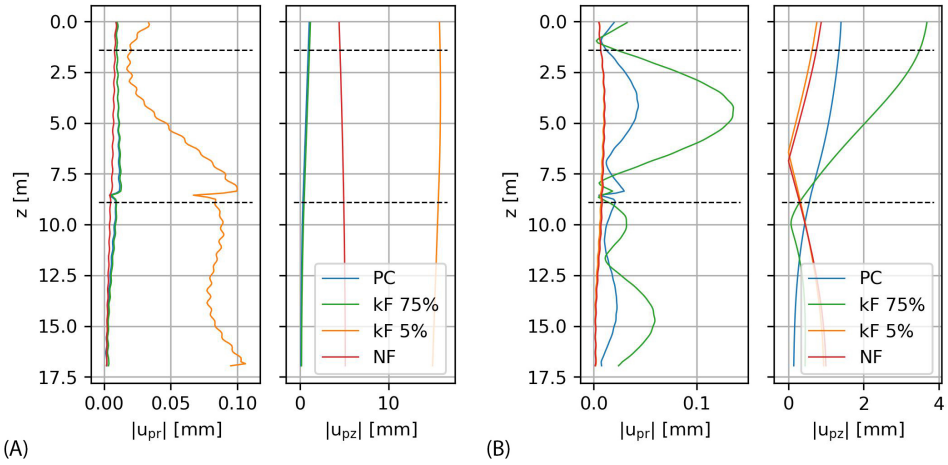


Figure 4.5: The amplitudes of the pile displacements in radial (u_{pr}) and vertical (u_{pz}) direction for a 1 MN harmonic force on top of the pile at 25 Hz and 125 Hz in **(A)** and **(B)**, respectively.

Allowing for relative motion between pile and soil affects the pile vibrations and the energy transferred to the surrounding domain. Figure 4.5 shows the amplitude of the pile displacements at 25 Hz and 125 Hz for varying values of $\tilde{k}_F$. The frequencies are chosen specifically at the driving frequency and the fourth super-harmonic. Fig. 4.5A shows that the rigid body motion governs the pile vibrations at low frequencies. For k_F 5%, the radial pile and soil displacements are amplified. This is counter-intuitive, but because the system has reduced soil stiffness and low damping, the resonance amplitude of the rigid body mode is amplified significantly. At higher frequencies, the dynamic response of the pile is strongly influenced by the pile-soil interface as shown in Fig. 4.5B, altering the noise source significantly in the fluid domain.

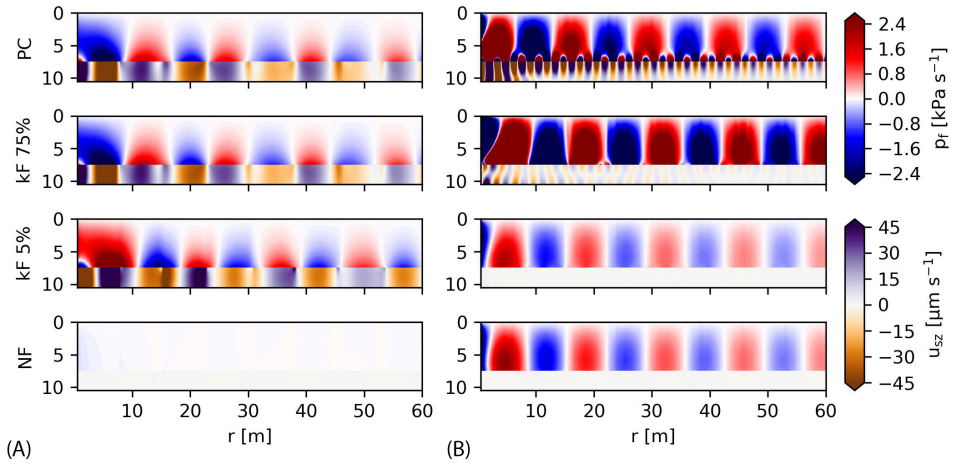


Figure 4.6: Figure **(A)** and **(B)** show the real part of the fluid pressure and vertical soil displacement for a harmonic 1 MN force at 25 Hz and 125 Hz respectively.

4.5.2. Underwater noise field and seabed vibrations

The change in pile dynamics affects the soil displacements and pressure levels in the fluid. The travelling waves in fluid and soil are visualised in Fig. 4.6. The figure shows snapshots of the fluid pressure and vertical soil displacement in the surroundings. Figure 4.6A shows that the Scholte waves govern the wavefield because the excitation frequency is below the cut-off frequency of this shallow fluid waveguide ($f_{\text{cut-off}} \approx 37.5$ Hz). The cut-off frequency linearly depends on water depth; thus, a pressure wave can exist at the driving frequency in the case of deeper waters. The Scholte wave is visible in the soil and fluid, though the amplitude is negligible in the case of perfect sliding conditions (NF case). The soil motion is amplified at k_{F} 5% because the main driving frequency is close to the eigenfrequency of the rigid body mode. It is debatable if this resonance is an artefact or physical. Experimental data should justify if it is indeed physical or if the artefact disappears with more realistic interface modelling, e.g. by including damping. Contrary, Fig. 4.6B clearly shows bulk pressure waves propagating through the fluid, while the Scholte waves influence a narrow zone close to the seabed. Next, the Scholte wave becomes visible with increasing pile-soil stiffness, though the penetration zone in the fluid reduces at higher frequencies due to the shorter wavelength of the Scholte waves. Figure 4.6 confirms the expectation that the interface conditions strongly affect both primary and secondary noise paths.

Figure 4.7 shows the sound pressure levels as a function of range and depth for varying cases. The pressure levels are highest above the seabed both from the primary and secondary noise path and decay with distance. With increasing contact stiffness k_{F}, the interference of pressure waves in the fluid and Scholte waves is clearly visible in Fig. 4.7B. Negligible noise is generated in the case of NF at 25 Hz because this frequency is below the cut-off frequency

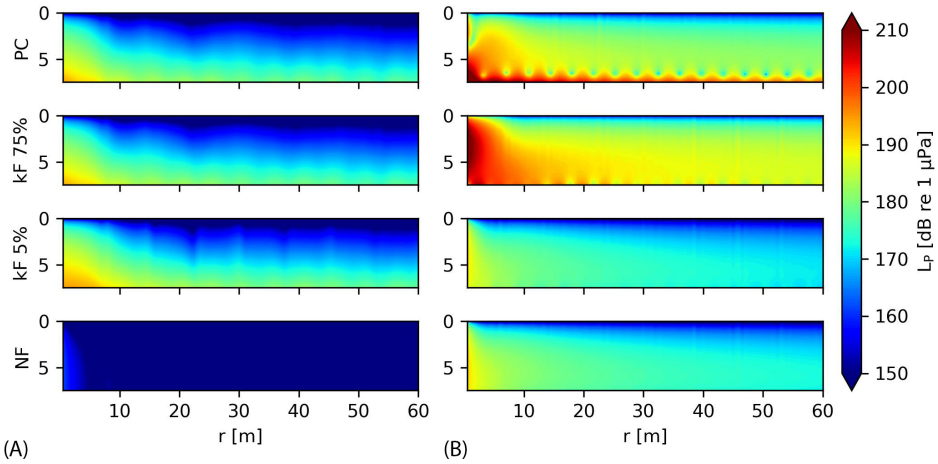


Figure 4.7: Figure **(A)** and **(B)** show the sound pressure levels in dB versus depth and height in the fluid for a harmonic 1 MN force at 25 Hz and 125 Hz respectively.

of propagating body modes in the fluid, and almost no energy is transferred to the Scholte waves due to the lack of shear excitation.

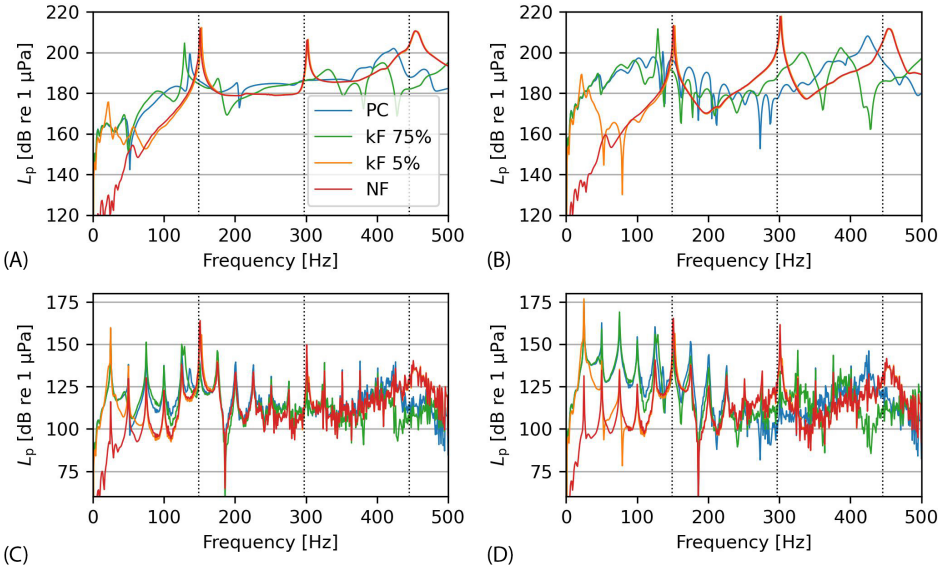


Figure 4.8: Figure **(A)** and **(B)** show the sound pressure level transfer functions for a 1 MN harmonic load on top of the pile at a 20 m radius and $z = 3$ m and $z = 7$ m, respectively. Figure **(C)** and **(D)** show the sound pressure levels resulting from the vibratory force from Fig. 4.4 at a 20 m radius and $z = 3$ m and $z = 7$ m, respectively. The dotted vertical lines indicate the eigenfrequencies of the pile.

The transfer functions or frequency response functions for a unit 1 MN harmonic load on top of the pile at a receiver point at a radius of 20 m are shown in Fig. 4.8A & Fig. 4.8B. The sound pressure level transfer functions depend strongly on the contact stiffness element. The sound pressure levels are significantly higher at 0.5 m above the seabed than in the middle of the fluid column for cases with Scholte waves. Scholte waves are most dominant at low frequencies (<200 Hz). At approximately 150, 300, and 450 Hz, the first in-vacuo eigenfrequencies of the pile are indicated with a black dotted vertical line. The sound pressure level amplifies around these frequencies if soil and pile are loosely coupled and the system experiences low damping. Thus, eigenfrequencies play an increasingly important role in the case of reduced resistance. The resonance of the rigid body mode, as discussed in Section 4.5.1, is visible at 23 Hz for k_F 5%. It is debatable whether this mode is physical or not. One might say that, in reality, this mode can exist at low frequencies with reduced soil resistance. On the other hand, it can be argued that frictional damping limits this resonance behaviour. Damping at the pile-soil surface via an imaginary part in k_F can represent the interface damping.

The importance of the sound pressure level transfer functions becomes evident when the actual force is applied at the top of the pile by multiplying the transfer functions with the spectrum of the force plotted in Fig. 4.4B. Figure 4.8C & Fig. 4.8D shows the periodicity of the peaks related to the force spectrum. The surface waves at low frequencies govern the noise field above the seabed except for the NF case as shown in Fig. 4.8D. In the middle of the fluid layer, the peaks are of similar amplitude for most super-harmonics. In the case of NF and k_F 5%, the in-vacuo eigenfrequencies of the pile amplify the sound pressure level next to the peaks enforced by the external force.

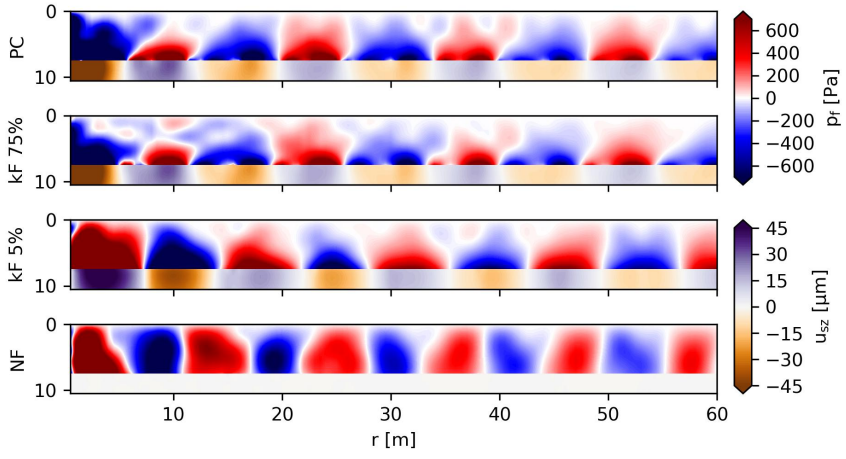


Figure 4.9: Snapshot of the time domain pressure field for the periodic force for varying interface conditions.

Applying the inverse Fourier transform gives the periodic time domain response of the fluid and soil. Figure 4.9 shows a snapshot of the time domain pressure field in the fluid and vertical displacements in the soil. The Scholte waves at the driving frequency govern the wavefield in all cases except for the case of NF. In the upper part of the fluid layer, interference patterns are visible in fluid pressure waves of varying wavelengths. The predominant pressure wave pattern in the case of NF corresponds to a frequency of approximately 150 Hz, i.e., the first eigenfrequency of the pile, in line with expectations from the earlier analysis.

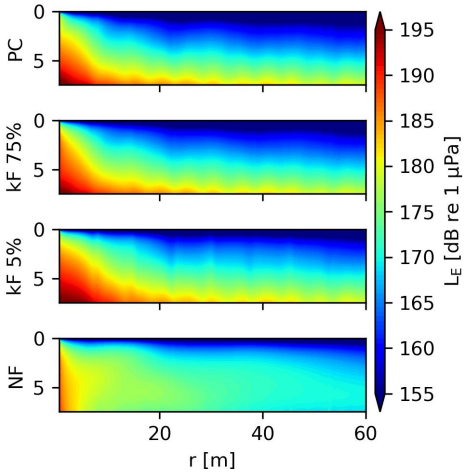


Figure 4.10: Sound exposure levels in dB versus depth and height in the fluid throughout 1 second forcing.

To examine the accumulative noise pollution over a time interval, the sound exposure levels (L_E) are calculated. The sound exposure level shows the time-integrated squared sound pressure in decibels and is calculated via (ISO, 2017a):

$$L_E = 10\log_{10}\left(\frac{E_p}{E_{ref}}\right), \quad E_p = \int_{t_1}^{t_2} p^2 \mathrm{d}t = \int_0^{\infty} 2|\tilde{p}|^2 \mathrm{d}f \tag{4.48}$$

with the reference value for sound pressure in fluids $E_{ref} = 1\mu Pa^2s$. Figure 4.10 shows the sound exposure levels in the fluid domain throughout 1 second of the forced response. The amplitude of the sound exposure levels varies strongly in various cases with no particular trend. In the NF case, the sound exposure is governed by the bulk pressure waves, while in the PC case, the Scholte waves contribute significantly. This shows that the sound exposure level above the seabed is highest in the presence of Scholte waves. In the case of NF, the bulk pressure wave causes lower sound exposure levels above the seabed but relatively higher levels in the middle and upper part of the fluid column.

Biologists are additionally interested in particle velocity of fluid and seabed for environmental assessment. Figure 4.11 shows the particle velocity norm and directionality at a

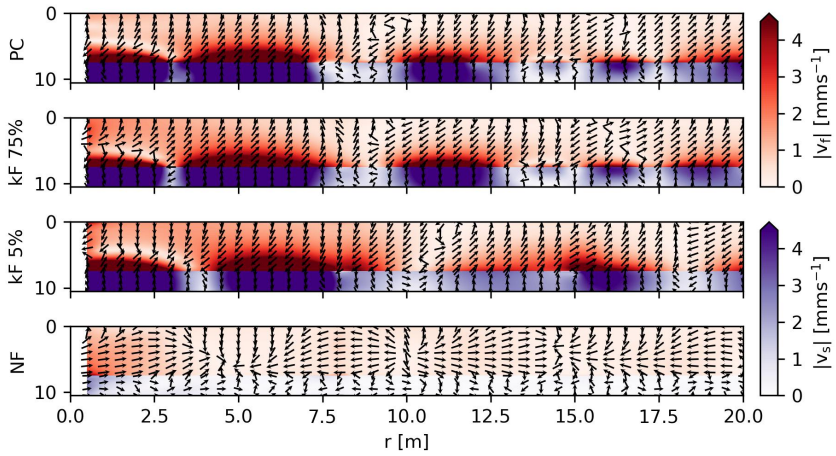


Figure 4.11: Snapshot of particle velocity norm in $\mathrm{mm\,s^{-1}}$ in fluid and soil domains including velocity directionality.

snapshot in time. The figure shows that the predominant particle motion is along the vertical direction at the seabed-water interface. However, in the absence of the Scholte waves, the particle motion direction is governed by the radial direction due to the bulk pressure waves alone.

4.5.3. Reduced soil shear stiffness

The experimental campaign in Dahl et al., 2015 consists of soil with high shear wave speed. In many known cases, the shear wave speed is significantly lower. Since the shear wave speed strongly influences the amplification of the Scholte waves, the analysis is repeated for a reduced shear wave speed of $150\ \mathrm{m\,s^{-1}}$, which is typical in marine environments with sandy sediments in the North Sea in Europe (Peng et al., 2021b). The rest of the parameters are given in Table 4.2. This results in a relative reduction of the stiffness to 95% and 20% compared to the static stiffness for the rigid body mode, for a contact spring element k_{F} of $5 \times 10^{8}\ \mathrm{N\,m^{-1}}$ and $5 \times 10^{6}\ \mathrm{N\,m^{-1}}$, respectively.

Figure 4.12 shows the transfer functions of the pressure field, similarly to Fig. 4.8A & Fig. 4.8B. Both figures show similar behaviour, though the differences in pressure levels between the cases in sound pressure levels are smaller with lower shear wave speed at frequencies between 100 Hz and 350 Hz.

Figure 4.13 shows a snapshot of the time domain fluid pressures and the vertical soil displacements. The Scholte waves visible differ significantly compared to Fig. 4.9. The Scholte wave has a shorter wavelength due to the lower shear wave speed and reduced penetration into the fluid zone. Thus, the primary noise path becomes more pronounced. The reduced penetration of the Scholte waves also explains the reason why the Scholte waves contribute

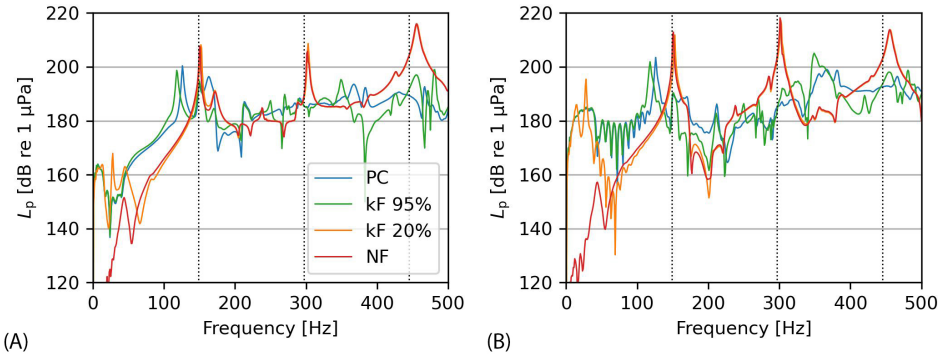


Figure 4.12: Figure **(A)** and **(B)** show the sound pressure level transfer functions for a 1 MN harmonic load on top of the pile at 20 m radius and soil with a low shear modulus.

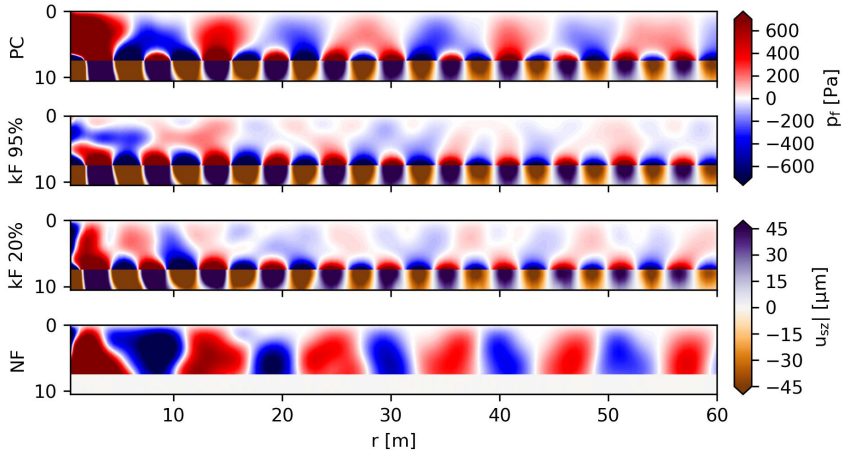


Figure 4.13: Snapshot of time domain pressure field for the periodic force for varying interface conditions with soil with a low shear modulus.

less to the sound pressure levels in Fig. 4.12 compared to the case shown earlier. On the contrary, the vertical displacements in the soil are of larger amplitude compared to Fig. 4.9. Otherwise, the principles of noise generation align with the original case. Even for soil with lower shear wave speeds, the role of the interface waves in the noise generation remains significant, causing dominant pressure levels and seabed vibrations.

4.6. Conclusions

This chapter concludes that models for impact pile driving are not directly applicable in vibratory pile driving because a more advanced description of pile-soil interaction is essential for predicting noise and vibrations accurately. The pile-soil interface condition strongly influences the dynamic response of the pile and the energy transfer mechanism in the surrounding domain. More specifically:

- The dynamic response of the pile depends strongly on the coupling to the soil, which, in turn, influences the primary noise and secondary noise paths.
- In case pile and soil are loosely coupled, the in-vacuo eigenfrequencies of the pile play an increasingly important role in noise generation. The reduced damping and stiffness in the system cause amplification of the structural vibrations around the eigenfrequencies of the coupled system.
- In the case of strong pile-soil coupling, Scholte interface waves are amplified and contribute significantly to the fluid pressures. The Scholte waves govern the seabed vibrations for high and low shear speeds. Due to the possible intense seabed vibrations, marine life on or above can potentially be harmed. The Scholte waves are significant at low frequencies and, therefore, more important in vibratory installation compared to impact pile driving.
- The pile-soil interface conditions strongly influence the particle velocity field.

Even with a relaxation of the pile-soil interface condition, the presence of the Scholte wave affects the sound field due to the relatively low primary excitation frequency. Therefore, models representing the soil by an acoustic fluid are insufficient in vibratory pile driving. This study shows the noise generation mechanisms qualitatively in the case of piles installed with vibratory tools. Future research in describing the interface condition and experimental data to validate the model is needed for a fully quantitative investigation.

5

Underwater noise from vibratory pile driving with non-linear frictional pile-soil interaction

This chapter introduces a novel methodology for underwater noise predictions during vibratory pile driving. A non-linear driveability model is utilised to derive realistic non-linear interface friction forces, which are then incorporated into a noise prediction model. The study emphasises the significance of integrating a driveability analysis, revealing substantial differences from traditional models that assume perfect contact between the pile and soil. Unlike traditional models designed for impact piling, the proposed model provides more realistic outcomes when considering smooth driving without refusal. The results illustrate noticeable deviations in pressure levels and seabed vibrations between the linear and presented methods at the driving frequency and its superharmonics. Furthermore, the research demonstrates that the noise field is highly sensitive to variations in system dynamics and excitation spectrum during driving, using both small- and large-diameter monopiles as examples. This research contributes to developing more effective driving techniques to reduce underwater noise pollution and facilitate sustainable offshore wind turbine installations.

This chapter has been published in the Journal of Sound and Vibrations, Volume 576, 28 April 2024, Molenkamp et al. (2024a).

5.1. Introduction

Underwater noise levels can be reduced in two ways: either at the source or via a noise mitigation system placed on the path to the receiver, such as air bubble curtains (Peng et al., 2021a; Tsouvalas and Metrikine, 2016a). Reducing noise emission at the source is achieved by adjusting the installation method, which vibratory methods have a high potential to accomplish. Vibratory hammers are developed for offshore applications (Moscoso del Prado Mazza and Holeyman, 2019) and scaled up to drive larger monopiles. Furthermore, a new vibratory technology called 'Gentle Driving of Piles' is developed to increase driving speed and further reduce noise emissions (Tsetas et al., 2023a).

Limited research has been conducted on underwater noise caused by vibratory pile driving techniques. Tsouvalas and Metrikine (2016b) predict the wave field emitted by impact-driven and vibratory-driven monopiles with a traditional noise-prediction model for impact piling. They observe that the highest noise levels are just above the seabed; this phenomenon is more substantial in vibratory pile driving due to the energy carried by the Scholte waves. The Scholte waves are even more dominant under low-frequency excitation, consistent with the primary driving frequency in vibratory pile driving (10~40 Hz). Furthermore, Tsouvalas and Metrikine note that the system is in a quasi-steady state during vibratory pile driving. Dahl et al. (2015) show the dominant presence of the superharmonics of the primary driving frequency (14 Hz) governing the underwater noise emission during vibratory driving. The highest sound pressure levels at 207 m are measured at 112 and 144 Hz; these are multiples of the driving frequency of 16 Hz. Frequencies between multiples of the driving frequency do not significantly contribute to noise emission, i.e. the emitted noise spectrum consists of specific toned components, the frequency of which is dictated by the primary excitation frequency, i.e. the driving frequency, and the non-linear pile-soil interaction. To what extent these superharmonics are induced by hammer excitation or non-linear pile-soil interaction through friction is unknown.

Molenkamp et al. (2023b) show that noise emission predictions are sensitive to pile-soil interaction modelling. The study introduces a model allowing motion between pile and soil to examine the effect of the pile slip relative to the soil in vibratory pile driving. At low frequencies, such as the primary driving frequency of vibratory devices, the Scholte wave can be the dominant noise carrier when the pile and soil are in perfect contact, i.e., there is no sliding. Contrarily, the first natural frequencies of the system are close to the in-vacuo eigenfrequencies of the pile if pile-soil coupling in the vertical direction is almost absent and noise radiation around those frequencies becomes dominant. For cases in between, no perfect contact with some pile slip is allowed; both mechanisms above are triggered. The chapter concludes that an improved description of the interface forces is necessary for accurate noise predictions.

Underwater noise generated by vibratory driving strongly depends on the vibrations of the pile, which act as the acoustic source in the application of interest. Pile vibrations depend strongly on excitation force and soil resistance. Accordingly, noise predictions are

sensitive to the description of pile-soil interaction. All available underwater noise prediction models use linear soil-pile interaction models, among other reasons, to achieve an acceptable computational time and thereby fail to have a correct physical representation of the interaction.

The novelty of the chapter lies in predicting underwater noise due to vibratory pile-driving, with an improved, physically correct representation of the pile-soil interaction. The chapter shows the complex dynamics that affect noise emission and examines the influence of the pile-soil interaction. Thus, the underwater noise predictions include non-linear pile-soil frictional interaction via Coulomb friction. The author believes the numerical model provides a better than previously reported physical representation of the pile-soil-fluid coupled system, improving our understanding of noise generation mechanisms during offshore vibratory pile driving. At low frequencies, it is essential to accurately calculate the amplitude of the Scholte interface waves, and at higher frequencies, the pile-soil coupling strongly affects the steady-state response of the system and the energy distribution into the various superharmonics. A non-linear pile driveability analysis provides information on the progression of the pile into the soil and the non-linear interaction forces.

The effect of the non-linear pile-soil interaction is implemented in a vibroacoustic model by utilising the output from a vibratory driving analysis, provided that the driveability model is three-dimensional. Tsetas et al. (2023e) developed a computationally efficient 3-D axisymmetric pile-soil model for vibratory driving and validated the numerical model predictions with field data. In particular, a linear elastic thin cylindrical shell and a linear elastic layered half-space describe the pile and soil medium, respectively. Their coupling is realised through a history-dependent frictional interface based on Coulomb friction. In that manner, a reliable estimation of the pile-soil interaction forces can be obtained and utilised as input for the subsequent step, namely the underwater noise predictions.

This chapter introduces a novel approach by integrating a comprehensive non-linear representation of pile-soil friction into an underwater noise prediction model. In doing so, the knowledge gaps in the field above are closed. The models and their interactions are described in Section 2. The approach is demonstrated via two case studies involving piles of different sizes. The case of a small-size pile refers to the practical application of a pin pile in a jacket structure and is examined in Section 3. The pile dimensions are chosen according to limited available combined data from two experimental campaigns, one onshore and one offshore. Section 4 discusses the case of a large-diameter monopile, referring to a commercial pile foundation for modern applications. While vibratory hammers have not been tested commercially, extrapolated data from small-scale tests is used to perform the underwater noise modelling. The impacts of driving frequency and penetration depth on noise emissions are explored. The research displays that accurate noise predictions during vibratory pile driving are sensitive to the resonances of the system, depending on the pile-soil interaction model. Acoustic pressure underwater depends strongly on the varied driving frequency, force spectrum, and pile penetration depth. The effect of non-linear pile-soil

interaction is compared to conventional models, and a theoretical rationale is presented for the noise generation phenomenon. The conclusions are provided in Section 5.

5.2. Methodology

This section introduces a methodology integrating realistic non-linear frictional interface forces into noise prediction analysis. To achieve this, a state-of-the-art driveability model for vibratory pile driving is utilised to simulate the process of pile penetration and generate non-linear friction forces throughout the driving procedure (Tsetas et al., 2023e). The friction forces are obtained at discrete pile penetration depths, transformed into the frequency domain, and used as input in the noise prediction model. The proposed noise prediction model (Molenkamp et al., 2023b) employs a boundary integral formulation to describe the fluid-soil domain, enabling the direct incorporation of the friction forces. This section presents the geometrical characteristics and fundamental equations of the proposed model. Subsequently, it briefly overviews both analysis methods and explains how the analyses fit into the methodology.

5.2.1. Geometrical characteristics and fundamental equations

Figure 5.1 visualises the configuration of a monopile installation offshore containing a hollow cylinder driven into the soil. The monopile occupies the domain $L_\mathrm{p} - L_\mathrm{p} < z < L_\mathrm{p}$, with pile length L_p, thickness h_p and diameter $2r_\mathrm{p}$. The problem is cylindrically symmetric, i.e., the cylindrical coordinate system (r, z) is employed, assuming no variation around the circumference.

The pile is modelled as a thin shell, and its modulus of elasticity, Poisson's ratio and pile density are E_p, ν_p, and ρ_p, respectively. The equation of motion of the pile reads:

$$\boldsymbol{L}_\mathrm{p}\boldsymbol{u}_\mathrm{p}(z,t) + \rho_\mathrm{p} h_\mathrm{p} \ddot{\boldsymbol{u}}_\mathrm{p}(z,t) = \boldsymbol{f}_\mathrm{p}(z,t) + f_\mathrm{ext}(t)\delta(z - z_\mathrm{top})\hat{\mathrm{e}}_\mathrm{z} \tag{5.1}$$

where $\boldsymbol{L}_\mathrm{p}$ represents the stiffness components of Flügge's thin shell theory (Leissa, 1973), $\hat{\mathrm{e}}_\mathrm{z}$ is the vertical normal vector. The vector of the pile displacements reads $\boldsymbol{u}_\mathrm{p}(z,t)$, $f_\mathrm{ext}(t)$ provides the external load on top of the pile, and $\boldsymbol{f}_\mathrm{p}(z,t)$ contains the distributed fluid and soil interaction forces. The overhead double dots refer to the second derivative in time: $\partial^2/\partial t^2$.

The seawater and soil are modelled as continua, occupying the domains $z_1 < z < z_2$ and $z > z_2$, respectively. The first is described as an acoustic fluid, while the latter is modelled as an elastic medium. The fluid wave speed and density are given by c_f and ρ_f, respectively. The soil is characterised by the Lamé constants λ_s and μ_s and density ρ_s. The equations of motion of the domains read:

$$\nabla^2\phi_\mathrm{f}(r,z,t) - \frac{1}{c_\mathrm{f}^2}\ddot{\phi}_\mathrm{f}(r,z,t) = s_\mathrm{f}(z,t)\delta(r - r_\mathrm{p}) \tag{5.2}$$

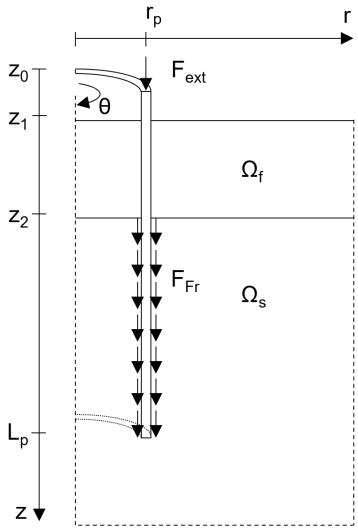


Figure 5.1: Model geometry with the acoustic fluid domain Ω_f and the elastic soil domain Ω_s. The pile is modelled by thin-shell theory at $r = r_\mathrm{p}$.

$$(\lambda_\mathrm{s} + \mu_\mathrm{s})\nabla(\nabla \cdot \boldsymbol{u}_\mathrm{s}(r,z,t)) + \mu_\mathrm{s}\nabla^2 \boldsymbol{u}_\mathrm{s}(r,z,t) + \boldsymbol{f}_\mathrm{s}(z,t)\delta(r - r_\mathrm{p}) = \rho_\mathrm{s}\ddot{\boldsymbol{u}}_\mathrm{s}(r,z,t) \tag{5.3}$$

The motion of the acoustic fluid is described by the displacement potential $\phi_\mathrm{f}(r,z,t)$, which relates to the displacement field via $\boldsymbol{u}_\mathrm{f}(r,z,t) = \nabla\phi_\mathrm{f}(r,z,t)$ and the fluid pressure $p_\mathrm{f}(r,z,t) = \rho_\mathrm{f}\omega^2\phi_\mathrm{f}(r,z,t)$ (Jensen et al., 2011). The soil equation of motion contains displacements vector $\boldsymbol{u}_\mathrm{s}(r,z,t)$ and body loads $\boldsymbol{f}_\mathrm{s}(z,t)$ applied at $r = r_\mathrm{p}$.

The fluid and soil are coupled through a standard set of interface conditions along the vertical coordinate valid at $r < r_\mathrm{p}$ and $r > r_\mathrm{p}$:

$$p_\mathrm{f}(r,z_2,t) = 0 \tag{5.4}$$

$$p_\mathrm{f}(r,L_\mathrm{p},t) + \sigma_{\mathrm{s},zz}(r,L_\mathrm{p},t) = 0 \tag{5.5}$$

$$u_{\mathrm{f},z}(r,L_\mathrm{p},t) - u_{\mathrm{s},z}(r,L_\mathrm{p},t) = 0 \tag{5.6}$$

$$\sigma_{\mathrm{s},zr}(r,L_\mathrm{p},t) = 0 \tag{5.7}$$

The coupling of the fluid and soil with the pile at $r = r_\mathrm{p}$ deviates from the standard linear underwater noise prediction models due to the introduction of friction at the pile-soil interface:

$$u_{\mathrm{p,r}}(z,t) = u_{\mathrm{f,r}}(r_\mathrm{p},z,t) \qquad z_1 < z < z_2 \tag{5.8}$$

$$f_{\mathrm{p,r}}(z,t) = -p_\mathrm{f}(r_\mathrm{p}^+,z,t) + p_\mathrm{f}(r_\mathrm{p}^-,z,t) \qquad z_1 < z < z_2 \tag{5.9}$$

$$u_{\mathrm{p,r}}(z,t) = u_{\mathrm{s,r}}(r_\mathrm{p},z,t) \qquad z_2 < z < L_\mathrm{p} \tag{5.10}$$

$$f_{\mathrm{p,r}}(z,t) = \sigma_{\mathrm{s,rr}}(r_{\mathrm{p}}^{+},z,t) - \sigma_{\mathrm{s,rr}}(r_{\mathrm{p}}^{-},z,t) \qquad z_2 < z < L_{\mathrm{p}} \tag{5.11}$$

$$f_{\mathrm{p,z}}(z,t) = F_{\mathrm{Fr}}(z,t) \qquad z_2 < z < L_{\mathrm{p}} \tag{5.12}$$

$$F_{\mathrm{Fr}}(z,t) = -\sigma_{\mathrm{s,rz}}(r_{\mathrm{p}}^{+},z,t) + \sigma_{\mathrm{s,rz}}(r_{\mathrm{p}}^{-},z,t) \qquad z_2 < z < L_{\mathrm{p}} \tag{5.13}$$

in which the interior and exterior domains are indicated with superscripts '-' and '+', respectively. Equations (5.8) and (5.9) describe the pile-fluid interaction along the radial direction. Equations (5.10) and (5.11) prescribe continuity of stresses and displacements between pile and soil in the radial direction. Friction is introduced as $F_{\mathrm{Fr}}(z,t)$ in Eqs. (5.12) and (5.13) being a distributed vertical force acting on the pile surface while balancing the difference between internal and external shear stresses in the soil. The driveability and noise prediction analyses are run sequentially to resolve the described problem statement as schematised in Fig. 5.2.

5.2.2. Driveability analysis

To perform a pile driving analysis, a non-linear pile-soil interaction model is necessary to describe the pile penetration into the seabed. In particular, various modelling developments are ongoing both in impact piling (Buckley et al., 2023; Salgado et al., 2015) and vibratory driving (Kaynia et al., 2022; Tsetas et al., 2023e), focusing on the challenges of offshore monopile installation. Tsetas et al. (2023e) developed an axisymmetric model for vibratory driving that is comprised of a linear elastic thin cylindrical shell and a linear elastic (layered) half-space. The fluid layer is excluded because its presence does not influence the driveability analysis, a commonly accepted assumption in driveability modelling. Specifically, the pile vibrations are modelled using the Semi-Analytical Finite Element (SAFE) method, where the cylindrical shell is discretised into a set of nodal rings. As regards the soil medium, the Thin-Layer Method (TLM) is employed to discretise the layered soil domain into homogeneous horizontal layers of small thickness (in finite element sense) (Kausel and Peek, 1982). It is noted that the half-space is accounted for in this model by utilising Perfectly Matched Layers (PMLs) coupled with the TLM (de Oliveira Barbosa et al., 2012; Kausel and de Oliveira Barbosa, 2012). Therefore, pile and soil modelling approaches employ a typical vertical discretisation grid. Furthermore, the non-linear pile-soil interaction is realised through a history-dependent frictional interface based on Coulomb friction that captures the progressive friction reduction at the pile-soil interface. The previous is commonly termed friction fatigue in the context of pile driving (Moriyasu et al., 2018). Finally, the vibratory pile driving model uses a visco-elasto-plastic tip reaction.

The friction force at $r = r_{\mathrm{p}}$ is expressed as follows:

$$F_{\mathrm{Fr}}(z,t) = f_{\mathrm{s,ult}}(z,t)\tanh\left(\frac{1}{v_{\mathrm{tol}}}\left(\frac{\partial u_{\mathrm{s,z}}(r_{\mathrm{p}},z,t)}{\partial t} - \frac{\partial u_{\mathrm{p,z}}(z,t)}{\partial t}\right)\right) \tag{5.14}$$

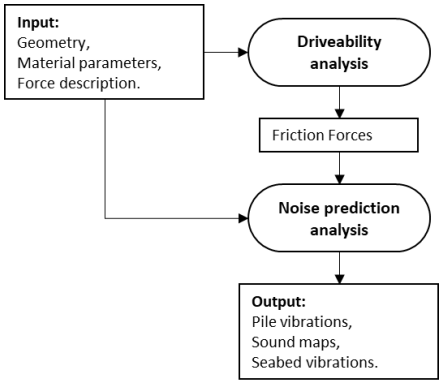


Figure 5.2: Flow chart of interaction between the driveability and the underwater noise prediction models.

where v_{tol} is a velocity tolerance parameter and $f_{\text{s,ult}}(z,t)$ defines the amplitude of the static (and kinetic) friction. It is noted that Eq. (5.14) accounts for the friction forces from both the inner and outer pile surfaces. Furthermore, in the present friction force formulation, the friction amplitude possesses history-dependence that is described as follows:

$$f_{\text{s,ult}}(z,t) = f_{\text{s,0}}(z)\left(\beta_\infty + (1-\beta_\infty)\mathrm{e}^{-c_N N_{\text{cycl}}(z,t)}\right) \tag{5.15}$$

where β_∞ is the ratio of the ultimately degraded friction amplitude to the initial one $f_{\text{s,0}}(z) = 0.012 q_{\text{c}}(z)$, $q_{\text{c}}(z)$ is the cone tip resistance of Cone Penetration Test (CPT), c_N is a memory parameter that controls the rate of degradation and $N_{\text{cycl}}(z,t)$ is the number of loading cycles accumulated at the soil position z during driving. Accordingly, as the pile penetrates the ground, the loading cycle accumulation at each soil material point reduces the friction force at the respective point.

The problem of non-linear dynamic pile-soil interaction is resolved by applying the Harmonic Balance Method (HBM) sequentially (Fontanela et al., 2019; Krack et al., 2013; Zhou et al., 2016). The HBM is used to determine a solution at each compatible position, where the elevations of the pile nodal rings align with the interfaces of soil layers. This solution remains valid for a time interval, significantly surpassing the fundamental period of the harmonic balance since the pile position and overall response change at a much slower pace compared to the driving frequency. This discrepancy in time scales allows for the sequential determination of harmonic balance coefficients for every pile position along the vertical mesh.

A more elaborate description of the model development, the friction parameters and the associated results can be found in Tsetas et al. (2023e); these will be omitted, as the focus herein lies in the underwater acoustics of vibratory pile installation. Further validation of the driveability model with field data regarding penetration rates and pile vibrations can also be found in (Tsetas, 2023; Tsetas et al., 2023d).

5.2.3. Noise prediction analysis

The underwater noise and seabed vibrations induced by vibratory pile driving are obtained via a noise prediction model. The model introduced in Molenkamp et al. (2023b) allows for relative motion between pile and soil, making it suitable to apply friction forces directly at the pile-soil interface. The governing equations for pile, fluid and soil are introduced in Section 5.2.1. The method describes the internal and external fluid and soil domains based on a boundary integral formulation of ring source Green's functions in the frequency domain. A modal summation of the in-vacuo modes represents the pile vibrations. The frequency domain representation of Eq. (5.1), including friction forces along the vertical direction and radial fluid and soil resistances, reads:

$$\boldsymbol{L}_\mathrm{p}\tilde{\boldsymbol{u}}_\mathrm{p}(z,\omega)-\rho_\mathrm{p}h_\mathrm{p}\omega^2\tilde{\boldsymbol{u}}_\mathrm{p}(z,\omega)=\tilde{F}_\mathrm{fsr}(z,\omega)\hat{\mathrm{e}}_\mathrm{r}-\tilde{F}_\mathrm{Fr}(z,\omega)\hat{\mathrm{e}}_\mathrm{z}+\tilde{f}_\mathrm{ext}(\omega)\delta(z-z_\mathrm{top})\hat{\mathrm{e}}_\mathrm{z} \tag{5.16}$$

where the tilde refers to the complex amplitude in the frequency domain. F_fsr contains the radial fluid and soil responses on the pile; these are found by convolution in z of the ring source Greens functions of the fluid and soil domain and the radial pile displacements and friction forces:

$$\tilde{F}_\mathrm{fsr}(z,\omega)=-\int_{z_2}^{L_\mathrm{p}}\tilde{\boldsymbol{K}}_\mathrm{fs}^{\mathrm{u_{pr}}}(\omega,z,\bar{z})\tilde{u}_\mathrm{pr}(\omega,\bar{z})\mathrm{d}\bar{z}+\int_{z_2}^{L_\mathrm{p}}\tilde{\boldsymbol{K}}_\mathrm{fs}^{\mathrm{F_{Fr}}}(\omega,z,\bar{z})\tilde{F}_\mathrm{Fr}(\omega,\bar{z})\mathrm{d}\bar{z} \tag{5.17}$$

in which $\tilde{\boldsymbol{K}}_\mathrm{fs}(\omega,z,\bar{z})$ contains the required Green's functions and Green's tensors of fluid and soil domains. A modal summation represents the pile displacements:

$$\tilde{\boldsymbol{u}}_\mathrm{p}(z,\omega)=\sum_{k=1}^{\infty}\tilde{\xi}_k(\omega)\boldsymbol{U}_{\mathrm{p},k}(z,\omega) \tag{5.18}$$

The mode shapes $\boldsymbol{U}_{\mathrm{p},k}(z,\omega)$ are found by solving the eigenvalue problem of the in-vacuo pile with free-end boundary conditions. The modal amplitudes $\tilde{\xi}_k(\omega)$ are obtained by applying the orthogonality of the structural modes in Eq. (5.16):

$$(\omega_k^2(1+\mathrm{i}\eta_\mathrm{p})-\omega^2)\tilde{N}_k(\omega)\tilde{\xi}_k(\omega)=\sum_l\int_0^{L_\mathrm{p}}\boldsymbol{U}_{\mathrm{pr},l}^T(z,\omega)\tilde{F}_\mathrm{fsr}(z,\omega)\mathrm{d}z-\int_{z_2}^{L_\mathrm{p}}\boldsymbol{U}_{\mathrm{pz},l}^T(z,\omega)\tilde{F}_\mathrm{Fr}(z,\omega)\mathrm{d}z+U_{\mathrm{pz},l}(0,\omega)f_\mathrm{ex} \tag{5.19}$$

in which η_p is the structural damping, only admissible for small values ($\eta_\mathrm{p}<10^{-2}$) as no effect of damping on the structural modes is considered, and N_k is the orthogonality condition of the pile modes:

$$\tilde{N}_k(\omega)=\rho_\mathrm{p}h_\mathrm{p}\int_0^{L_\mathrm{p}}\boldsymbol{U}_{\mathrm{p},k}^T(z,\omega)\boldsymbol{U}_{\mathrm{p},k}(z,\omega)\mathrm{d}z \tag{5.20}$$

The integrals in Eq. (5.19) and in the convolutions in Eq. (5.17) are solved by numerical integration. After finding the pile vibrations and having the friction forces, the waves are

Table 5.1: Parameters for the small diameter monopile case study (Dahl et al., 2015; Peng et al., 2021b)

Parameter		unit	Parameter		unit
Sea surface depth [z_1]	0	m	Fluid wave speed [c_f]	1500	$\mathrm{m\,s^{-1}}$
Seabed depth [z_2]	7.5	m	Fluid density [ρ_f]	1000	$\mathrm{kg\,m^{-3}}$
Pile length [L_p]	17.4	m	Compression wave speed soil [c_L]	1800	$\mathrm{m\,s^{-1}}$
Pile thickness [t_p]	2.54	cm	Shear wave speed soil [c_T]	200	$\mathrm{m\,s^{-1}}$
Pile radius [r_p]	0.381	m	Soil density [ρ_s]	1900	$\mathrm{kg\,m^{-3}}$
Pile Poissons ratio [ν_p]	0.28	-	Compressional wave attenuation [α_L]	0.80	dB/λ
Pile Youngs modulus [E_p]	210	GPa	Shear wave attenuation [α_T]	0.20	dB/λ
Pile density [ρ_p]	7850	$\mathrm{kg\,m^{-3}}$	Cone tip resistance [q_c]	10	MPa
Structural damping [η_p]	0.001	-			

straightforwardly propagated at larger distances from the pile by employing Green's functions and Green's tensors of ring sources. A more elaborated model description and detailed derivation of Green's functions and Green's Tensors are found in Molenkamp et al., 2023b.

5.2.4. Integrating driveability effects in noise prediction analysis

The driveability analysis subsequently provides the non-linear frictional interface forces at each driving depth, described in Eq. (5.14). The friction forces are consecutively substituted in the noise prediction analysis. Since the driveability model employs the HBM around each driving depth, all forces and displacements are expressed by a summation of harmonics. Thus, the friction forces can straightforwardly be substituted in Eq. (5.19), the noise prediction analysis, to find the frequency domain pile vibrations, fluid pressures and soil vibrations. The analysis is run in the state of constant driving, excluding refusal, which is defined as the state where the pile does not progress into the soil.

A significant benefit of combining both methods is the computational efficiency of the independent components. A single analysis, i.e. a single driving force, of the large monopile was executed on an Intel(R) Xeon(R) W-2155 CPU @ 3.30 GHz in 142 minutes. The driveability analysis took 36 minutes, generating the soil and fluid Boundary Element Method (BEM) 34 minutes, calculating the fluid and soil propagation matrix 56 minutes and performing the acoustic frequency domain analysis 16 minutes. The computation time depends mainly on the number of frequencies, pile and BEM discretisation and the number of receiver points in the soil and fluid. This study does not include further considerations, such as parallel computation optimisation for increased computational speed.

5.3. Underwater noise field of a small-size monopile

The underwater noise field generated during the driving of a small-scale monopile with a vibratory hammer is examined based on experimental data. The case study consists of a small monopile with a diameter of 0.762 m as used in the experimental campaign of both Tsetas et al. (2023a) and Dahl et al. (2015). The geometry is taken from Dahl et al. (2015),

and common values are used for sandy soil and fluid retrieved from Peng et al. (2021b). The parameters are outlined in Table 5.1.

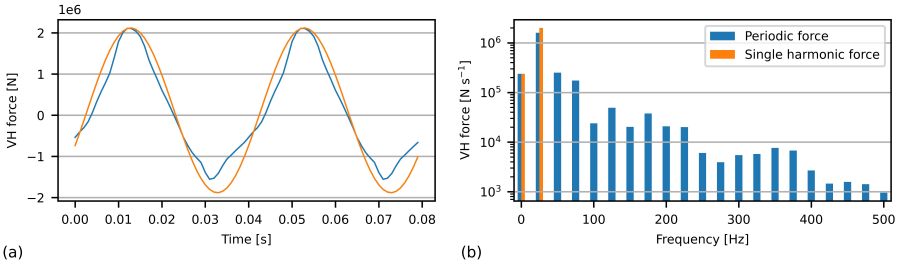


Figure 5.3: (a) Two cycles of the single harmonic and periodic force in the time domain and (b) the amplitude per frequency.

Two external forcing functions are applied to the pile. First, a single harmonic excitation is combined with a static load, referring to a perfect vibratory hammer. Second, a driving force is deduced from measurements during the test campaign of Tsetas et al. (2023a); the first is referred to as the single harmonic force and the latter as the periodic force.

A static load is assumed to be 120 kN, and the single harmonic force excites 25 Hz with an amplitude of 2.0 MN. These values result in the same pile penetration rate as the force obtained from the test campaign with the same primary driving frequency. The obtained force from measurements is periodic, with a primary driving frequency of 25 Hz plus excitation at several superharmonics. Accordingly, the force is described by the following Fourier series:

$$f_{\text{ext}}(t) = \sum_{n=0}^{20} c_n e^{i2\pi f_0 n} \tag{5.21}$$

with f_0 being the primary driving frequency and c_n the complex valued amplitude. The number of superharmonics is truncated to 20, corresponding to 500 Hz since the sampling rate was at one kHz. The Fourier component at $n = 0$ corresponds to the static force on top of the pile. Figure 5.3 shows each force's time series and amplitude-frequency spectra. The contributions of the superharmonics in the periodic force obtained from the test campaign are magnitudes smaller than the primary driving frequency and decrease with increasing frequency; the figure justifies that frequencies above 500 Hz are not expected to contribute significantly to the response of the coupled system. The periodic force represents the hammer force on top of the pile based on measurements. However, the real force and corresponding spectrum depend on driving depth, pile size, soil conditions, and hammer type; during this analysis, the spectral distribution of the force is assumed to be constant.

5.3.1. Single harmonic force

Two wave paths are typically identified in noise generation during offshore pile driving. The primary noise path is considered the direct noise path of the pile radiating noise into

the fluid; the secondary noise path contains the noise that is generated indirectly by soil vibrations, e.g. by the Scholte interface wave, i.e. the pile excites the soil, and via seabed vibrations the fluid is excited. Figure 5.4 shows the underwater pressure field and seabed vibrations excited by a single harmonic force at a driving depth of $L_\mathrm{p} = 14$ m; this is halfway through the driving process. The primary noise path is visible in the fluid domain, where the fluid is directly excited by the pile vibrations; the second noise path is clearly visible in the soil vibrations but is more difficult to detect in the fluid. Nonetheless, pressure waves propagate just above the seabed with a quarter-period shift from the vertical soil velocity. The phase shifts originate from pressure being proportional to accelerations, and the interface waves have an exponential decay from the seabed into the fluid layer. Observing the primary noise path, an interference of multiple waves is shown. However, the dominant wavelength of the body waves is approximately ten m, corresponding to waves with a frequency of 150 Hz, which is not the primary driving frequency. The frictional resistance at the pile-soil interface obtained by the non-linear driveability model is the only mechanism that can redistribute energy in this model from the single harmonic excitation to superharmonics.

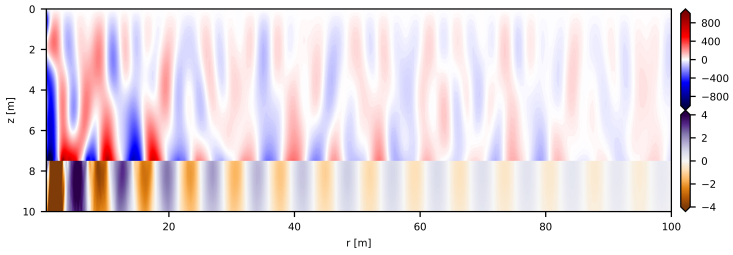


Figure 5.4: Snapshot of the underwater pressure and vertical seabed velocity at a driving depth of $L_\mathrm{p} = 14$ m due to a single harmonic force. The blue-red scale shows the fluid pressure in Pa, and the yellow-purple scale shows the vertical soil particle velocity in mm s^{-1}.

Sound pressure levels give insight into the contribution of each frequency to the noise field. The sound pressure levels L_P are calculated via (ISO, 2017a):

$$L_\mathrm{p} = 20 \log_{10} \left(\frac{p_\mathrm{rms}}{p_\mathrm{ref}} \right) \tag{5.22}$$

in which the real mean square in the frequency domain equals $p_\mathrm{rms}^2 = \frac{1}{2}|\tilde{p}^2|$ and the reference pressure in underwater acoustics is $p_\mathrm{ref} = 1$ µPa.

Figure 5.5 clearly shows that energy shifted to super harmonics and that these higher harmonics govern the noise field. This confirms the significance of combining driveability analysis with noise predictions since linear models cannot predict energy redistribution into higher harmonics that govern the sound radiation.

The sound pressure levels amplify around the natural frequencies of the in-vacuo pile, which are indicated with red dotted vertical lines in Fig. 5.5. The axisymmetric pile modes

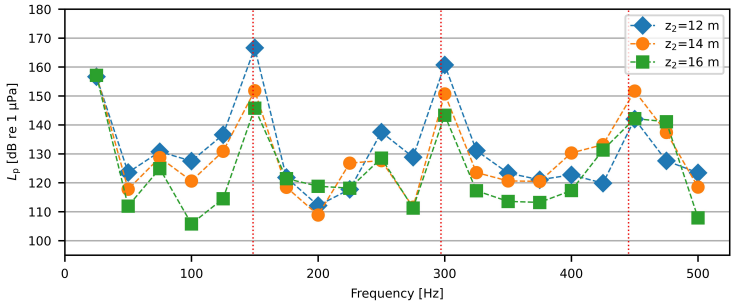


Figure 5.5: Sound pressure levels above the seabed at $r = 50$ m and $z = 4$ m for three different driving depths. The red dotted vertical lines represent the pile's first three in-vacuo natural frequencies.

have significantly larger vertical than radial deformations at the first few natural frequencies. Consequently, the first few resonant frequencies of the immersed structure shift only slightly from the in-vacuo natural frequencies of the pile since the pile and surrounding media are coupled only strongly in the radial direction when relative vertical motion is allowed between pile and soil (Molenkamp et al., 2023b).

The superharmonics at 150, 300 and 450 Hz almost coincide with the natural frequencies of the in-vacuo pile with free-edge boundary conditions at 149, 297 and 445 Hz, resulting in significant radial vibrations. Consequently, the fluid pressure is governed by the body waves radiated from the pile at these frequencies, even though the hammer force does not directly excite these frequencies. Thus, the sound pressure levels are highest at frequencies excited by frictional resistance, underlining the importance of an accurate pile-soil interface description.

Figure 5.5 presents the sound pressure levels at three driving depths of the pile. The sound pressure levels significantly reduce with driving depth at frequencies between 100 and 150 Hz. At other frequencies, the difference is more minor. The sound pressure levels at the primary driving frequency remain largely unaffected by the driving depth. Driving depth significantly affects the dynamic behaviour of the immersed structure, but the effect is not straightforwardly predictable.

5.3.2. Periodic force

A periodic force on top of the pile provides a more realistic case. Figure 5.6 shows the underwater pressure field and seabed vibrations at a driving depth of $L_p = 14$ m. The Body waves with a ten m wavelength, corresponding to a frequency of 150 Hz, dominate the pressure field in the fluid. This aligns with the observed pressure field in Fig. 5.4, but the wavelength frequency is even more pronounced and of larger amplitude in Fig. 5.6. The soil vibrations show the presence of the Scholte wave. In the first 20 m, interferences of multiple soil waves are visible, while from 30 m onwards, the Scholte wave at the main

driving frequency is clearly visible. Still, this secondary noise path does not affect the fluid pressures visually due to the presence of larger amplitude body waves in the seawater.

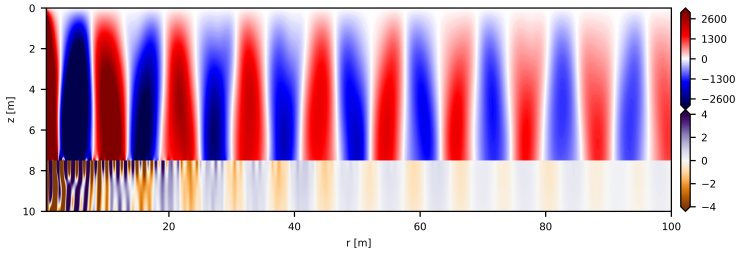


Figure 5.6: Snapshot of the underwater pressure and vertical seabed velocity at a driving depth of $L_p = 14$ m. The blue-red scale shows the fluid pressure in Pa, and the yellow-purple scale shows the vertical soil particle velocity in $\mathrm{mm\,s^{-1}}$.

The sound pressure levels at two locations shown in Fig. 5.7 confirm the dominant levels at 150 Hz. Both cases show strong sensitivity to the resonant frequencies of the system. The sound pressure levels induced by the periodic force are significantly larger at almost all frequencies at both locations. The presented case study confirms the hypothesis that the energy in superharmonics is caused by hammer excitation while the non-linear pile-soil interaction plays a secondary role. However, research is required to determine whether the same holds in other conditions, such as variations in hammer characteristics, soil profiles, and pile dimensions.

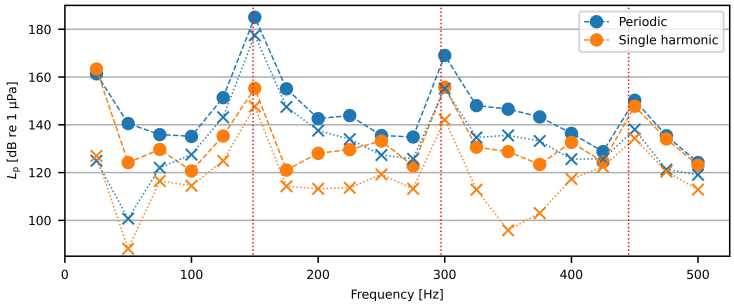


Figure 5.7: Sound pressure levels at $r = 25$ m and $z = 7$ m (dashed lines with circle markers) and at $r = 100$ m and $z = 4$ m (dotted lines with crosses) induced by the periodic and single harmonic force, and at a driving depth of $L_p = 14$ m. The red dotted vertical lines represent the pile's first three in-vacuo natural frequencies.

At the primary driving frequency, the contribution of the Scholte wave to the noise field is observed just above the seabed. Contrary to the periodic force, the case of a single harmonic excitation has the largest noise levels above the seabed at the primary driving frequency. At $z = 4$ m and $r = 100$ m, the Scholte waves are not observed since the waves exponentially decay with depth and minimally affect the upper part of the fluid column.

Since body waves cannot travel in the present geometry below the cut-off frequency of the fluid layer (≈ 50 Hz), sound pressure levels are minimal at the main driving frequency away from the pile.

5.3.3. Comparison with limit cases

The performance of the proposed model is evaluated by comparing it to two linear limit cases of the friction law to assess its added benefits. The first case assumes Perfect Contact (PC) between the pile and soil, which is the traditional approach for modelling the interaction between pile and soil in impact pile driving models. The PC case is obtained by replacing the interface conditions, Eqs. (5.12) and (5.13) by:

$$u_{\mathrm{p,z}}(z) = u_{\mathrm{s,z}}(r_{\mathrm{p}}, z) \qquad z_2 < z < L_{\mathrm{p}} \tag{5.23}$$

$$F_{\mathrm{p,z}}(z) = -\sigma_{\mathrm{s,rz}}(r_{\mathrm{p}}^{+}, z) + \sigma_{\mathrm{s,rz}}(r_{\mathrm{p}}^{-}, z) \qquad z_2 < z < L_{\mathrm{p}} \tag{5.24}$$

Second, the assumption of No Friction (NF) is made; this is obtained by modifying Eqs. (5.12) and (5.13) and setting $F_{\mathrm{Fr}}(z) = 0$. Therefore, the pile and surrounding media are coupled only in the radial direction. Both limit cases are compared to the case with the Driveability Analysis (DA), i.e. the proposed method.

Due to the linear characteristics when the excitation is harmonic, i.e. at $f = 25$ Hz, both PC and NF models respond to that same frequency because no energy redistributes to higher harmonics. The PC case returns 160, 157 and 155 dB re 1 µPa and the NF case 104, 109 and 114 dB re 1 µPa at $r = 50$ m and $z = 4$ m for the three driving depths of 12, 14 and 16 m, respectively, as presented in Fig. 5.5. The PC model provides an upper bound for the noise levels at 25 Hz due to the strong presence of the Scholte wave. Contrarily, little noise is produced in the NF case at this low frequency. The pile only interacts with the fluid and soil in the radial direction, and at 25 Hz, no fluid body waves are generated because the driving frequency is below the cut-off frequency of the fluid layer.

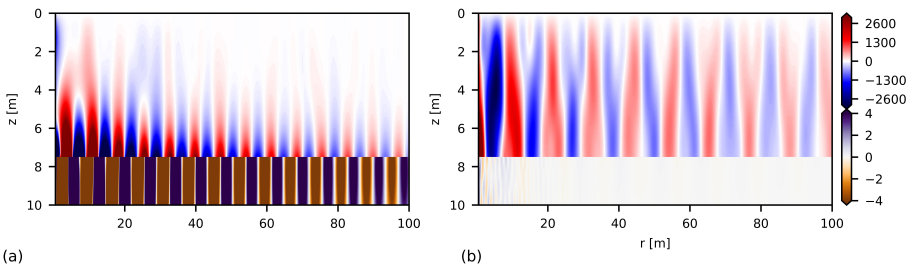


Figure 5.8: (a) and (b) show the underwater pressure and seabed vibrations in time at a driving depth of $L_{\mathrm{p}} = 14$ m for the periodic force, and the case of PC and NF, respectively. The blue-red scale shows the fluid pressure in Pa and the yellow-purple scale the vertical soil velocity in mm s^{-1}.

Figure 5.8 shows fluid pressure and vertical soil velocity excited with the periodic force for the PC and NF cases. The pressure fields significantly differ from those shown in Fig. 5.6. The body waves at 150 Hz are not observed as strongly in the PC case compared to the proposed method. The NF case shows a wavefield with wavelengths similar to those of the proposed method, though the amplitude of the pressure waves is reduced, and no seabed vibrations are observed. The NF case underestimates the pressure around the seabed and the seabed vibrations. This is the consequence of neglecting all frictional soil forces.

On the contrary, the Scholte interface waves govern the pressure field in the PC case, carrying energy along the seabed-water interface. This is easily observed since the wavelength in soil and fluid matches the wavelength of the Scholte wave at the driving frequency. In the PC case, the vertical velocity of the soil is significantly larger than in other cases; thus, it can be concluded that the PC case overestimates the amplitude of the Scholte wave when the pile and soil are in the sliding mode, which is expected due to the perfect contact of the soil with the pile (Molenkamp et al., 2023b). This conclusion does not hold when the pile and soil are in sticking mode, i.e., no slip.

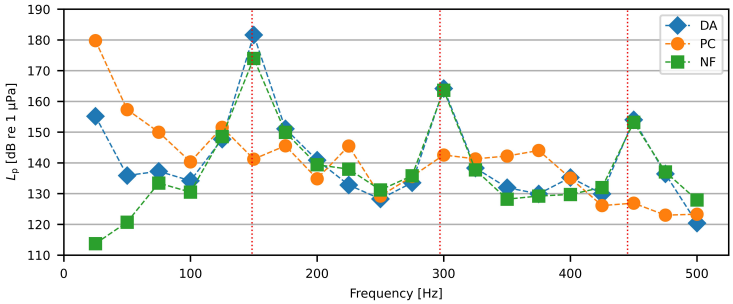


Figure 5.9: Sound pressure levels for the three cases at $r = 50$ m and $z = 7$ m and for a driving depth $L_p = 14$ m.

Figure 5.9 presents the sound pressure levels of the three cases half a meter above the seabed. Except at the low frequencies, the DA case's sound pressure levels show a similar trend to the NF case. However, sound pressure levels deviate by several decibels at some frequencies. Depending on the phase between the superharmonics of the periodic force and the frictional response, friction can dampen or amplify the pile and soil vibrations and, consequently, the fluid pressure levels.

At 150 Hz, the DA case predicts ~ seven dB more than the NF case. Since decibels represent the pressure on a logarithmic scale, fluid pressures and pile vibrations are of different magnitudes. This can only be explained by the friction, which acts as a source at this frequency, exciting the pile vibrations instead of dampening them. This phenomenon is universal and was observed at varying driving depths and excitation frequencies in more cases. The system is susceptible to the dynamic interaction of the components. This observation is consistent with Coulomb friction responding to the sign of the relative pile-soil

velocity; thus, the friction changes sign based on the dominant frequency, i.e. the primary driving frequency. Additionally, due to its non-linear characteristics, Coulomb friction distributes energy from the driving frequency to higher harmonics. Consequently, the primary damping mechanism of the pile vibrations at all frequencies except the primary driving frequency is in the radial direction, as in the NF case. The damping obtained is relatively low compared to the PC case, while the radial vibrations of the pile are much smaller in magnitude than the vertical vibrations.

On the other hand, the DA case shows the frequency contribution of the Scholte wave at the 25 Hz that is missing in the NF case, but the effect of the Scholte wave is reduced compared to the PC case. Combining a driveability model with a noise prediction analysis provides results that reasonably close the gap between the two extreme models. Still, an indication of the system resonances at higher harmonics might be possible based on the case of no friction, and an upper bound of the Schotle wave can be deduced from the PC case. It should be considered that the presented case assumes only the state of continuous smooth driving, i.e. no refusal.

5.3.4. Sensitivity to the driving frequency

The previous analysis clearly shows that the emitted noise field amplifies around the system's resonant frequencies, which, in the case of loose pile-soil coupling along the vertical coordinate, are close to the natural frequencies of the in-vacuo pile. In the examined case, the superharmonics of the periodic force trigger these resonant frequencies. In practice, the driving frequency is adjustable and, thus, an important instrument in reducing noise emissions. This section reduces the primary driving frequency, f_0, from 25 to 23 Hz. The Fourier coefficients c_n do not alter; thus, the force amplitude remains unchanged. First, the effect on driveability must be examined to justify that the change in frequency does not affect driveability. Figure 5.10 shows comparable penetration rates for driving at these frequencies, which justifies further the detailed acoustic analysis.

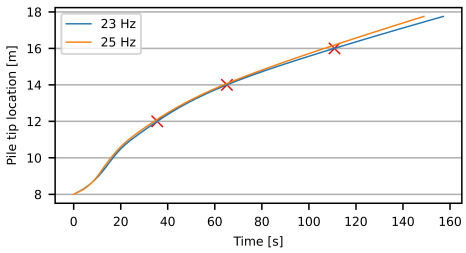


Figure 5.10: Pile penetration versus time at 23 and 25 Hz. The red crosses indicate the driving depths at which the noise emission is evaluated.

The sound pressure levels in the frequency domain vary greatly in both cases, as shown in Fig. 5.11. The peak in the spectrum of the pressure field at 150 Hz has reduced significantly

with the slight reduction of the driving frequency at 23 Hz because the superharmonics are further away from the resonant frequency. The neighbouring superharmonics at 138 and 161 Hz do not resonate as in the case of driving at 25 Hz. The noise radiation around the second and third natural frequencies of the pile is of more comparable amplitude for the two cases. Last, the amplitude of the Scholte wave seems unaffected since equivalent sound pressure levels are predicted at the driving frequency.

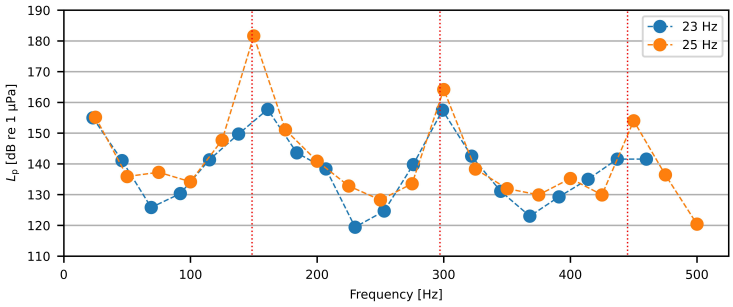


Figure 5.11: Comparison of sound pressure levels at $r = 50$ m and $z = 7$ m.

Another widely used indicator of the emitted noise is the Sound Exposure Level (SEL). The SELs are found by time-integration of the squared sound pressure (ISO, 2017a):

$$L_E = 10\log_{10}\left(\frac{E_p}{E_{ref}}\right), \quad E_p = \int_{t_1}^{t_2} p^2 \mathrm{d}t \tag{5.25}$$

with the reference value for the underwater sound pressure $E_{ref} = 1\ \mu\text{Pa}^2\text{s}$.

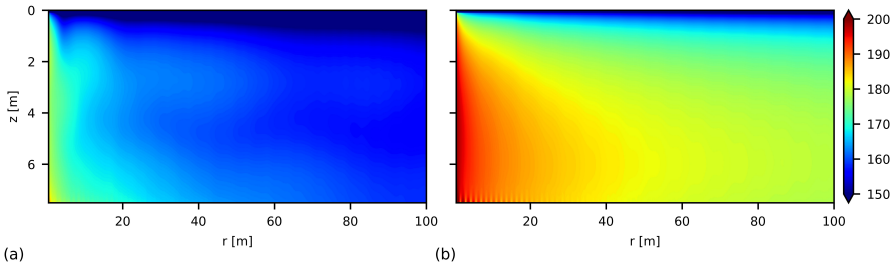


Figure 5.12: (a) and (b) show the SELs, driving with a primary driving frequency of 23 and 25 Hz, respectively, at 14 m driving depth. SELs are given in dB re 1 µPa.

Figure 5.12 shows significant differences in the SELs between the two cases of different driving frequencies. The SELs differ as much as 20 dB at $r = 100$ m due to the reduced noise emission around 150 Hz. Next to the amplitude, the spatial distribution of the noise also differs. In Fig. 5.12a, it is observed that the acoustic field is excited by the second in-vacuo mode of the pile. This pile mode has zero radial displacements at the centre of the

Table 5.2: Parameters for the large diameter monopile case study (Peng et al., 2021b)

Parameter		unit	Parameter		unit
Sea surface depth [z_1]	0	m	Fluid wave speed [c_f]	1500	ms^{-1}
Seabed depth [z_2]	40	m	Fluid density [ρ_f]	1000	kgm^{-3}
Pile length [L_p]	76.9	m	Compression wave speed soil [c_L]	1979	ms^{-1}
Pile thickness [t_p]	9	cm	Shear wave speed soil [c_T]	349	ms^{-1}
Pile radius [r_p]	4	m	Soil density [ρ_s]	1950	kgm^{-3}
Pile Poissons ratio [ν_p]	0.30	-	Compressional wave attenuation [α_L]	0.27	dB/λ
Pile Youngs modulus [E_p]	210	GPa	Shear wave attenuation [α_T]	1.09	dB/λ
Pile density [ρ_p]	7850	kgm^{-3}	Cone tip resistance [q_c]	18	MPa
Structural damping [η_p]	0.001	-			

pile. This corresponds to a driving depth of 14 m with a depth of 5.3 m. Both at the pile's surface and further away from it, the noise levels are significantly lower at this particular depth. Figures 5.11 and 5.12 confirm that the noise levels are sensitive to excitation around the resonant frequency of the immersed structure. This noise reduction mechanism at the source shows high potential in vibratory installation but requires a combined study to optimise pile driveability and noise emission. None of the existing linear models can predict this complex behaviour to optimise the installation both from a driveability and noise emission perspective.

5.4. Underwater noise field of a large-diameter monopile

The trend towards larger monopile foundations for offshore wind turbines is notable. This section delves into the case of an 8-meter diameter monopile installed through impact piling in the German North Sea, as detailed by (Peng et al., 2021b). The hypothetical scenario is investigated in which a vibratory installation tool drives the same foundation pile into the soil. This section contains an analysis that compares sound levels with limit case elastic models, evaluates the influence of driving depth on sound emission, and explores the sensitivity of sound emission to a shift in primary driving frequency. The relevant geometric and material properties are outlined in Table 5.2. Two cases considered run with a periodic force atop the large-diameter monopile with a primary driving frequency of $f_0 = 23$ and 25 Hz. The spectral distribution of the force amplitude is the same as in the small diameter case. The amplitudes are increased by 30 to ensure a continuous and sensible penetration rate of approximately three cms^{-1}, illustrated in Fig. 5.13.

5.4.1. Comparison with limit cases

Figure 5.14 compares the sound pressure levels 5 m above the seabed at 50 m radius for the cases of DA, PC and NF. Besides the sound pressure levels, vertical red dashed lines indicate the pile's first five axisymmetric in-vacuo eigenfrequencies, and the blue dotted line indicates the ring frequency. The first few in-vacuo eigenfrequencies of the large-diameter

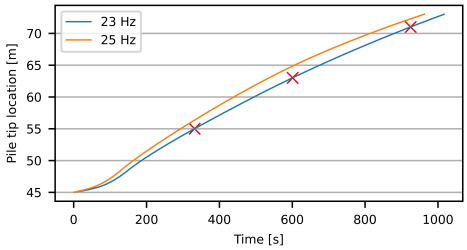


Figure 5.13: Penetration of large-diameter monopile versus time with driving frequencies $f_0 = 23$ and 25 Hz. The red crosses indicate driving depths at which the noise emission is evaluated.

monopile are notably lower than those of smaller-diameter piles, approaching the primary driving frequency. Consequently, tuning the driving frequency to avoid interference with the sensitive frequency response of the coupled system becomes quite challenging. The graphical representation underscores the interference of the second superharmonic at 69 Hz with the second resonance frequency of the in-vacuo pile (67 Hz), resulting in amplified sound levels. This resonance behaviour aligns with observations in the smaller-diameter pile scenario, where resonant frequencies minimally deviate from the eigenfrequencies of the in-vacuo pile. A similar, though less pronounced, interference is evident at 145 Hz. On the contrary, the monolithic connection makes all resonances less prominent in the PC case.

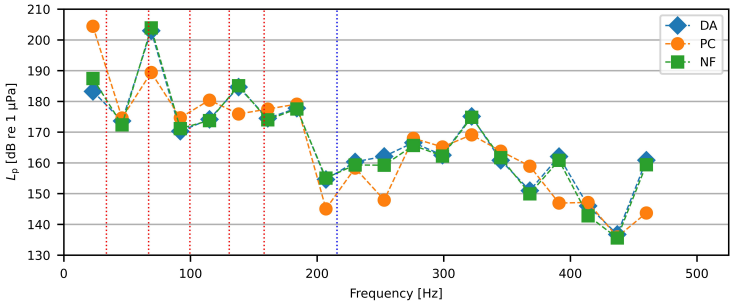


Figure 5.14: Sound pressure levels compared to the cases of perfect contact and no friction at $f_0 = 23$ Hz, $r = 50$ m, $z = 35$ m and $L_p = 63$ m. Vertical red dotted lines indicate the first 5 in-vacuo eigenfrequencies of the pile, and the blue dotted line indicates the ring frequency.

The modal density is highest around the ring frequency at 216 Hz. However, waves excited around this frequency do not typically generate noise because the energy barely propagates through the pile due to the low vertical group velocity. An exception exists when the top of the pile is submerged. This observation persists across all three cases presented in Fig. 5.14.

Similar to the small-diameter pile scenario, the NF approximation exhibits analogous trends to the proposed method across frequencies, except at the driving frequency. Differ-

ences in sound pressure levels between NF and DA cases are minor, suggesting diminished prominence of friction-induced vibrations relative to excitation by the energy introduced in the superharmonics by the hammer. At the driving frequency, PC and NF approximations exhibit discrepancies in sound levels compared to the DA case, attributed to monolithic coupling and strong excitation of surface waves along the seabed in the PC case and the lack of frictional forces in the NF case.

5.4.2. Effect of driving depth

Several factors influence the dynamic response and sound levels as the driving depth increases. These include added mass, damping, and stiffness due to soil and fluid in the radial direction, frictional pile-soil resistance, friction degradation, and the location with modal nodes with no radial displacements. Consequently, predicting the influence of driving depth on dynamic response and sound levels necessitates detailed analysis.

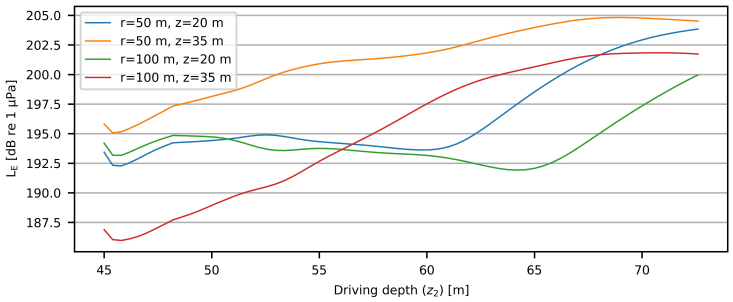


Figure 5.15: SELs during driving with a driving force of 23 Hz at four observation points in the fluid.

Figure 5.15 illustrates substantial SEL variations based on driving depth. Changes in SEL exhibit distinct patterns depending on the observer's location. Notably, an increase in SEL is observed after 60 meters of driving when the observer point is halfway through the fluid column. At the same time, a gradual increase with a slight decrease upon reaching full penetration is evident just above the seabed. These trends contrast the decreasing sound levels with driving depth observed in small-diameter monopiles.

The snapshots in time presented in Fig. 5.16 offer insight into the fluid pressure and SEL changing in the entire fluid column. The dominance of the second flexural mode of the pile in noise generation is evident. The second in-vacuo pile mode has a node in the middle of the pile, located at $z = 16.55$, 24.55 and 32.55 m for the three considered driving depths, respectively. At the node, the mode has no radial displacement. These depths are visually identified in the pressure field since pressures here are significantly lower. Also, the SELs presented in Fig. 5.16b, clearly indicate the locations of the modal node. At almost complete penetration, the place where radial deformations of the second mode are maximal, i.e. a

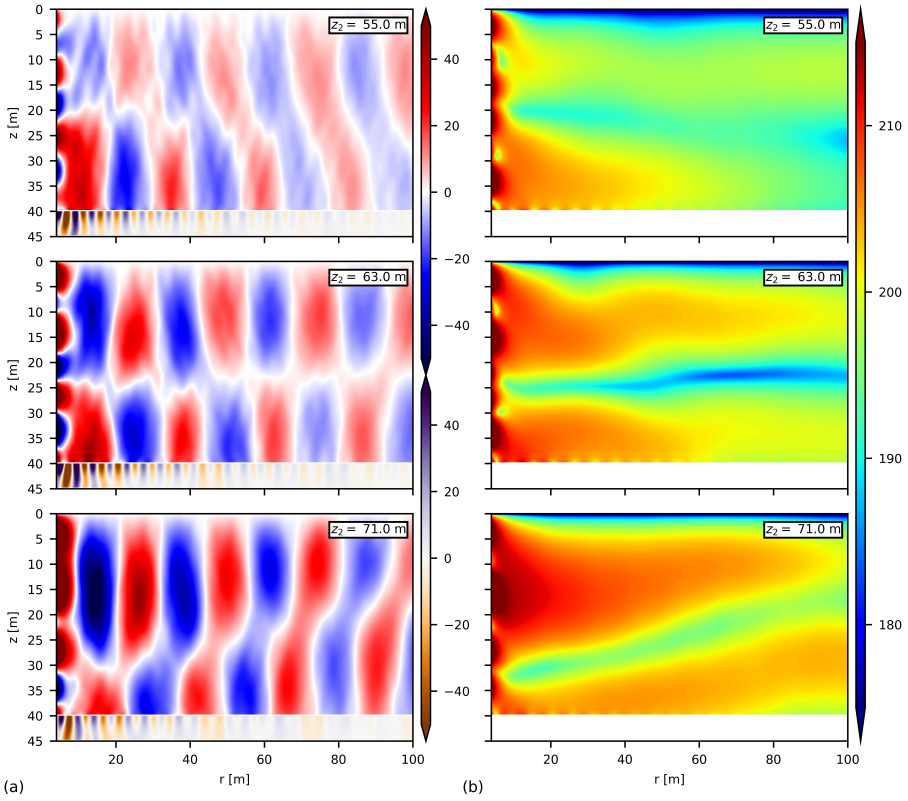


Figure 5.16: (a) Snapshots in time of the pressure levels and vertical seabed velocity at three driving depths, in kPa and mm s^{-1}, respectively and (b) the SELs in dB re 1 µPa.

quarter of a pile length, is in the middle of the fluid column, leading to the highest noise levels in the field.

Additionally, waves with shorter wavelengths near the pile surface are observed, belonging to the evanescent field, which does not propagate radially. It should be noted that sound levels do not depend solely on the generated pressure field but also on the energy that can propagate away from the pile surface. Finally, Scholte waves are generated at the primary driving frequency but have a negligible impact on the SELs, except for positions on the seabed surface or at a short distance from the pile's surface. The frequency of the Scholte wave is identified by its wavelength of about 14 m, examining the vertical soil velocity. Based on the above observations, a singular noise prediction based on a single driving depth is deemed inadequate for determining the highest expected sound levels during vibratory pile driving installations.

5.4.3. Sensitivity to driving frequency

Slight deviations in the excitation frequency of the hammer significantly influence the spectral noise levels for the large-diameter monopile, shown in Fig. 5.17, akin to the scenario with the small-diameter pile. Interference between the superharmonics at 25 Hz and higher harmonics of the pile occurs. However, amplification of sound levels is not observed, i.e. the sound levels show no resonance around the second in-vacuo frequency of the pile when driving at 25 Hz. Multiple attributes contribute to the presence of resonance, e.g., the location of the pile nodes, resonance frequencies being shifted or eliminated due to added mass, damping or stiffness of fluid and soil, and sound not propagating because evanescent modes instead of propagating modes are excited. Kaynia et al. (2022) have reported similar observations in vibro-driving of monopiles, where strong frequency-dependence of dynamic stiffness was associated with the dynamic behaviour of the inner soil column. The complex and non-linear nature of the system suggests that a detailed analysis is imperative to incorporate sensitivity to driving frequencies in noise predictions.

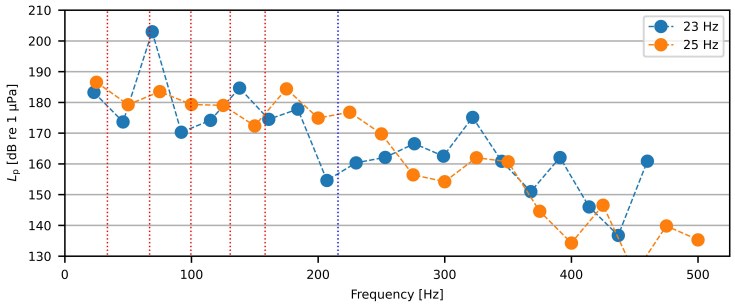


Figure 5.17: Sound pressure levels driving at 23 and 25 Hz at $r = 50$ m, $z = 35$ m and $L_p = 63$ m. Vertical red dotted lines indicate the first five in-vacuo eigenfrequencies of the pile, and the blue dotted line indicates the ring frequency.

5.5. Conclusions

The chapter introduces a novel methodology for underwater noise predictions during vibratory pile driving. A non-linear driveability model is used to obtain realistic interface friction forces as input for a noise prediction model. The chapter demonstrates the importance of incorporating a driveability analysis, finding significant differences from traditional models that assume perfect contact between the pile and soil. The author contends that the proposed model yields more realistic results under the assumption of smooth driving without refusal compared to traditional linear models that assume perfect contact used in impact piling. The results show a clear deviation in pressure levels and seabed vibrations between the linear and presented methods at the driving frequency and superharmonics. A few significant findings are discussed below:

- The primary source of noise generation is the radial vibrations of the pile. These are amplified around the resonant frequencies of the coupled system, which are close to the in-vacuo frequencies of the pile when loosely coupled. The coexistence of the resonant frequencies and superharmonics of the force can amplify the sound pressure levels. Thus, even a small shift in driving frequency can significantly decrease the noise generated, a promising finding from a practical perspective.
- The noise field is found to be highly sensitive to the change in the system dynamics during penetration of both small and large monopiles. The driving depth of the pile significantly affects the dynamic response as various conditions alter during driving. Based on the cases presented, the critical driving depth is unclear. Therefore, noise predictions are advised throughout the driving process in vibratory pile driving.
- The Coulomb friction responds mainly to the driving frequency and shifts energy to higher harmonics. Depending on the phase, this can either excite or dampen the pile vibrations. A reasonable first approximation of the noise field is obtained by assuming no friction between the pile and soil. However, seabed vibrations cannot be predicted through the no-friction assumption, and pile vibrations may be inaccurate in certain soil configurations.
- Noise predictions during vibro-driving are heavily influenced by the superharmonics generated by the hammer. These superharmonics, resulting from the periodic signal of the hammer, appear to have greater significance than vibrations induced by friction. However, several factors influence the force exerted by the vibro hammer, including driving frequency, hammer type, pile size, soil characteristics, pile-hammer connection, and line load. The amount of energy in the superharmonics will significantly affect the predicted noise levels. Therefore, future research incorporating extensive experimental data is necessary to establish generalised conclusions.
- Efforts to optimise the vibro hammer to minimise the generation of superharmonics can positively reduce noise levels. However, even with single-harmonic excitation, the friction causes energy to shift towards higher harmonics. Acknowledging that friction forces are highly non-linear is essential. Consequently, friction forces do not scale linearly with excitation or frequency shifts, resulting in changing underwater noise levels that are difficult to predict without detailed analysis.

We conclude that the dynamic interaction between all components in the system plays a crucial role in predicting underwater noise levels during vibratory pile driving. The system is primarily sensitive to the driving frequency and its superharmonics, which may strongly interfere with the system's resonant frequencies. Hence, a detailed analysis, including an accurate description of the pile-soil interface, is essential to accurately predicting the underwater noise field and seabed vibrations.

6

Sound generated during gentle driving of piles

To reduce sound levels during vibratory driving, Gentle Driving of Piles (GDP) is introduced as a promising alternative driving method. This chapter briefly describes the experimental campaign within the GDP project. The experimental findings demonstrate that GDP is more efficient than traditional Vibratory Hammer (VH) installation methods. Specifically, the vertical vibrations in GDP have smaller amplitudes than traditional VH driven piles. This efficiency is achieved because the torsional component reduces vertical frictional resistance. Based on the analysis of pile vibrations and excitation forces measured during the GDP campaign, a hypothetical scenario is considered, and the respective sound fields are analysed. The forcing functions are derived from measured pile vibrations and accelerations obtained during the experimental campaign. Noise predictions indicate that the GDP technique shows promise in reducing sound emissions. However, resonance at higher harmonics poses a risk due to the increased number of superharmonics excited by the two driving frequencies in GDP.

The section on the experimental campaign in this chapter strongly corresponds to the work published in Ocean Engineering, Volume 270, April 2022, Tsetas et al. (2023a) and the work that will be published in the Proceedings of the 30th International Congress on Sound and Vibration, July 2024, Molenkamp and Tsouvalas (2024b, July).

6.1. Introduction

The GDP 1.0 project attempts to develop and showcase the advantages of an innovative vibratory pile installation technique that relies on the simultaneous application of vibratory loads in both the vertical and torsional directions. The first version of the GDP installation tool used in the experimental campaign has been designed to exert both low-frequency and high-frequency vibrations applied in the vertical and torsional directions, respectively, intending to reduce the driving loads and sound generated during installation. The term "gentle" stems from the anticipated ability to reduce the sound emission generated during installation while delivering a smooth installation performance. The overarching objective is to develop the GDP technique, not to compromise the crucial aspects of pile penetration speed and soil-bearing capacity, which are indispensable for the stable operation of offshore wind turbines. The GDP shaker used during the experimental campaign is shown in Fig. 6.1.



Figure 6.1: Photograph of the GDP shaker on top of a driven monopile during the GDP experimental campaign.

The experimental campaign consisted of two distinct phases. In the first phase, piles were installed, and in the subsequent phase, the lateral bearing capacity of the piles was examined. Throughout the process, a comprehensive array of measurements was employed to gather data on various parameters related to the pile and soil vibrations during the installation process and their post-installation behaviour. A detailed account of the experimental setup and the collected data during installation can be found in Tsetas et al. (2023a). Furthermore, Kementzetzidis et al. (2023) discusses the results obtained from the post-installation lateral load experiments.

This section provides a brief overview of the experimental campaign conducted, noise predictions with the GDP method, and a scientific justification of assumptions necessary to do so. These assumptions are based on the conclusions drawn in the preceding chapters (Molenkamp et al., 2023b). Based on the experimental findings, two hypothetical scenarios compare the sound predictions in GDP with those of monopiles driven with traditional VH tools.

6.2. Experimental campaign

The GDP shaker generates low-frequency axial and high-frequency torsional motions at the pile head. A novel GDP shaker was specifically designed and constructed to facilitate GDP-driving tests. Figure 6.1 shows the shaker, consisting of three interconnected gear trains linked directly to counter-rotating masses with a fixed eccentricity. These masses are housed within exciter blocks, securely fastened to a support structure. Initially, the GDP shaker was powered by hydraulic motors and connected to each test pile using a bolted flange connection. This initial solution was implemented as a preliminary measure for the GDP.

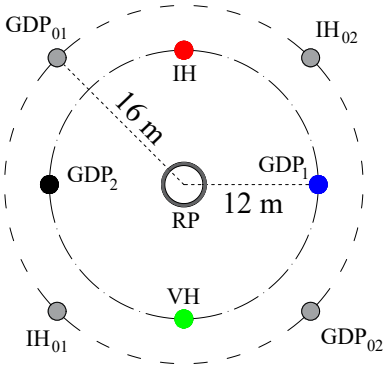


Figure 6.2: Schematization of the installed piles during the GDP experimental campaign.

In this study, a total of eight test piles were installed in the vicinity of a larger Reaction Pile (RP). The RP was designated explicitly for post-installation loading tests, as outlined in the accompanying publication by Kementzetzidis et al. (2023). All the piles shared a uniform specification, measuring 10 m long and 0.762 m in diameter. The embedded length was 8 m, i.e. 2 m less than the length of the piles.

Four piles were identified as the Main Test Piles (MTPs) and were extensively instrumented. These MTPs were strategically positioned at a radial distance of 12 m from the RP. On the other hand, the remaining four piles called Auxiliary Test Piles (ATPs), were installed without instrumentation for initial testing purposes. The ATPs were positioned at a greater distance of 16 m from the RP (Fig. 6.2). The four MTPs were subjected to different driving

forces during installation: Impact Hammer (IH), axial VH, and GDP, as shown in Fig. 6.2. The Hydrohammer S-90 and the Vibro-hammer CV-25 were utilised for the IH and VH piles, respectively, representing the standard driving methods.

6.2.1. Observations during pile installation

Figure 6.3 presents the penetration time series for the VH and two GDP piles. The solid lines represent the displacement measured by the potentiometer for GDP_1 and VH, while data for GDP_2 is unavailable due to sensor failure. Markers in the figure represent the Driving Logging (DL) system measurements, which record displacement values every 25 cm of penetration. The average penetration rates determined from the DL system are 20.9 $mm\,s^{-1}$ for VH, 37.1 $mm\,s^{-1}$ for GDP_1, and 18.7 $mm\,s^{-1}$ for GDP_2. The potentiometer data shows slightly lower average rates of 19.8 $mm\,s^{-1}$ for VH and 34.3 $mm\,s^{-1}$ for GDP_1. However, these values are considered overly close to the one measured by the DL system for practical purposes.

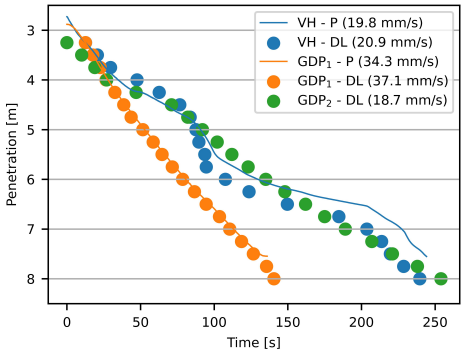


Figure 6.3: Pile penetration rates for piles installed with VH and GDP (Tsetas et al., 2023a).

GDP_1 had a shorter installation time and higher penetration rate than VH and GDP_2. This difference in rate is attributed to the lower cone resistance and relative density of the soil at the location of GDP_1. Although VH was installed in even softer soil, GDP_1 penetrated at almost double the average rate. GDP_2, driven into the stiffest soil among the test locations, had a similar penetration rate to VH. Based on the potentiometer, GDP_1's penetration rate remained relatively constant during installation. In contrast, VH exhibited more abrupt changes in the penetration speed, likely influenced by the transition from unsaturated to saturated soil. Notably, no refusal occurred while driving in all cases, as indicated by the steady penetration rates in Fig. 6.3. Additionally, the GDP shaker demonstrated during the installation of one of the ATPs without instrumentation that it could drive and remove the pile solely with torsional excitation, thereby increasing its potential to prevent noise generation.

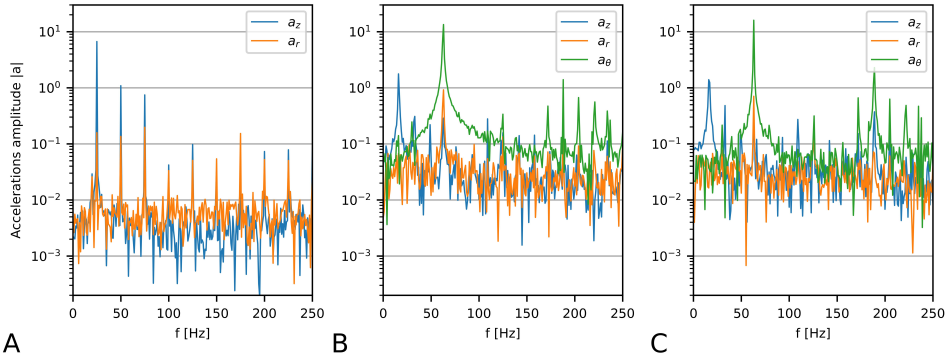


Figure 6.4: Radial, torsional and vertical measured acceleration on top of the pile for (A) the Vibro hammer-driven pile and (B) and (C) the GDP-driven piles.

The acceleration spectra of the piles, obtained at the top of the pile during driving, provide valuable information about the dynamic response of the pile. These spectra involve acceleration measurements in the radial, vertical, and circumferential directions on two diametrically opposite sides of the pile. The amplitude spectra of the recorded accelerations are illustrated in Fig. 6.4, denoted as $|a_z|$ (vertical), $|a_r|$ (radial), and $|a_\theta|$ (circumferential).

The driving frequency of the axial vibratory hammer was 22-25 Hz, while the GDP shaker in the axial direction exhibited a frequency of 16 Hz. These frequencies correspond to prominent peaks in Fig. 6.4, indicated by the blue lines. In addition to these primary amplitude peaks, which directly correspond to the primary driving frequencies, the pile response amplifies at multiple superharmonics, i.e., multiples of the driving frequency.

The energy distribution in these superharmonics can be explained as follows. Firstly, the shaker excites the system at various superharmonics due to minor imperfections in the rotation of the eccentric masses. Secondly, due to the frictional interaction between the pile and surrounding soil, the system's dynamic response is inherently nonlinear, even at low vibration amplitudes. This nonlinearity can further amplify the energy distributed in the superharmonics. The quantitative contribution of each mechanism to the superharmonics energy content has not yet been determined. However, it is believed that the excitation by the shaker is the primary cause.

In addition to the frequencies excited by the axial component, the GDP spectra also reveal vibrations caused by the torsional excitation induced by the GDP shaker. The circumferential acceleration spectra exhibit distinct peaks at the primary torsional driving frequency of approximately 63 Hz. Furthermore, peaks at about 125 Hz and 188 Hz correspond to the first and second superharmonics associated with the circumferential excitation. In the acceleration spectra of the GDP piles, two additional significant peaks are observed slightly lower and higher than the 188 Hz peak, predominantly in the torsional and vertical directions. These peaks are likely due to the coupling of the vertical and torsional excita-

tions. By comparing the spectra in Fig. 6.4A and Fig. 6.4B, it is evident that the acceleration response is fairly similar despite moderately different soil conditions. This finding indicates a strong dependence on the GDP hammer excitation.

6.3. Underwater sound predictions

The test campaign reveals numerous uncertainties affecting sound predictions during driving with GDP. As the installation tool is still under development, the forcing signal of both hammer excitations may not accurately represent future designs. This chapter aims to predict the expected noise levels produced using GDP 1.0 during the experimental campaign and compare them with the predictions from the traditional VH under specific assumptions. The comparison is based on the presented experimental campaign and the collected measurements. It's important to note that generalizing or extrapolating quantitative conclusions from this comparison is impossible. However, qualitative statements can still be made.

Initially, perfect cylindrical symmetry is assumed. It is assumed that the coupling between torsional and vertical excitation is retained via the prescribed force on top of the pile based on the acceleration and strain measurements. The assumption implies that the axisymmetric torsional vibrations of the pile only generate horizontally polarised shear waves in the soil while emitting no waves in the fluid medium. Since the soil waves lack a vertical component, they do not propagate sound to the fluid, theoretically resulting in no sound emission caused by torsional excitation, except for frictional coupling, which is discussed later.

Chapter 3 demonstrates that non-symmetries in the first circumferential mode do not significantly impact the sound levels in impact piling. However, driving with GDP might be more sensitive to non-symmetries due to the substantial amplitude of torsional vibrations shown in Fig. 6.4B and C, which might emit sound via non-symmetric modes. Although circumferential variation is not thoroughly measured, more evidence is required to support assumptions other than cylindrical symmetry.

Next, the pile and soil interaction plays a crucial role in sound predictions for vibratory devices, as demonstrated by Molenkamp et al., 2023b and in Chapter 5. This chapter examines two extreme cases of pile-soil interaction: a scenario with No Friction (NF) and another with Perfect Contact (PC) between the pile and the soil. Both pile-soil interface descriptions have their limitations but can serve as extreme cases. The NF case is presumably the most representative, while the relative velocity vector between pile and soil will have a component that is predominantly along the horizontal direction. This results in reduced frictional resistance in the vertical direction.

On the other hand, excitation of the vertical vibrations of the pile by friction forces at the torsional excitation frequency can occur due to the change in the effective friction angle. It is argued that the excitation of vertical pile vibration by friction is partly reflected in the measurements and thus accounted for indirectly. This assumption simplifies the GDP sound prediction model to be equivalent to the VH sound prediction model, introducing

the differences via the forcing on top of the pile. The subsequent subsections will discuss the examined case study and compare the sound predictions for VH and GDP based on the PC and NF interface condition assumptions.

6.3.1. Case study

The case study considers a small diameter pile. It has a diameter of 0.762 m and a length of 17.4 m driven into the sediment. The water depth is 10 m, respectively. This case study aligns with the case study in Chapter 5. The dimensions described in Table 5.1 are used to illustrate the differences in sound generation during pile driving with VH and GDP. The case studied contains an elongated pile configuration related to the presented experimental campaign. The vertical forces applied atop the pile for both hammer types are deduced from empirical data and showcased in Fig. 6.5. The assumption of cylindrical symmetry leads to the omission of the rotational force component; nevertheless, its influence on vertical excitation is indirectly incorporated through the recorded vertical forces. It is crucial to emphasize the disparity in primary vertical driving frequencies between the GDP and VH. The vertical hammer in the GDP tool operates at 16 Hz, whereas the VH functions at a higher frequency of 25 Hz. This difference critically influences the superharmonic frequencies excited by each driving tool and, thereby, the generated sound field.

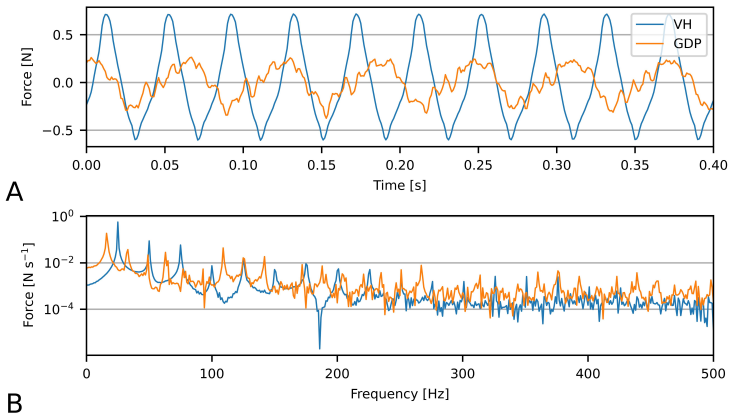


Figure 6.5: Time signal (A) and spectrum (B) of the representative forcing on top of the pile exited by the traditional VH and GDP.

As illustrated in Fig. 6.5A, the vertical force induced by the GDP hammer has a smaller amplitude compared to the excitation from the VH. Despite this, the signal remains significant due to the strong coupling of vertical and torsional vibrations within the shaker itself. This coupling is expected to be significantly reduced in the second generation of GDP shakers. The time signal of the vertical force induced by the GDP hammer is dominated by two frequencies, one being the primary frequency of the torsional excitation and the other

coming directly from the vertical shaker of the GDP hammer, at respectively 63 and 16 Hz. The VH signal is periodic at 25 Hz, though it is not perfectly sinusoidal.

The periodicity of the forcing signals is clearly seen in Fig. 6.5B, where peaks are shown at the driving frequencies and their multiples. The VH forcing has a significantly higher amplitude at the primary driving frequency, but the force induced by GDP exhibits more peaks of relatively high amplitude within the frequency range of interest than the forces generated by VH. The additional peaks in the GDP spectra are mainly due to the lower primary driving frequency used during the experimental campaign. The difference in primary driving frequencies between VH and GDP complicates the quantitative comparison of noise levels between the two installation tools. Additionally, the choice of the primary driving frequency, which is not tool-specific, significantly influences sound generation.

6.3.2. Perfect contact between pile and soil

This section explains the differences in expected sound emissions between VH and GDP assuming PC between the pile and the soil. The conventional modelling of PC between the pile and the soil is prevalent in impact pile driving models. However, despite the indications that PC might not precisely forecast the sound generated for vibratory devices as in Chapters 4 and 5, the absence of empirical data necessitates exploring limiting scenarios.

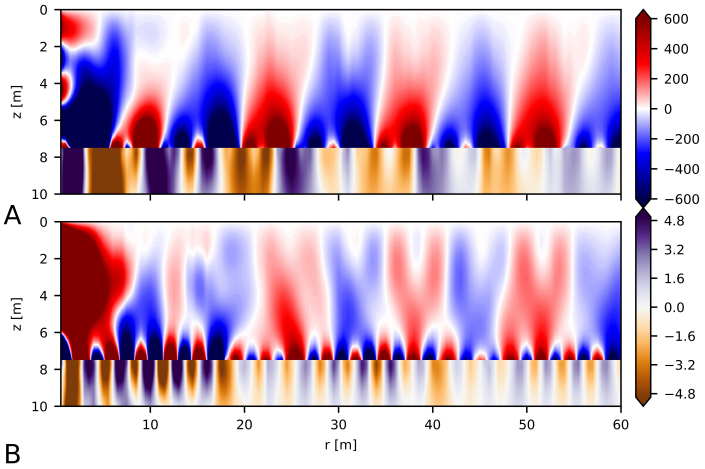


Figure 6.6: Snapshot of fluid pressure [Pa] and vertical soil velocity [mm s^{-1}] induced by VH (A) and GDP (B) hammer under PC assumption.

Figure 6.6 presents a snapshot of the wavefield induced in both media, i.e. the sound pressure in the seawater and the vertical soil vibrations in the seabed. Upon initial examination, the fluid pressure exhibits comparable amplitudes except above the seabed, where the VH produces Scholte waves of greater magnitude that dominate the wave field near the seabed-water interface. The seabed vibrations substantiate this observation, manifesting

waves of greater amplitude and wavelength correlated with Scholte waves excited at a lower frequency. In the case of GDP, Scholte waves of shorter wavelength and smaller influence zones in the fluid medium are observed due to the shorter wavelength and smaller force amplitude at the primary driving frequency.

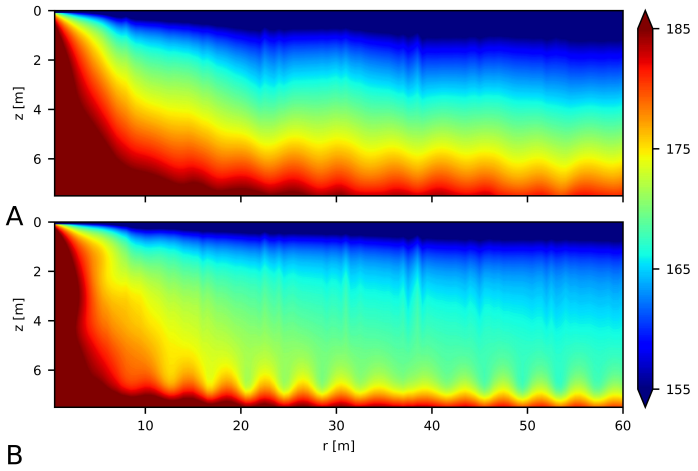


Figure 6.7: Sound exposure levels in dB integrated over 1 second due to VH (A) and GDP (B) hammering under PC assumption.

The sound exposure levels in Fig. 6.7 corroborate the inference in the time-domain plot of Fig. 6.6. The highest sound levels develop just above the seabed due to the propagating Scholte wave along the seabed. In the VH scenario, the influence zone is broader and characterised by higher amplitude. The dominant Scholte wave in the scenario of PC aligns with the observation made in Chapters 4 and 5, where soil excitations are likely amplified due to the underlying pile-soil interface assumption.

The sound pressure levels above the seabed illustrate that the fundamental driving frequency dominates the sound field generated by the VH. In contrast, the highest sound levels in the GDP scenario are evident around 120 Hz. This discrepancy accounts for the variation in wavelengths of the Scholte waves as observed in Fig. 6.6. Once again, the significance of the superharmonics demands emphasis, as those exert considerable influence on the sound field for both hammers.

6.3.3. No friction between pile and soil

All types of vibratory piling involve consistently exerting a force at the top of the pile, causing the pile to vibrate and move relative to the soil continuously, assuming the pile slips and no refusal is met. Past studies have indicated that frictional forces add to the noise produced during this process. However, when the hammer vibrations produce significant superharmonics, it can be reasonably assumed that friction plays a secondary role. This assumption

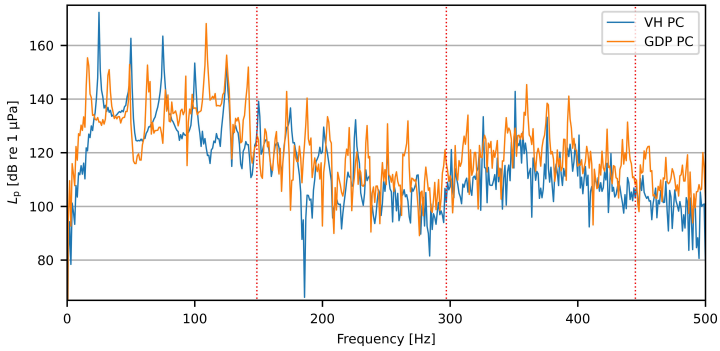


Figure 6.8: Sound pressure levels 0.25 m above the seabed at $r = 60$ m, with the red vertical lines indicating the in-vacuo eigenfrequencies of the pile.

is made under the belief that the hammer vibrations at higher harmonics outweigh the effects of friction as an excitation mechanism for pile vibrations. In the case of GDP, the assumption of NF in the vertical direction seems even more suitable since the friction angle will mainly be governed by the torsional motion instead of the vertical motion, minimalising the contribution in the vertical component of the friction forces, assuming again that the torsional and axial motions are decoupled and the contribution of the torsional component is included in the axial hammer force.

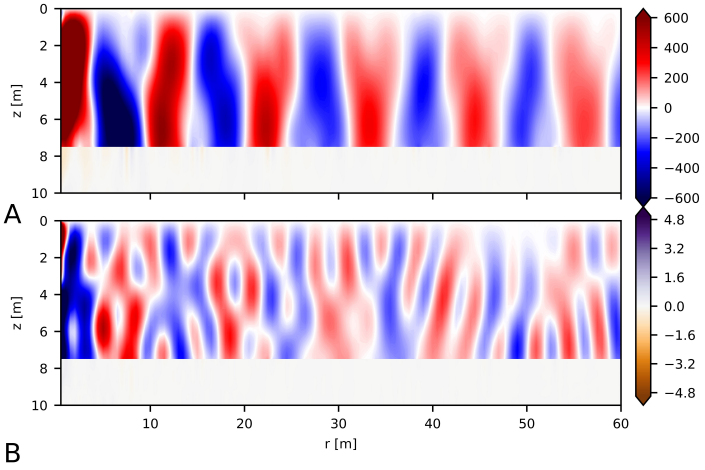


Figure 6.9: Snapshot of fluid pressure [Pa] and vertical soil velocity [mm s^{-1}] induced by VH (A) and GDP (B) hammer under NF assumption.

Figure 6.9 presents a snapshot of the generated sound field and soil vibrations while assuming the absence of frictional forces. It becomes immediately apparent that the two

sound profiles significantly differ, and both cases exhibit minimal soil vibrations. The lack of soil wave propagation is inherent to the frictionless assumption, where soil perturbations originate solely from the pile's radial deformation. This likely results in underestimating the soil vibrations since shear waves and Scholte interface waves are not excited due to the NF assumption.

The pressure field produced by the VH hammer is primarily governed by a wave that extends across the fluid column. In contrast, the pressure field induced by the GDP hammer comprises numerous waves of shorter wavelengths, manifesting radially and vertically. This differential behaviour indicates distinct pile vibration modes, resulting in dissimilar sound emission compared to the PC scenario.

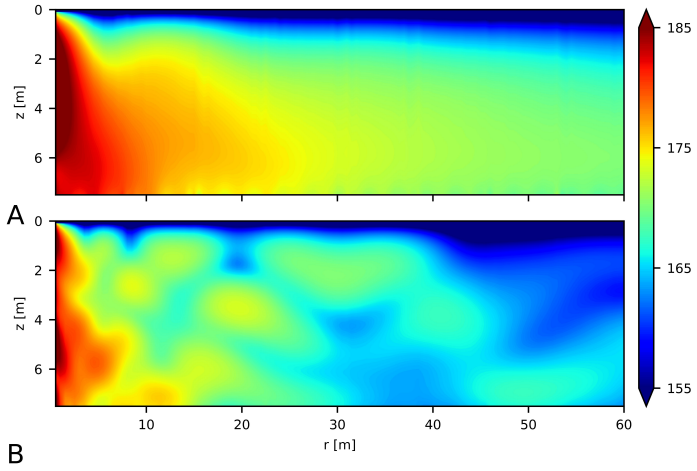


Figure 6.10: Sound exposure levels in dB integrated over 1 second due to VH (A) and GDP (B) hammering under NF assumption.

The corresponding sound exposure levels depicted in Fig. 6.10 exhibit a gradual attenuation throughout the fluid column radially in the case of VH excitation. On the contrary, sound exposure levels associated with GDP excitation reveal a more oscillatory pattern characterised by a superposition of multiple waves. Nevertheless, the sound levels emitted by the GDP hammer are markedly lower than those generated by the VH hammer. Evidently, the amplification of sound levels due to the Scholte wave above the seabed is absent in both cases.

Figure 6.11 presents the sound pressure levels, shedding light on the origins of the pressure fields. The sound pressure levels highlight the peak pressures around the in-vacuo eigenfrequencies of the pile, suggesting minimal shifts from in-vacuo eigenfrequency to resonant frequencies of the immersed pile due to the assumed NF pile-soil interaction. For both forces, the superharmonics of the excitation force aligning with the system's resonant frequencies cause the highest sound levels. Notably, the VH hammer generates substantially

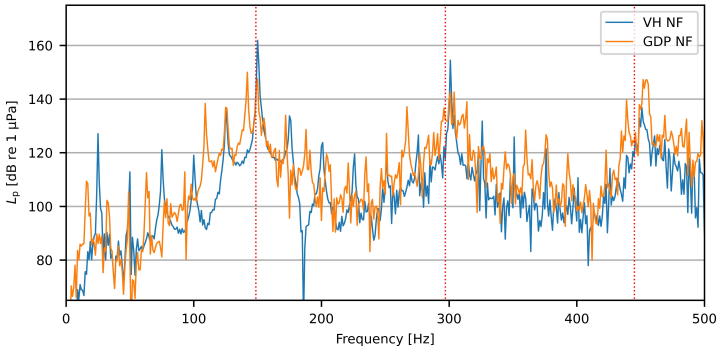


Figure 6.11: Sound pressure levels 0.25 m above the seabed at $r = 60$ m, with the red vertical lines indicating the in-vacuo eigenfrequencies of the pile.

higher sound levels at the first resonant frequency than the subsequent two frequencies. The GDP hammer emits sound at the first three resonant frequencies with comparable amplitudes, contributing to a more frequency-rich sound field.

Once again, Fig. 6.11 emphasises the significance of adequately accounting for superharmonics in the forcing signal. Small shifts in excitation frequency and superharmonics can result in substantial fluctuations in the sound levels. While the GDP hammer excites a more significant number of superharmonics due to its dual excitation and due to the lower primary vertical driving frequency, these are more likely to coincide with resonant frequencies. Moreover, in this case, complex coupling of frequencies is expected between the two driving mechanisms due to the non-linear frictional response and coupling in the hammer. In contrast, the driving frequency and superharmonics of the VH type of installation tools can, from an engineering perspective, be more straightforwardly adjusted and calculated. Furthermore, it has been demonstrated during the experimental campaign that the GDP driving can be accomplished with a much lower vertical excitation force and, ultimately, on an instrumented pile even without it. This means that the complexity and intensity of the GDP-induced sound can be reduced significantly.

6.4. Discussion

This chapter reflects on the potential of GDP as a silent vibratory pile-driving device. Despite the shaker being in its initial design iteration for the experimental campaign and requiring further validation with full-scale experimental data, the presented data and numerical simulations substantiate the envisaged capabilities of the GDP shaker.

The experimental campaign emphasises that the GDP shaker requires significantly reduced vertical force to drive a pile into the soil at a comparable or heightened pace. The reduction in vertical shaker amplitude directly influences sound emissions. However, it may not result in lower sound levels due to excitation at superharmonics. The data shows

that there is a coupling between torsional and vertical driving frequencies. Energy in more frequencies can lead to higher sound emissions, especially in the case of large piles, whereas these piles are more susceptible to low-frequency excitation (Molenkamp et al., 2024a). However, this effect is not observed in the case of small piles.

The significant torsional movement in the GDP shaker is expected to lead to minimal vertical frictional resistance. As a result, the process of driving the pile encounters less resistance in the vertical direction, making it smoother and faster. However, this may also make the pile more susceptible to resonant responses, as the coupling between the pile and its surroundings is limited. Given the dual excitation frequencies of the GDP, there is a potential risk of resonance frequencies causing issues. Decreasing the energy in superharmonics has the potential to reduce sound emissions in all vibratory installation methods, including the GDP. Furthermore, a shift in primary driving frequencies of only a few hertz can significantly alter the generated sound.

In theory, friction couples both torsional and vertical excitation, yielding a multifaceted frictional reaction, engendering various combinations of superharmonics from both excitation forces, contingent on the pile's velocity angle. Although this aspect has not been incorporated in this model, the frictional forces possibly excite pile vibrations at any combination of super- and subharmonics of the excitation frequencies. While the amplitudes are anticipated to be modest, this phenomenon can potentially initiate pile vibrations and consequent sound emissions at hard-to-predict frequencies (Tsetas et al., 2023d).

The Scholte wave predominantly governs the sound emission in the numerical scenario in which pile and soil are monolithically connected, i.e. PC. While acknowledging the non-physical nature of this scenario, this extreme case highlights that GDP is inclined to radiate less energy in the form of the Scholte waves due to the substantially reduced vertical force atop the pile.

Despite various assumptions, the potential of the GDP as a silent vibratory shaker is convincingly substantiated across all modelled scenarios. The fact that the vertical primary driving frequency of the GDP hammer was lower than the VH resulted in more harmonics. However, this is not a characteristic of the GDP hammer but an operational choice. On the other hand, the lower amplitude of the vertical excitation is a consequence of the GDP principle, potentially sound emissions. The additional torsional excitation leads to energy in additional frequencies. However, the coupling is aimed to be reduced in future designs, and due to its higher primary frequency, the number of additional harmonics at which potential noise is emitted is minimal.

Future research must demonstrate the performance of the GDP in offshore environments and at full scale, utilizing a further developed installation tool with the potential to reduce sound further. Addressing or mitigating energy in superharmonics and decoupling vertical and torsional excitations are crucial considerations for the future design of the GDP shaker and traditional VH. The GDP shaker stands out as a highly promising solution for

reducing noise emissions in offshore pile driving, owing to the significantly lower to no vertical excitation required when executed proficiently.

7

Conclusions

This thesis focuses on predicting underwater noise resulting from vibratory pile driving, a promising approach for reducing offshore construction noise. The central theme revolves around enhancing the pile-soil interface description in existing sound prediction models, initially developed for impact pile driving simulations. The thesis presents a progressively detailed physical description of the pile-soil interface.

This thesis's main contribution is understanding underwater sound emissions from vibratory pile driving. Additionally, it addresses the effect of non-symmetric impact forces and pile inclination on underwater noise emissions, which is primarily visible around the pile's ring frequency. The study suggests that unintended non-symmetries are unlikely to significantly affect sound levels, except when specific frequency distributions, significant ring frequency energy, or piles of large radii are of interest.

The dissertation reveals that models developed to predict the sound and vibration fields in the environment surrounding the pile in the case of impact hammering cannot be applied to vibratory pile installation. Accurate noise and vibration predictions necessitate a more tailored description of pile-soil interaction, significantly influencing pile dynamics and energy transfer mechanisms. The study elucidates the main wave generation mechanisms, considering linear and non-linear pile-soil interface conditions. Linear interaction assumes perfect contact, no friction, or complex-valued interface springs in the frequency domain, while non-linear friction forces are included, employing a driveability model.

The model with non-linear friction interface conditions provides the best physical representation of the problem. A critical discovery with this model is the significant amplification of radial pile vibrations near the resonant frequencies of the emerged pile, leading to a noticeable increase in sound levels at the superharmonics of the driving force. The resonance at superharmonics is only weekly influenced by the pile-soil friction for the following

reasons. Coulomb friction is collinear with the relative velocity vector. The primary driving frequency governs the relative velocity; therefore, the friction provides minimal damping and can even amplify pile vibrations at higher harmonics. While other damping mechanisms might prevent this resonant behaviour. Incorporating more complex descriptions of pile-soil interaction, such as liquefaction or advanced friction laws, introduces greater complexity and requires additional input parameters. Therefore, using Coulomb friction to describe pile-soil interaction under vibratory loading remains debatable but offers a rather practical estimate aligned with driveability data, enhancing our understanding of pile-soil interaction in offshore vibratory pile driving. It should be noted that the assumed Coulomb friction satisfies driveability analyses but might not be adequate for sound models in which a good estimation of attenuation at the higher harmonics is required.

Simplifying the pile-soil interaction to a linear interface model may suffice for approximating underwater sound levels. This work considers two limit cases, i.e. no friction and perfect contact between pile and soil in the vertical direction. Assuming perfect contact is deemed invalid since the pile is expected to be in constant motion relative to the soil. This model-limited case overestimates soil vibrations, while pile vibrations exhibit increased damping at higher harmonics. Conversely, assuming no friction underestimates the soil reaction, especially evident at lower frequencies. However, these model predictions that assume no pile-soil frictional interaction align better with the non-linear interface model results at higher harmonics. The argument of modelling no pile-soil friction holds even more for piles driven by the Gentle Driving of Piles method, where torsional motion reduces vertical frictional resistance.

A distributed frequency-dependent complex-valued interface model could represent the dynamic soil reaction for acoustic purposes in the frequency domain. However, accurately predicting the dynamic properties of these interface springs across different soil conditions, pile sizes, and hammer settings requires extensive data. Given the driveability analysis-derived friction forces at hand and a lack of comprehensive data for precise parameter tuning, leveraging detailed driveability data to define pile-soil interaction forces is considered the most accurate strategy for understanding sound generation in offshore vibratory pile driving.

Minimal available measurement data shows that sound spectra during vibratory driving are governed by higher harmonics, supporting the modelling of the pile-soil interface as non-friction since low-frequency sound at the primary driving frequency does not govern broadband sound levels in vibratory pile driving. However, these measurements were primarily conducted on small-diameter piles and in shallow water depths. The assumption that the primary frequency is unimportant might not hold for large-diameter piles, which intrinsically emit sound at lower frequencies or for piles at large water depths that allow for low-frequency sound to propagate more efficiently. Furthermore, changes in dynamic conditions, such as soil parameters, are not quantified. Therefore, the best practice for vibratory pile-driving sound predictions in the current research phase is employing a non-

linear frictional interface description. Alternatively, no friction potentially suffices in sound predictions during Gentle Driving of Piles, where the vertical friction component is minor, and friction forces are difficult to predict due to the coupling of vertical and torsional friction components. Yet, such model simplifications will still be prone to errors in sound emission estimations.

Another significant uncertainty in the model input originates from properly describing the excitation force at the top of the pile. Throughout the dissertation, the hammer force of the vibratory devices is based on measured pile vibrations at the top of the pile, assuming these vibrations are mainly induced by the installation tool, including superharmonics. However, friction can also redistribute energy to higher harmonics. In this work, the excitation force is obtained for a small-diameter monopile and linearly scaled to apply to the larger pile. However, it is unknown if the vibratory hammer emits a force with a similar frequency spectrum when used on larger piles. Modelling of the hammer may be the only alternative accurately given the energy exchange between the pile and the driving tool.

There is great potential in managing sound by shifting primary driving frequencies. Extensions of the vibratory driving principle can result in lower sound levels. Though in early design stages and tested solely onshore, the Gentle Driving of Piles shaker demonstrates the potential to reduce noise emissions due to reduced vertical driving forces, with the potential to drive without vertical forcing. Torsional motion in the Gentle Driving of Piles shaker minimizes vertical frictional resistance between the pile and its surroundings. However, it is essential that superharmonic excitation and coupling between vertical and torsional motion in the hammer are minimized.

It should be noted that there is not yet a proper way to compare vibratory sound with impact sound. The sound signals are intrinsically different, with one being continuous and the other consisting of short pulses. Regulations and research should progress towards establishing thresholds to value continuous noise.

The primary limitation of this thesis is the need for experimental data to validate the model results. Obtaining such data from offshore campaigns is challenging but essential due to growing environmental concerns and the increasing scale of offshore projects, which contribute to higher sound levels. Follow-up research should focus on further validating the developed model. Sound data from piles driven with vibratory devices is required. Experimental campaigns are being planned to address this need to apply vibratory hammers on a practical scale. These experiments promise to validate the presented models, which offer flexibility in accounting for the growing complexity of the pile-soil interface. Gathering underwater sound data and excitation signals is crucial for validation purposes. Another step could be reducing noise by optimizing the vibratory hammer's primary driving frequencies or, in the case of Gentle Driving of Piles, the combined driving frequencies. Reducing energy channelled in the superharmonics seems promising for achieving lower sound levels. Environmental impact studies are required to generate sound thresholds.

In summary, the dynamic interaction between system components is crucial for sound prediction during vibratory pile driving. Superharmonics generated by the hammer's periodic signal have a significant impact, as do factors like driving frequency, hammer type, pile size, soil characteristics, and pile-hammer connection. Efforts to minimize the energy in the superharmonics will likely reduce noise. Quantitative conclusions require further research with extensive experimental data to generalize the conclusions presented in this thesis.

Bibliography

References for Chapter 1

Belgische Staat. (2018). Actualisatie van de initiële beoordeling voor de Belgische mariene wateren. Kaderrichtlijn Mariene Strategie – Art 8 lid 1a and 1b. BMM, Federale Overheidsdienst Volksgezondheid, Veiligheid van de Voedselketen en Leefmilieu, 243.

Bellmann, M., Müller, T., Scheiblick, K., & Betke, K. (2023). *Experience report on operational noise: Cross-project evaluation and assessment of underwater noise measurements from the operational phase of offshore wind farms* (tech. rep.). itap.

Benhemma-Le Gall, A., Graham, I. M., Merchant, N. D., & Thompson, P. M. (2021). Broad-Scale Responses of Harbor Porpoises to Pile-Driving and Vessel Activities During Offshore Windfarm Construction. *Frontiers in Marine Science*, *8*(July), 1–18.

BSH. (2013). Investigation of the Impacts of Offshore Wind Turbines on the Marine Environment (StUK4), 86.

Burghardt-Kaufmann, A. (2019, April 26). *Germany*. White and Case LLP. https://www.whitecase.com/insight-our-thinking/germany

Dahl, P. H., Dall'Osto, D. R., & Farrell, D. M. (2015). The underwater sound field from vibratory pile driving. *The Journal of the Acoustical Society of America*, *137*(6), 3544–3554.

Dahl, P. H., Miller, J. H., Cato, D. H., & Andrew, R. K. (2007). Underwater Ambient Noise. *Acoustics Today*, *3*(1), 23.

Dekeling, R. P. A., Tasker, M. L., Van der Graaf, A. J., Ainslie, M. A., Andersson, M. H., André, M., Borsani, J. F., Brensing, K., Castellote, M., Cronin, D., Dalen, J., Folegot, T., Leaper, R., Pajala, J., Redman, P., Robinson, S. P., Sigray, P., Sutton, G., Thomsen, F., ... Young, J. V. (2014). *Monitoring guidance for underwater noise in European seas. Part II: Monitoring guidance specifications. JRC Scientific and Policy Report EUR 26555 EN, Publications Office of the European Union, Luxembourg, 2014*.

Deng, Q., Jiang, W., Tan, M., & Xing, J. T. (2016). Modeling of offshore pile driving noise using a semi-analytical variational formulation. *Applied Acoustics*, *104*, 85–100.

Elzinga, J., Mesu, A., van Eekelen, E., Wochner, M., Jansen, E., & Nijhof, M. (2019). Manuscript Title: Installing Offshore Wind Turbine Foundations Quieter: A Performance Overview of the First Full-Scale Demonstration of the AdBm Underwater Noise Abatement System. *Offshore Technology Conference*, D021S019R003.

European Commission. (2020). *Communication from the Commission to the European Parliament, the Council, the European Economic and Social Committee and the Committee of the Regions: An EU Strategy to harness the potential of offshore renewable energy for a climate neutral future* (tech. rep.).

Fernandez-Betelu, O., Graham, I. M., Brookes, K. L., Cheney, B. J., Barton, T. R., & Thompson, P. M. (2021). Far-Field Effects of Impulsive Noise on Coastal Bottlenose Dolphins. *Frontiers in Marine Science*, *8*(July), 1–12.

Finneran, J. J., & Jenkins, A. K. (2012). April 2012 Criteria and Thresholds for U . S . Navy Acoustic and Explosive Effects Analysis Criteria And Thresholds For U . S . Navy Acoustic And Explosive Effects. (April).

Finneran, J. J. (2015). Noise-induced hearing loss in marine mammals: A review of temporary threshold shift studies from 1996 to 2015. *The Journal of the Acoustical Society of America*, *138*(3), 1702–1726.

Fricke, M. B., & Rolfes, R. (2015). Towards a complete physically based forecast model for underwater noise related to impact pile driving. *The Journal of the Acoustical Society of America*, *137*(3), 1564–1575.

Göttsche, K. M., Steinhagen, U., & Juhl, P. M. (2015). Numerical evaluation of pile vibration and noise emission during offshore pile driving. *Applied Acoustics*, *99*, 51–59.

Grow. (2021). *Sustainable Installation of XXL Monopiles (SIMOX)*. https://grow-offshorewind.nl/project/simox

Hall, M. V. (2015). An analytical model for the underwater sound pressure waveforms radiated when an offshore pile is driven. *The Journal of the Acoustical Society of America*, *138*(2), 795–806.

Heinis, F., de Jong, C., & von Benda-Beckmann, A. (2022). Kader Ecologie en Cumulatie 2021 (KEC 4.0) – zeezoogdieren, 86.

ISO. (2017a). ISO 18405:2017 Underwater acoustics — Terminology. https://www.iso.org/standard/62406.html

ISO. (2017b). ISO 18406:2017 Underwater acoustics — Measurement of radiated underwater sound from percussive pile driving. https://www.iso.org/standard/62406.html

Jonker, G. (1987). Vibratory pile driving hammers for pile installations and soil improvement projects. *Offshore Technology Conference*, OTC–5422.

Lippert, S., Nijhof, M., Lippert, T., Wilkes, D., Gavrilov, A., Heitmann, K., Ruhnau, M., von Estorff, O., Schafke, A., Schafer, I., Ehrlich, J., MacGillivray, A., Park, J., Seong, W., Ainslie, M. A., de Jong, C., Wood, M., Wang, L., & Theobald, P. (2016). COMPILE—A Generic Benchmark Case for Predictions of Marine Pile-Driving Noise. *IEEE Journal of Oceanic Engineering*, *41*(4), 1061–1071.

Lippert, T., Ainslie, M. A., & von Estorff, O. (2018). Pile driving acoustics made simple: Damped cylindrical spreading model. *The Journal of the Acoustical Society of America*, *143*(1), 310–317.

Lippert, T., Galindo-Romero, M., Gavrilov, A. N., & Von Estorff, O. (2015). Empirical estimation of peak pressure level from sound exposure level. Part II: Offshore impact pile driving noise. *J. Acoust. Soc. Am*, *138*, 287–292.

Lippert, T., Heitmann, K., Ruhnau, M., Lippert, S., & Estorff, O. (2013). On the prediction of pile driving induced underwater sound pressure levels over long ranges. *20th Interna-*

tional Congress on Sound and Vibration, 8. http://mhk.pnl.gov/publications/prediction-pile-driving-induced-underwater-sound-pressure-levels-over-long-ranges

Lippert, T., & Lippert, S. (2012). Modelling of pile driving noise by means of wavenumber integration. *Acoustics Australia*, *40*(3), 178–182.

Lippert, T., & von Estorff, O. (2014a). On a Hybrid Model for the Prediction of Pile Driving Noise from Offshore Wind Farms. *Acta Acustica united with Acustica*, *100*(2), 244–253.

Lippert, T., & von Estorff, O. (2014b). The significance of parameter uncertainties for the prediction of offshore pile driving noise. *The Journal of the Acoustical Society of America*, *136*(5), 2463–2471.

MacGillivray, A. O. (2013). A model for underwater sound levels generated by marine impact pile driving. *The Journal of the Acoustical Society of America*, *134*(5), 4024–4024.

Madsen, P., Wahlberg, M., Tougaard, J., Lucke, K., & Tyack, P. (2006). Wind turbine underwater noise and marine mammals: implications of current knowledge and data needs. *Marine Ecology Progress Series*, *309*(Tyack 1998), 279–295.

Marine Scotland, The Crown Estate, Robinson, S., Lepper, P., & Hazelwood, R. (2014). Good Practice Guide for Underwater Noise Measurement. *NPL Good Practice Guide No. 133*, 96.

Masoumi, H. R., Degrande, G., & Lombaert, G. (2007). Prediction of free field vibrations due to pile driving using a dynamic soil-structure interaction formulation. *Soil Dynamics and Earthquake Engineering*, *27*(2), 126–143.

Nijhof, M. J. J., Binnerts, B., De Jong, C. A. F., & Ainslie, M. A. (2014). An efficient model for prediction of underwater noise due to pile driving at large ranges. *Proceedings of the INTERNOISE 2014—43rd International Congress on Noise Control Engineering: Improving the World through Noise Control*.

Peng, Y., Jarquin Laguna, A., & Tsouvalas, A. (2023). A multi-physics approach for modelling noise mitigation using an air-bubble curtain in impact pile driving. *Frontiers in Marine Science*, *10*(October), 1–13.

Peng, Y., Tsouvalas, A., Metrikine, A., & Belderbos, E. (2018). Modelling and development of a resonator-based noise mitigation system for offshore pile driving. *Proceedings of the 25th International Congress on Sound and Vibration*.

Peng, Y., Tsouvalas, A., Stampoultzoglou, T., & Metrikine, A. V. (2021a). Study of the Sound Escape with the Use of an Air Bubble Curtain in Offshore Pile Driving. *Journal of Marine Science and Engineering*, *9*(2), 232.

Peng, Y., Tsouvalas, A., Stampoultzoglou, T., & Metrikine, A. V. (2021b). A fast computational model for near- and far-field noise prediction due to offshore pile driving. *The Journal of the Acoustical Society of America*, *149*(3), 1772–1790.

Popper, A. N., & Hawkins, A. D. (2018). The importance of particle motion to fishes and invertebrates. *The Journal of the Acoustical Society of America*, *143*(1), 470–488.

Ramirez, L., Fraile, D., & Brindely, G. (2021). *Offshore Wind in Europe* (tech. rep.). Wind Europe. Brussels.

Reinhall, P. G., & Dahl, P. H. (2011). Underwater Mach wave radiation from impact pile driving: Theory and observation. *The Journal of the Acoustical Society of America*, *130*(3), 1209–1216.

Schecklman, S., Laws, N., Zurk, L. M., & Siderius, M. (2015). A computational method to predict and study underwater noise due to pile driving. *The Journal of the Acoustical Society of America*, *138*(1), 258–266.

Southall, B. L. (2021). Evolutions in Marine Mammal Noise Exposure Criteria. *Acoustics Today*, *17*(2), 52.

Southall, B. L., Bowles, A. E., Ellison, W. T., Finneran, J. J., Gentry, R. L., Greene, C. R., Kastak, D., Ketten, D. R., Miller, J. H., Nachtigall, P. E., Richardson, W. J., Thomas, J. A., & Tyack, P. L. (2007). Marine mammal noise-exposure criteria: Initial scientific recommendations. *Aquatic Mammals*, *33*, 411–521.

Southall, B. L., Finneran, J. J., Reichmuth, C., Nachtigall, P. E., Ketten, D. R., Bowles, A. E., Ellison, W. T., Nowacek, D. P., & Tyack, P. L. (2019). Marine Mammal Noise Exposure Criteria: Updated Scientific Recommendations for Residual Hearing Effects. *Aquatic Mammals*, *45*(2), 125–232.

Tougaard, J., Wright, A. J., & Madsen, P. T. (2015). Cetacean noise criteria revisited in the light of proposed exposure limits for harbour porpoises. *Marine Pollution Bulletin*, *90*(1-2), 196–208.

Tsetas, A., Tsouvalas, A., Gómez, S. S., Pisanò, F., Kementzetzidis, E., Molenkamp, T., Elkadi, A. S., & Metrikine, A. V. (2023a). Gentle Driving of Piles (GDP) at a sandy site combining axial and torsional vibrations: Part I - installation tests. *Ocean Engineering*, *270*(April 2022), 113453.

Tsouvalas, A., & Metrikine, A. V. (2013). A semi-analytical model for the prediction of underwater noise from offshore pile driving. *Journal of Sound and Vibration*, *332*(13), 3232–3257.

Tsouvalas, A., & Metrikine, A. V. (2014a). A three-dimensional vibroacoustic model for the prediction of underwater noise from offshore pile driving. *Journal of Sound and Vibration*, *333*(8), 2283–2311.

Tsouvalas, A. (2020). Underwater Noise Emission Due to Offshore Pile Installation: A Review. *Energies*, *13*(12), 3037.

Tsouvalas, A., & Metrikine, A. V. (2014b). Wave radiation from vibratory and impact pile driving in a layered acousto-elastic medium. *Proceedings of the 9th International Conference on Structural Dynamics, EURODYN*, (June), 3137–3144.

Tsouvalas, A., & Metrikine, A. V. (2016b). Structure-borne wave radiation by impact and vibratory piling in offshore installations: From sound prediction to auditory damage. *Journal of Marine Science and Engineering*, *4*(3).

Von Pein, J., Lippert, T., Lippert, S., & Von Estorff, O. (2022). Scaling offshore pile driving noise: examples for scenarios with and without a big bubble curtain. *Proceedings of Meetings on Acoustics*, *47*, 70015.

von Pein, J., Lippert, T., Lippert, S., & von Estorff, O. (2022). Scaling laws for unmitigated pile driving: Dependence of underwater noise on strike energy, pile diameter, ram weight, and water depth. *Applied Acoustics*, *198*, 108986.

Warrington, D. (1989). Theory and development of vibratory pile-driving equipment. *Offshore Technology Conference*, OTC–6030.

Wilkes, D. R., Gourlay, T. P., & Gavrilov, A. N. (2016). Numerical Modeling of Radiated Sound for Impact Pile Driving in Offshore Environments. *IEEE Journal of Oceanic Engineering*, *41*(4), 1072–1078.

Wood, M. A. (2016). *Modelling and Prediction of Acoustic Disturbances From Off-Shore Piling* [Doctoral dissertation, University of Southampton].

Würsig, B., Greene, C. R., & Jefferson, T. A. (2000). Development of an air bubble curtain to reduce underwater noise of percussive piling. *Marine Environmental Research*, *49*(1), 79–93.

Zampolli, M., Nijhof, M. J. J., de Jong, C. A. F., Ainslie, M. A., Jansen, E. H. W., & Quesson, B. A. J. (2013). Validation of finite element computations for the quantitative prediction of underwater noise from impact pile driving. *The Journal of the Acoustical Society of America*, *133*(1), 72–81.

References for Chapter 2

Jensen, F. B., Kuperman, W. A., Porter, M. B., & Schmidt, H. (2011). *Computational Ocean Acoustics* (W. M. Hartmann, Ed.; Seccond Ed). Springer New York.

Kallehave, D., Byrne, B. W., LeBlanc Thilsted, C., & Mikkelsen, K. K. (2015). Optimization of monopiles for offshore wind turbines. *Philosophical Transactions of the Royal Society A: Mathematical, Physical and Engineering Sciences*, *373*(2035), 20140100.

Kaplunov, J. D., Kossovich, L. Y., & Nolde, E. V. (1998). *Dynamics of thin walled elastic bodies*. Academic Press.

Kausel, E. (1974). *Forced vibrations of circular foundations on layered media*. [Doctoral dissertation, Massacusetts Institute of Technology].

Kirkup, S. (2019). The boundary element method in acoustics: A survey. *Applied Sciences (Switzerland)*, *9*(8), 1642.

Leissa, A. W. (1969). *Vibration of plates*.

Leissa, A. W. (1973). *Vibration of shells* (tech. rep.). Scientific, Technical Information Office National Aeronautics and Space Administration. Washington, D.C.

Loy, C. T., Lam, K. Y., & Shu, C. (1997). Analysis of cylindrical shells using generalized differential quadrature. *Shock and Vibration*, *4*(3), 193–198.

Tsouvalas, A., & Metrikine, A. V. (2014a). A three-dimensional vibroacoustic model for the prediction of underwater noise from offshore pile driving. *Journal of Sound and Vibration*, *333*(8), 2283–2311.

Tsouvalas, A. (2015). *Underwater noise generated by offshore pile driving* (Publication No. november) [Doctoral dissertation, Delft University of Technology].

Zhou, H., Li, W., Lv, B., & Li, W. L. (2012). Free vibrations of cylindrical shells with elastic-support boundary conditions. *Applied Acoustics*, *73*(8), 751–756.

References for Chapter 3

COMSOL Multiphysics®. (2022). COMSOL Multiphysics® v. 6.1. www.comsol.com. COMSOL AB, Stockholm, Sweden.

Deng, Q., Jiang, W., Tan, M., & Xing, J. T. (2016). Modeling of offshore pile driving noise using a semi-analytical variational formulation. *Applied Acoustics*, *104*, 85–100.

ISO. (2017a). ISO 18405:2017 Underwater acoustics — Terminology. https://www.iso.org/standard/62406.html

Leissa, A. W. (1973). *Vibration of shells* (tech. rep.). Scientific, Technical Information Office National Aeronautics and Space Administration. Washington, D.C.

Lippert, S., Nijhof, M., Lippert, T., Wilkes, D., Gavrilov, A., Heitmann, K., Ruhnau, M., von Estorff, O., Schafke, A., Schafer, I., Ehrlich, J., MacGillivray, A., Park, J., Seong, W., Ainslie, M. A., de Jong, C., Wood, M., Wang, L., & Theobald, P. (2016). COMPILE—A Generic Benchmark Case for Predictions of Marine Pile-Driving Noise. *IEEE Journal of Oceanic Engineering*, *41*(4), 1061–1071.

Lippert, T., Ainslie, M. A., & von Estorff, O. (2018). Pile driving acoustics made simple: Damped cylindrical spreading model. *The Journal of the Acoustical Society of America*, *143*(1), 310–317.

Molenkamp, T., Tsouvalas, A., & Metrikine, A. (2024c). A numerical study on the effect of asymmetry on underwater noise emission in offshore monopile installation. *Ocean Engineering*, *299*, 117351.

Peng, Y., Tsouvalas, A., Stampoultzoglou, T., & Metrikine, A. V. (2021b). A fast computational model for near- and far-field noise prediction due to offshore pile driving. *The Journal of the Acoustical Society of America*, *149*(3), 1772–1790.

Reinhall, P. G., & Dahl, P. H. (2011). Underwater Mach wave radiation from impact pile driving: Theory and observation. *The Journal of the Acoustical Society of America*, *130*(3), 1209–1216.

Tsouvalas, A., & Metrikine, A. V. (2013). A semi-analytical model for the prediction of underwater noise from offshore pile driving. *Journal of Sound and Vibration*, *332*(13), 3232–3257.

Veritas, D. N. (2004). Design of Offshore Wind Turbine Structure.

Wilkes, D. R., & Gavrilov, A. N. (2017). Sound radiation from impact-driven raked piles. *The Journal of the Acoustical Society of America*, *142*(1), 1–11.

Zampolli, M., Nijhof, M. J. J., de Jong, C. A. F., Ainslie, M. A., Jansen, E. H. W., & Quesson, B. A. J. (2013). Validation of finite element computations for the quantitative prediction of underwater noise from impact pile driving. *The Journal of the Acoustical Society of America*, *133*(1), 72–81.

References for Chapter 4

COMSOL Multiphysics®. (2022). COMSOL Multiphysics® v. 6.1. www.comsol.com. COMSOL AB, Stockholm, Sweden.

Cui, C., Meng, K., Xu, C., Wang, B., & Xin, Y. (2022). Vertical vibration of a floating pile considering the incomplete bonding effect of the pile-soil interface. *Computers and Geotechnics*, *150*(April), 104894.

Dahl, P. H., Dall'Osto, D. R., & Farrell, D. M. (2015). The underwater sound field from vibratory pile driving. *The Journal of the Acoustical Society of America*, *137*(6), 3544–3554.

Holeyman, A. (2002). Soil behaviour under vibratory driving. *Proceedings of the International Conference on vibratory pile driving and deep soil compaction*, (10), 3–20.

ISO. (2017a). ISO 18405:2017 Underwater acoustics — Terminology. https://www.iso.org/standard/62406.html

Jensen, F. B., Kuperman, W. A., Porter, M. B., & Schmidt, H. (2011). *Computational Ocean Acoustics* (W. M. Hartmann, Ed.; Seccond Ed). Springer New York.

Kirkup, S. (2019). The boundary element method in acoustics: A survey. *Applied Sciences (Switzerland)*, *9*(8), 1642.

Leissa, A. W. (1973). *Vibration of shells* (tech. rep.). Scientific, Technical Information Office National Aeronautics and Space Administration. Washington, D.C.

Lippert, S., Nijhof, M., Lippert, T., Wilkes, D., Gavrilov, A., Heitmann, K., Ruhnau, M., von Estorff, O., Schafke, A., Schafer, I., Ehrlich, J., MacGillivray, A., Park, J., Seong, W., Ainslie, M. A., de Jong, C., Wood, M., Wang, L., & Theobald, P. (2016). COMPILE—A Generic Benchmark Case for Predictions of Marine Pile-Driving Noise. *IEEE Journal of Oceanic Engineering*, *41*(4), 1061–1071.

Markou, A. A., & Kaynia, A. M. (2018). Nonlinear soil-pile interaction for offshore wind turbines. *Wind Energy*, *21*(7), 558–574.

Molenkamp, T., Tsouvalas, A., & Metrikine, A. (2023b). The influence of contact relaxation on underwater noise emission and seabed vibrations due to offshore vibratory pile installation. *Frontiers in Marine Science*, *10*(March), 357.

Nogami, T., & Konagai, K. (1987). Dynamic Response of Vertically Loaded Nonlinear Pile Foundations. *Journal of Geotechnical Engineering*, *113*(2), 147–160.

Novak, M. (1991). Piles under dynamic loads. *Second International Conference on Recent Advances In Geotechnical Earthquake Engineering and Soil Dynamics*, (2), 2433–2456. https://mospace.umsystem.edu/xmlui/handle/10355/42505

Peng, Y., Tsouvalas, A., Stampoultzoglou, T., & Metrikine, A. V. (2021b). A fast computational model for near- and far-field noise prediction due to offshore pile driving. *The Journal of the Acoustical Society of America*, *149*(3), 1772–1790.

Tsetas, A., Tsouvalas, A., Gómez, S. S., Pisanò, F., Kementzetzidis, E., Molenkamp, T., Elkadi, A. S., & Metrikine, A. V. (2023a). Gentle Driving of Piles (GDP) at a sandy site combining axial and torsional vibrations: Part I - installation tests. *Ocean Engineering*, *270*(April 2022), 113453.

Tsetas, A., Tsouvalas, A., & Metrikine, A. V. (2023c). A non-linear three-dimensional pile-soil model for vibratory pile installation in layered media. *International Journal of Solids and Structures*, *269*(March), 112202.

Tsouvalas, A. (2020). Underwater Noise Emission Due to Offshore Pile Installation: A Review. *Energies*, *13*(12), 3037.

Tsouvalas, A., & Metrikine, A. V. (2016b). Structure-borne wave radiation by impact and vibratory piling in offshore installations: From sound prediction to auditory damage. *Journal of Marine Science and Engineering*, *4*(3).

References for Chapter 5

Buckley, R., Chen, Y. M., Sheil, B., Suryasentana, S., Xu, D., Doherty, J., & Randolph, M. (2023). Bayesian optimization for CPT-based prediction of impact pile drivability. *Journal of Geotechnical and Geoenvironmental Engineering*, *149*(11), 04023100.

Dahl, P. H., Dall'Osto, D. R., & Farrell, D. M. (2015). The underwater sound field from vibratory pile driving. *The Journal of the Acoustical Society of America*, *137*(6), 3544–3554.

de Oliveira Barbosa, J. M., Park, J., & Kausel, E. (2012). Perfectly matched layers in the thin layer method. *Computer Methods in Applied Mechanics and Engineering*, *217*, 262–274.

Fontanela, F., Grolet, A., Salles, L., & Hoffmann, N. (2019). Computation of quasi-periodic localised vibrations in nonlinear cyclic and symmetric structures using harmonic balance methods. *Journal of Sound and Vibration*, *438*, 54–65.

ISO. (2017a). ISO 18405:2017 Underwater acoustics — Terminology. https://www.iso.org/standard/62406.html

Jensen, F. B., Kuperman, W. A., Porter, M. B., & Schmidt, H. (2011). *Computational Ocean Acoustics* (W. M. Hartmann, Ed.; Seccond Ed). Springer New York.

Kausel, E., & de Oliveira Barbosa, J. M. (2012). PMLs: A direct approach. *International journal for numerical methods in engineering*, *90*(3), 343–352.

Kausel, E., & Peek, R. (1982). Dynamic loads in the interior of a layered stratum: an explicit solution. *Bulletin of the Seismological Society of America*, *72*(5), 1459–1481.

Kaynia, A. M., Hebig, J., Pein, T., & Shin, Y. (2022). Numerical model for dynamic installation of large diameter monopiles. *Soil Dynamics and Earthquake Engineering*, *161*, 107393.

Krack, M., Panning-von Scheidt, L., & Wallaschek, J. (2013). A high-order harmonic balance method for systems with distinct states. *Journal of Sound and Vibration*, *332*(21), 5476–5488.

Leissa, A. W. (1973). *Vibration of shells* (tech. rep.). Scientific, Technical Information Office National Aeronautics and Space Administration. Washington, D.C.

Molenkamp, T., Tsetas, A., Tsouvalas, A., & Metrikine, A. (2024a). Underwater noise from vibratory pile driving with non-linear frictional pile–soil interaction. *Journal of Sound and Vibration*, *576*, 118298.

Molenkamp, T., Tsouvalas, A., & Metrikine, A. (2023b). The influence of contact relaxation on underwater noise emission and seabed vibrations due to offshore vibratory pile installation. *Frontiers in Marine Science*, *10*(March), 357.

Moriyasu, S., Kobayashi, S., & Matsumoto, T. (2018). Experimental study on friction fatigue of vibratory driven piles by in situ model tests. *Soils and foundations*, *58*(4), 853–865.

Moscoso del Prado Mazza, N., & Holeyman, A. (2019). Frequency-Penetration Response Spectrum on Vibratory Amplitude Matching of Monopiles, 468–492.

Peng, Y., Tsouvalas, A., Stampoultzoglou, T., & Metrikine, A. V. (2021a). Study of the Sound Escape with the Use of an Air Bubble Curtain in Offshore Pile Driving. *Journal of Marine Science and Engineering*, *9*(2), 232.

Peng, Y., Tsouvalas, A., Stampoultzoglou, T., & Metrikine, A. V. (2021b). A fast computational model for near- and far-field noise prediction due to offshore pile driving. *The Journal of the Acoustical Society of America*, *149*(3), 1772–1790.

Salgado, R., Loukidis, D., Abou-Jaoude, G., & Zhang, Y. (2015). The role of soil stiffness non-linearity in 1D pile driving simulations. *Géotechnique*, *65*(3), 169–187.

Tsetas, A. (2023). *A unified modelling framework for vibratory pile driving methods* [Doctoral dissertation, Delft University of Technology].

Tsetas, A., Tsouvalas, A., Gómez, S. S., Pisanò, F., Kementzetzidis, E., Molenkamp, T., Elkadi, A. S., & Metrikine, A. V. (2023a). Gentle Driving of Piles (GDP) at a sandy site combining axial and torsional vibrations: Part I - installation tests. *Ocean Engineering*, *270*(April 2022), 113453.

Tsetas, A., Tsouvalas, A., & Metrikine, A. V. (2023d). The mechanics of the Gentle Driving of Piles. *International Journal of Solids and Structures*, *282*, 112466.

Tsetas, A., Tsouvalas, A., & Metrikine, A. V. (2023e). A non-linear three-dimensional pile–soil model for vibratory pile installation in layered media. *International Journal of Solids and Structures*, *269*, 112202.

Tsouvalas, A., & Metrikine, A. V. (2016a). Noise reduction by the application of an air-bubble curtain in offshore pile driving. *Journal of Sound and Vibration*, *371*, 150–170.

Tsouvalas, A., & Metrikine, A. V. (2016b). Structure-borne wave radiation by impact and vibratory piling in offshore installations: From sound prediction to auditory damage. *Journal of Marine Science and Engineering*, *4*(3).

Zhou, S., Cao, J., Inman, D. J., Lin, J., & Li, D. (2016). Harmonic balance analysis of nonlinear tristable energy harvesters for performance enhancement. *Journal of Sound and Vibration*, *373*, 223–235.

References for Chapter 6

Kementzetzidis, E., Pisanò, F., Elkadi, A. S., Tsouvalas, A., & Metrikine, A. V. (2023). Gentle Driving of Piles (GDP) at a sandy site combining axial and torsional vibrations: Part II - cyclic/dynamic lateral loading tests. *Ocean Engineering*, *270*(April 2022), 113452.

Molenkamp, T., Tsetas, A., Tsouvalas, A., & Metrikine, A. (2024a). Underwater noise from vibratory pile driving with non-linear frictional pile–soil interaction. *Journal of Sound and Vibration*, *576*, 118298.

Molenkamp, T., & Tsouvalas, A. (2024b, July). Underwater Noise from Gentle Driving of Piles. In W. van Keulen & J. Kok (Eds.), *Proceedings of the 30th International Congress on Sound and Vibration*. The International Institute of Acoustics; Vibration.

Molenkamp, T., Tsouvalas, A., & Metrikine, A. (2023b). The influence of contact relaxation on underwater noise emission and seabed vibrations due to offshore vibratory pile installation. *Frontiers in Marine Science*, *10*(March), 357.

Tsetas, A., Tsouvalas, A., Gómez, S. S., Pisanò, F., Kementzetzidis, E., Molenkamp, T., Elkadi, A. S., & Metrikine, A. V. (2023a). Gentle Driving of Piles (GDP) at a sandy site combining axial and torsional vibrations: Part I - installation tests. *Ocean Engineering*, *270*(April 2022), 113453.

Tsetas, A., Tsouvalas, A., & Metrikine, A. V. (2023d). The mechanics of the Gentle Driving of Piles. *International Journal of Solids and Structures*, *282*, 112466.

A

Dynamic response of two interacting extensible bars in frictional contact

This appendix develops a new model to describe the nonlinear dynamics of two axially deformable bars sliding relative to each other in which the interaction is governed by friction. The first bar is fixed at one end and is subjected to a distributed normal force perpendicular to its axis to activate friction at the common interface. In contrast, the second bar can slide relative to the fixed one. A semi-analytical solution method is developed to address only the nonlinear interaction numerically. The dynamic behaviour of the bars is expressed as a summation of vibration modes, including the necessary rigid body mode to allow for the permanent sliding of one bar relative to the other. This results in a computationally efficient scheme without compromising the accuracy of the solutions. The developed model can be used in pile driveability studies. In this case, the fixed bar resembles the soil column, while the second bar describes the dynamics of the driven pile.

This chapter has been published in EURODYN 2020 XI International Conference on Structural Dynamics, November 2020, Molenkamp et al. (2020a).

A

A.1. Introduction

Friction plays an important role in many engineering fields, including pile driving. For example, accurate prediction of underwater noise generated in the seawater during pile driving with vibratory devices requires the simultaneous prediction of the pile progression into the soil and, thus, the incorporation of a proper frictional model to describe the pile-soil slip behaviour. State-of-the-art models in underwater noise prediction for impact pile driving all assume perfect contact between pile and soil (Fricke and Rolfes, 2015; Tsouvalas and Metrikine, 2014a). Problems, including high-frequency bands solved with a fixed FE-mesh, need fine spatial and time discretization to describe the propagating waves. This results in enormous computational efforts for insolvable problems (Fricke and Rolfes, 2015). As a first step towards developing a computationally efficient model that predicts noise during vibratory pile driving, including slippage of the pile, the dynamics of two elastic bars in frictional contact are studied in this chapter.

The inclusion of friction complicates the problem, as it introduces a strong nonlinearity. To describe the forces at a frictional interface, an appropriate frictional law should be chosen (Berger, 2002). Since the focus herein is on noise generated during the driving process of piles with vibratory devices, the interest is in a straightforward frictional model that can describe the sliding between pile and soil. The most common frictional model is based on the Coulomb friction law. Coulomb's friction can be applied in many fields, such as in a simplified model for belt driving mechanics, in which Coulomb's friction law represents the dry friction between the belt and support (Leamy et al., 1998). Variations on Coulomb's friction for multi-body mechanical systems are described, for example, by Marques et al. (2016). The Coulomb friction, which is multivalued at zero velocity, can be approximated by alternative methods which deviate from Coulomb's friction below a certain velocity threshold and have a finite slope at zero velocity, e.g. linear velocity-dependent friction at low velocities and an approximation by a hyperbolic tangent (Marques et al., 2016). Another alternative is introduced by Threlfall; the method avoids the discontinuity in the transition between positive and negative, and it has a higher resemblance with the Coulomb friction law at velocities below a certain threshold (Threlfall, 1978). This last friction law fits the problem of vibratory pile driving since it is smooth, and the pile is assumed to slide continuously to the soil while sticking can be neglected.

The model discussed in this work can be seen as a predecessor of a three-dimensional model for pile-driving noise prediction, including the effect of pile-soil slip in section 2; the problem statement is explained, including the equations of motions, boundary conditions and Threlfall's friction law. Hereafter, the solution method is described. The solution approach is mainly analytical; a numerical scheme only evaluates standard integrals. Section 3 describes the method's limitations in terms of convergence, including criteria for the truncation of the number of modes used in this work. Section 4 shows results for the case

of an impact load represented by a block function and a harmonic load. Finally, section 5 contains conclusions regarding the model performance.

A.2. Mathematical Formulation

A.2.1. Governing equations

The model under consideration is schematized in Fig. A.1. It consists of two bars, which can deform in the axial direction and interact through a frictional interface. The equations of

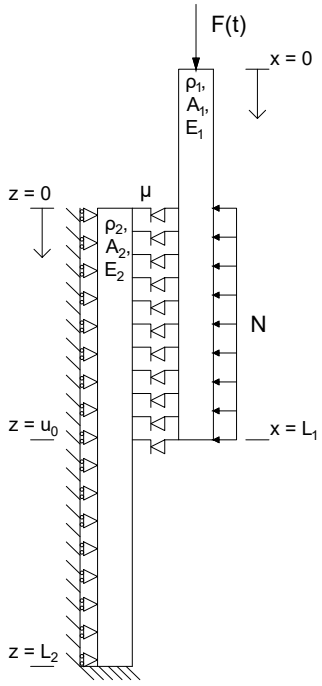


Figure A.1: Schematization of the problem statement

motion describing the dynamics of the two bars read:

$$\rho_1 A_1 \ddot{u}_1(x,t) = E_1 A_1 u_1''(x,t) - T_1(x,t) + F(t)\delta(x) \tag{A.1}$$

$$\rho_2 A_2 \ddot{u}_2(z,t) = E_2 A_2 u_2''(z,t) - T_2(z,t) \tag{A.2}$$

in which subscript 1 refers to the forced bar and subscript 2 to the constrained bar, hereafter called bars 1 and 2. The constants ρ, A and E define the density, area and elasticity of the bars, respectively. $T_{1,2}(x,t)$ represents the friction that acts on either bar. The driving force $F(t)$ can be included in a time-dependent boundary Aranda-Ruiz and Fernández-Sáez, 2012. However, the interest here is not precisely describing the top boundary stresses. A local coordinate system is adopted for bar 1. The progression of the lower end of bar 1 concerning

the upper end of bar 2 is characterized by $u_0(t)$ as shown in Fig. A.1. The prime and dot indicate derivatives of spatial coordinates and time, respectively. Threlfall's friction law is adopted, i.e. the signum function that is smoothed around zero velocity:

$$T_1(x,t) = \mu N \operatorname{sgn}(\Delta v_1(x,t)) \left(1 - e^{-k\frac{\Delta v_1(x,t)}{v_{95}}}\right) H(x - L_1 + u_0(t)) \tag{A.3}$$

$$T_2(z,t) = \mu N \operatorname{sgn}(-\Delta v_2(z,t)) \left(1 - e^{-k\frac{\Delta v_2(z,t)}{v_{95}}}\right) H(u_0(t) - z) \tag{A.4}$$

with:

$$\Delta v_1(x,t) = \dot{u}_1(x,t) - \dot{u}_2(x - L_1 + u_0(t), t) \tag{A.5}$$

$$\Delta v_2(z,t) = \dot{u}_2(z,t) - \dot{u}_1(z + L_1 - u_0(t), t) \tag{A.6}$$

where H is the Heaviside function and v_{95} is a velocity threshold above which the friction behaves almost velocity independent, i.e. at $\Delta v = v_{95}$: $T \approx 0.95 T_{max}$ for $k = 3$. The velocity threshold is based on the maximum modal change of velocity amplitude per time step, derived based on the results of Appendix A.2.2 of this chapter as:

$$v_{95} = \frac{4\mu N \Delta t}{\pi \rho_1 A_1} \tag{A.7}$$

The boundary conditions read:

$$u_1'(0,t) = u_1'(L_1,t) = u_2'(0,t) = u_2(L_2,t) = 0 \tag{A.8}$$

The initial conditions are:

$$u_1(x,t_0) = u_{t_0}, \quad \dot{u}_1(x,t_0) = \dot{u}_{t_0}, \quad u_2(x,t_0) = w_{t_0}, \quad \dot{u}_2(x,t_0) = \dot{w}_{t_0} \tag{A.9}$$

Equations (A.1) to (A.9) govern the dynamics of the coupled system in the time domain.

A.2.2. Solution method

A modal solution approach is adopted. Therefore, the displacements are expressed as a summation of modes:

$$u_1(x,t) = \sum_{n=1}^{\infty} \phi_n(x)\eta_n(t), \qquad u_2(z,t) = \sum_{m=1}^{\infty} \psi_m(z)\zeta_m(t) \tag{A.10}$$

Bar 1 is allowed to slide concerning bar 2; the relative motion is governed by the rigid body motion of bar 1; relative displacement due to the deformation of either bar is neglected.

Substitution of Eq. (A.10) into Eqs. (A.1) and (A.2) yields:

$$\sum_{n=1}^{\infty} \phi_n(x)\ddot{\eta}_n(t) + \omega_n^2 \phi_n(x)\eta_n(t) = \frac{F(t)\delta(x) - T_1(x,t)}{\rho_1 A_1} \tag{A.11}$$

$$\sum_{m=1}^{\infty} \psi_m(z)\ddot{\xi}_m(t) + \omega_m^2 \psi_m(z)\xi_m(t) = -\frac{T_2(z,t)}{\rho_2 A_2} \tag{A.12}$$

with:

$$\phi_n(x) = \cos\left(\frac{\omega_n x}{c_1}\right), \qquad \omega_n = \frac{n\pi c_1}{L_1} \qquad n = 0,1,2,\ldots \tag{A.13}$$

$$\xi_m(z) = \cos\left(\frac{\omega_m z}{c_2}\right), \qquad \omega_m = \frac{(2m-1)\pi c_2}{2L_2} \qquad m = 1,2,3,\ldots \tag{A.14}$$

being the spatial eigenfunctions satisfying Eqs. (8). Equations (A.11) and (A.12) are multiplied by another mode and integrated over the length of each bar, using the orthogonality relation of the modes. After substituting Eqs. (A.3) and (A.4) into Eqs. (A.11) and (A.12), one obtains:

$$\ddot{\eta}_n(t) + \omega_n^2 \eta_n(t) = \frac{1}{\rho_1 A_1 a_n}\left(F(t) - \mu N \int_{L_1 - u_0(t)}^{L_1} \phi_n(x)\,\mathrm{sgn}(\Delta v_1(x,t)) \times \left(1 - e^{-k\frac{\Delta v_1(x,t)}{v_{95}}}\right)\mathrm{d}x\right) \tag{A.15}$$

$$\ddot{\xi}_m(t) + \omega_m^2 \xi_m(t) = -\frac{\mu N}{\rho_1 A_1 a_m}\int_0^{u_0(t)} \psi_m(z)\,\mathrm{sgn}(\Delta v_2(z,t))\left(1 - e^{-k\frac{\Delta v_2(z,t)}{v_{95}}}\right)\mathrm{d}z \tag{A.16}$$

with:

$$a_n = \int_0^{L_1} \phi_n(x)^2 \mathrm{d}x = \begin{cases} L_1 & n = 0 \\ \frac{1}{2}L_1 & n \neq 0 \end{cases}, \quad a_m = \int_0^{L_2} \psi_m(z)^2 \mathrm{d}z = \frac{1}{2}L_2 \tag{A.17}$$

To facilitate a computationally efficient solution of Eqs. (A.15) and (A.16), a straightforward time-stepping scheme is chosen, assuming that the relative velocity, $\Delta v_{1,2}(z,t)$, and the progression $u_0(t)$ are constant during a time step. Under the stated assumptions, Eqs. (A.15) and (A.16) act linear during a time step, and the modal amplitudes η_n and ξ_m can be found using the Duhamel's integral for each time step. The closed-form solution to Eq. (A.15) reads:

$$\eta_n(t_{i+1}) = A_n \sin(\omega_n t_{i+1}) + B_n \cos(\omega_n t_{i+1}) + \frac{1}{\omega_n a_n \rho_1 A_1}\int_{t_i}^{t_{i+1}} F(\tau)\sin(\omega_n(t_{i+1} - \tau))\mathrm{d}\tau - \frac{\mu N(1 - \cos(\omega_n \Delta t))}{\omega_n^2 a_n \rho_1 A_1} \times \int_{L_1 - u_0(t_i)}^{L_1} \phi_n(x)\,\mathrm{sgn}(\Delta v_1(x,t_i))\left(1 - e^{-k\frac{\Delta v_1(x,t_i)}{v_{95}}}\right)\mathrm{d}x \tag{A.18}$$

in which A_n and B_n are found by the previous time step:

$$\begin{aligned} A_n &= \frac{\sin(\omega_n t_i)\,\omega_n \eta_n(t_i) + \cos(\omega_n t_i)\,\dot{\eta}_n(t_i)}{\omega_n} \\ B_n &= \frac{\cos(\omega_n t_i)\,\omega_n \eta_n(t_i) - \sin(\omega_n t_i)\,\dot{\eta}_n(t_i)}{\omega_n} \end{aligned} \tag{A.19}$$

and in the special case of the initial time step:

$$\eta_n(t_0) = \frac{\int_0^{L_1} u_{t_0}\,dx}{a_n}, \qquad \dot{\eta}_n(t_0) = \frac{\int_0^{L_1} \dot{u}_{t_0}\,dx}{a_n} \tag{A.20}$$

The time derivative of $\eta_n(t)$ is given as:

$$\begin{aligned} \dot{\eta}_n(t_{i+1}) = {} & A_n(t_i)\omega_n \cos(\omega_n t_{i+1}) - B_n(t_i)\omega_n \sin(\omega_n t_{i+1}) \\ & + \frac{1}{a_n \rho_1 A_1} \int_{t_i}^{t_{i+1}} F(\tau)\cos(\omega_n(t_{i+1}-\tau))\mathrm{d}\tau - \frac{\mu N \sin(\omega_n \Delta t)}{\omega_n a_n \rho_1 A_1} \\ & \times \int_{L_1-u_0(t_i)}^{L_1} \phi_n(x)\,\mathrm{sgn}(\Delta v_1(x,t_i))\left(1 - e^{-k\frac{\Delta v_1(x,t_i)}{v_{95}}}\right)\mathrm{d}x \end{aligned} \tag{A.21}$$

with $\Delta t = t_{i+1} - t_i$. Similar procedure for ξ_m results in:

$$\begin{aligned} \xi_m(t_{i+1}) = {} & C_m(t_i)\sin(\omega_m t_{i+1}) + D_m(t_i)\cos(\omega_m t_{i+1}) \\ & - \frac{\mu N(1-\cos(\omega_m \Delta t))}{\omega_m^2 a_m \rho_2 A_2} \int_0^{u_0(t_0)} \psi_m(z)\,\mathrm{sgn}(\Delta v_2(z,t_i))\left(1 - e^{-k\frac{\Delta v_2(z,t_i)}{v_{95}}}\right)\mathrm{d}z \end{aligned} \tag{A.22}$$

$$\begin{aligned} \dot{\xi}_m(t_{i+1}) = {} & C_m(t_i)\omega_m \cos(\omega_m t_{i+1}) - D_m(t_i)\omega_m \sin(\omega_m t_{i+1}) \\ & - \frac{\mu N \sin(\omega_m \Delta t)}{\omega_m a_m \rho_2 A_2} \int_0^{u_0(t_i)} \psi_m(z)\,\mathrm{sgn}(\Delta v_2(z,t_i))\left(1 - e^{-k\frac{\Delta v_2(z,t_i)}{v_{95}}}\right)\mathrm{d}z \end{aligned} \tag{A.23}$$

Where C_m and D_m are found similar to A_n and B_n. As mentioned earlier, the spatial integrals, including the friction terms, need numerical evaluation. The time step needs to be chosen to be smaller than a tenth of the smallest period in the system: $\Delta t < 2\pi/\max(\omega_i)/10$.

A.2.3. Linear equivalent model

The model is compared to a fully linear model that is valid for the case of no sliding. The linear equivalent problem is composed of three bars as shown in Fig. A.2, where the material properties of the second bar are based on the weighted averages of bars 1 and 3. The equation

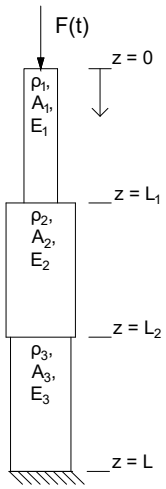


Figure A.2: Schematization of the linear equivalent model

of motion of the whole system for each bar reads:

$$\begin{aligned} \rho_1 A_1 \ddot{u}_1 - E_1 A_1 u_1''(z,t) &= F(t)\delta(z) \qquad 0 < z < L_1 \\ \rho_2 A_2 \ddot{u}_2 - E_2 A_2 u_2''(z,t) &= 0 \qquad L_1 < z < L_2 \\ \rho_3 A_3 \ddot{u}_3 - E_3 A_3 u_3''(z,t) &= 0 \qquad L_2 < z < L \end{aligned} \tag{A.24}$$

The top boundary is stress-free since the applied force is accounted for in the equation of motion, and the bottom boundary is fixed; furthermore, the interface conditions describe the continuity of displacements and stresses. The modes of the system can be found by solving the eigenvalue problem formed after substituting the general solution for each of the bars in the boundary and interface conditions. The modes are orthogonal to the density and area Yeh, 1976:

$$\int_0^{L_1} \rho_1 A_1 \phi_m(z)\phi_n(z)dz + \int_{L_1}^{L_2} \rho_2 A_2 \phi_m(z)\phi_n(z)dz + \int_{L_2}^{L} \rho_3 A_3 \phi_m(z)\phi_n(z)dz = a_n \delta_{nm} \tag{A.25}$$

The modal amplitudes are found analytically by making use of the orthogonality of the modes:

$$\eta_n(t) = A_n \sin(\omega_n t) + B_n \cos(\omega_n t) + \frac{1}{\omega_n a_n} \int_0^t F(\tau) \sin(\omega_n (t-\tau)) \mathrm{d}\tau \tag{A.26}$$

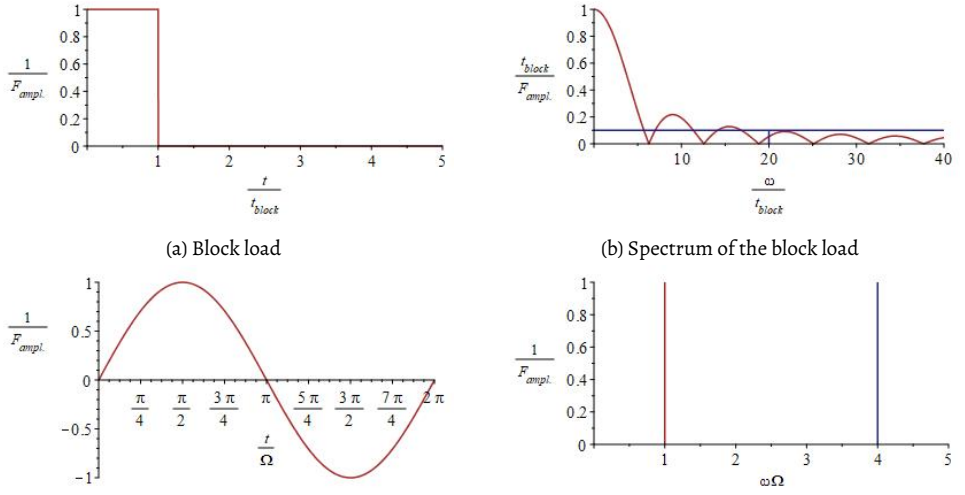
A_n and B_n are found by the initial conditions at $t = 0$:

$$A_n = \frac{1}{a_n \omega_n} \sum_{i=1}^{3} \int_{L_i} \rho_i A_i \phi_n(z) \dot{u}_i(z,0) dz \tag{A.27}$$

$$B_n = \frac{1}{a_n} \sum_{i=1}^{3} \int_{L_i} \rho_i A_i \phi_n(z) u_i(z,0) \mathrm{d}z \tag{A.28}$$

A.3. Results

Two cases will be examined: a block function load and a high-frequency harmonic excitation. The two load cases are visualized in the time and frequency domain in Fig. A.3. The material



(a) Block load

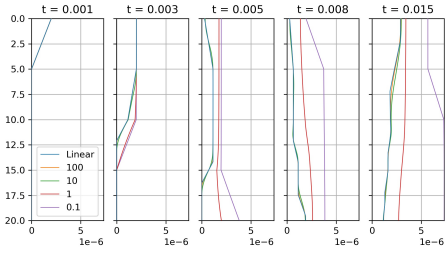
(b) Spectrum of the block load

(c) Harmonic load

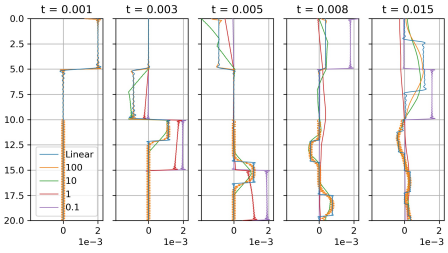
(d) Spectrum of the harmonic load

Figure A.3: Load in time and frequency domain (red), and the minimum of frequencies included in the results (blue)

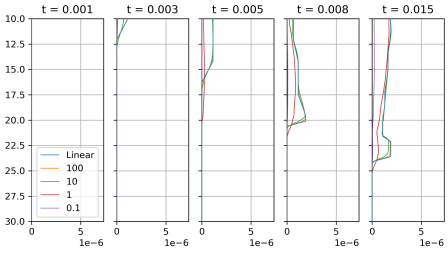
properties are chosen such that the wave speeds in both bars represent steel and sandy soil. For bar 1 the properties are: $\rho_1 A_1 = 1$, $E_1 A_1 = 5000^2$, $c_1 = 5000$ and $L_1 = 20$, for bar 2: $\rho_2 A_2 = 5$, $E_2 A_2 = 500^2$ $c_2 = 500$ and $L_2 = 20$. In the initial state, the friction interface is half of bar 1, i.e. $u_0(0) = 10$. The duration of the applied block load is $t_{block} = 0.001$. The harmonic load starts at $t = 0$ with $\Omega = 1000$. The amplitude of both loads is 10. The influence of the friction coefficient μN is shown in the graphs, where μN varies from 0.1 to $100\mu N$. $\mu N = 100$ is chosen sufficiently high to approximate the linear case, where both bars move together, and no sliding occurs. This case serves as validation of the description of the model with friction. The number of modes considered is based on the eigenfrequencies of the modes. At least frequencies excited by the block load, with an amplitude higher than 10% of the maximum amplitude or frequencies up to four times the excitation frequency of the



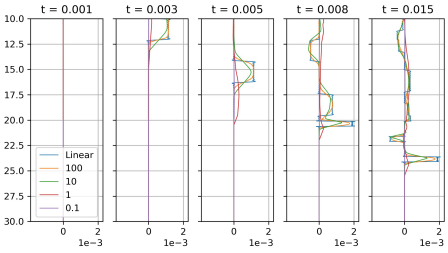
(a) Displacement of bar 1



(b) Velocity of bar 1

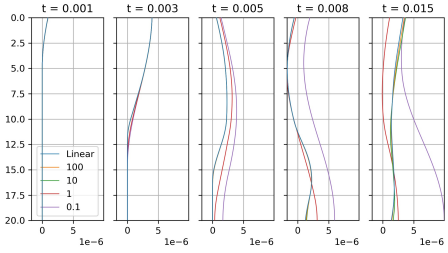


(c) Displacement of bar 2

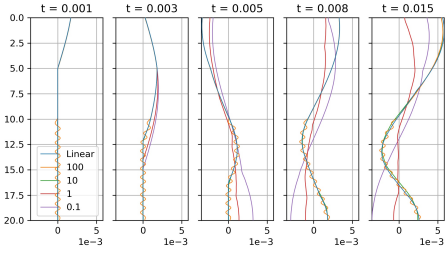


(d) Velocity of bar 2

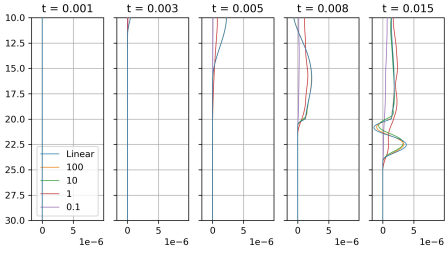
Figure A.4: The dynamic response of the bars when bar 1 is subjected to the block load for different values of μN



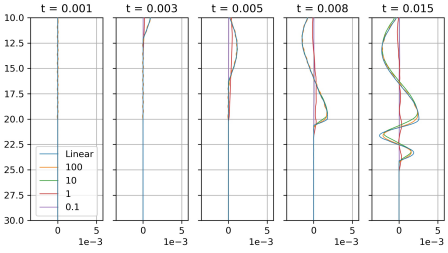
(a) Displacement of bar 1



(b) Velocity of bar 1



(c) Displacement of bar 2



(d) Velocity of bar 2

Figure A.5: The dynamic response of the bars when bar 1 is subjected to a sinusoidal load for different values of μN

harmonic load are included, as indicated with the blue lines in Figs. A.3b and A.3d. For the block load and harmonic load, this results in $\omega_{max} = 20.000$ and $\omega_{max} = 4.000$ respectively. This relates to about 25 and 5 flexible modes of bar 1 and about 250 and 50 modes of bar 2. While the friction force is based on the relative velocity of the bars, the velocities are preferably described with the same accuracy, i.e. the smallest wavelength of both bars is of the same order. Since both bars have the same length, the same number of modes are included, governed by the highest number required.

Figure A.4 shows the displacement and velocity of both bars due to a block load, representing impact pile driving. It can be seen that the summation of modes represents the block function well. Therefore, higher modes are also activated along the whole bar. This can be seen in the amplification of higher modes ahead of the wave-front in Fig. A.4a, especially in the case of high friction forces. Although present, these vibrations cancel out over time and do not excite the system. For low friction coefficients, almost no energy dissipates into bar 1. Therefore, the wave reflects back and forth virtually undisturbed.

In the case of the response to a harmonic load, shown in Fig. A.5, higher frequencies are not excited from the beginning. Therefore, the results are more smooth. In all cases, the highest friction $\mu N = 100$ agrees with the linear results. Both bars converge to the same displacement and velocity for $\mu N = 100$. On the contrary, the unconstrained bar slides over the constrained bar for low friction amplitudes. Due to that, final displacements are more significant at $t = 0.015$, best shown in Fig. A.4a. Generally, the model behaves as expected, e.g. the wavefronts align for all waves in the first bar when they start interacting with the second bar, and then for high friction amplitudes, the wave speed of both bars is based on a weighted average. In contrast, the wave speed is less affected by the second bar for low-frequency amplitudes. This is best shown in Figs. A.4c and A.4d, where at $t = 0.004$, the three different wavefronts are visible.

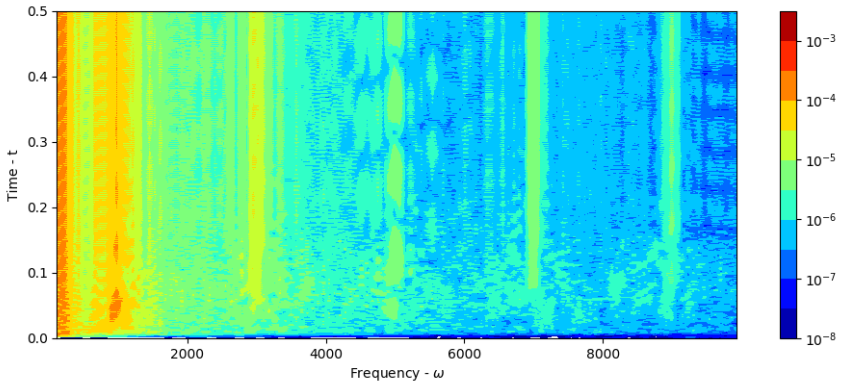


Figure A.6: Time-frequency response of bar 2 for μN = 1

Figure A.6 points to the importance of including the frictional interface in noise-generating

models for vibratory pile driving. The time-frequency plot identifies the presence of the odd higher-order harmonics that are excited in the system due to the presence of the frictional surface.

A.4. Convergence

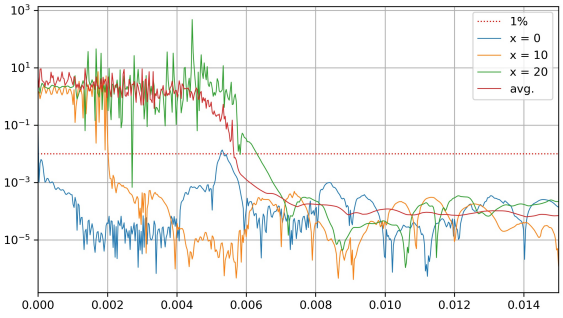
The convergence of the model is satisfied based on displacements and velocities. Due to the delta function, the model cannot describe the stress at the top boundary correctly. However, the exact boundary stress at the top is not interesting; with increasing modes, a good approximation of the stress close to the boundary can be obtained. Since the time step is chosen sufficiently small: $\Delta t < 2\pi / \max(\omega_i)/10$, and depends on the number of modes in the system, the convergence of the solution depends on the truncation of the modes. The truncation criterion is based on the displacement of the bar at the final time step:

$$\delta(x, t_{i_{max}}) = \frac{\left|\sum_{n=1}^{0.9N} u_n(x,t) - \sum_{m=1}^{N} u_m(x,t)\right|}{\left|\sum_{m=1}^{N} u_m(x,t)\right|} < 1\% \tag{A.29}$$

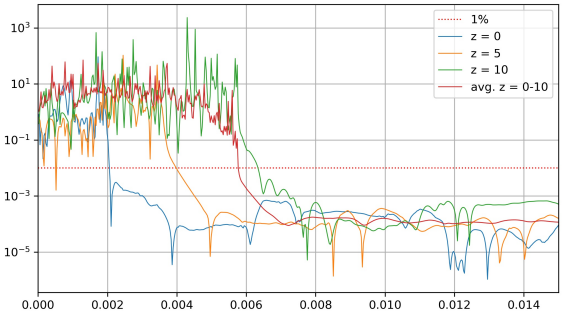
where N is the number of modes. It must be mentioned that the convergence criterion only holds at each point from the moment onwards when the first wave reaches the point, while before that, the denominator is zero. The convergence over time for the block load case from Appendix A.3 and $\mu N = 10$ is studied for both bars. Since the final wavefront just passed half of bar 2, only the upper half of bar 2 is considered. The convergence is checked between $N = 225$ and $N = 250$ modes. Figure A.7 shows that the displacements converge directly after the first wavefront arrives at $\delta < 0.1\%$. It confirms that the number of modes chosen in Appendix A.3 is more than sufficient for converging the displacements.

A.5. Conclusions on two extensible bars in frictional contact

The modelling technique presented in this chapter is suitable for describing the interaction of two flexible bars in frictional contact. Although the stick is not included in the model, high friction forces approximate the linear model corresponding to bars under the stick condition. The accuracy of the solution increases with the number of modes included. The number of modes included is a trade-off between computational efficiency and accuracy, whereas the length of the time signal is linearly related to the computation time. More modes must be included to approximate sudden jumps in stress or velocity. This is important in impact excitations, but sudden jumps are unexpected since the work focuses on harmonic excitations. Conclusively, the modelling approach seems suitable for the field of application since the excitation is mainly harmonic, and the non-linear behaviour of the interface can be included without compromising the computational time compared to linear models.



(a) $\delta(x, t_i)$ of bar 1



(b) $\delta(z, t_i)$ of bar 2

Figure A.7: Relative error between 225 and 250 modes for $t = 0 \rightarrow 0.015$

A

References

Aranda-Ruiz, J., & Fernández-Sáez, J. (2012). On the use of variable-separation method for the analysis of vibration problems with time-dependent boundary conditions. *Proceedings of the Institution of Mechanical Engineers, Part C: Journal of Mechanical Engineering Science*, *226*(12), 2912–2924.

Berger, E. (2002). Friction modeling for dynamic system simulation. *Applied Mechanics Reviews*, *55*(6), 535.

Fricke, M. B., & Rolfes, R. (2015). Towards a complete physically based forecast model for underwater noise related to impact pile driving. *The Journal of the Acoustical Society of America*, *137*(3), 1564–1575.

Leamy, M. J., Barber, J. R., & Perkins, N. C. (1998). Distortion of a harmonic elastic wave reflected from a dry friction support. *Journal of Applied Mechanics, Transactions ASME*, *65*(4), 851–857.

Marques, F., Flores, P., Pimenta Claro, J. C., & Lankarani, H. M. (2016). A survey and comparison of several friction force models for dynamic analysis of multibody mechanical systems. *Nonlinear Dynamics*, *86*(3), 1407–1443.

Molenkamp, T., Tsetas, A., Tsouvalas, A., & Metrikine, A. V. (2020a). Dynamic response of two interacting extensible bars in frictional contact. *Proceedings of the International Conference on Structural Dynamic , EURODYN*, *1*(December), 252–264.

Threlfall, D. C. (1978). The Inclusion of Coulomb Friction in Mechanisms Programs with Particular Reference to DRAM. *Mechanism and Machine Theory*, *13*(4), 475–483.

Tsouvalas, A., & Metrikine, A. V. (2014a). A three-dimensional vibroacoustic model for the prediction of underwater noise from offshore pile driving. *Journal of Sound and Vibration*, *333*(8), 2283–2311.

Yeh, H. C. (1976). Solving boundary value problems in composite media by separation of variables and transient temperature of a reactor vessel. *Nuclear Engineering and Design*, *36*(2), 139–157.

B

Analytical expressions for the inverse Hankel Transforms

The inverse Hankeltransforms obtained in Chapter 2 are partially discontinuous, though analytical expressions can be found for the internal and external domains. There are three types of inverse Hankel Transforms that can be solved analytically:

$$\int_0^\infty \frac{\mathrm{J}_n(kr_s)r_s}{k^2-k_\alpha^2}\mathrm{J}_{n+1}(kr)k^2\mathrm{d}k = \mathrm{i}\hat{k}_\alpha r_s \begin{cases} -\mathrm{K}_n(\mathrm{i}\hat{k}_\alpha r_s)\mathrm{I}_{n+1}(\mathrm{i}\hat{k}_\alpha r) & r<r_s \\ \mathrm{I}_n(\mathrm{i}\hat{k}_\alpha r_s)\mathrm{K}_{n+1}(\mathrm{i}\hat{k}_\alpha r) & r>r_s \end{cases} \tag{B.1}$$

$$\int_0^\infty \frac{\mathrm{J}_n(kr_s)r_s}{k^2-k_\alpha^2}\mathrm{J}_{n}(kr)k\mathrm{d}k = r_s \begin{cases} \mathrm{K}_n(\mathrm{i}\hat{k}_\alpha r_s)\mathrm{I}_{n}(\mathrm{i}\hat{k}_\alpha r) & r<r_s \\ \mathrm{I}_n(\mathrm{i}\hat{k}_\alpha r_s)\mathrm{K}_{n}(\mathrm{i}\hat{k}_\alpha r) & r>r_s \end{cases} \tag{B.2}$$

$$\begin{aligned} \int_0^\infty \frac{\mathrm{J}_n(kr_s)r_s}{k^2-k_\alpha^2}\frac{\mathrm{d}}{\mathrm{d}r}\mathrm{J}_n(kr)k\mathrm{d}k &= \int_0^\infty \frac{\mathrm{J}_n(kr_s)r_s}{k^2-k_\alpha^2}\left(-\mathrm{J}_{n+1}(kr)k+\frac{n}{r}\mathrm{J}_n(kr)\right)k\mathrm{d}k \\ &= r_s \begin{cases} \mathrm{i}\hat{k}_\alpha \mathrm{K}_n(i\hat{k}_\alpha r_s)\mathrm{I}_{n+1}(\mathrm{i}\hat{k}_\alpha r)+\frac{n}{r}\mathrm{K}_n(\mathrm{i}\hat{k}_\alpha r_s)\mathrm{I}_n(\mathrm{i}\hat{k}_\alpha r) & r<r_s \\ -\mathrm{i}\hat{k}_\alpha \mathrm{I}_n(i\hat{k}_\alpha r_s)\mathrm{K}_{n+1}(\mathrm{i}\hat{k}_\alpha r)+\frac{n}{r}\mathrm{I}_n(\mathrm{i}\hat{k}_\alpha r_s)\mathrm{K}_n(\mathrm{i}\hat{k}_\alpha r) & r>r_s \end{cases} \end{aligned} \tag{B.3}$$

with $\mathrm{i}\hat{k}_\alpha = \sqrt{-k_\alpha^2}$.

The fluid and soil sources cause discontinuities in the displacement and stress fields. These discontinuities do not converge. The non-converging terms are analytically found by taking the limit of k to infinity.

$$u_{fr} = \int_0^\infty \frac{s_\mathrm{f}\left(e^{-\alpha_f \frac{h}{2}}-1\right)\mathrm{J}_n(kr_s)r_s}{\alpha_f^2}\frac{\mathrm{d}}{\mathrm{d}r}\mathrm{J}_n(kr)k\mathrm{d}k \tag{B.4}$$

$$= \int_0^\infty \frac{s_\mathrm{f}\left(e^{-\alpha_f \frac{h}{2}} - 1\right)\mathrm{J}_n(kr_s)r_s}{\alpha_f^2}\left(\frac{n}{r}\mathrm{J}_n(kr) - k\mathrm{J}_{n+1}(kr)\right)k\mathrm{d}k \tag{B.5}$$

$$= \text{For large k} \rightarrow \int_0^\infty \frac{s_\mathrm{f}\mathrm{J}_n(kr_s)r_s}{k^2}k\mathrm{J}_{n+1}(kr)k\mathrm{d}k \tag{B.6}$$

$$\tag{B.7}$$

The slow converging term, causing jump:

$$\int_0^\infty \frac{s_\mathrm{f}\mathrm{J}_n(kr_s)r_s}{k}\mathrm{J}_{n+1}(kr)k\mathrm{d}k = s_f\begin{cases}0 & r < r_s\\ r_s^{n+1}r^{-1-n} & r_s \leq r\end{cases} \tag{B.8}$$

Radial soil source:

$$s_{rr} = \int_0^\infty -(\lambda_\mathrm{s} + 2\mu_s)kU_1^P(k,z)\mathrm{J}_n(kr)k\mathrm{d}k \tag{B.9}$$

$$= \int_0^\infty -(\lambda_\mathrm{s} + 2\mu_s)k^2\frac{F_1}{k\alpha_s^2\left(\lambda_s + 2\mu_s\right)}\mathrm{J}_n(kr)k\mathrm{d}k \tag{B.10}$$

$$= \int_0^\infty -k\frac{\frac{\mathrm{d}}{\mathrm{d}r}\mathrm{J}_n(kr_s)r_s q_r}{k\alpha_s^2}\mathrm{J}_n(kr)k\mathrm{d}k \tag{B.11}$$

$$= \int_0^\infty -\frac{\left(\frac{n}{r_s}\mathrm{J}_n(kr_s) - k\mathrm{J}_{n+1}(kr_s)\right)r_s q_r}{\alpha_s^2}\mathrm{J}_n(kr)k\mathrm{d}k \tag{B.12}$$

$$= \text{For large k} \rightarrow \int_0^\infty \frac{k\mathrm{J}_{n+1}(kr_s)r_s q_r}{k^2}\mathrm{J}_n(kr)k\mathrm{d}k \tag{B.13}$$

The slow converging term, causing jump:

$$\int_0^\infty \frac{\mathrm{J}_{n+1}(kr_s)r_s q_r}{k}\mathrm{J}_n(kr)k\mathrm{d}k = q_r\begin{cases}r^n r_s^{-n} & r < r_s\\ 0 & r_s \leq r\end{cases} \tag{B.14}$$

Vertical soil source:

$$s_{rz} = \int_0^\infty -\mu_s kU_3^P(k,z)\mathrm{J}_{n+1}(kr)k\mathrm{d}k \tag{B.15}$$

$$= \int_0^\infty -\mu_s k k^2\frac{F_3}{k^2\beta_s^2\mu_s}\mathrm{J}_{n+1}(kr)k\mathrm{d}k \tag{B.16}$$

$$= \int_0^\infty -k\frac{\mathrm{J}_n(kr_s)r_s q_z}{\beta_s^2}\mathrm{J}_{n+1}(kr)k\mathrm{d}k \tag{B.17}$$

$$= \text{For large k} \rightarrow -\int_0^\infty \frac{k\mathrm{J}_n(kr_s)r_s q_z}{k^2}\mathrm{J}_{n+1}(kr)k\mathrm{d}k \tag{B.18}$$

Slow converging term, causing jump:

$$\int_0^\infty -\frac{\mathrm{J}_n(kr_s)r_s q_z}{k}\mathrm{J}_{n+1}(kr)k\mathrm{d}k = -q_z\begin{cases}0 & r < r_s\\ r_s^{n+1}r^{-1-n} & r_s \le r\end{cases} \tag{B.19}$$

Curriculum Vitæ

Timo Molenkamp

26-02-1994 Born in Enschede, Netherlands

Education

2005–2011 VWO
Het Assink Lyceum, Haaksbergen, the Netherlands

2011–2014 Bachelor in Architecture, Urbanism and Building Sciences
Eindhoven University of Technology

2014–2018 Master in Civil Engineering
Delft University of Technology
Thesis: Soil structure interaction for shallow foundations in 2D and 3D
Supervisors: Prof. dr. it. A.V. Metrikine, Dr. ir. A. Tsouvalas, Ir. F.Besseling, Dr. ir, K.N. van Dalen

2018–2023 PhD Research
Delft University of Technology
Thesis: Sound emission in offshore pile driving by vibratory devices
Promotor: Dr. ir. A. Tsouvalas
Promotor: Prof. dr. it. A.V. Metrikine

Industry

2023– Delft Cymatics B.V.
Co-founder

List of Publications

Journal publications

5. **Molenkamp**, **T.**, Tsouvalas, A., & Metrikine, A. (2024). A numerical study on the effect of asymmetry on underwater noise emission in offshore monopile installation. *Ocean Engineering*, *299*, 117351
4. **Molenkamp**, **T.**, Tsetas, A., Tsouvalas, A., & Metrikine, A. (2024). Underwater noise from vibratory pile driving with non-linear frictional pile–soil interaction. *Journal of Sound and Vibration*, *576*, 118298
3. **Molenkamp**, **T.**, Tsouvalas, A., & Metrikine, A. (2023). The influence of contact relaxation on underwater noise emission and seabed vibrations due to offshore vibratory pile installation. *Frontiers in Marine Science*, *10*, 357
2. Tsetas, A., Tsouvalas, A., Gómez, S. S., Pisanò, F., Kementzetzidis, E., **Molenkamp**, **T.**, Elkadi, A. S., & Metrikine, A. V. (2023). Gentle Driving of Piles (GDP) at a sandy site combining axial and torsional vibrations: Part I - installation tests. *Ocean Engineering*, *270*, 113453
1. Tsetas, A., Tsouvalas, A., **Molenkamp**, **T.**, & Metrikine, A. V. (2022). A mode-matching method for the prediction of stick-slip relative motion of two elastic rods in frictional contact. *Acta Mechanica*, *233*, 753–773

Conference publications

9. **Molenkamp**, **T.**, & Tsouvalas, A. (2024). Underwater Noise from Gentle Driving of Piles. *Proceedings of the 30th International Congress on Sound and Vibration*
8. Peng, Y., Tsetas, A., **Molenkamp**, **T.**, Sertlek, O., & Tsouvalas, A. (2024). Underwater Sound Modelling and Sound Mapping in Vibratory Pile Driving. *Proceedings of the 30th International Congress on Sound and Vibration*
7. Tsetas, A., Kementzetzidis, E., Gómez, S. S., **Molenkamp**, **T.**, Elkadi, A. S. K., Pisanò, F., Tsouvalas, A., & Metrikine, A. V. (2024). Gentle Driving of Piles: Field Observations, Quantitative Analysis and Further Development. *Proceedings of the Offshore Technology Conference*
6. **Molenkamp**, **T.**, Tsouvalas, A., & Metrikine, A. (2022, September). The effect of pile slip on underwater noise emission in vibratory pile driving. In A. Zingoni (Ed.). CRC Press

5. **Molenkamp**, **T.**, Tsouvalas, A., & Metrikine, A. (2022). The effect of pile-slip sliding on underwater noise from vibratory pile driving. *Proceedings of In Proceedings of the 28th International Congress on Sound and Vibration*

4. Tsetas, A., Gómez, S. S., Tsouvalas, A., van Beek, K., Tehrani, F. S., Kementzetzidis, E., Pisanò, F., Elkadi, A., Segeren, M., **Molenkamp**, **T.**, & Metrikine, A. V. (2020). Experimental identification of the dynamic behaviour of pile-soil system installed by means of three different pile-driving techniques. *Proceedings of the International Conference on Structural Dynamic , EURODYN*, *2*, 3005–3015

3. Tsouvalas, A., **Molenkamp**, **T.**, Canny, K., Kroon, D., Versluis, M., Peng, Y., & Metrikine, A. V. (2020). A mode matching technique for the seismic response of liquid storage tanks including soil-structure interaction. *Proceedings of the International Conference on Structural Dynamic , EURODYN*, *1*, 1–14

2. **Molenkamp**, **T.**, Tsetas, A., Tsouvalas, A., & Metrikine, A. V. (2020). Dynamic response of two interacting extensible bars in frictional contact. *Proceedings of the International Conference on Structural Dynamic , EURODYN*, *1*, 252–264

1. Metrikine, A. V., Tsouvalas, A., Segeren, M. L. A., Ekadi, A. S. K., Tehrani, F. S., Gómez, S. S., Atkinson, R., Pisanò, F., Kementzetzidis, E., Tsetas, A., **Molenkamp**, **T.**, van Beek, K., & de Vries, P. (2020). GDP: A New Technology for Gentle Driving of (Mono)Piles. *In Proceedings of the 4th International Symposium on Frontiers in Offshore Geotechnics*, 16–19. https://www.researchgate.net/publication/367177118